



UNIVERSITÀ
DEGLI STUDI
DI PALERMO

INTEGRATED MULTI-PHYSICS DESIGN TOOL FOR FUSION BREEDING BLANKET SYSTEMS - DEVELOPMENT AND VALIDATION

Corso di Dottorato di Ricerca in
“**Energia e Tecnologie dell’Informazione - curriculum Fisica Tecnica e
Ingegneria Nucleare**”
Dipartimento di Ingegneria
Settore Scientifico Disciplinare ING-IND/19

IL DOTTORE
GANDOLFO ALESSANDRO SPAGNUOLO

I TUTOR
PROF. PIETRO ALESSANDRO DI MAIO
PROF. DR.-ING. ROBERT STIEGLITZ

IL COORDINATORE
PROF. MAURIZIO CELLURA

CICLO XXXII
ANNO CONSEGUIMENTO TITOLO 2020



**INTEGRATED MULTI-PHYSICS DESIGN TOOL FOR
FUSION BREEDING BLANKET SYSTEMS -
DEVELOPMENT AND VALIDATION**

Zur Erlangung des akademischen Grades eines
DOKTORS DER INGENIEURWISSENSCHAFTEN (Dr.-Ing.)

von der KIT-Fakultät für Maschinenbau des
Karlsruher Instituts für Technologie (KIT)

angenommene
DISSERTATION

von
GANDOLFO ALESSANDRO SPAGNUOLO

Tag der mündlichen Prüfung: 8 Juli 2020

Hauptreferent: Prof. Dr.-Ing. Robert Stieglitz
Karlsruher Institut für Technologie (KIT)

Korreferent: Prof. Pietro Alessandro Di Maio
Università degli Studi di Palermo

Abstract

The Breeding Blanket (BB) of the DEMO reactor represents a harsh system in a dangerous environment.

It has to satisfy engineering requirements and constraints that are of nuclear, thermo-structural, material and safety kind. For these reasons, the application of advanced simulation tools, based on a multi-physics approach, is required for its comprehensive design. These tools have to simultaneously perform different kinds of analyses among which three, and namely nuclear, thermofluid-dynamic and thermo-mechanical, can be prioritized and considered as propaedeutic for the investigation of all the other issues related to the BB.

In this dissertation, a multi-physic approach, covering the three pillars of the BB design (the neutronics, thermal-hydraulics and thermo-mechanics), is proposed. These analyses have to be conducted in a strongly integrated way, allowing a holistic assessment of volumetric heat loads, thermal performances of coolant and structures as well as their stress and deformation states.

The strategy, followed for the achievement of this challenge, consists of creating a CAD-centric and loosely-coupled procedure for the BB concepts design adopting a sub-modelling technique, named Multi-physics Approach for Integrated Analysis (MAIA). The MAIA procedure bases its architecture on the use of validated codes and the minimisation of their number. It is articulated in 10 main steps that go from the decomposition of generic CAD in a format suitable for neutron/photon transport analysis to the nuclear analysis for the assessment of volumetric heating, from the assessment of temperature and velocity fields within coolant and structure to the evaluation of their displacement, deformation and stress fields, from the evaluation of nitrogen isotopes production rates from water oxygen activation to the calculation of their concentration spatial distribution taking into account the effects of passive convective transport. All the steps share the same geometry details and the consistency between input and output parameters. The new MAIA procedure differs from the conventional coupling approach for three key aspects. First, it does not introduce homogenisations of models and loads. Second, MAIA can capture local load gradients at high resolution in the three directions for all the analysis involved without requiring prohibitive computational efforts. And third, MAIA keeps the consistency between the three analyses maintaining the congruence between inputs and outputs.

However, the computational effort required by the CAD-centric feature of MAIA procedure imposes the representation of BB portions and, therefore, the definition and validation of boundary conditions for each performed calculation.

Regarding the nuclear analysis, it has been found that the set of reflecting and white conditions in the poloidal and toroidal directions, respectively, together with the presence of Vacuum Vessel (VV) and the definition of local neutron and photon source, produces a mismatch of -0.48 % in terms of power deposition between the DEMO and the local (e.g. slice) models. It has been demonstrated that the neutronic symmetry conditions are valid in the entire module up to the last slices nearby the caps. Furthermore, a sensitivity analysis on the angular distribution of local neutron and photon source has been performed indicating in 10 cosine bins the optimal discretisation choice in terms of compromise between the fidelity of the results obtained with respect to those of the reference model and the relevant computational effort.

Concerning the analysis of thermal-hydraulic boundary conditions, it has been found that the variation on mass flow rates (comprised between the \sim -1.3 % and the \sim -0.6 %) as well as power density fluctuation (up to the \sim 6 % in the neighbouring domains) affect the temperature distribution for less than \pm 2.4 % demonstrating the applicability of poloidal symmetry conditions.

As far as the thermo-mechanical analyses are concerned, it has been identified the set of boundary conditions (radial and toroidal displacements prevented to the nodes lying in the rear of the back supporting structure along the toroidal and poloidal direction, symmetry at the lower cut surface and Generalised Plane Strain to the top one) that produce a discrepancy in terms of displacement in the sub-model comprised between the -6 % and the 4 % as well as a conservative assessment of membrane and bending stresses both for primary and secondary stresses. The impact of the temperature variation has also been investigated showing that the fluctuations on total deformation are comprised between -0.3 % and the 1.7 %, on equivalent membrane stress up to 15 % while on equivalent bending stress between the -7 % and the 5 %.

As a proof-of-concept, the MAIA procedure has been then used to evaluate the impact on the BB design, demonstrating that some criticalities are present in the design. In particular, the fluid-dynamic results show a violation of the temperature requirement limits that have not been solved introducing proper design solutions. Furthermore, these violations of thermal-hydraulic requirements produce very intense values of Von Mises equivalent stresses that could jeopardize the structural integrity of the segment box. This demonstrates that MAIA procedure can become the reference tool for the design of the BB. Moreover, the MAIA procedure has proven the possibility to locally map important variables such as the neutron flux and the temperature as well as the primary and secondary stress that are used for the determination of the allowable stress and applied for comparing with design criteria.

To further demonstrate the versatility and adaptability of the MAIA procedure, the water activation issue occurring within the blanket Primary Heat Transfer System (PHTS) has been studied. Using MAIA procedure, it has been possible to take into account the effects of the flow on the nitrogen concentration and to provide useful information for the development of both BB design and its PHTS.

Sommario

Il Breeding Blanket (BB) del reattore DEMO rappresenta un sistema complesso in un ambiente pericoloso. Infatti, deve soddisfare diversi requisiti e vincoli ingegneristici sia di tipo nucleare, termo-strutturale che di sicurezza. Per questi motivi, è necessaria una progettazione omnicomprensiva che preveda l'applicazione di strumenti avanzati di simulazione basati su approcci multi-fisici. Questi strumenti devono eseguire simultaneamente diversi tipi di analisi. Tre di esse possono essere considerate prioritarie e propedeutiche per lo studio di tutti gli altri fenomeni riguardanti il BB, vale a dire l'analisi nucleare, termo-fluidodinamica e strutturale.

In questa tesi, è proposto un innovativo approccio multi-fisico che copre i tre pilastri principali su cui è basato il progetto del BB (la neutronica, la termoidraulica e la termo-meccanica). Queste analisi devono essere condotte in maniera integrata, consentendo una valutazione olistica dei carichi volumetrici di potenza, delle prestazioni termiche sia del fluido di raffreddamento che delle strutture, nonché dei campi di tensione e deformazione.

La strategia seguita per il conseguimento di questa sfida consiste nella creazione di una procedura "CAD-centric" e "loosely-coupled" (debolmente accoppiata) per la progettazione dei concetti di BB utilizzando una tecnica di analisi basata su sotto-modelli. Questa procedura prende il nome di Multi-physics Approach for Integrated Analysis (MAIA). La sua architettura si basa sull'uso di codici validati e sulla minimizzazione del loro numero. In particolare, MAIA è articolata in 10 fasi principali che vanno dalla creazione di un modello per le analisi nucleari, generato dalla decomposizione in geometrie semplici di un generico CAD, alla valutazione della potenza volumetrica, dal calcolo dei campi di temperatura e velocità nella struttura e nel refrigerante alla valutazione dei campi di spostamento, deformazione e stress, dalla stima dei tassi di produzione degli isotopi dell'azoto prodotti dall'attivazione dell'ossigeno presente nell'acqua al calcolo della loro distribuzione spaziale di concentrazione tenendo conto degli effetti del trasporto convettivo. Tutti i vari passaggi condividono gli stessi dettagli geometrici.

In particolare, MAIA differisce dagli approcci convenzionali usati nell'accoppiamento multi-fisico su tre aspetti chiave. Innanzitutto, non introduce omogeneizzazioni/semplificazioni dei modelli e dei carichi. In secondo luogo, MAIA permette di determinare, con un'alta risoluzione spaziale, i gradienti dei carichi per tutte le analisi coinvolte senza richiedere sforzi computazionali proibitivi. In terzo luogo, MAIA permette di mantenere la coerenza tra le tre analisi garantendo la congruenza tra gli input e gli output.

Tuttavia, l'onere computazionale richiesto dall'approccio CAD-centric, su cui si basa la procedura MAIA, non permette di rappresentare il BB nel suo complesso ma solo alcune sue porzioni (una slice, per esempio). Ciò impone la definizione e, conseguentemente, la validazione di opportune condizioni al contorno per ogni sotto-modello utilizzato e per ogni analisi eseguita.

A tal proposito, per quanto riguarda le analisi nucleari, le condizioni al contorno utilizzate nel modello locale della slice sono: definizione di una sorgente locale neutronica/fotonica per tener in conto l'effetto albedo dell'intero reattore, rappresentazione del Vacuum Vessel (VV) per simulare il back scattering verso il BB, e l'applicazione di condizioni di riflessione ("mirror", specchio/simmetria, nella direzione poloidale e "white", riflessione isotropica, in quella toroidale) per simulare la presenza delle slice adiacenti a quella analizzata.

I risultati ottenuti mostrano una variazione della potenza depositata del -0.48 % tra il modello di riferimento DEMO e quello locale (slice) usato in MAIA. Inoltre, è stata eseguita un'analisi di sensibilità sulla distribuzione angolare della sorgente neutronica/fotonica locale determinando una discretizzazione

ottimale in 10 suddivisioni poloidali in coseno. Questa suddivisione rappresenta un buon compromesso sia in termini di fedeltà dei risultati ottenuti nel modello locale rispetto a quelli del modello di riferimento (DEMO), che di minimizzazione dell'onere computazionale.

Per quanto riguarda l'analisi delle condizioni al contorno termo-idrauliche usate nel modello locale della slice, è stata applicata una condizione di simmetria termica poloidale. Assumendo una variazione delle portate comprese tra $\sim -1.3\%$ e $\sim 0.6\%$ e una fluttuazione della densità di potenza fino a $\sim 6\%$ tra slice adiacenti, è stata ottenuta una variazione della distribuzione delle temperature solo del $\pm 2.4\%$ dimostrando, quindi, l'applicabilità di tali condizioni.

Per quanto riguarda le analisi termo-meccaniche, le condizioni al contorno identificate per il modello locale della slice sono: simmetria sul piano inferiore della slice, Generalised Plane Strain su quello superiore e spostamenti radiali e toroidali impediti ai nodi che giacciono nella parte posteriore della Back Supporting Structure del BB lungo la direzione toroidale e poloidale. Queste condizioni, applicate al sotto-modello, producono una variazione compresa tra il -6% e il 4% tra gli spostamenti calcolati in MAIA nella slice e quelli nel modello di riferimento DEMO, nonché una stima conservativa delle tensioni primarie e secondarie sia di membrana che di flessione. Inoltre, è stato anche studiato l'impatto della variazione ($\pm 2.4\%$) di temperatura dimostrando che le fluttuazioni sulle deformazioni totale sono comprese tra il -0.3% e l' 1.7% , fino a un massimo del 15% sulle tensioni equivalenti di membrana e tra il -7% e il 5% su quelle di flessione.

Infine, la procedura MAIA è stata utilizzata per valutare l'impatto sul design del BB. La sua applicazione ha dimostrato la presenza di alcune criticità nel progetto. In particolare, i risultati fluidodinamici mostrano una violazione dei limiti di temperatura che non sono stati risolti introducendo soluzioni progettuali adeguate. Inoltre, queste violazioni producono, a loro volta, valori molto intensi delle tensioni equivalenti di Von Mises che potrebbero indicare un pericolo per l'integrità strutturale del BB.

L'applicazione di MAIA al design del BB ha permesso di dimostrare il valore aggiunto di questa procedura la quale potrebbe diventare uno strumento fondamentale e di riferimento per la progettazione del BB.

Inoltre, la procedura MAIA ha permesso di mappare localmente variabili importanti come flussi neutronici e temperature, nonché le tensioni primarie e secondarie che sono utilizzate per la determinazione delle tensioni ammissibili applicate per la verifica dei criteri di progettazione.

Al fine di dimostrare ulteriormente la versatilità e l'adattabilità della procedura MAIA, è stato studiato il problema dell'attivazione dell'acqua del sistema di trasferimento di calore primario (Primary Heat Transfer System, PHTS). Utilizzando la procedura MAIA, è stato possibile prendere in considerazione gli effetti dell'efflusso sulla concentrazione degli isotopi dell'azoto e fornire informazioni utili per lo sviluppo sia del design del BB che del suo PHTS.

Kurzfassung

Das Brut-Blanket (BB) des DEMO-Reaktors ist ein anspruchsvolles System in gefährlicher Umgebung. Es unterliegt nukleartechnischen, thermisch-strukturellen sowie material- und sicherheitsrelevanten Anforderungen und Voraussetzungen, und seine komplexe Auslegung bedingt den Einsatz hochentwickelter multiphysikalischer Simulationstools. Diese Tools müssen die gleichzeitige Durchführung verschiedener Analysen erlauben. Drei dieser Analyseverfahren, nämlich das nukleare, das thermofluiddynamische und das thermomechanische Verfahren, können priorisiert und als vorbereitend für die Untersuchung aller weiteren Fragen im Zusammenhang mit dem Brut-Blanket betrachtet werden.

Diese Dissertation schlägt einen die drei Säulen der Brut-Blanket-Auslegung (Neutronik, Thermohydraulik und Thermomechanik) umfassenden multiphysikalischen Ansatz vor. Zur Gewährleistung einer gesamtheitlichen Beurteilung der volumetrischen Wärmelasten, der thermischen Leistungen von Kühlmittel und Strukturmaterial sowie der Spannungs- und Verformungszustände müssen die entsprechenden Analysen im Verbund durchgeführt werden.

Die Strategie zur Bewältigung dieser Herausforderung besteht in der Entwicklung eines CAD-zentrierten und lose gekoppelten Verfahrens für die Auslegung des Brut-Blankets mit Hilfe der Teilmodellierungstechnik MAIA (Multi-physics Approach for Integrated Analysis). Die Architektur von MAIA basiert auf der Verwendung validierter Codes und der Minimierung der Anzahl dieser Codes. Das Verfahren gliedert sich in zehn Hauptschritte, angefangen mit der Umwandlung des generischen CAD-Modells in ein für die Neutronen-/Photonentransportanalyse geeignetes Format, der kerntechnischen Analyse zur Beurteilung der volumetrischen Erwärmung und der Beurteilung der Temperatur- und Geschwindigkeitsfelder innerhalb von Kühlmittel und Strukturmaterial über die Bewertung der Verschiebungs-, Verformungs- und Spannungsfelder, die quantitative Bewertung der Erzeugung von Stickstoffisotopen durch Sauerstoffaktivierung des Wasser bis hin zur Berechnung der Konzentrationsverteilung unter Berücksichtigung der Auswirkungen des passiven konvektiven Transports. Allen Schritten gemeinsam sind die geometrischen Details und die Übereinstimmung zwischen Input- und Output-Parametern. Das neue MAIA-Verfahren unterscheidet sich vom konventionellen Kopplungsansatz in drei wesentlichen Aspekten: 1. Modelle und Lasten werden nicht homogenisiert. 2. Lastgradienten können mit hoher Auflösung in drei Richtungen für alle relevanten Analysen ohne übermäßigen Rechenaufwand erfasst werden. 3. Die Übereinstimmung zwischen den drei Analyseverfahren und die Kongruenz zwischen Inputs und Outputs wird gewährleistet.

Der durch die CAD-zentrierte Funktion des MAIA-Verfahrens erforderliche Rechenaufwand bedingt allerdings die Darstellung von Teilen des Brut-Blankets und damit die Definition und Validierung von Randbedingungen für jede durchgeführte Berechnung. In Bezug auf die kerntechnische Analyse hat sich gezeigt, dass die relevanten Reflexions- und Weißzustände in poloidaler bzw. toroidaler Richtung zusammen mit dem Vorhandensein des Vakuumbehälters und der Definition lokaler Neutronen- und Photonquellen zu einer Diskrepanz von -0,48 % in Bezug auf die aufgenommene Leistung zwischen DEMO-Reaktor und lokalen (z.B. Scheiben-)Modellen führen. Die neutronenphysikalischen Symmetriebedingungen gelten für das gesamte Modul einschließlich der Scheiben in der Nähe der Caps. Es wurde eine Sensitivitätsanalyse im Hinblick auf die Winkelverteilung der lokalen Neutronen- und Photonquelle durchgeführt, die in 10 Cosinus-Bins die optimale Diskretisierung in Bezug auf den Kompromiss zwischen der Genauigkeit der erhaltenen Ergebnisse und den Ergebnissen des Referenzmodells und dem entsprechenden Rechenaufwand angibt.

Bei der Analyse der thermohydraulischen Randbedingungen wurde festgestellt, dass die

Beeinflussung der Temperaturverteilung durch die Abweichung der Massenströme (zwischen $\sim -1,3\%$ und $\sim -0,6\%$) und die Leistungsdichteschwankungen (bis zu $\sim 6\%$ in den benachbarten Bereichen) weniger als $\pm 2,4\%$ beträgt. Dies belegt die Anwendbarkeit der poloidalen Symmetriebedingungen.

Im Verlauf der thermomechanischen Analysen wurden die Randbedingungen (d.h. radiale und toroidale Verschiebungen, die an den Knoten auf der Rückseite der hinteren Stützstruktur in toroidaler und poloidaler Richtung verhindert werden, Symmetrie an der unteren sowie generalisierter ebener Verformungszustand an der oberen Schnittfläche) bestimmt, die zu einer Diskrepanz in Bezug auf die Verschiebung im Teilmodell zwischen -6% und 4% und einer konservativen Bewertung der primären und sekundären Membran- und Biegespannungen führen. Darüber hinaus wurden die Auswirkungen der Temperaturschwankungen untersucht. Dabei zeigten sich Schwankungen der Gesamtverformung zwischen $-0,3\%$ und $1,7\%$, Schwankungen der äquivalenten Membranspannung von bis zu 15% und Schwankungen der äquivalenten Biegespannung zwischen -7% und 5% .

Das MAIA-Verfahren wurde anschließend zur Bewertung diverser Auswirkungen auf die Auslegung des Brut-Blankets herangezogen. Dabei wurden einige Kritikpunkte offenbar. Insbesondere zeigen die strömungsdynamischen Ergebnisse Überschreitungen der Grenztemperatur. Hierfür konnten keine geeigneten Konstruktionslösungen gefunden werden. Diese Nichteinhaltung der thermohydraulischen Anforderungen führt darüber hinaus zu sehr hohen, die Segmentstabilität möglicherweise gefährdenden Werten der von-Mises-Vergleichsspannungen. Im Hinblick auf das oben Gesagte kann das MAIA-Verfahren als Referenztool für die Auslegung des Brut-Blankets verwendet werden. Darüber hinaus hat das Verfahren die Möglichkeit aufgezeigt, sowohl wichtige zur Bestimmung der zulässigen Spannung und zur Erfüllung der Auslegungskriterien erforderliche Variablen wie den Neutronenfluss und die Temperatur als auch Primär- und Sekundärspannungen lokal abzubilden.

Zur weiteren Veranschaulichung der Vielseitigkeit und Anpassungsfähigkeit des MAIA-Verfahrens wurde das Problem der Wasseraktivierung innerhalb des Blanket Primary Heat Transfer Systems (PHTS) untersucht. Mit MAIA konnten die Auswirkungen der Strömung auf die Stickstoffkonzentration berücksichtigt und nützliche Informationen für die Entwicklung der Brut-Blanket-Auslegung und des PHTS geliefert werden.

Contents

| | |
|---|-------|
| Abstract | v |
| Sommario | vii |
| Kurzfassung..... | ix |
| List of Acronyms..... | xiii |
| List of Symbols | xv |
| Latin Symbols..... | xv |
| Greek Symbols | xviii |
| 1 Introduction | 1 |
| 1.1 Notes on Nuclear Fusion..... | 2 |
| 1.2 The Demonstration Fusion Reactor DEMO and the Breeding Blanket Systems..... | 4 |
| 1.2.1 Helium-Cooled Pebble Beds Design Configuration..... | 6 |
| 1.2.2 Water-Cooled Lithium-Lead Design Configuration..... | 8 |
| 1.3 Blanket Challenges and State-of-the-Art of Coupling Analyses | 9 |
| 1.4 Objectives of a New Multi-Physics Approach for Integrated Analysis..... | 11 |
| 1.5 Organization of the Thesis | 13 |
| 2 Theories and Mathematical Models of Coupling | 15 |
| 2.1 Neutronic Model | 15 |
| 2.1.1 Neutron and Photon Transport..... | 15 |
| 2.1.2 Monte Carlo Method and MCNP for Transport Modes | 18 |
| 2.2 Thermal-Hydraulic Model | 20 |
| 2.2.1 Thermal-Hydraulic General Conservation Laws..... | 20 |
| 2.2.2 Computational Fluid Dynamics Model | 24 |
| 2.3 Thermo-Mechanic Model | 25 |
| 2.3.1 Elements of Structural-Mechanics..... | 25 |
| 2.3.2 Finite Element Method | 28 |
| 3 Description of Multi-Physics Approach for Integrated Analysis (MAIA)..... | 31 |
| 3.1 Structure of the MAIA Coupling Procedure | 31 |
| 3.2 Geometry Decomposition and Conversion in MAIA Procedure | 33 |
| 3.2.1 CSG Modelling..... | 33 |
| 3.2.2 Hybrid Modelling | 35 |
| 3.3 Neutronic Analysis in MAIA Procedure..... | 36 |
| 3.3.1 Neutron and Photon Local Source Definition..... | 37 |
| 3.3.2 Boundary Conditions for Local Neutronic Models | 38 |
| 3.4 CFD Analysis in MAIA Procedure..... | 39 |
| 3.4.1 Mapping of Heat Generation | 40 |
| 3.4.2 Thermal-hydraulic Boundary Conditions for Local Models | 41 |
| 3.5 Thermo-Mechanical Analysis in MAIA Procedure | 42 |
| 3.5.1 Mapping of Temperature Field..... | 42 |
| 3.5.2 Boundary Conditions for Local Models | 42 |
| 4 Validation of MAIA Procedure Applied to the Breeding Blanket and Sensitivity Analysis | 45 |
| 4.1 Consistency Check of Local Source and Boundary Conditions for Neutronic Analysis..... | 45 |
| 4.1.1 Boundary Conditions Consistency Verification | 46 |

| | | |
|-------|---|-----|
| 4.1.2 | Local Source Representation and Sensitivity Analysis | 58 |
| 4.2 | Consistency Verification of MAIA Thermal-Hydraulic Model..... | 60 |
| 4.2.1 | Adequateness of Boundary Conditions | 65 |
| 4.2.2 | Sensitivity Analysis of Symmetry Conditions..... | 68 |
| 4.3 | Consistency Verification of MAIA Thermo-Mechanical Model..... | 70 |
| 4.3.1 | Consistency Check of Boundary Conditions | 70 |
| 4.3.2 | Sensitivity Analysis of Deformation and Stress Fields | 83 |
| 5 | Application of the MAIA Procedure for the HCPB Breeding Blanket Test Case..... | 85 |
| 5.1 | Neutronic Analysis HCPB Breeding Blanket Slice Test Case | 85 |
| 5.1.1 | Neutron/Photon Radiation Transport Model Setup | 85 |
| 5.1.2 | Nuclear Heating..... | 86 |
| 5.2 | Computational Fluid Dynamics Analysis of HCPB Breeding Blanket Slice Test Case..... | 91 |
| 5.2.1 | Computational Domain..... | 91 |
| 5.2.2 | Thermal-Hydraulic Analysis | 92 |
| 5.3 | Structural Assessment of HCPB Breeding Blanket Slice Test Case..... | 94 |
| 5.3.1 | Finite Element Model | 94 |
| 5.3.2 | Structural Analysis | 95 |
| 6 | Application of MAIA Procedure for Nuclear Safety Assessment..... | 99 |
| 6.1 | General Introduction to Nuclear Safety Analysis for Fusion..... | 99 |
| 6.2 | Water Activation in Fusion Nuclear Reactors | 99 |
| 6.3 | Enhanced Use of MAIA Procedure for Water Activation Analysis on WCLL BB..... | 102 |
| 6.3.1 | Adaptation of MAIA Procedure for Water Activation Studies on WCLL BB..... | 102 |
| 6.3.2 | ¹⁶ N and ¹⁷ N Volumetric Density Distributions of WCLL Breeder Unit..... | 104 |
| 6.3.3 | Fluid-Dynamic Analysis of WCLL Breeder Unit ¹⁶ N and ¹⁷ N Concentrations..... | 108 |
| 7 | Summary and Outlook..... | 113 |
| 7.1 | Summary..... | 113 |
| 7.2 | Outlook and Future Work | 115 |
| 8 | References | 117 |
| 9 | Appendix | 123 |
| 9.1 | Volume Comparison between ANSYS DesignModeler and CSG Modelling..... | 123 |
| 9.2 | PS and GPS Definition..... | 131 |
| 9.3 | MAIA Neutron and Photon Transport Analysis Consistency Verification | 133 |
| 9.4 | MAIA Thermal-hydraulic Symmetry Condition Consistency Verification..... | 139 |
| 9.5 | MAIA Thermal-hydraulic Symmetry Condition Sensitivity Analysis | 141 |
| 9.6 | MAIA Thermo-mechanic Conditions Consistency Verification | 145 |
| 9.7 | MAIA Procedure HCPB Test Case..... | 155 |
| 9.8 | Validation of the Enhanced MAIA procedure for Water Activation Analysis..... | 157 |
| 9.9 | Conventional and EMBEE Tallies Comparison for Nitrogen Production Rate..... | 161 |
| | Acknowledgements | 163 |

List of Acronyms

| | |
|-----------------|--|
| ACPs | Activated Corrosion Products |
| BB | Breeding Blanket |
| BoP | Balance of Plant |
| BP | Backplate |
| BRep | Boundary Representation |
| BSS | Back Supporting Structure |
| BU | Breeder Unit |
| BZ | Breeder Zone |
| C&S | Code&Standard |
| CAE | Computer-Aided Engineering |
| CEL | CFX Expression Language |
| CFD | Computational Fluid Dynamics |
| CP | Cooling Plates |
| CSG | Constructive Solid Geometry |
| CV | Control Volumes |
| D | Deuterium |
| DBTT | Ductile-Brittle Transition Temperature |
| DEMO | Demostration |
| DEMO2015 | EU-DEMO Baseline 2015 |
| DoE | Design Of Experiment |
| DOF | Degree Of Freedom |
| dpa | displacement per atom |
| EB | Energy Bin |
| EU | European Union |
| FDf | Fusion Development Facility |
| FDM | Finite Difference Method |
| FEM | Finite Element Method |
| FENDL | Fusion-Evaluated Data Library |
| FM | Flux Multiplier |
| FoM | Figure of Merit |
| FPP | Fusion Power Plant |
| FVM | Finite Volume Method |
| FW | First Wall |
| GPS | Generalised Plane Strain |
| H&CD | Heating and Current Drive |
| HCPB | Helium Cooled Pebble Beds |
| Hex20 | 20-Noded Hexahedral |
| HTC | Heat Transfer Coefficient |

| | |
|---------------|---|
| IB | Inboard |
| IFMIF | International Fusion Materials Irradiation Facility |
| ipn | integration points |
| LiPb | Lithium-Lead |
| LOCA | Loss Of Coolant Accident |
| MAIA | Multi-Physics Approach For Integrated Analysis |
| MC | Monte Carlo |
| mfp | mean free path |
| MHD | Magnetohydrodynamic |
| MP | Manifold purge |
| MS-FAD | Materials-Specific Failure Assessment Diagram |
| NPP | Nuclear Power Plant |
| NWL | Neutron Wall Load |
| OB | Outboard |
| PFC | Plasma Facing Components |
| PS | Plane Strain |
| PSr | Plane Stress |
| PWR | Pressurized Water Reactor |
| RAMI | Reliability/Maintainability/Availability/Inspectability |
| T | Tritium |
| TBR | Tritium Breeding Ratio |
| TCC | Thermal Contact Conductance |
| Tet10 | 10-Noded Tetrahedral |
| UM | Unstructured Mesh |
| VV | Vacuum Vessel |
| WCLL | Water Cooled Lithium-Lead |
| Wed15 | 15-Noded Prism |
| WPBB | Work Package Breeding Blanket |

List of Symbols

Latin Symbols

| Symbol | Unit | Description |
|---------------|----------------------------------|---|
| a | $[\text{kg}^{-1} \text{m}^{-1}]$ | Coefficient of pressure drop characteristic curve |
| A | $[\text{m}^2]$ | Area |
| A_{TALLY} | $[\text{m}^2]$ | Surface for biasing neutrons and photons in cosine and energy |
| a_{UP} | $[-]$ | Coefficient multiplied to the power density of UP neighbouring slice |
| b | $[-]$ | Coefficient of pressure drop characteristic curve |
| \mathbf{B} | $[\text{T}]$ | Vectorial magnetic field distribution |
| b_{DOWN} | $[-]$ | Coefficient multiplied to the power density of DOWN neighbouring slice |
| C_i | $[-]$ | Cosine emission probability |
| C_0 | $[\text{J MeV}^{-1}]$ | Energy unit conversion constant |
| c_{UP} | $[-]$ | Coefficient multiplied to the mass flow rate of UP neighbouring slice |
| d_{ij} | $[\text{Pa}]$ | Dynamic term of fluid stress tensor σ_{ij}^f |
| d^3r | $[\text{cm}^3]$ | Infinitesimal volume |
| $d\mathbf{S}$ | $[\text{cm}^2]$ | Elementary surface vector |
| d_{DOWN} | $[-]$ | Coefficient multiplied to the mass flow rate of DOWN neighbouring slice |
| e | $[\text{J m}^{-3}]$ | Fluid energy density |
| e_{tot} | $[\text{J m}^{-3}]$ | Fluid total energy density |
| E | $[\text{Pa}]$ | Young's modulus |
| E_{fus} | $[\text{MeV}]$ | Fusion reaction energy yield |
| E_k | $[\text{J}]$ | Kinetic energy |
| E_i | $[\text{MeV}]$ | Energy bins |
| $E_{i,j}$ | $[-]$ | Energy emission probability for each cosine bin |
| f | $[-]$ | Probability density |
| F | $[\text{Pa}]$ | Peak stress |
| \mathbf{F} | $[\text{J}]$ | Vectorial external force acting on the system |
| F_i | $[\text{J}]$ | i-th component of \mathbf{F} |
| $F1$ | $[-]$ | Surface current tally |
| $F1_{NET}$ | $[-]$ | Net surface flux entering the biasing surface from the plasma |
| $F2$ | $[\text{cm}^{-2}]$ | Average surface flux tally |
| $F4$ | $[\text{cm}^{-2}]$ | Average cell flux tally |
| $F6$ | $[\text{MeV g}^{-1}]$ | Energy deposition tally |

| Symbol | Unit | Description |
|-----------------|--------------------------------------|--|
| G | [Pa] | Shear modulus |
| G_i | [kg s ⁻¹] | Inlet mass flow rate |
| G_{nom} | [kg s ⁻¹] | Nominal mass flow rate |
| g_i | [m s ⁻²] | acceleration force along a direction |
| H | [MeV g ⁻¹] | Heating number or average energy released per reaction at the incident particle energy |
| H_t' | [MeV g ⁻¹] | Total energy deposition per unit source emitted particle |
| \mathbf{j} | [cm ⁻²] | Vectorial phase space current density function or the angular current density |
| \mathbf{J} | [cm ⁻²] | Vectorial particle current density |
| J_{\pm} | [cm ⁻²] | Partial particle current density |
| K | [J] | Kinetic system energy |
| K | | Resistance loss coefficient |
| \underline{k} | [W m ⁻¹ K ⁻¹] | Thermal conductivity second order tensor |
| m | [kg] | Mass |
| M_{V_i} | [kg] | System total mass contained in the volume V_i |
| N | [cm ⁻³] | Average particle density |
| n | [cm ⁻³] | Phase space particle density |
| \mathbf{n} | [-] | Unit vector normal to the surface |
| n_N | [cm ⁻³] | Isotope volumetric density |
| $n_{N,Inlet}$ | [cm ⁻³] | ¹⁶ N and ¹⁷ N inlet concentrations |
| $n_{N,Outlet}$ | [cm ⁻³] | ¹⁶ N and ¹⁷ N outlet concentrations |
| \mathbf{p} | [kg m s ⁻¹] | System momentum |
| p | [Pa] | Fluid pressure |
| p^{in} | [Pa] | Inlet fluid pressure |
| p_i^{out} | [Pa] | Outlet fluid pressure |
| P_{ij} | [-] | Probability that a particle starts from surface A_{TALLY} with a cosine in $[\mu_i, \mu_{i+1}]$ and in the energy bin $[E_j, E_{j+1}]$ |
| P_{fus} | [W] | Fusion power |
| P_b | [Pa] | Primary bending stress |
| P_l | [Pa] | Primary local membrane stress |
| P_m | [Pa] | Primary membrane stress |
| \dot{q} | [W kg ⁻¹] | Volumetric heat addition per unit mass |

| Symbol | Unit | Description |
|----------------|-----------------------|---|
| q'' | [W m ⁻²] | Heat flux |
| q_g'' | [W m ⁻³] | Volumetric density or heat power or power density generated within the body |
| q_{nom}'' | [W m ⁻³] | Nominal power density |
| Q | [-] | Plasma fusion gain |
| Q | [J] | Heat supplied to the system |
| Q_{dep} | [W] | Total deposited power |
| Q_{np} | [W] | Power deposited by neutrons and photons due to the neutronic interaction with the materials |
| $Q_{p,albedo}$ | [W] | Power deposited by photons produced due to neutronic interaction and scattered into the sub-model |
| Q_b | [Pa] | Secondary bending stress |
| Q_l | [Pa] | Secondary local membrane stress |
| Q_m | [Pa] | Secondary membrane stress |
| \mathbf{r} | [m] | Position vector |
| \mathbf{R}_S | [m] | Position vector of surface dS |
| R | [-] | Relative error |
| R_i | [-] | Tally score per cosine bin |
| s | [cm ⁻³] | Source density function |
| S_t | [cm ²] | Surface area |
| $S_{i,j}$ | [-] | Local source probability component |
| S_{cap} | [m ²] | Internal surface of cap |
| S_{res} | [m ²] | Resistant section |
| t | [s] | Time |
| \tilde{t} | [s] | Transit time of water outside the BB |
| T | [K] | Temperature |
| T^{in} | [K] | Inlet fluid temperature |
| TBR | [-] | Tritium Breeding Ratio |
| \mathbf{u} | [m] | Vectorial displacement field |
| u | [m] | Component along x of vectorial displacement field \mathbf{u} |
| \mathbf{u}_f | [m s ⁻¹] | Vectorial fluid velocity |
| u_i | [m s ⁻¹] | Flow velocity along one dimension |
| U | [J] | Internal system energy |
| v | [m] | Component along y of vectorial displacement field \mathbf{u} |
| \mathbf{v}_r | [cm s ⁻¹] | Vectorial velocity |
| V_t | [m ³] | Arbitrary volume |

| Symbol | Unit | Description |
|------------------------------|--------------------|--|
| w | [m] | Component along z of vectorial displacement field \mathbf{u} |
| W | [J] | Work performed by the system |
| x | [m] | Radial coordinate in the global coordinate system |
| X | [N] | Components of external loads along x acting on the domain |
| $\langle x \rangle, \bar{x}$ | [-] | Mean sample value |
| y | [m] | Poloidal coordinate in the global coordinate system |
| Y | [N] | Components of external loads along y acting on the domain |
| Y_{DEMO} | [s ⁻¹] | DEMO neutron yield |
| Y_{LOCAL} | [s ⁻¹] | Local neutron or photon yield |
| z | [m] | Toroidal coordinate in the global coordinate system |
| Z | [N] | Components of external loads along z acting on the domain |

Greek Symbols

| Symbol | Unit | Description |
|---------------------------------------|-----------------------------------|--|
| α | [m ⁻¹] | Coefficient of resistance loss coefficient characteristic curve |
| β | [-] | Coefficient of resistance loss coefficient characteristic curve |
| Γ | [m ² s ⁻¹] | isotope scalar diffusivity |
| δ_{ij} | [-] | Kronecker delta |
| Δp | [Pa] | Pressure drop |
| $\underline{\underline{\varepsilon}}$ | [Pa] | Strain field second order tensor |
| ε_{ii} | [Pa] | Normal strain |
| ε_{ij} | [Pa] | Shear strain |
| $\varepsilon_{,Qdep}$ | [-] | Error comparison |
| η | [-] | Figure of merit. Ratio between External “uncollided” neutron flux and the total flux |
| θ | [K] | Relative thermal field function with respect to the reference temperature |
| λ | [s ⁻¹] | Decay constant |
| λ_k | [s ⁻¹] | Isotope decay constant |
| μ | [-] | Cosine |
| μ_f | [Pa s ⁻¹] | Fluid viscosity |

| Symbol | Unit | Description |
|----------------------------------|-------------------------------------|---|
| μ_0 | [-] | Null hypothesis |
| μ_a | [-] | Alternative hypothesis |
| ν | [-] | Poisson's modulus |
| ζ | [-] | Random number |
| ρ | [kg m ⁻³] | Fluid density |
| ρ_a | [cm ⁻³] | Atom density |
| σ | [barn] | Microscopic cross section of the nuclear interaction x of the isotope i |
| σ_t | [barn] | Microscopic total cross section |
| σ | [-] | Sample standard deviation |
| σ_{eq} | [Pa] | Von Mises equivalent stress |
| σ_{ij}^f | [Pa] | Fluid stress tensor |
| $\underline{\underline{\sigma}}$ | [Pa] | Stress field second order tensor |
| σ_{ij} | [Pa] | Components of stress field second order tensor $\underline{\underline{\sigma}}$ |
| σ_{ii} | [Pa] | Normal stress |
| $(\sigma_{ij})_b$ | [Pa] | Bending stress tensor component |
| $(\sigma_{ij})_m$ | [Pa] | Membrane stress tensor component |
| Σ | [cm ⁻¹] | Macroscopic cross section of the nuclear interaction x of the isotope i |
| $\Sigma_{(n,p)}^{O_k}$ | [cm ⁻¹] | Macroscopic cross section for the (n,p) reaction for Oxygen isotopes |
| τ_{ij} | [Pa] | Shear stress |
| φ | [cm ⁻² s ⁻¹] | Angular flux or phase space flux |
| $\varphi_{EX_{UN}}$ | [cm ⁻² s ⁻¹] | External "uncollided" neutron flux |
| ϕ | [cm ⁻² s ⁻¹] | Velocity integrated flux |
| ψ | [cm ⁻² s ⁻¹] | Neutron flux angular energy density |
| Ω | [sr] | Vectorial solid angle |
| Ω_i | [sr] | Solid angle component |

1 Introduction

Nowadays, in an era where the link between the human activities and the climatic changes is becoming increasingly clear, it is imperative to achieve a sustainable growth able to satisfy the welfare request of population preserving, at the same time, the environment for the next generations.

The world energy consumption in the past years displays a constant growth mainly driven by emerging countries like India and China (more than 40% of the whole increment in 2017 [1]). A direct consequence is the increase of carbon dioxide (CO₂) emissions due mostly to fossil fuels (72% for 2017) since only a minority energy share comes from renewables and nuclear [1]. For the future, the world situation could be even worse than the current state. Indeed, the combined increase in income and population (increment of 1.7 billion people to 2040 [2]) will blow up the global energy consumption by more than 25% in 20 years changing completely the equilibria between west and east in favour of the latter [2, 3]. These themes are attracting more and more the attention of people who started to change their behaviour with respect to the environment. In particular, it is chronicle in these days, the creation of people movements to protest against the lack of action of governments on the climate change crisis (e.g. “*Fridays For Future*” movement [4]).

In this framework, policies at the international level have already developed new strategies in order to create a competitive and decarbonized energy system able to sustain the energy demand. Europe is a fundamental actor in the realisation of a low-carbon economy. As stated in the European energy roadmap 2050 [5], the European Union (EU) policies and measures are devoted to achieve a greenhouse gas emission reduction to 80-95% below 1990 levels by 2050 [5].

This goal, besides being ambitious, poses also an important challenge in the renewal of electricity production and opens up to the role of nuclear fusion in the mix of carbon-free energy resources. Indeed, from the interim evaluation of the 2014-2018 Euratom programme, the development of fusion technology has emerged as a relevant activity for the EU [6]. In order to make fusion a credible option, the EU has stated its own strategy within the “European Research Roadmap to the realisation of fusion energy” [7]. Its achievement is articulated in three main steps [7]:

- i) to demonstrate the scientific and technological feasibility of fusion as energy source by means of the international ITER tokamak reactor,
- ii) to realise a neutron source facility for materials development and qualification (IFMIF-DONES) and
- iii) to realise a fusion power plant which will deliver electricity to the grid and will operate with a closed self-sufficient fuel-cycle.

These steps are organised in three main stages that cover until the 2050 [7] ensuring a long-term research strategy in which all the European research centres will be strongly involved. In particular, this work will deal with the third pillar of the fusion roadmap.

The research on a fusion reactor to produce electricity has already started in the eighties demonstrating the feasibility of the fusion reaction without gaining net energy from it. For instance, the JET reactor, which is the largest tokamak currently operated in Europe, has produced a peak fusion power that is the 60% of the heating necessary to initiate and sustain the plasma using deuterium-tritium mixture [8]. Other machines, like ITER, should demonstrate the self-heating of the plasma producing 10 times more fusion power [9] but it will not have a self-sufficient fuel cycle as well as electricity production. For these reasons, in the European Roadmap [7], it has been foreseen another advancement, the so-called DEMOstration (DEMO) reactor. In DEMO reactor, one of the main components is the Breeding Blanket (BB) that has several functions and will be also the main subject of this dissertation. The main role of BB is to produce a fuel surplus, in order to allow successor power plants to start up. The BB has also the function to extract power

at high temperature and transfer it to the power conversion system for electricity production. However, the BB has to achieve these functions in a vacuum environment subjected to high neutron and thermal fluxes as well as strong magnetic fields. In order to consider all these characteristics and to avoid neglecting important issues maintaining the consistency within the project, the design of the BB has to investigate all these aspects at the same time using a holistic approach. Starting from these considerations, a multi-physics approach for the design of the BB based on the sub-modelling techniques and on the coupling of neutronic, thermal-hydraulic and structural analysis is proposed and critically discussed in this dissertation.

1.1 Notes on Nuclear Fusion

The nuclear fusion is the exergonic reaction in which the nuclei of two light elements, interacting, produce energy and a stable nucleus heavier than either one. The resulting nucleus is more bounded compared to the reacting nuclei due to the increasing forces per nucleon. Looking to the average binding energy per nucleon (Figure 1.1), the light nuclides are less tied, therefore, thermodynamically less stable. This means that, with “appropriate” conditions, they will transit into the more stable central zone by means of the fusion reaction. The fusion reaction is thermodynamically, but not kinetically favoured unless the kinetic energy of the reactions impacting nuclei is huge. Despite this, due to the quantum tunneling effect, the cross-section, even at low energies, is different from zero and the fusion reaction can occur [10].

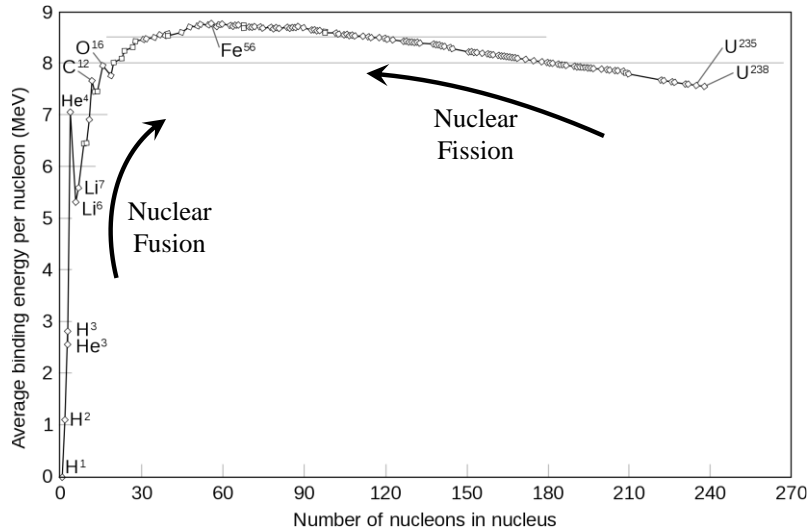


Figure 1.1. Binding energy per nucleon of common isotopes. The stability of a given isotope is evaluated dividing the binding energy by the number of nucleons. The range of higher stability is between the mass number $A=10$ and $A=120$ with a peak for ^{62}Ni and ^{56}Fe that are the most tightly bound nucleus. Indeed below $A=10$, the fusion reaction is favoured while, for A greater than 120, the fission one. Figure reproduced according to [11] (Public Domain).

Considering that, during a fusion reaction, the mass after the reaction is slightly lower than before, it is possible to define the fusion reaction Q-value that express the energy associated to the mass difference [10]

$$Q_{ab} = (-\Delta m)_{ab} c^2. \quad (1.1)$$

Eq. (1.1) shows that the excess mass Δm is converted into kinetic energy of the produced nucleon. Numerous types of fusion reaction for which $Q_{ab} > 0$ (exothermic reaction) have been identified (eq. (1.2) - (1.5)) and their occurrence probability, of some of those, is reported in Figure 1.2. All most favourable fusion reactions involve isotopies of hydrogen (deuterium, D, and tritium, T), since this minimizes the Coulomb repulsive force, which prevents fusion. Among all the fusion reactions, the D-T reaction (1.4) is more promising because it has a larger cross-section (Figure 1.2) with respect to the other. The energy produced in D-T fusion reaction (1.4) is partitioned among the reaction products in an inversely

proportional manner to their mass ($E_n = 14.1$ MeV to the neutron and $E_\alpha = 3.5$ MeV to the alpha particle) [10]. This reaction is the first to be used for power generation purposes and, for this reason, taken as reference in this dissertation.

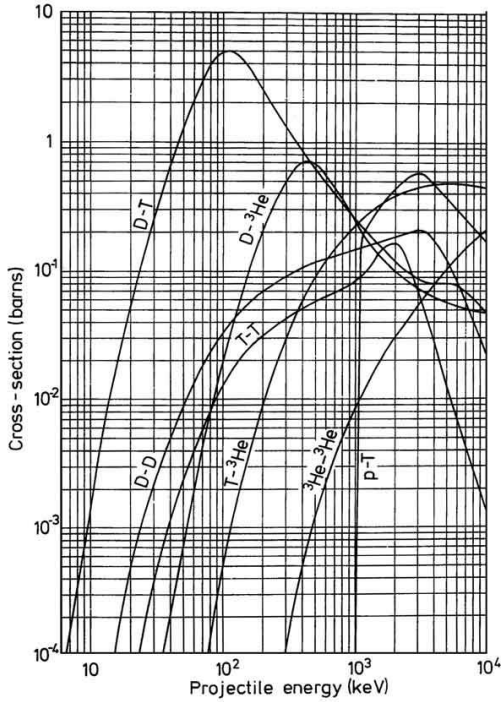
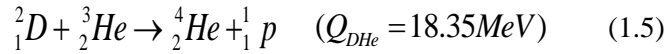
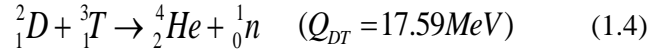
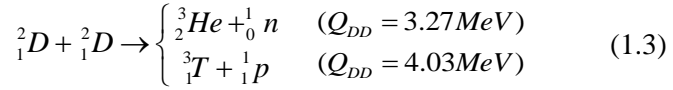
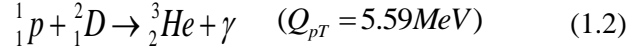
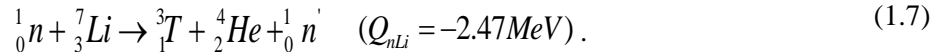
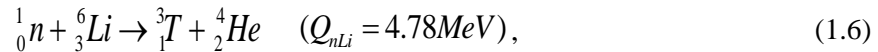


Figure 1.2. Cross-section of main thermonuclear fusion reactions as a function of the incident nucleus energy. Figure reproduced according to [12].



The exploitation of D-T reaction depends on accessibility of reactants but, while deuterium is widely available in the water of sea and rivers (0.0153 at.% in sea-water [13]), there are no natural resources for tritium that undergoes beta decay with a half-life of 12.3 yr. The only way to make use of this reagent is to breed it inside the reactor, thanks to the reaction between lithium isotopes (e.g. 6Li and 7Li) and fusion neutrons (eq. (1.6) and (1.7) [10])



In order to make the reaction between lithium and neutrons happen, it is necessary that both reactants are available in the same place, in other words within the BB where the breeding occurs. However, for each neutron produced by D-T reaction a n-Li interaction has to occur if a closed self-sufficient fuel-cycle has to be maintained. For this reason, a neutron multiplier (e.g. Beryllium, Be, or Lead, Pb) is employed in order to increase the neutronic population inside the reactor by means of (n, 2n) reactions that compensate the parasitic losses in all materials different that those used for T-breeding, as well as losses due to neutron leaking and streaming. On the other side, to create the plasma, it is necessary to heat a gas of deuterium and tritium at high temperature (about 10^8 K) so that, by atomic collisions, the atoms completely ionize. From a technological point of view, in order to obtain a sufficiently high energy density, it is essential to have kinetic energy for the reactant nuclei higher than the Coulomb barrier (370 keV for D-T reaction [10]), and these conditions must be sustained in a specified reactor domain for a sufficiently long time. For these reasons, several confinement methods have been investigated. Some of them [13] such as the gravitational

and electrostatic confinements are not so plausible due to the material temperature limits as well as gravitational pressure required. Some others as the inertial and magnetic confinement methods are most effective from a technological point of view [13].

The magnetic confinement is the method on which the scientific efforts have been most focused. It is based on the bordering of plasma charged particles using a special configuration of magnetic fields.

Indeed, in case of a solenoidal magnetic field \mathbf{B} , the charged particle moves along a helical path in the direction of the field with a pitch that depends on the ratio of the parallel and orthogonal components of its velocity with respect to \mathbf{B} . In this way, the particle is confined in two dimensions perpendicular to the magnetic field but not in the parallel one. One of the drawbacks of this method is the loss of particles in the direction of the field. In order to solve this problem, two solutions have been proposed. One is to use magnetic mirrors to reflect the particle and bring them back, the other is to use a closed-field geometry in which the particle can move indefinitely [10]. In particular, in the second case, the highly developed form of field is a torus, which is produced by passing a current through a solenoid closed on itself. Theoretically, a particle trapped in a toroidal field can travel indefinitely but, practically, a toroidal magnetic field is never uniform and it becomes increasingly feeble for large radii. Two configurations have been found for correcting the orbit with a second poloidal field: *stellarator* [14] and *tokamak* [15].

The fusion reactors under development are based mainly on the *tokamak* concept (JET in Europe, TFTR in USA and JT-60 in Japan). The same configuration will be applied to the next machines (ITER and DEMO). This thesis will focus on the tokamak fusion reactor and, more specifically, to European DEMO reactor unless differently specified.

1.2 The Demonstration Fusion Reactor DEMO and the Breeding Blanket Systems

Currently, the ongoing research on fusion reactors has demonstrated the feasibility of the fusion reaction without gaining net energy from it and without producing electricity [8, 9]. The main efforts are currently dedicated to the construction of the first fusion reactor, namely ITER, that will demonstrate the scientific and, above all, technological feasibility and controllability of fusion energy and will be used also as test machine for the technologies to be used in further demonstration fusion power plant [16]. Therefore, in the European Roadmap [5], DEMO reactor has been foreseen as ITER's successor for demonstrating the commercial practicality of fusion power and the transition of fusion research to industry and technology-drive programme. The DEMO top-level functions are [9, 17-19]:

- (i) to demonstrate power extraction at high temperature delivering a net electrical output to the grid (~300-500 MWe [16]);
- (ii) to demonstrate a tritium self-sufficiency and a closed tritium fuel cycle producing more tritium than the one consumed (e.g. the number of tritium atoms produced per fusion neutron also known as tritium breeding ratio (TBR) has to be greater than 1 with a design value of 1.05);
- (iii) to demonstrate attractive safety and low environmental impact minimising the worker exposure and the radioactive wastes with no need of long-term storage; and
- (iv) to demonstrate acceptable Reliability/Maintainability/Availability/Inspectability (RAMI) using remote maintenance and minimising the number of unscheduled shutdown.

Together with these challenging functions, several outstanding technology and integration issues must be solved and some of them present very strong interdependencies that impose a holistic design view since the early phases. They may include the selection of BB concept and the relative balance of plant (BoP), the divertor (i.e. plasma facing component representing a major interface with the charged particles escaping the confinement region) layout and configuration, the design and integration of first-wall (FW, i.e. the

actively cooled plate of the BB facing the plasma) to the BB taking into account the high heat loads and the consequent mechanical and hydraulic issues, the selection of remote maintenance scheme and the Heating and Current Drive (H&CD, i.e. system used to provide external heating source in order to compensate the unavoidable plasma energy losses due to advective and conductive transport and electromagnetic radiation mechanisms) mix to be used according to the compatible plasma scenario [9].

For these reason, so far, several DEMO plant concepts have been investigated with the aim to find an optimum configuration by means of fusion system codes like PROCESS [20], SYCOMORE [21] and, the more recent, MIRA [22], which rely on a reduced physics but couple several physics frames in an integrated way to enable a holistic view as well as to identify essential design sensitivities.

The fundamental reference in this work is the EU-DEMO design baseline 2015 (DEMO2015) [23], with a fusion power of 2037 MW. With reference to Figure 1.3, it consists of the following main systems [17]:

- A Cryostat, housing the magnet system;
- Toroidal, poloidal field coils and central solenoid, which provide the magnetic field required to shape and confine the plasma, to drive its current and to define its poloidal structure;
- A Vacuum Vessel (VV) serving the primary vacuum and shielding the magnet system from neutrons. It is a torus-shaped double-walled pressure vessel composed of three nested shells;
- Upper, lower and equatorial ports that provide the access to the In-Vessel components like the BB and the divertor;
- A thermal shield which shields the cryogenic magnet system from radiation heat coming from the VV. It is a shell-like structure that encloses the VV and the ports;
- Divertor, which is a high heat flux component, and collects most of the particles and energy exhausted by the plasma. The magnetic topology is chosen in order to intersect the divertor with the last closed magnetic flux surface.
- Breeding blanket which surrounds the plasma removing the thermal power released by neutrons and alpha-particles, produces tritium and shields the VV and coils.

Axisymmetric objects like tokamaks are regularly illustrated using a global radial/poloidal/toroidal coordinate system (x, y, z), as shown in Figure 1.3. DEMO2015 consists of 18 sectors of 20° in the toroidal direction subdivided according to the number of coils. In each sector, there are, going in radial direction, 5 BB segments, 2 in inboard (IB) and 3 in outboard (OB).

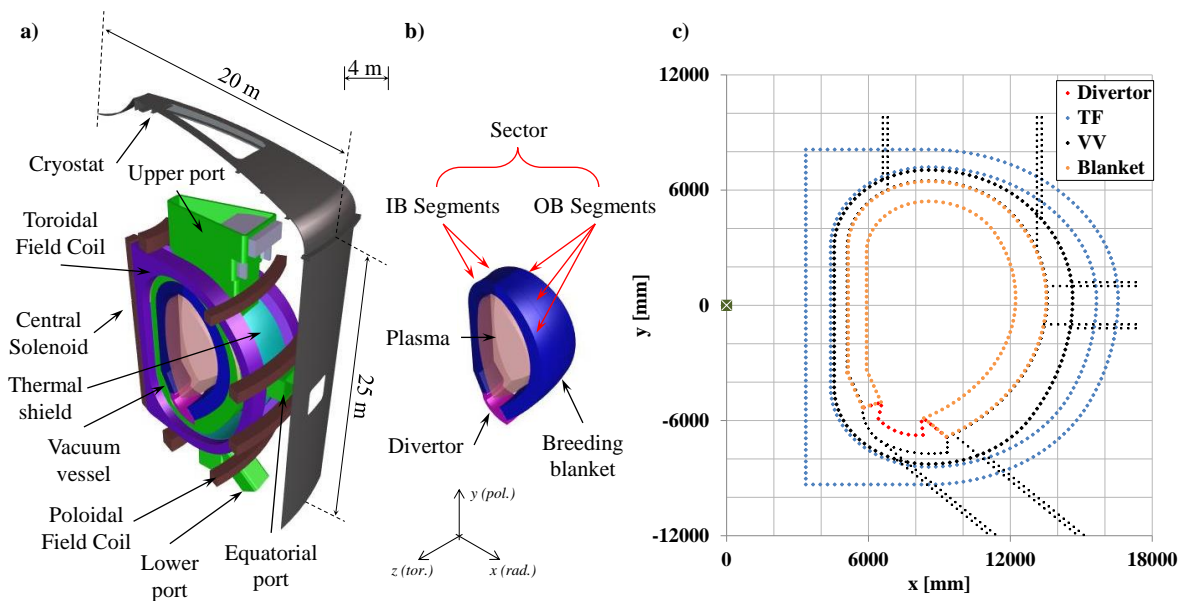


Figure 1.3. DEMO2015 baseline configuration. Left (a) and centre (b): 3D EU-DEMO 2015 configuration with details of the main

systems inside the Cryostat. Right (c): 2D scheme of EU-DEMO2015 with main dimension in radial (x) and poloidal (y) dimension. Figure a) and b) reproduced according to [24], figure c) reproduced according to [25].

DEMO2015 uses a water cooled divertor with Plasma Facing Components (PFC) covered with tungsten [9]. Since a tokamak is intrinsically a pulsed reactor, the operation is divided in a power producing time period called “pulse” followed by a sequence to restore magnetic energy named as “dwell time”.

The duration of the foreseen plasma pulse is 2 hours with a dwell time between 10 min and 30 min [9]. The structural material used for the BB is the reduced activation ferritic-martensitic steel Eurofer 97 [26] with imposed dpa ceiling limit for the “starter” blanket of 20 dpa throughout its lifetime. AISI ITER-grade316 has been selected for the VV [9]. In order to cover the wide spectrum of breeder and multiplier as well as coolant solutions that have been investigated, the helium-cooled pebble beds (HCPB) and the water-cooled lithium-lead (WCLL) BBs have been adopted as reference technologies.

Independently of the selected BB concept, the blanket represents a key system for a fusion reactor and its design has to accomplish, at least, with 3 basic functions that are strictly connected to the stakeholder goals of DEMO. Indeed, the BB must (i) breed tritium in order to achieve the self-sufficiency, (ii) transfer the thermal power released by neutrons and photons and plasma charged particles to the BOP with thermal-hydraulic conditions suitable for electricity production and (iii) contribute to shield the VV and the superconducting magnets against the neutron radiation [27].

1.2.1 Helium-Cooled Pebble Beds Design Configuration

The HCPB, investigated within the EUROfusion consortium [27], uses a ternary Li-ceramic compound (Li_4SiO_4) enriched in ^6Li as breeder, while the multiplier is metallic beryllium (Be). Both are in the form of pebbles distributed on beds. [26]. Helium is used in a high pressured form as coolant and at low pressure flow as purge gas through the pebble beds to extract the tritium from the tritium breeder materials and transport it to the tritium plant.

Considering the DEMO baseline 2015 and with reference to Figure 1.4 [26], each HCPB segment (IB and OB) is divided into 7 modules (Figure 1.4 - a). The breeder zone (BZ) (highlighted in yellow in Figure 1.4 - b) is housed behind a U-shape FW with the two remaining sides closed by caps, forming a structural box/module that is attached to the back supporting structure (BSS). Within the BZ the pebble beds of Li_4SiO_4 and Be are alternating by arranged beds separated by helium cooled cooling plates (CPs). Within the CP, 32 cooling channels are routed in the toroidal direction for cooling down the structure using a counter-current flow scheme. In-between these “functional” cooling channels, the so-called “dummy” channels are implemented so as to minimize the steel volume fraction in the BZ, thus reducing the parasitic neutron absorption in the BZ and maximizing the T breeding [28]. The half of the pebbles beds and one cooling plate form the elementary cell that is repeated in the poloidal direction. In this thesis, the term “slice” will be used to indicate this elementary unit (Figure 1.4 – c). The FW is covered with a W-armour layer and it shall tolerate the high heat flux coming from the plasma and sufficient neutron transport to fulfil tritium breeding function. The BSS has a structural function in the poloidal direction to support all the blanket modules at the right position. Within the BSS, the manifolds for coolant and purge gas are routed to distribute through the Manifold Purge (MP) and collect He in the various blanket modules.

The coolant pressure and inlet temperature are assumed to be 8 MPa and 300 °C, respectively. The coolant outlet temperature is set to 500 °C, as the Eurofer creep strength is greatly reduced at temperatures above ~550 °C. The cooling scheme, within the modules, is articulated in two parallel circuits that take the 50% of coolant, therein a counter-current flow scheme in the FW and BZ is realised for safety reasons (Figure 1.4-d). Beginning from the BSS at 300 °C, the first cooling loop (namely, loop1) cools the 50% of the FW and then of the CPs, exiting the BZ and entering again the BSS, where the flow at about 500°C is routed out of the VV. At the same time, the second cooling loop (namely, loop2) covers the other 50% in the opposite direction ensuring a fully counter-flow of FW and CPs.

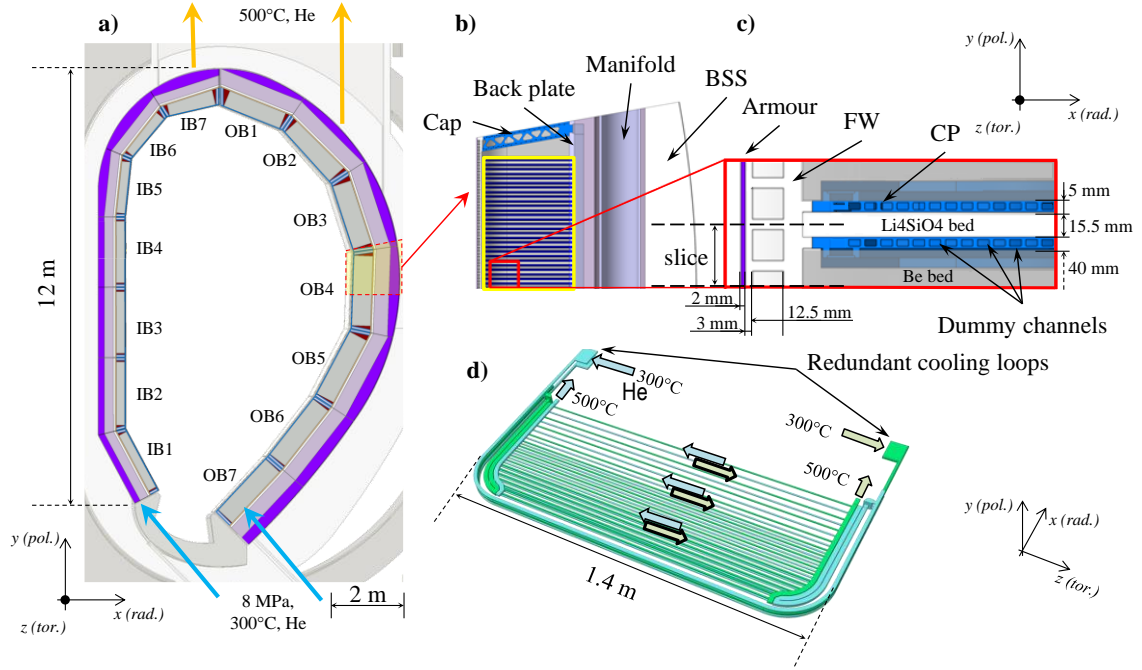


Figure 1.4. HCPB BB concept segmentation and module details in the EU DEMO2015 tokamak complex. Left (a): BB module labelling and piping routing. Centre (b): an example of the equatorial OB blanket module. Right (c): detail of the OB4 BB module and principal dimensions of the FW, CP and bed thicknesses. Bottom (d): coolant flow scheme with symmetric 50% + 50% coolant distribution arrangement in the BZ Figure reproduced according to [26] and [28].

The purge gas is helium with an addition of 0.1% vol. H_2 . Its pressure is set to 0.2 MPa and it exits the BSS at about ~ 450 °C. The inlet coolant manifolds enter from the bottom part of the segment while the outlet coolant manifolds are routed at the upper part (Figure 1.4-a) [26]. In Table 1.1, the main design features adopted for the HCPB BB in the EU-DEMO2015 baseline are summarised.

Table 1.1. HCPB blanket design features adopted for the EU-DEMO 2015 baseline [28].

| Region | IB | OB |
|--|--------------------------------------|--------|
| Segments per sector | 2 | 3 |
| Breeder/multiplier | Li ₄ SiO ₄ /Be | |
| Coolant | Helium | |
| Inlet/outlet coolant temperature | 300/500 °C | |
| Coolant pressure | 8 MPa | |
| Structural material | Eurofer | |
| ⁶ Li enrichment | 60 % | |
| Purge gas (Tritium carrier) pressure | 0.2 MPa | |
| Inlet/outlet tritium carrier temperature | 450 °C | |
| Armour | 2 mm | |
| FW | 25 mm | |
| BZ | 230 mm | 520 mm |
| BP | 85 mm | 85 mm |
| BSS ¹ | 460 mm | 620 mm |

¹ The radial dimension of the BSS in general varies along the radial direction, as shown in the radial-poloidal cross section highlighted in violet in Figure 1.4-a. For this reason, the thickness values reported in Table 1.1 represents a mean value along the poloidal direction.

1.2.2 Water-Cooled Lithium-Lead Design Configuration

The WCLL, within the EUROfusion consortium [27], uses water as coolant while the breeder and the multiplier are mixed in a liquid metal alloy ($Pb_{83}Li_{17}$) Lithium-Lead (LiPb) enriched at 90% in 6Li .

In the WCLL, water at Pressurized Water Reactor (PWR) conditions (pressure 15.5 MPa, inlet temperature 295 °C and outlet temperature 328 °C) is used [29].

Considering the DEMO baseline 2015 and with reference to Figure 1.5 [30], each WCLL segment (IB and OB) is divided into 7 modules (the OB segment is shown in Figure 1.5-a).

Like for the HCPB, the BZ is housed by U-shape FW, caps and back plate (highlighted in yellow in Figure 1.5-b).

The BZ is divided into elementary cells that are repeated in the poloidal direction to which, in the following, it will refer as breeder unit (BU) (Figure 1.5-c).

Within the BU the Eurofer steel stiffeners are placed in radial-toroidal and radial-poloidal plane and the cooling water flows through 22 C-shape double wall tubes routed in the radial-toroidal plane. The LiPb flows in the radial-poloidal direction between each BU at relatively low velocity exiting from the BSS with a temperature of 326 °C (Figure 1.5-c).

The cooling circuits of the FW and BZ are separated although they have the same thermal-hydraulic conditions allowing different regulation of FW and BZ flow rates (Figure 1.5-d).

The inlet manifold (both for FW and BZ) enters from the bottom part of the segment while the outlet manifold is routed at the upper part (Figure 1.5-a).

In Table 1.2, the main design features adopted for the WCLL BB in the EU-DEMO2015 baseline are summarised.

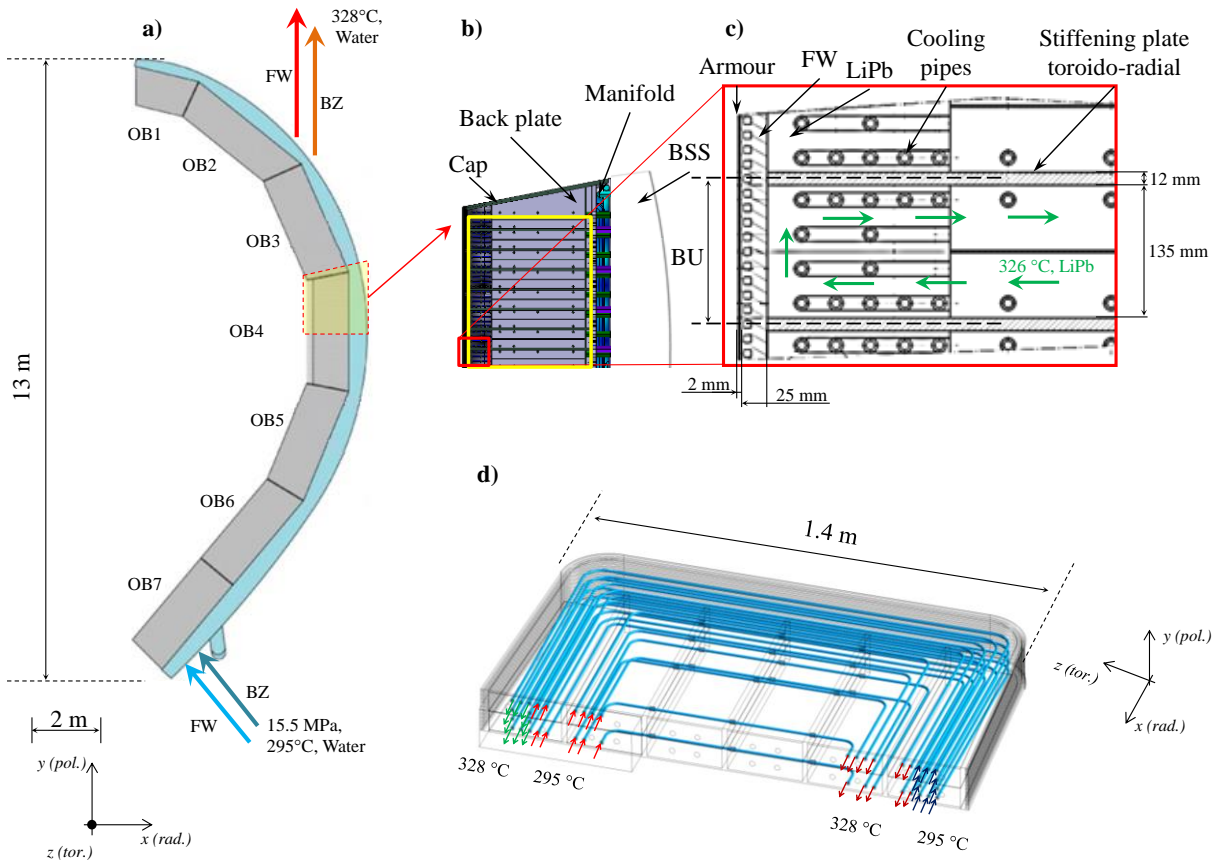


Figure 1.5. WCLL BB concept segmentation and module details in the EU DEMO2015 tokamak complex. Left (a): BB module labelling and piping routing. Centre (b): example of the equatorial OB blanket module. Right (c): detail of the OB4 BB module and principal dimensions. Bottom (d): coolant flow scheme arrangement in the BZ Figure a) reproduced according to [31], figures b), c) and d) reproduced according to [32].

Table 1.2. HCPB blanket design features adopted for the EU-DEMO 2015 baseline [32].

| Region | IB | OB |
|--|------------|--------|
| Segments per sector | 2 | 3 |
| Breeder/multiplier | LiPb | |
| Coolant | Water | |
| Inlet/outlet coolant temperature | 295/328 °C | |
| Coolant pressure | 15.5 MPa | |
| Structural material | Eurofer | |
| ⁶ Li enrichment | 90 % | |
| PbLi (Tritium carrier) pressure | 4.5 MPa | |
| Inlet/outlet tritium carrier temperature | 326 °C | |
| Armour | 2 mm | |
| FW | 25 mm | |
| BZ | 470 mm | 800 mm |
| BP | 75 mm | 75 mm |
| BSS ² | 208 mm | 398 mm |

1.3 Blanket Challenges and State-of-the-Art of Coupling Analyses

As discussed in the previous paragraphs, the BB is a key nuclear component for fusion reactor and several challenges have to be overcome for its design, construction and operation.

It is possible to highlight for each concept the main technical issues that need to be solved.

For instance, the HCPB suffers from an important issue related to the large number of very small coolant channels in the large number of CPs. This issue causes high pressure drop necessitating high pumping power and therefore impacting the reactor efficiency. Additionally, due to the large number of sub-components and welds low reliability is evaluated [19]. Other difficulties are related to the estimation over the time of effective thermal conductivity and interface conductance between pebble beds and the structure [19]. This issue is compounded by radiation damage (i.e. swelling) over the life time of the reactor that changes the thermal-physical properties of pebble beds jeopardising the heat transfer and, so, the BB structural integrity. Other problems are related to the control of tritium releases and inventories [19].

Considering the WCLL, instead, it is possible to underline the issues related to the LiPb corrosion or the dangerous creation of He pockets within the BB box that may impede the correct LiPb flow compromising locally the heat exchange as well as increasing the tritium permeation through the structure [19]. Other issues are related to the water activation that poses safety constraints to the active operating systems (e.g. valves) and to the human activities.

However, more in general, the BB, independently of the concept considered, is a complex and unique system that has to operate in a harsh environment satisfying simultaneously several key functions for the correct operation of DEMO reactor. Indeed, the BB is subjected at the same time to high neutron and particle fluxes, to surface and bulk heating, to strong magnetic field varying in space and time, to mechanical and electromagnetic forces, to radiation damage, etc. All these loads make the realisation of a design a real challenge for the scientific community. The design of the BB requires several analyses to be performed (e.g. neutronic, thermal-hydraulic, structural, tritium permeation, magneto-hydrodynamic, etc.)

² The radial dimension of the BSS in general varies along the radial direction, as shown in the radial-poloidal cross section highlighted in violet in Figure 1.5-a. For this reason, the thickness values reported in Table 1.2 represents a mean value along the poloidal direction.

and most of them have to be conducted simultaneously in order to better understand the overall behaviour. However, looking in more detail, three of them represent the basic investigations from which all the other studies derive. These are the neutronic, thermal-hydraulic and thermo-mechanical calculations that will be also the main subjects addressed in this work.

As stated in [19], the main characteristic of a multi-physics field is the presence of strong gradients in the various loads and responses that have to be considered synergistically if new phenomena have to be discovered. Therefore, it becomes more important to use coupling procedures among each analysis field in order to study the synergistic interactions and effects as well as to avoid excessive simplifications in the geometry and load representation that could hide driving design gradients.

Furthermore, nuclear engineering is probably one of the fields most strongly linked to the numerical processes simulation due to the difficulty in the definition of lab experiments for depicting all the occurring phenomena for safety checks [33]. The level of performance achieved over the years by the tools supporting the design of nuclear systems, in particular fission ones, is such that it has slowed the development and innovation of the used calculation procedures. Only recently, the exponential growth of computing capacity has motivated a radical change in the field of nuclear coding. These new possibilities have also led to the conception of multi-physical instruments, capable of simultaneously dealing with multiple fields like neutronics, thermal-hydraulics and thermo-mechanics, with an incredible level of geometric detail [34].

This holistic approach is already well developed in fission technology, where the direct coupling between the neutronic calculations and the computational fluid dynamics (CFD) has become a must for the estimation of the nuclear cross sections, the local temperature distribution which acts on structures (expanding them) and the fluid temperature (density changes and, therefore, alters the moderation of neutrons) both translate to reactivity changes and different power distribution [35].

Another interesting coupling example between neutronic and thermal-hydraulic analysis is reported in [36]. In this work, the author improved a multi-physics and multi-scale methodology for the study of PWR and their safety investigation. Indeed, coupling to a 3D neutronic model of the reactor core a 3D thermal-hydraulic model, the following was investigated: local safety parameters related to the nuclear boiling, the minimum critical power ratio, the maximum cladding and the fuel temperature, relaxing the conservative assumptions that before was based on hot channel factors [36].

In [37], P. J. Turinsky describes a complete coupling between the neutronic, fluid-dynamic and structural analyses applied to nuclear reactors. He underlines the benefit from the use of high performance computing for nuclear power plant applications in terms of improvements for the design and of a heightened assurance of nuclear safety. Other examples of multi-physics coupling application can be found in the latest generation nuclear power plants, and for instance, in the studies related to the development of generation IV reactors that use molten salt [38].

An interesting application of coupling analysis based on the use of a mesh-oriented database MOAB library [39] is reported in [40]. The authors use a bottom-up methodology to multi-physics simulations based on the mixture of loosely-coupled approach, in which the codes are run in sequence, and “monolithic” approach, in which the physics models are combined within an ad-hoc infrastructure. This work represents also a sort of bridge between fission and fusion. Indeed, the approach has been applied also for the study of the neutron transport in the Fusion Development Facility (FDF) [41] but detailed explanations on the methodology or further applications have not been found.

It is important to underline that not all the coupling procedures, developed for fission applications, can be directly transferred to fusion. Indeed, the geometries (e.g. complex structures with thousands of components), the dimensions (e.g. huge components like the BB, VV, etc.) and, in some cases, the physics (e.g. high-energy and high-intensity neutron fluxes [42]) of fusion machine are different and, for this reason, the coupling strategies used for fission as well as the assumptions made are not valid for the direct

transfer to fusion applications.

For this reason, since the beginning, the international fusion community has sought to create high detailed computational models to be used for multi-field analyses. The main efforts have been devoted to the realisation of high-fidelity 3-D neutronic models, for the assessment of heating, radiation damage and helium production profile [43], or to the development of tools for studying the tritium permeation, the fluid dynamic and the structure mechanic behaviour [44]. However, these attempts have been conducted as standalone activities without pursuing a real integration in a unique approach able to keep the consistency between the input/output flow of data (geometry, loads, etc.). Only some studies have been made for the development of neutronic – thermal-hydraulic – mechanic coupled platform [45, 46]. For instance, in [45], the BB is designed using an iterative process for optimising its structure but with several simplifications: the neutronic model is a 1-D cylinder where the materials are homogenised in the radial direction and the thermal-hydraulic model is based on a 2-D approximation in the radial-poloidal direction.

Q. Yuefeng in [46] reports a multi-physics approach integrated into SALOME simulation platform [47] based on advanced Monte Carlo (MC) modelling and CFD calculations. This study represents a valuable progress in the development of coupled multi-physics approach but with some limitations. Indeed, the definition of neutronic and photonic local sources as well as the boundary conditions for the neutronic calculation have not been investigated. Moreover, additional tools are employed conditioning their use to a prior verification and validation if used for the licensing of the breeding blanket.

Y. Huang et al. in [48] use a multi-physics framework to assess the loading conditions for a multiscale design, extending the criteria to progressively incorporate continuum plasticity models and microstructure-based representation of deformation and fracture. In the same study advanced fracture mechanics concepts based on a Materials-Specific Failure Assessment Diagram (MS-FAD) is also integrated. However, the neutronic part is not at all considered and the fluid-dynamic is approximated using a 1-D representation.

J. Shimwell et al. in [49] reports a novel blanket design tool which automates the creation of heterogeneous 3D neutronic models for each BB concept. In this work, although the neutronic analysis is versatile and allows the investigation of a wide solution spectrum, the thermal hydraulic part is still simplified and based on empirical correlations like the ones used in systems codes. The thermo-mechanical analysis, instead, is completely missing in the proposed coupling approach.

Furthermore, these tools and approaches are poorly applied to drive the BB design in the EUROfusion consortium. Indeed, currently in the Work Package BB (WPBB), the coupling among the design analyses is done manually and involves several teams. Moreover, the models used for the simulations are often inconsistent due to the nature of modelling approach. For instance, the neutronic calculation is usually based on homogenised or simplified geometry representation because its aim is to provide integral information on the whole reactor at the expense of geometric detail. These simplifications are in contrast with the detailed geometry representation required by CFD and mechanical simulations and the coupling procedure can take several months before to close the loop involving team with different expertise and needs. This procedure opens easily the way to the error propagation and to the difficulties in keeping the input/output data consistency.

1.4 Objectives of a New Multi-Physics Approach for Integrated Analysis

Considering the weaknesses highlighted in the conventional coupling approach currently used in fusion community, the development of the fusion technology reliability involves, among other issues, the improvement of simulation tools to be used for the design of reactor key components, such as the BB, where the engineering requirements and constraints are of nuclear, material and safety kind.

For this reason, advanced simulation tools are needed. In the European DEMO project, the research is

currently focused on the development of an integrated simulation-design tool able to carry out a range of analysis using a multi-physics approach. As anticipated, the BB is a complex system that requires a complex set of analyses that have to be studied simultaneously. However, it is possible to prioritize three of them that are used as basement for the investigation of all the other issues related to the BB.

The multi-physics approach, herewith proposed, has to cover these three pillars of the BB design: the neutronic, thermal-hydraulic and thermo-mechanic. Neutronics analyses calculate volumetric thermal load and neutron flux (in case of BB also the tritium production distribution or the production rate of activated isotopes), thermal-hydraulic analysis defines thermal limits of structures and coolant and, the structural analyses evaluate stresses and deformations comparing them with allowable design limits.

These analyses have to be conducted in a strong integrated way. Therefore, the need of the scientific community to adopt a numerical tool that can integrate various computational codes in a multi-physics approach is clear.

Commonly, the codes used for the neutronic analysis are based on the deterministic or stochastic approaches while the thermal-hydraulic and thermo-mechanical analyses are based on the Finite Volume and Finite Element Methods. In particular, it is widely used the Monte Carlo N-particles transport method for neutron and photon transport calculations using codes such as MCNP and TRIPOLI, and multi-physics codes such as ANSYS and ABAQUS/CAE for the thermal-hydraulic and thermo-mechanical ones. These softwares, although powerful means of calculus, extensively verified and validated, are used separately and the coupling among them is user demanded.

The main goal of this PhD research activity is to cover this gap proposing a novel approach to the BB design where the neutronic, thermal-hydraulic and structural analyses are fully integrated and based on the same geometrical detail overcoming the criticisms highlighted in the previous paragraph.

The work has been aimed to develop and validate the Multi-physics Approach for Integrated Analysis named “*MAIA procedure*” with the main objectives:

1. to propose a complementary methodology for BB design;
2. to outline a procedure for the coupling of neutronic, thermal-hydraulic and structural analysis based on the sub-modelling methodology.
3. To create an integrated approach for BB design that is: a) flexible, b) accurate and c) “quick”.

Regarding the first objective, MAIA procedure may complement and support the different approaches currently used to drive the BB design. The second objective aims at creating a solid base for the integration of the three pillar analyses from which it is possible to spread into new fields of investigation. Concerning the last point, MAIA has to adapt to the specific designer’s requests giving reliable results in a certain limit of application and it has to speed up the computational process for investigating a wide range of solution.

The main characteristics of MAIA procedure can be summarized in the following points:

- use of refined local models (i.e. slice or BU) just of the area of interest (sub-modelling);
- use of the same geometric details for all the analyses involved;
- input/output consistency.

The method, herewith presented, uses a loosely-coupled approach based on the sub-modelling technique. The CAD-based solid model represents the common element across physical disciplines and helps in maintaining the consistency in the geometric representation among the analysis codes.

In order to accomplish the achievement of the objectives, MAIA procedure has been tested on HCPB and WCLL BB concepts that together cover the whole spectrum of breeder/multiplier and coolant BB solutions in the current reference EU DEMO and ITER’s EU TBM. In particular, after the consolidation of the three pillars, mentioned above, on the HCPB BB, the enhancement of MAIA procedure has been pursued studying the water activation in WCLL BB.

1.5 Organization of the Thesis

This thesis consists of seven main chapters, hereafter briefly summarised.

This introduction. The theoretical background behind the MAIA procedure is described with particular focus to the basic laws and numerical methods used for the characterization of the three analysis field in Chapter 2.

The description of the MAIA procedure, the details about the logical connection and the implementation are reported in Chapter 3.

In Chapter 4, the verification of boundary conditions consistency to be used for the sub-models in each analysis is described. Particular efforts have been spent to identify the limits of applicability of MAIA procedure.

In Chapter 5, the MAIA procedure has been applied to the HCPB BB demonstrating the benefits that may come from detailed representation. Some effects that are not visible with the common coupling approach are also highlighted and critically discussed.

Once the basement has been substantiated in the previous chapters, an enhanced application of MAIA procedure is reported in Chapter 6 for the water activation study in the WCLL concept. The aim of this chapter is to demonstrate the flexibility of MAIA procedure that allows the investigation of further issues starting from the consolidated results of three pillar analyses.

Finally, the main conclusions and outlooks for the future activities for the improvement of MAIA procedure are summarised in Chapter 7. Additional details and information are reported in the Appendix.

2 Theories and Mathematical Models of Coupling

In this Chapter, a brief overview of the three main pillars of the coupling is reported. The basic theories and the mathematical models of neutronics, thermal-hydraulics and thermo-mechanics are described with particular attention to their numerical implementation.

2.1 Neutronic Model

The term “transport theory” is usually referred to as the mathematical description of particle transport through a medium. For instance, using this theory, it is possible to describe the interactions of neutrons and photons with the BB and to estimate the energy that they release.

The transported neutrons can come directly from the plasma (i.e. direct neutrons), due to the D-T fusion reaction, or they can be generated by reactions of direct neutrons with the surrounding matter. While the photons, in a fusion reactor, are X-rays and bremsstrahlung radiation or secondary products of neutron interactions. For the D-T reaction, producing He and a neutron, 80% of fusion energy is carried by the kinetic energy of the resulting neutrons and their interaction with their surroundings. These interactions transforms part of their kinetic energy into heat by scattering or nuclear reactions with other elements, which in turn are the source of radiation damage into structural materials. For this reason, it is necessary to adopt neutron and photon transport models.

2.1.1 Neutron and Photon Transport

The random nature of neutron and photon interaction events leads to unpredictability with the certainty of the exact number of particles in a certain region in a given time. For this reason, in the transport theory, the field of probability densities or distribution functions is introduced. From it can be derived that only expected or average particles density $N(\mathbf{r}, t)$ can be calculated. Indeed, assuming that the motion of a particle (neutron or photon) is free between two subsequent interactions (no influence of polarisation or spin effects) and defining the expected number of particles in a volume about \mathbf{r} with velocity in the phase space about \mathbf{v} at time t as the *phase space density* $n(\mathbf{r}, \mathbf{v}, t)$, the particle density is given by eq. (2.1) [50]

$$N(\mathbf{r}, t) = \int n(\mathbf{r}, \mathbf{v}, t) d^3v. \quad (2.1)$$

The function $n(\mathbf{r}, \mathbf{v}, t)$ represents the expected number of particles in a volume about \mathbf{r} with velocity in the phase space about \mathbf{v} at time t . Using the kinetic theory, the probability density or distribution function $f(\mathbf{r}, \mathbf{v}, t)$ can be calculated normalising $n(\mathbf{r}, \mathbf{v}, t)$ by dividing through the particle density $N(\mathbf{r}, t)$

$$f(\mathbf{r}, \mathbf{v}, t) = \frac{n(\mathbf{r}, \mathbf{v}, t)}{N(\mathbf{r}, t)}. \quad (2.2)$$

Usually, it is convenient to decompose the velocity vector \mathbf{v} in the kinetic energy and in the direction of the motion. The kinetic energy is defined as $E_k = \frac{1}{2}mv^2$ while, for the direction of particle motion, a unit vector $\boldsymbol{\Omega}$ in the direction of the velocity vector \mathbf{v} is introduced (2.3) [51]

$$\boldsymbol{\Omega} = \frac{\mathbf{v}}{|\mathbf{v}|}. \quad (2.3)$$

Using (2.3) and the kinetic energy definition, it is possible to define the phase space density in terms of the new variables E and $\boldsymbol{\Omega}$ as,

$$n(\mathbf{r}, E, \boldsymbol{\Omega}, t) d^3r dE d\boldsymbol{\Omega}, \quad (2.4)$$

that represents the expected number of particles in a volume d^3r about \mathbf{r} with kinetic energy E_k in dE moving in a direction $\boldsymbol{\Omega}$ in solid angle $d\boldsymbol{\Omega}$. The average particles density can be re-written integrating the

(2.4) equation over the velocity space variables (eq. (2.5)) [50],

$$N(\mathbf{r}, t) = \int_0^\infty dE \int n(\mathbf{r}, E, \boldsymbol{\Omega}, t) d\boldsymbol{\Omega}. \quad (2.5)$$

Another concept that is necessary to define for the derivation of the transport equation is the *phase space current density* function or the *angular current density* $\mathbf{j}(\mathbf{r}, \mathbf{v}, t)$ that is defined as

$$\mathbf{j}(\mathbf{r}, \mathbf{v}, t) \cdot d\mathbf{S} d^3v = \mathbf{v} n(\mathbf{r}, \mathbf{v}, t) \cdot d\mathbf{S} d^3v, \quad (2.6)$$

which represents the expected number of particles that cross a specific area $d\mathbf{S}$ per second with a velocity \mathbf{v} in the velocity space d^3v at time t . Integrating this quantity over particle velocities, it is possible to determine the particle *current density* $\mathbf{J}(\mathbf{r}, t)$ as

$$\mathbf{J}(\mathbf{r}, t) = \int \mathbf{j}(\mathbf{r}, \mathbf{v}, t) d^3v. \quad (2.7)$$

From (2.7), it is possible to derive the *partial current density* $J_\pm(\mathbf{r}, t)$, which defines the rate of particles flowing through an area in a given direction (2.8) [52]

$$J_\pm(\mathbf{r}, t) = \pm \int_\pm \mathbf{n} \cdot \mathbf{j}(\mathbf{r}, \mathbf{v}, t) d^3v, \quad (2.8)$$

where \mathbf{n} is the unit vector normal to the surface dS and the particle velocity space is taken over the selected positive or negative direction. From the definition of the partial current density, it is possible to define the net current density on a given surface as

$$\mathbf{n} \cdot \mathbf{J}(\mathbf{r}, t) = J_+(\mathbf{r}, t) - J_-(\mathbf{r}, t). \quad (2.9)$$

The transport equation is given by simply balancing all the mechanisms of gaining or losing particles from a generic volume of material. Therefore, looking to the Figure 2.1, considering an arbitrary volume V of the Euclidean space \mathbb{R}^3 in which the infinitesimal volume d^3r is identified, it is possible to calculate the time rate of change of particles, having velocities \mathbf{v} in d^3v , in the given volume.

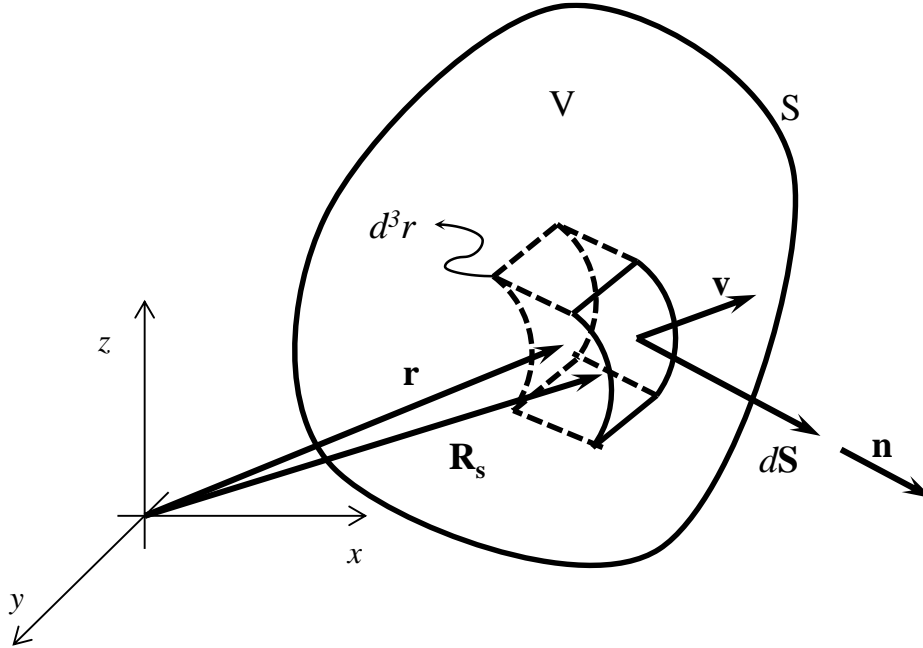


Figure 2.1. A schematic diagram of arbitrary volume V . S represents the surface area, \mathbf{r} the position vector, \mathbf{v} the velocity vector, d^3r the infinitesimal volume, $d\mathbf{S}$ is the elementary surface vector (it is equal to $dS\mathbf{n}$) and \mathbf{R}_s is the position vector of surface dS .

Neglecting macroscopic forces (free motion between two subsequent interactions), the only differences in the particle number are due to leakage through the surface S , collisions that change the velocities of

particles and source in V . The mathematical balance in these conditions is

$$\frac{\partial}{\partial t} \int_V n(\mathbf{r}, \mathbf{v}, t) d^3 r d^3 v = \int_S \mathbf{j}(\mathbf{r}, \mathbf{v}, t) \cdot d\mathbf{S} d^3 v + \int_V \left(\frac{\partial n}{\partial t} \right)_{coll} d^3 r d^3 v + \int_V s(\mathbf{r}, \mathbf{v}, t) d^3 r d^3 v, \quad (2.10)$$

where $s(\mathbf{r}, \mathbf{v}, t)$ is a source density function and $\left(\frac{\partial n}{\partial t} \right)_{coll}$ is the time rate of change due to collisions.

Selecting an arbitrary volume that is not dependent on time and using the Gauss law for writing the surface integral of leakage contribution as a volume integral

$$\frac{\partial}{\partial t} \int_V n(\mathbf{r}, \mathbf{v}, t) d^3 r d^3 v = \int_V \mathbf{v} \cdot \nabla n(\mathbf{r}, \mathbf{v}, t) d^3 r d^3 v + \int_V \left(\frac{\partial n}{\partial t} \right)_{coll} d^3 r d^3 v + \int_V s(\mathbf{r}, \mathbf{v}, t) d^3 r d^3 v. \quad (2.11)$$

Considering that V is an arbitrary volume, equation (2.11) will be satisfied for each V , so it is possible to write the general form of transport equation as reported in (2.12) [50]

$$\frac{\partial n}{\partial t} + \mathbf{v} \cdot \nabla n(\mathbf{r}, \mathbf{v}, t) = \left(\frac{\partial n}{\partial t} \right)_{coll} + s(\mathbf{r}, \mathbf{v}, t). \quad (2.12)$$

The analytical description of the particle transport requires also the definition of initial ($n(\mathbf{r}, \mathbf{v}, 0)$) and boundary conditions. The latter depends on the problem analysed, for this reason, several specifications are possible:

- Free surface. The particle can only escape through the boundary surface, so $n(\mathbf{R}_S, \mathbf{v}, t) = 0$;
- Reflecting boundary. The particles are reflected at the boundary with the reflection angle equal to the incident one, consequently $n(\mathbf{R}_S, \mathbf{v}, t) = n(\mathbf{R}_S, \mathbf{v}_r, t)$; where \mathbf{v}_r is the reflecting velocity such that $\mathbf{v} \cdot \mathbf{n} = \mathbf{v}_r \cdot \mathbf{n}$.
- Albedo boundary. It is a variation of reflecting boundary in which the incoming density is reduced by factor α , then $n(\mathbf{R}_S, \mathbf{v}, t) = \alpha n(\mathbf{R}_S, \mathbf{v}_r, t)$;
- Periodic boundary. The particles outgoing in a certain boundary is equated with the incoming particle on another boundary.

Integrating (2.12), the product $vn(\mathbf{r}, \mathbf{v}, t)$ is commonly obtained that, in the transport theory, is known as the angular flux or phase space flux $\phi(\mathbf{r}, \mathbf{v}, t)$. From this, the velocity integrated flux is defined as follows [50]

$$\phi(\mathbf{r}, t) = \int \phi(\mathbf{r}, \mathbf{v}, t) d^3 v = \int vn(\mathbf{r}, \mathbf{v}, t) d^3 v. \quad (2.13)$$

The collision term $\left(\frac{\partial n}{\partial t} \right)_{coll}$ can be made clear through the (2.14) [51].

$$\left(\frac{\partial n}{\partial t} \right)_{coll} = \int v' \Sigma(\mathbf{r}, \mathbf{v}' \rightarrow \mathbf{v}) n(\mathbf{r}, \mathbf{v}', t) d^3 v' - v \Sigma(\mathbf{r}, \mathbf{v}) n(\mathbf{r}, \mathbf{v}, t), \quad (2.14)$$

where:

$\Sigma(\mathbf{r}, \mathbf{v}' \rightarrow \mathbf{v})$ represents the *collision kernel*. It defines the probability per unit distance that an incident

particle with velocity \mathbf{v}' interacts producing a secondary particle with a velocity \mathbf{v} ;

$\Sigma(\mathbf{r}, \mathbf{v})$ is the *macroscopic cross section*. It is related to the *microscopic cross section* σ through the background medium number density $N_B(\mathbf{r})$. Indeed, $\Sigma(\mathbf{r}, \mathbf{v}) = N_B(\mathbf{r})\sigma(\mathbf{v})$.

Using (2.3), (2.13), (2.14) and the kinetic energy definition, the Boltzmann transport equation (2.12) can be rewritten in terms of angular flux $\varphi(\mathbf{r}, \mathbf{\Omega}, E, t)$ as follows [52]:

$$\begin{aligned} & \frac{1}{v} \frac{\partial \varphi(\mathbf{r}, \mathbf{\Omega}, E, t)}{\partial t} + \mathbf{\Omega} \cdot \nabla \varphi(\mathbf{r}, \mathbf{\Omega}, E, t) + \Sigma(\mathbf{r}, E) \varphi(\mathbf{r}, \mathbf{\Omega}, E, t) = \\ & = \int_0^{+\infty} \int_{4\pi} \Sigma(\mathbf{r}, \mathbf{\Omega}' \rightarrow \mathbf{\Omega}, E' \rightarrow E) \varphi(\mathbf{r}, \mathbf{\Omega}', E', t) d\mathbf{\Omega}' dE' + s(\mathbf{r}, \mathbf{\Omega}, E, t) \end{aligned} \quad (2.15)$$

Eq. (2.15) is commonly used to describe the transport of neutrons and photons through a medium.

2.1.2 Monte Carlo Method and MCNP for Transport Modes

The Boltzmann equation (2.15) provides a mathematical representation of the physical transport problem but its analytical resolution is limited to few specific cases with many simplifications. For this reason, computational codes based on deterministic or Monte Carlo methods are used to assess the neutron and photon transport through a medium [53].

The Monte Carlo method simulates the average behaviour of individual particles recording some aspects (tallies). It does not solve analytically the transport equation but it solves a transport problem by simulating particle histories.

Practically, the particle is followed from a source through its life until its death (absorption, escape, etc.) and the probability distribution governing these events are randomly sampled using the transport data to describe the total phenomenon [53].

One of the most used codes, based on Monte Carlo method, is the Monte Carlo N-Particle (MCNP). It is a “*general-purpose, continuous-energy, generalized-geometry, time-dependent, coupled neutron/photon/electron Monte Carlo transport code*” [53]. It can transport several particles like neutron, photon, electron and some of their combinations covering a vast regime of energies (from 10^{-11} to 20 MeV for neutrons, from 1 keV to 100 GeV for photons and from 1keV to 1 GeV for electrons). The user defines an input file, which then is read by MCNP, containing information about the problem in terms of geometry specification, material composition and cross sections, location and features of neutron or photon source and type of tallies desired as output [53].

The fundamental unit of an MCNP solid model is a cell where the geometry can be defined by means of two representations: the Constructive Solid Geometry (CSG) and the Hybrid. The CSG solid models are defined by means of Boolean operations between surfaces of 1st and 2nd degree and elliptical tori of 4th degree [53]. In the Hybrid representation, a geometry mesh (structure or unstructured) from an external file can be embedded into cells of a CSG model using the "universe" construct [54].

Physical quantities of interest, both for CSG and Hybrid representation, can be evaluated by MCNP using tallies. It provides seven standard tally types normalised per starting particle that can be modified by the user in many ways.

In this dissertation, due to the investigated phenomena, only some of them are used, in particular: the surface current tally (type F1), the average surface flux tally (type F2), the average cell flux tally (type F4) and the energy deposition averaged over a cell tally (type F6) [53].

The F1 tally counts the number of particles crossing a surface in specified bins. Remembering the definition of angular current density reported in eq. (2.6) and expressing it in terms of energy and angular distribution, assuming that $\mathbf{j}(\mathbf{R}_s, E, \mathbf{\Omega}, t) \equiv \mathbf{\Omega} \varphi(\mathbf{R}_s, E, \mathbf{\Omega}, t)$, the F1 tally would measure

$$\begin{aligned}
F1 &= \int d\mathbf{S} \int dt \int dE \int \mathbf{n} \cdot \mathbf{j}(\mathbf{R}_s, E, \mathbf{\Omega}, t) d\mathbf{\Omega}, \\
&= \int d\mathbf{S} \int dt \int dE \int |\mathbf{\Omega} \cdot \mathbf{n}| v n(\mathbf{R}_s, E, \mathbf{\Omega}, t) d\mathbf{\Omega}.
\end{aligned} \tag{2.16}$$

The energy (E_i) and angle/cosine ($\mathbf{\Omega}_k/\mu$) bins are controlled through the E and C cards in MCNP [53].

The F2 tally evaluates the average surface flux over a surface assuming that $\varphi(\mathbf{R}_s, E, \mathbf{\Omega}, t)$ is the energy and angular distribution of the fluence as function of position (eq. (2.17)) [53]

$$F2 = \frac{1}{S} \int d\mathbf{S} \int dt \int dE \int \varphi(\mathbf{R}_s, E, \mathbf{\Omega}, t) d\mathbf{\Omega}. \tag{2.17}$$

The F4 tally is used to estimate the track length of cell flux according to the (2.18) [53]

$$\begin{aligned}
F4 &= \frac{1}{V} \int d^3\mathbf{r} \int dt \int dE \int \varphi(\mathbf{r}, E, \mathbf{\Omega}, t) d\mathbf{\Omega} \\
&= \frac{1}{V} \int d^3\mathbf{r} \int dt \int dE \int v n(\mathbf{r}, E, \mathbf{\Omega}, t) d\mathbf{\Omega}
\end{aligned} \tag{2.18}$$

The F6 tally estimates the track length of energy deposition. It counts for the total energy deposition in a cell (i.e. the deposited heating) as follows

$$F6 = \frac{\rho_a}{m} \int d^3\mathbf{r} \int dt \int dE \int \sigma_r(E) H(E) \varphi(\mathbf{r}, E, \mathbf{\Omega}, t) d\mathbf{\Omega}, \tag{2.19}$$

where ρ_a is the atom density, m is the cell mass and $H(E)$ is heating number that depends on the particle considered (neutrons or photons) and counts the average energy released for all reactions at the incident particle energy [53].

In addition to the standard tallies, MCNP provides also a superimposed mesh tally (FMESH) of type 4 that can be modified through the tally flux multiplier (FM) card to obtain other quantities like heating deposition and isotope production rate.

The tallies, so far defined, are applicable both to the CSG and Hybrid representations but for the latter additional cards are used to obtain the results in each element/voxel (e.g. cards EMBEE, EMBEB) [54].

Another important concept equal in stature to the tally is the statistical error associated with the results. Indeed, in a Monte Carlo simulation, each particle is followed during its life and it contributes a score x_i to the tally.

The probability that a history contributes a score between x and $x+dx$ is given by $p(x)dx$ where $p(x)$ is the probability distribution function. As stated before, in Monte Carlo calculations, the searched answer is given by the mean value $\langle x \rangle$ that in MCNP simulation is approximated according to (2.20) [53]:

$$\bar{x} \equiv \frac{1}{N} \sum_{i=1}^N x_i, \tag{2.20}$$

where N is the number of problem histories and x_i is the value of x selected from $p(x)$.

The variance of the population of x values measures the spread in these values as stated in (2.21) [53]

$$S^2 \equiv \frac{1}{N-1} \sum_{i=1}^N (x_i - \bar{x})^2, \tag{2.21}$$

where $\overline{x^2} \equiv \frac{1}{N} \sum_{i=1}^N x_i^2$ and then the approximated variance of the average \bar{x} is

$$S_x^2 \equiv \frac{1}{N} S^2. \tag{2.22}$$

Using (2.20) and (2.22), in an MCNP simulation, the uncertainty associated with the result is evaluated

through the *relative error* R of the average \bar{x} of the N particles scores [53]

$$R \equiv \frac{S_{\bar{x}}}{\bar{x}}. \quad (2.23)$$

The *relative error* R is a useful parameter to estimate the goodness of the results: lower than 5% the results are assumed reliable, between the 5-10% reliable except for point detector, between 10-20% questionable and above the latter limit as factor of a few or not reliable at all [53]. Besides R , MCNP produces other 9 statistical tests to verify the "convergence" of the given calculation.

Regarding to the boundary conditions introduced in paragraph 2.1.1, reflecting, white and periodic boundaries can be defined in MCNP.

When reflecting boundaries are used, any particle hitting this surface is specularly reflected as a mirror. This condition is used in case of geometry symmetries for reducing the calculation domain.

The white surfaces are used to approximate an infinite scatterer. Particles hitting a white boundary are reflected, with respect to the surface normal, with a cosine distribution ($p(\mu) = \mu$), where $\mu = \sqrt{\xi}$ and ξ is a random number. While periodic boundary conditions are used to simulate an infinite lattice pairing the planes.

2.2 Thermal-Hydraulic Model

The nuclear analysis for given configuration geometry/materials provides loads (e.g. volumetric thermal heat) that are used as inputs for thermal-hydraulic and thermo-mechanical ones.

In fluid dynamics, the behaviour of a fluid from a macroscopic point of view is described by Navier-Stokes equations [55]. They are a system of non-linear partial differential equations based on the hypothesis that the fluid can be modelled as a deformable continuum. Therefore, they suppose the continuity of the fluid under examination.

The system of equations involves five differential scalar equations to the partial derivatives and 20 variables (1 for the density, 3 for the velocity vector, 1 for the pressure, 9 for the viscous stress tensor, 3 for the convective acceleration vector, 1 for the internal energy and 2 for the thermal conductivity and temperature). The balance between equations and unknowns is achieved (as described later) with the definition of the fluid properties. The equations can only be solved if boundary and initial conditions or the state equation in the case of a gas mixture are provided, otherwise the amount of solution is infinite. Moreover, due to their non-linearity, the Navier-Stokes equations almost never admit an analytical solution but exclusively numerical (section 2.2.2).

Setting the condition of deformable continuum, the Navier-Stokes equations are the mathematical formalization of three physical principles to which the fluids respond: principle of mass conservation (continuity equation), second principle of dynamics (balance of momentum) and first principle of thermodynamics (energy conservation). For this reason, they are termed as balance equations [56].

2.2.1 Thermal-Hydraulic General Conservation Laws

For the derivation of the general conservation laws, a control volume for the fluid as reported in Figure 2.2 is assumed. The material volume V_t is assumed variable in time and enclosed by a surface $S_t = \partial V_t$ such that every point of it and every point inside it moves at the same speed of the external motion field (Lagrangian point of view). Accordingly, the flow through the surface S_t is assumed null because the relative velocity between the external field of motion and the surface itself is zero at any point of S_t .

Therefore, the volume V_t is a closed system, in the sense that the mass inside it does not change, but there may be external forces acting on the system and there may be energy passing (heat and/or work of external forces) across the surface S_t .

The three fundamental laws that must to be necessarily verified are [56]:

1. Conservation of mass: $M_{V_t} = \text{const.} \Rightarrow \frac{dM_{V_t}}{dt} = 0$;
2. Conservation of momentum (Newton's 2nd law): $\frac{d\mathbf{p}}{dt} = \mathbf{F}$;
3. Conservation of energy (first law of thermodynamics): $\frac{dE}{dt} = \frac{dQ}{dt} - \frac{dW}{dt}$,

where M_{V_t} is the system total mass contained in the volume V_t at time t , \mathbf{p} is the system momentum, \mathbf{F} is the result of external forces acting on the system, E is the system total energy, Q is the heat supplied to the system and W is the work performed by the system.

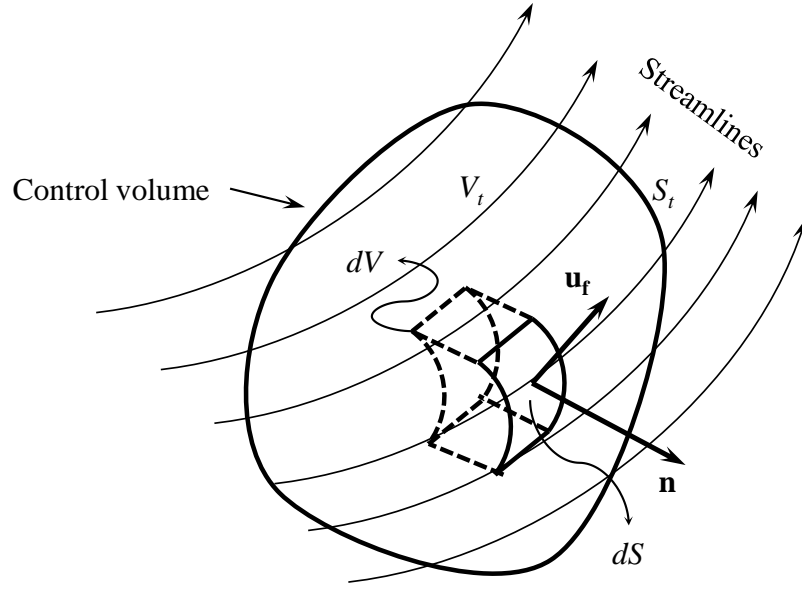


Figure 2.2. A schematic view of arbitrary fluid volume V_t . S_t represents the surface area, \mathbf{u}_f the velocity fluid vector, dV the infinitesimal fluid volume, dS is the elementary surface and \mathbf{n} is the normal unit vector.

In the case of a system consisting of a fluid in motion, total energy E is intended as the sum of the internal energy U and kinetic energy K . If ρ indicates the density of the fluid, \mathbf{u}_f its velocity, e the energy density and e_{tot} the total energy density, the sum of the densities (per unit of mass) of internal and kinetic energy is

$$e_{tot} = e + \frac{|\mathbf{u}_f|^2}{2}, \quad (2.24)$$

then, it is possible to write [57]

$$\frac{d}{dt} \int_{V_t} \rho dV = \int_{V_t} \left[\frac{\partial \rho}{\partial t} + \nabla \cdot (\rho \mathbf{u}_f) \right] dV = 0, \quad (2.25)$$

$$\frac{d}{dt} \int_{V_t} \rho \mathbf{u}_f dV = \int_{V_t} \left[\frac{\partial \rho \mathbf{u}_f}{\partial t} + \nabla \cdot (\rho \mathbf{u}_f \times \mathbf{u}_f) \right] dV = \mathbf{F}, \quad (2.26)$$

$$\frac{d}{dt} \int_{V_t} \rho e_{tot} dV = \int_{V_t} \left[\frac{\partial \rho e_{tot}}{\partial t} + \nabla \cdot (\rho e_{tot} \mathbf{u}_f) \right] dV = \frac{dQ}{dt} - \frac{dW}{dt}. \quad (2.27)$$

The expression (2.25) expresses the conservation of mass in an integral form. It has to be noted that the choice of the volume of control V_t is absolutely arbitrary while the relation (2.25) imposes the equality for

any choice of V_t . The only possibility for this to happen is that the integral function is zero, consequently

$$\frac{\partial \rho}{\partial t} + \nabla \cdot (\rho \mathbf{u}_f) = 0. \quad (2.28)$$

Eq. (2.28) is the equation of conservation of mass in differential form and represents the first equation of Navier-Stokes system. As for Newton's second law (eq. (2.26)), the sum of the forces \mathbf{F} acting on the volume is due both to the volume and surface forces. The latter is the result of the integral of the stresses on the surface S_t . Considering the i -th component of \mathbf{F} , it possible to write [57]

$$F_i = \int_{V_t} \rho g_i dV + \int_{S_t} \sigma_{ij}^f n_j dS, \quad (2.29)$$

where g_i is a volumetric force per unit mass in the direction x_i , practically an acceleration, and σ_{ij}^f is the fluid stress tensor. The stress tensor is composed of two terms: one static ($-p\delta_{ij}$) due to normal stresses, usually of compression, of equal intensity in the three directions (i.e. pressure), and one dynamic (d_{ij}) due to the fluid motion. For a Newtonian fluid, the dynamic term (d_{ij}) is expressed through (2.30) [57]:

$$d_{ij} = \mu_f \left(\frac{\partial u_i}{\partial x_j} + \frac{\partial u_j}{\partial x_i} - \frac{2}{3} \frac{\partial u_s}{\partial x_s} \delta_{ij} \right), \quad (2.30)$$

where μ_f is the fluid viscosity and δ_{ij} is the Kronecker delta. Therefore the fluid stress tensor σ_{ij}^f is defined as follows [57]:

$$\sigma_{ij}^f = -p\delta_{ij} + \mu_f \left(\frac{\partial u_i}{\partial x_j} + \frac{\partial u_j}{\partial x_i} - \frac{2}{3} \frac{\partial u_s}{\partial x_s} \delta_{ij} \right). \quad (2.31)$$

Applying to (2.29) the theorem of divergence and substituting the definition of stress tensor (2.31) as well as the (2.30), it is possible to write [57]

$$F_i = \int_{V_t} \left\{ \rho g_i - \frac{\partial p}{\partial x_i} + \frac{\partial}{\partial x_j} \left[\mu_f \left(\frac{\partial u_i}{\partial x_j} + \frac{\partial u_j}{\partial x_i} - \frac{2}{3} \frac{\partial u_s}{\partial x_s} \delta_{ij} \right) \right] \right\} dV. \quad (2.32)$$

Substituting the expression (2.32) in (2.26) and considering that it has to be satisfied for any volume V_t , the momentum equations for the Navier-Stokes system can be written as follows [57]:

$$\frac{\partial \rho u_i}{\partial t} + \frac{\partial \rho u_i u_j}{\partial x_j} = \rho g_i - \frac{\partial p}{\partial x_i} + \frac{\partial}{\partial x_j} \left(\mu_f \left(\frac{\partial u_i}{\partial x_j} + \frac{\partial u_j}{\partial x_i} - \frac{2}{3} \frac{\partial u_s}{\partial x_s} \delta_{ij} \right) \right). \quad (2.33)$$

As far as the energy equation (2.27) is concerned, two main contributions have to be considered: (i) the volumetric heating due to the adsorption/emission of radiation and (ii) the heat transfer across the volume surface generated by the temperature gradients.

Regarding the first contribution, the volumetric heat addition per unit mass, \dot{q} , is derived by the neutron/photon transport analysis and represents the average power released for all the reaction between the incident particles and the BB materials (the numerical approximation of \dot{q} is given by F6 tally of eq. (2.19)). Considering that the mass of moving fluid element is ρdV , the volumetric heating of a fluid volume is $\rho \dot{q} dV$. In the next, the product $\rho \dot{q}$ will be indicated as volumetric density of heat power q_g''' .

Concerning the second contribution, it is fundamental to define the state of a thermodynamic system as a system in which its conditions are in thermodynamic equilibrium. It is said that a system is in thermodynamic equilibrium if its thermodynamic variables (typically pressure, volume and temperature) are well defined and do not vary over time. Clearly, a fluid in motion, which exchanges heat, cannot be in

global thermodynamic equilibrium since the thermodynamic variables change both in space and in time. However, it is possible to think that the thermodynamic variables vary slowly both in time and in space in the neighbourhood of a fluid point. This means that the fluid can be assumed in a *local* thermodynamic equilibrium on a small scale [56]. This local thermodynamic assumption is a crucial pre-requisite, indeed assuming that is valid, all perturbations propagating in a time scale in dimensions of the order of the problem cannot be treated. Under this fundamental hypothesis of local thermodynamic equilibrium, it is assumed that the thermal power is transmitted only by conduction within fluid according to the Fourier's law:

$$\underline{\underline{q}} = -\underline{\underline{k}}\nabla T, \quad (2.34)$$

where $\underline{\underline{q}}$ is the heat flux, $\underline{\underline{k}}$ is the thermal conductivity tensor and ∇T is the temperature gradient.

Under the hypothesis of isotropic fluid (its physical properties do not depend on the particular spatial direction), the thermal conductivity is a scalar (namely, kI where I is the unit matrix). From (2.34) for isotropic fluid, it is possible to define the incoming thermal power through the surface S_i as [57]

$$\frac{dQ}{dt} = \int_{V_i} \underline{\underline{q}} \cdot dV + \int_{S_i} \underline{\underline{q}} \cdot (-\mathbf{n}) dS = \int_{V_i} \underline{\underline{q}} \cdot dV + \int_{S_i} k \nabla T \cdot \mathbf{n} dS = \int_{V_i} \underline{\underline{q}} \cdot dV + \int_{S_i} k \frac{\partial T}{\partial x_j} n_j dS. \quad (2.35)$$

Regarding the force power acting on the material volume V_i and remembering that the mechanical power is the scalar product between the agent force and the speed of displacement, it is possible to write

$$\frac{dW}{dt} = -\int_{V_i} \rho g_i u_i dV - \int_{S_i} \sigma_{ij} n_j u_i dS, \quad (2.36)$$

where the first term on the right side is the volumetric forces while the second term the surface ones.

Using the divergence theorem for (2.35) and (2.36), substituting (2.31), (2.35) and (2.36) in (2.27) and remembering the expression must be verified for any V_i , the first principle of Thermodynamics for a fluid in motion written in tensorial form becomes [57]

$$\left[\frac{\partial \rho e_{tot}}{\partial t} + \frac{\partial \rho e_{tot} u_j}{\partial x_j} \right] = \underline{\underline{q}} + \frac{\partial}{\partial x_j} \left(k \frac{\partial T}{\partial x_j} \right) - \frac{\partial p u_j}{\partial x_j} + \frac{\partial}{\partial x_j} \left(u_i \mu_f \left(\frac{\partial u_i}{\partial x_j} + \frac{\partial u_j}{\partial x_i} - \frac{2}{3} \frac{\partial u_s}{\partial x_s} \delta_{ij} \right) \right) + \rho g_i u_i. \quad (2.37)$$

The expression (2.37) represents the energy balance equation of Navier-Stokes system. It is composed of 5 equations: one for the mass conservation (2.28), three for the momentum balance (2.33) and one for the energy balance (2.37). The unknowns are seven (the fluid density ρ , the fluid pressure p , the internal energy of the fluid e and the three velocities u_1 , u_2 and u_3) so the problem seems apparently not well defined. Adding the fluid state equation $F(\rho, p, T) = 0$, which links the three variables of state (density, pressure and temperature), and the dependence of the internal energy e and the thermodynamic state of the system, it is possible to close the problem. Therefore, if the thermodynamic state of the system is expressed through pressure and temperature (two thermodynamic variables), it is possible to write two equations (2.38) that complete the system of equations pairing the number of unknowns [56],

$$\rho = \rho(T, p) \quad \text{and} \quad e = e(T, p). \quad (2.38)$$

Several boundary and initial conditions can be defined according to the phenomenon under study. Usually it is necessary to satisfy, at least, the no-slip condition (perfect adhesion of the fluid to solid surfaces) as boundary condition. In general, the analysis of boundary conditions for the Navier-Stokes equations is a rather complex matter and a mathematical demonstration of existence and uniqueness of the

solution does not exist except for very schematic cases and simplified situations. For these reasons, it will not be treated in this dissertation.

2.2.2 Computational Fluid Dynamics Model

The Navier-Stokes equations are differential equations that describe flows and related phenomena but cannot be solved analytically except for special cases. An approximated numerical solution can be obtained using a discretisation method for approximating the differential equations with algebraic ones which can be solved on a computer. The branch of science that uses numerical analysis for studying problems, where a fluid is involved, is called CFD. It is composed of the following ingredients [58]:

- *Mathematical model.* According to the target application, in a numerical simulation, it has been selected the appropriate physical model (e.g. incompressible, turbulent, two or three dimensional, etc.) able to approximate the real phenomenon. The derived equations (based on physical models) are then the mathematical model. The mathematical models usually include approximation of the conservation laws found in section 2.2.1.
- *Discretisation model.* The method has to be selected to approximate the differential equation using a system of algebraic equations for the variables at some set of discrete locations in space and time. Several methods are used for the discretisation: Finite Difference Method (FDM), Finite Volume Method (FVM) and Finite Element Method (FEM). The FDM uses the conservation equations in differential form that are approximated replacing the partial derivatives by expressions of the nodal values of the functions. The FVM uses the integral form of conservation equations that are solved in a finite number of Control Volumes (CVs). The FEM is very similar to the FVM except that the equations are multiplied by a weight function before to be integrated over the domain. In FEM, the solution is approximated by a shape function within the element that allows the continuity of the solution across the element boundaries.
- *Numerical grid (or mesh).* The grid is the discrete representation of the geometric domain where the variables are to be calculated according with the mathematical and discretisation model. The grid can be structured, unstructured or block-structured. The structured mesh consists in families of grid lines that do not cross each other allowing a consecutively numbering. The unstructured mesh is the most flexible type of grid that can be adapted to complex geometries. The elements can have any shape and there are not restrictions on the number of neighbour elements or nodes. In the block-structured mesh, there are several levels of subdivision of solution domain that can be irregular (unstructured) and regular (structured).
- *Solution method.* The selection of the solution method depends on the problem and of the discretisation model selected as well as on the grid. Usually, the solution methods use successive linearization scheme of the equations and then the resulting linear system is solved by iterative techniques.

The CFD analysis is strongly applied for assessing temperature and velocity fields in the structure material and in the fluid. For this reason, this analysis is used to drive the design of HCPB and WCLL BBs by means of commercial code ANSYS CFX [59] (it will be also used in the following for testing the MAIA procedure). ANSYS CFX uses an element-based finite volume method.

The spatial domain is meshed to construct finite volumes (or CVs) where relevant quantities such as mass, momentum, and energy are estimated. The conservation equations ((2.28), (2.33) and (2.37)), used in ANSYS CFX, are discretised over the volume and surface elements. Volume integrals are solved within each CV, while surface integrals at the integration points (ipn) (the centre of each surface element) and then distributed to the neighbour CVs [59].

2.3 Thermo-Mechanic Model

2.3.1 Elements of Structural-Mechanics

The aim of the thermo-mechanical investigation for a complex 3D system, such as the DEMO BB, consists in the assessment of displacement, stress, thermal and strain fields that originate within the geometry due to the application of boundary conditions and thermal and mechanical loads selected for representing the problem under study.

Regarding the thermal field, it is a scalar depending on the spatial and temporal variables, as follows

$$T = T(x, y, z, t). \quad (2.39)$$

The temperature field that originates within a 3D body is a consequence of the internal and external thermal loads.

In the case of the BB, the thermal loads are mainly due to the heat generation within the body due to the heat flux coming from the plasma and to the interactions between photons/neutrons and the BB materials.

It is possible to write the pure conduction equation obtained as a special case of thermal balance equation applied to solid bodies [60]

$$\rho c_p \frac{\partial T}{\partial t} = q_g''' + \text{div}[-\mathbf{q}''], \quad (2.40)$$

where $q_g''' = q_g'''(x, y, z, t)$ is the volumetric density of heat power generated within the body (source term) and $\mathbf{q}'' = \mathbf{q}''(x, y, z, t)$ represents the thermal heat flux, determined by the Fourier's law according to (2.34).

Considering a uniform, homogeneous and isotropic body, the thermal conductivity can be represented by the product of a scalar for the unit matrix and it can depend, at most, only on the temperature like the other physical quantities.

Combining equations (2.40) and (2.34) and imposing a set of thermal boundary conditions aimed to represent, under the thermal standpoint, the physical reality at the boundaries of the investigated domain, it is possible to integrate the resolving equation in order to obtain the thermal field function $T(x, y, z, t)$ [60].

The obtainment of an analytical solution is difficult unless the system under study is characterised by high geometric and physical property regularity that can be represented by simplified hypotheses.

However, this is not the case of DEMO BB where the geometric and physical features are characterised by a high degree of complexity that makes practically impossible to obtain an analytical resolution of the thermal problem.

For this reason, numerical methods are used for approximating the solutions.

Concerning the stress field, it is a tensor of the second order and function of the spatial and temporal variables,

$$\underline{\underline{\sigma}}(x, y, z, t) = \begin{vmatrix} \sigma_{xx} & \sigma_{xy} & \sigma_{xz} \\ \sigma_{yx} & \sigma_{yy} & \sigma_{yz} \\ \sigma_{zx} & \sigma_{zy} & \sigma_{zz} \end{vmatrix}, \quad (2.41)$$

where $\sigma_{ij} = \sigma_{ij}(x, y, z, t)$, with i and j variables in x , y and z , is the stress tensor component in the j direction for the stress acting on the plane with i as normal [61]. In particular, the normal stresses are defined as $\sigma_{ii} = \sigma_{ii}(x, y, z, t)$ while the shear stresses as $\sigma_{ij} = \sigma_{ij}(x, y, z, t)$, with $i \neq j$, and are also designated as $\tau_{ij} = \tau_{ij}(x, y, z, t)$ [61].

Regarding the strain field, it is a tensor of the second order and function of the spatial and temporal variables,

$$\underline{\underline{\varepsilon}}(x, y, z, t) = \begin{vmatrix} \varepsilon_{xx} & \varepsilon_{xy} & \varepsilon_{xz} \\ \varepsilon_{yx} & \varepsilon_{yy} & \varepsilon_{yz} \\ \varepsilon_{zx} & \varepsilon_{zy} & \varepsilon_{zz} \end{vmatrix}, \quad (2.42)$$

where $\varepsilon_{ij} = \varepsilon_{ij}(x, y, z, t)$, with i and j variables in x , y and z , is the strain tensor component in the j direction for the strain acting on the elementary fibres with i as normal. In particular, the normal strains are defined as $\varepsilon_{ii} = \varepsilon_{ii}(x, y, z, t)$ while the shear strains as $\varepsilon_{ij} = \varepsilon_{ij}(x, y, z, t)$, with $i \neq j$ [61].

The displacement field, instead, is a vector function of spatial and temporal variables,

$$\mathbf{u}(x, y, z, t) = \begin{vmatrix} u \\ v \\ w \end{vmatrix}. \quad (2.43)$$

Applying the Theory of Elasticity and under the hypothesis of small strains, it is possible to obtain the solution of the thermo-mechanical problem solving the system of equations composed by indefinite equilibrium equations, the strain-displacement equations and the constitutive equations [61].

The indefinite equilibrium equations express the elemental volume equilibrium condition (both translation and rotation) of a continuum 3D elastic body, under steady-state conditions. They are represented by a system of 6 partial differential equations where the 9 stress field functions are the unknowns [62]

$$\begin{cases} \frac{\partial \sigma_{xx}}{\partial x} + \frac{\partial \tau_{yx}}{\partial y} + \frac{\partial \tau_{zx}}{\partial z} + X = 0; & \tau_{yx} = \tau_{xy} \\ \frac{\partial \tau_{xy}}{\partial x} + \frac{\partial \sigma_{yy}}{\partial y} + \frac{\partial \tau_{zy}}{\partial z} + Y = 0; & \tau_{zx} = \tau_{xz} \\ \frac{\partial \tau_{xz}}{\partial x} + \frac{\partial \tau_{yz}}{\partial y} + \frac{\partial \sigma_{zz}}{\partial z} + Z = 0; & \tau_{zy} = \tau_{yz} \end{cases}, \quad (2.44)$$

where X , Y and Z are the components of external loads acting on the domain along the three directions and, therefore, the σ and τ represents the tensions that arise in contrast to these loads.

The strain-displacement equations express the functional dependence between the strain and displacement function components.

This interdependency between strains and displacements ensures the respect of the body continuity without experiencing self-penetrations as well as separations of the fibres. They are represented by a system of 9 partial differential equations where the 9 strain field functions together with the 3 displacements field functions are the unknowns [62]

$$\begin{cases} \varepsilon_{xx} = \frac{\partial u}{\partial x}; & \varepsilon_{yx} = \frac{\partial u}{\partial y} + \frac{\partial v}{\partial x} & \text{with} & \varepsilon_{yx} = \varepsilon_{xy} \\ \varepsilon_{yy} = \frac{\partial v}{\partial y}; & \varepsilon_{zx} = \frac{\partial u}{\partial z} + \frac{\partial w}{\partial x} & \text{with} & \varepsilon_{zx} = \varepsilon_{xz} \\ \varepsilon_{zz} = \frac{\partial w}{\partial z}; & \varepsilon_{zy} = \frac{\partial v}{\partial z} + \frac{\partial w}{\partial y} & \text{with} & \varepsilon_{zy} = \varepsilon_{yz} \end{cases}. \quad (2.45)$$

The constitutive equations express the functional dependence between the stress and strain field components describing the reactions of a body subjected to the application of thermo-mechanical loads.

Assuming that the body is homogeneous, isotropic and linear-elastic, they are represented by a system of 6 algebraic equations where the stress and strain fields are the unknowns [62]

$$\begin{cases} \varepsilon_{xx} = \frac{1}{E} [\sigma_{xx} - \nu(\sigma_{yy} + \sigma_{zz})] + \alpha\theta; & \varepsilon_{yx} = \frac{1}{G} \tau_{xy} \\ \varepsilon_{yy} = \frac{1}{E} [\sigma_{yy} - \nu(\sigma_{xx} + \sigma_{zz})] + \alpha\theta; & \varepsilon_{zx} = \frac{1}{G} \tau_{xz} \\ \varepsilon_{zz} = \frac{1}{E} [\sigma_{zz} - \nu(\sigma_{xx} + \sigma_{yy})] + \alpha\theta; & \varepsilon_{zy} = \frac{1}{G} \tau_{zy} \end{cases}, \quad (2.46)$$

where E , G and ν represent the Young's Modulus, the shear Modulus and the Poisson's Modulus respectively while $\theta(x, y, z)$ represents the relative thermal field function given by the difference between the local temperature $T(x, y, z)$ and the reference temperature, namely that temperature at which the body does not show any thermal induced stress or strain [62].

Composing together in a system the indefinite equilibrium, congruence and constitutive equations, this leads to a system of 21 linearly independent algebraic and partial differential equations with 21 unknowns composed of the 9 stress field functions, the 9 strain field functions and the 3 displacement field functions.

The system can be reduced to 3 second order partial differential equations, complete and coupled, with non-constant coefficients where the 3 displacement field functions are the unknowns [62]

$$\begin{cases} \frac{E}{2(1+\nu)} \Delta u + \frac{E}{2(1+\nu)(1-2\nu)} \frac{\partial}{\partial x} [div(\mathbf{u})] - \frac{\alpha}{(1-2\nu)} \frac{\partial \theta}{\partial x} + X = 0 \\ \frac{E}{2(1+\nu)} \Delta v + \frac{E}{2(1+\nu)(1-2\nu)} \frac{\partial}{\partial y} [div(\mathbf{u})] - \frac{\alpha}{(1-2\nu)} \frac{\partial \theta}{\partial y} + Y = 0 \\ \frac{E}{2(1+\nu)} \Delta w + \frac{E}{2(1+\nu)(1-2\nu)} \frac{\partial}{\partial z} [div(\mathbf{u})] - \frac{\alpha}{(1-2\nu)} \frac{\partial \theta}{\partial z} + Z = 0 \end{cases}, \quad (2.47)$$

where the Δu , Δv and Δw are the Laplacian of the displacements along the three directions.

The system (2.47) can be integrated assuming adequate boundary conditions and the 3 displacement field functions can be calculated. Once the displacement field is obtained, it is possible to assess the strain field by means of the strain-displacement equations (2.45) and, consequently, the stress field function by the constitutive equations (2.46). In this way, the solution of the thermo-mechanical problem for a given 3D body is achieved.

Actually the resolution of the system (2.47) is so complex that an analytical solution cannot be found unless for an extremely regular geometric and physic body and, thus, not feasible for complex 3D systems such as the DEMO BB, for which theoretical-numerical methods are necessary.

Several boundary conditions can be defined according to the phenomena that are investigated. The most interesting and general ones are [63] [64]:

- (i) Plane Strain (PS) that assumes a plane and parallel deformation of fibres;
- (ii) Generalised Plane Strain (GPS) that assumes uniform through-the-thickness extensional strain in the thickness direction (i.e a plane deformation of the fibres); and
- (iii) Plane Stress (PSr) that assumes a stress state where non-zero stress components act in one plane only.

Regarding the PS, the strain and stress tensors are written as [63]

$$\underline{\underline{\varepsilon}}(x, y, z, t) = \begin{vmatrix} \varepsilon_{xx} & \varepsilon_{xy} & 0 \\ \varepsilon_{yx} & \varepsilon_{yy} & 0 \\ 0 & 0 & \varepsilon_{zz} \end{vmatrix}; \quad \underline{\underline{\sigma}}(x, y, z, t) = \begin{vmatrix} \sigma_{xx} & \sigma_{xy} & 0 \\ \sigma_{yx} & \sigma_{yy} & 0 \\ 0 & 0 & \sigma_{zz} \end{vmatrix}. \quad (2.48)$$

In this case the strain components $\varepsilon_{xz} = \varepsilon_{yz} = 0$, ε_{zz} has to be independent of x and y , $\sigma_{zz} \neq 0$ and

equal to [63]

$$\sigma_{zz} = \frac{Ev}{(1+\nu)(1-2\nu)}(\varepsilon_{xx} + \varepsilon_{yy}). \quad (2.49)$$

In the GPS case the strain component ε_{zz} varies linearly on x and y as shown in eq. (2.50):

$$\underline{\underline{\varepsilon}}(x, y, z, t) = \begin{vmatrix} \varepsilon_{xx} & \varepsilon_{xy} & 0 \\ \varepsilon_{yx} & \varepsilon_{yy} & 0 \\ 0 & 0 & ax + by + c \end{vmatrix}. \quad (2.50)$$

Concerning the PSr, the stress and strain tensors assume the following form [63]:

$$\underline{\underline{\sigma}}(x, y, z, t) = \begin{vmatrix} \sigma_{xx} & \sigma_{xy} & 0 \\ \sigma_{yx} & \sigma_{yy} & 0 \\ 0 & 0 & 0 \end{vmatrix}; \quad \underline{\underline{\varepsilon}}(x, y, z, t) = \begin{vmatrix} \varepsilon_{xx} & \varepsilon_{xy} & 0 \\ \varepsilon_{yx} & \varepsilon_{yy} & 0 \\ 0 & 0 & \varepsilon_{zz} \end{vmatrix}. \quad (2.51)$$

In this case the strain components $\sigma_{xz} = \sigma_{yz} = \sigma_{zz} = 0$ but $\varepsilon_{zz} \neq 0$ and equal to [63]:

$$\varepsilon_{zz} = -\frac{\nu}{E}(\sigma_{xx} + \sigma_{yy}). \quad (2.52)$$

Generally, for the analysis of the BB, the PS and GPS are applied when sub-models are used.

2.3.2 Finite Element Method

As said, for complex systems like the BB having specific geometric and physical features, it is extremely difficult to solve the system of equations governing the thermo-mechanical problem obtaining an exact solution. For this reason, numerical methods are commonly used for the solution approximation of the thermo-mechanical problem in 3D systems characterised by high degree of structural and physics complexity.

One of the most used numerical methods used for the resolution of the thermo-mechanical problem is the Finite Element Method (FEM) that has been introduced since the 1950s [65].

The FEM is based on finite elements used to model a continuum body as an ensemble of regions formed by volumes with simple shape that are juxtaposed each other. The elements are characterised by a number of vertexes known as nodes that are connected with the nodes of the adjacent elements.

In this way, a continuum body is topologically approximated by means of simple domains that allow also a simplification of the resolution of the thermo-mechanical governing equations.

The fundamental hypothesis, on which the FEM is based, is that the field function values at a generic element depend on the values of the nodes through some shape functions. These analytical expressions depend on the type of selected element [65].

In each node, a number of degree of freedom, related to the physical variables like temperature, stress, displacement and pressure, is defined. The number of degrees of freedom depends on the type of selected element (linear, quadratic etc.) and determines the degree of approximation of the field function trend characterising also the element behaviour.

The nodalisation and the solving procedure by means of FEM are articulated in the following steps [65]:

- 1) *Continuum discretisation.* The continuum domain is split, by means of subsequent divisions, in finite elements. This process, known as meshing, consists in the creations of several arrays where the node coordinates and element connections are reported. According to the element selected and to the investigated problem, the nodal variables are assigned.
- 2) *Interpolation functions of governing equations.* The governing equations of the continuous field

-
-
- variables are reduced to algebraic equations and interpolated, according to the shape function, over the elements.
- 3) *Assembly of finite element equations.* As the elements, connected through the nodes, are assembled to discretise continuous system body, in the same manner, the finite element governing equations are connected to form a matrix of equations that relates the unknown values of the nodes to other parameters. Different approaches like variational approach or the Galerkin method are used for this task.
 - 4) *Selection of boundary conditions.* According to the physical problem that is studied, a set of boundary conditions is selected and imposed modifying the structure of the original matrix of discretised field equations.
 - 5) *Solve the global matrix of equations.* The finite element global system of equation, typically sparse, symmetric and positive definite, is solved through the adoption of direct and iterative numerical methods.
 - 6) *Evaluation of results.* After the solution of displacement field with the global system of equations, additional parameters, for instance strain and stress, are assessed starting from the calculated independent nodal variables.

The FEM always follows the 6 steps reported above for the formulations and the resolutions of physical problems. This method is also applied in several FEM codes like ANSYS Mechanical [66] that will be used in the following for the thermo-mechanical calculations.

3 Description of Multi-Physics Approach for Integrated Analysis (MAIA)

In this Chapter, the functional description of the multi-physics approach for integrated analysis, namely MAIA, is reported. The aim of this Chapter is to give an overall overview about all the steps to be followed for the application of the MAIA procedure without focusing on the particular results obtained for each analysis. For these reasons, the reported figures have only the scope to illustrate and make clear the data transfer and the consistency maintained among all analyses involved.

3.1 Structure of the MAIA Coupling Procedure

MAIA is a CAD-centric and a loosely-coupled procedure for the design of the BB concepts based on the coupling of the three main pillar analyses (i.e. neutronic, thermal-hydraulic and thermo-mechanic calculations) adopting sub-modelling techniques.

The CAD-centric feature is strictly linked to the sub-modelling technique. Therefore, in all the three calculations currently considered, the geometric characteristics of the computational models have the same degree of detail avoiding the introduction of simplifications as well as homogenisation. This feature is crucial if local phenomena have to be discovered and described. Indeed, the investigation of local effects depends mainly on the tool resolution and geometry detail representation. Furthermore, this characteristic allows keeping the consistency during the transfer of data from one analysis to another also when different meshes are used to respect the computational requirements of each analysis field. Moreover, it allows to investigate local integration issues taking into account all the step gradient that would be created by geometry discontinuities.

However, according to the computational effort, the CAD-centric feature imposes the nodalisation of portions of BB domain if a high geometric detail has to be maintained. Therefore, the models are limited to the geometric unit like the HCPB slice or the WCLL BU already described in paragraph 1.2. For this reason, a set of boundary condition has to be defined for each analysis in order to simulate the interactions between the investigated domain and its environment.

The verification of the local boundary conditions consistency is postponed to Chapter 4.

The loosely-coupled feature, instead, is strictly linked to the three fields of calculation.

The neutronic, thermal-hydraulic and thermo-mechanic analyses have different requirements in term of nodalisation, mathematical models and solving methods. They require also different resources and it is difficult to optimise the performances of all the three analyses when, in particular, they are coupled in a “monolithic” approach. For these reasons, according also to the work done in [44], three different optimised codes, which are run in sequence, have been used and specific in-house scripts have been created when needed in order to speed up the coupling and limit errors linked to the human activity.

The selection of the three codes has followed two main criteria:

- (i) validated codes to be used in front of the Notified Body (e.g. MAIA procedure might be used for the BB design and optimisation so it is important that the codes are verified and validated according to the Code&Standard (C&S));
- (ii) minimise the number of codes involved in the coupling process.

Applying these criteria, the codes that have been selected are: MCNP5/6 [53, 54] for neutronic/photonic transport calculations, ANSYS CFX [59] for the fluid-dynamic and heat transfer analyses, and ANSYS Mechanical [66] for the structural assessment. These codes are largely applied for the design of fission and fusion nuclear reactors and they have faced strong verification and validation campaign [67]. Furthermore, they are currently used for the BB design. Therefore, for these reasons and for ensuring a wide application

of the MAIA procedure, they have been selected and used in this work.

It is also important to notice that the principles, on which the MAIA procedure is based, could be also applied to other verified and validated codes without compromising the validity of the achieved results.

The MAIA procedure is articulated in 8 steps as reported in the functional flow diagram in Figure 3.1.

Each step has to be executed in sequence and the user has to evaluate the results according to the BB requirements and design criteria.

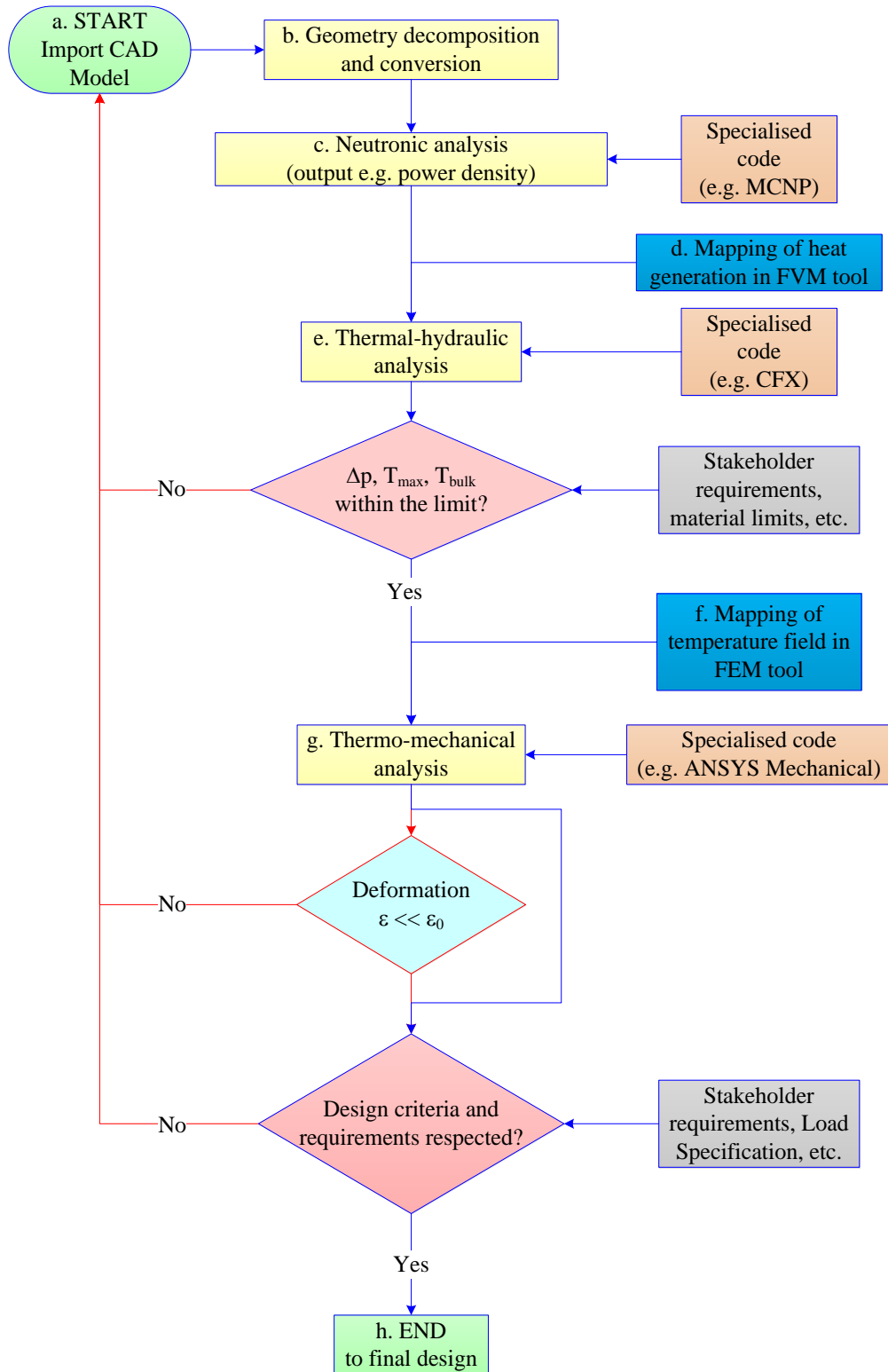


Figure 3.1. MAIA procedure functional flow diagram. Figure reproduced according to [68].

With reference to Figure 3.1, a generic CAD model representing the reference geometry (e.g. slice or breeder unit) is imported within ANSYS DesignModeler [69] (a). Then, the model is prepared for conversion (b) in a format suitable for neutronic analysis to be performed with MCNP. Two different methodologies can be used for the direct creation of the MCNP neutronic input by means of ANSYS, one based on Constructive Solid Geometry (CSG) representation [53] and the second based on the hybrid geometry definition where the Unstructured Mesh (UM) is embedded into the CSG model [54]. Then, the neutronic model, created using ANSYS, is checked by means of the stochastic volume estimation and the neutronic analysis (c) is performed by means of MCNP. Adopting a set of neutron/photon source and of boundary conditions, the 3D profile of the power density is calculated and mapped (d) into Finite Volume Method (FMV) code like CFX [59]. At this point, the fluid-dynamic calculation is carried out (e). Once the thermal-hydraulic requirements are checked and satisfied, the temperature field is mapped (f) into Finite Element Method (FEM) tool like ANSYS Mechanical [66] and a structural analysis is performed (g). If the pressure drop and temperature limits, the deformation field as well as the compliance with the design criteria and requirements imposed by Stakeholder are not respected, the geometry is modified and the procedure restarted from (a), otherwise, if all the limits are respected after these steps, the convergence to final design solution is obtained (h). In the following paragraphs, each step of the MAIA procedure is described in more detail. The attention will be placed more on the blue path of Figure 3.1 than on the red one because the latter represents a mere application of the MAIA procedure using a slightly different geometry.

3.2 Geometry Decomposition and Conversion in MAIA Procedure

Commonly, the CAD engineering models contain geometry details that are not represented in the neutronic input because their representation would require big efforts for the creation of the model as well as excessive computational power. As proved in [19], the omission of details hides local gradients that could jeopardise the structural integrity of BB design. For this reason, a detailed geometry representation has to be pursued.

For the automatic generation of a neutronic input by means of ANSYS [68] (Figure 3.1 step (b) of the MAIA procedure), two different methodologies have been investigated.

The first one is based on the representation of geometrical regions by means of first and/or second order surfaces, known as CSG representation [53]. The second one, instead, is based on the hybrid representation where the UM is embedded in the legacy CSG [54]. These two representations will be indicated in the following as *CSG Modelling* and *Hybrid Modelling*. These two methodologies have been applied to HCPB slice and WCLL BU.

3.2.1 CSG Modelling

The CAD-MCNP conversion, using the CSG Modelling, is made with DesignModeler [69] that requires few manual decompositions before translating the geometry Boundary Representation (BRep) into an MCNP model. These manual modifications are mainly due to the limitation of MCNP that, indeed, does not support the representation of spline boundary surfaces but only first and second order analytic surfaces or tori. Before using the DesignModeler capability to generate an input for MCNP, tiny geometry surfaces with small areas or overlaps have to be checked. ANSYS DesignModeler provides functions for the detection of small features (small faces, edges and steps) and for their removal. After this control procedure, the complex solid must be decomposed into a combination of simple convey solids such as boxes, cylinders, spheres, etc. This is realised slicing the geometry into simpler configurations easily definable by one and two-dimensional surfaces [70]. However, even if ANSYS DesignModeler already provides the decomposition function, for some structure, a manual intervention is required. According to the different materials of the components, the decomposed solids are grouped into several groups and a material number

and a density can be associated to each body as required by MCNP card definition [53]. The nuclear definition of material isotopes is then performed using an ad-hoc script and subsequently added to the neutronic input by the user.

As shown in Figure 3.2, the CSG Modelling procedure has been applied to the HCPB slice and cap. On the left (Figure 3.2 a and c), the CAD models of HCPB slice and cap before the conversion are reported. On the right (Figure 3.2 b and d), the neutronic models are shown. The geometry details of the CAD models are faithfully reproduced in the neutronic models. All the details in terms of cooling and dummy channels, CP features, manifolds layout as well as material definition have been nodalised in the MCNP model keeping the consistency between the BRep and the CSG representation. In order to verify the correct definition of the cells in the neutronic model and the conservation of the volumes, a stochastic volume estimation based on the ray tracing technique has been carried out [53].

For the estimation of the volume of the neutronic model to be compared with the reference CAD geometry, a particle tracing calculation, using empty materials and a cell flux tally, has been performed [53]. The results show that the maximum volume deviation between the BRep CAD geometric model and the neutronic one is +0.81%/-0.73% for the HCPB slice [70] and +1.91%/-3.87% for the HCPB cap, respectively. The overall volume variation for the two components is 0.01% and -0.002% for the slice and cap, respectively. The detailed comparison cell by cell is reported in Appendix 9.1, Table A.1 and Table A.2. The variations are limited to few percent indicating that the CAD and the neutronic models are in good agreement and represent the same geometry.

The highest variations encountered in the cap neutronic model occur in very small volume where the particle tracing calculation is not efficient (e.g. the -3.87% is related to a volume of $5.72E-04 \text{ cm}^3$, Table A.3). However, these deviations do not affect the overall volume estimation that is well below the 1% for both models.

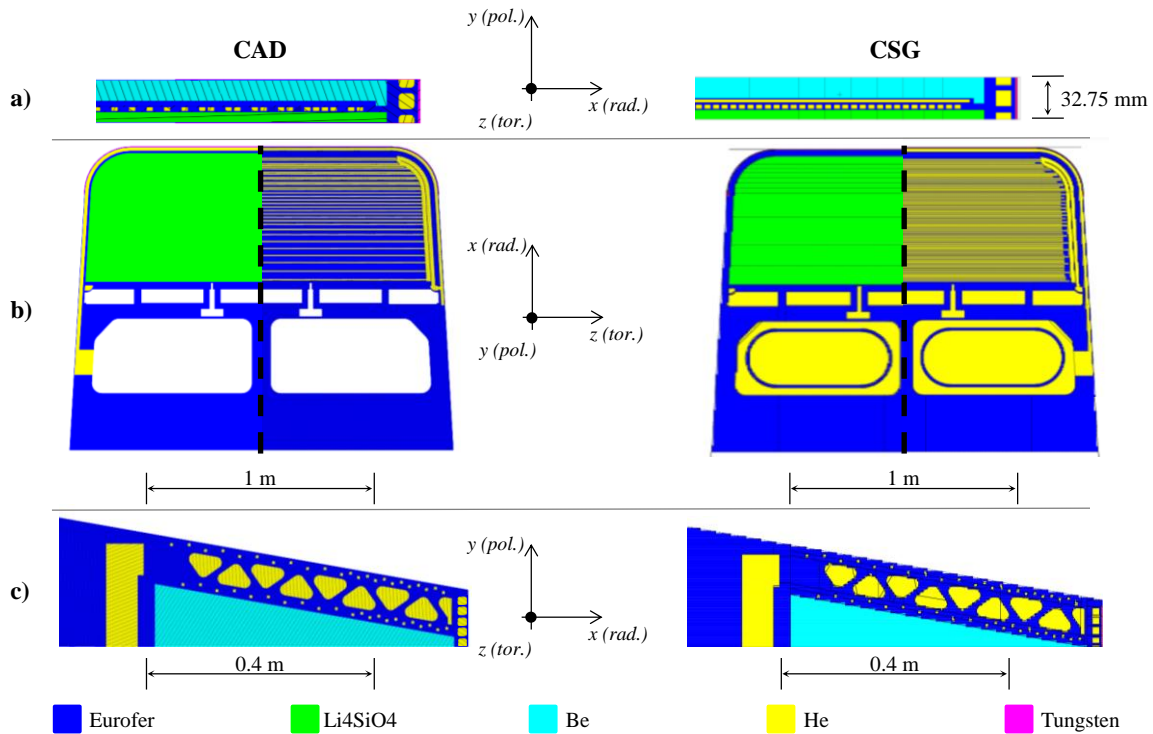


Figure 3.2. CAD and CSG neutronic models of HCPB slice and cap. Top (a): radial-poloidal cut detail of the HCPB slice CAD (left) and CSG (right) model. Centre (b): radial-toroidal cut of HCPB slice CAD (left) and CSG (right) model at lithium Orthosilicate and CP level. Bottom (c): radial-poloidal cut of HCPB cap CAD (left) and CSG (right) model. Note: in the CAD model of the CP (a and b left), the purge gas as well as the dummy channels and the helium manifold in the BSS are not highlighted in yellow because they are empty while in the neutronic they are present.

3.2.2 Hybrid Modelling

The possibility to import in MCNP6 the unstructured mesh geometry descriptions generated by a Computer-Aided Engineering (CAE) alongside its legacy CSG description [54] has been already developed. However, limited applications have been found in literature to effectively couple MCNP and the multi-physics codes such as ANSYS. The UMs, such as those created by the Finite Element code ABAQUS/CAE, can be directly imported into MCNP6 allowing a more precise representation of the geometry in the neutronic model. Different kind of elements can be used for the geometry nodalisation. Indeed, element of the first and/or second order can be selected to obtain a good agreement between the real geometry and its approximation/appearance through the mesh. The selection of the element to be used is demanded to the user that should find a compromise between the geometry representation and the limitation on the number of elements for each part due to the increasing of the run time when more than 5E04 elements are accommodated in a part [54].

The first step for using the Hybrid modelling is to create parts composed by UMs. These UMs/parts in MAIA procedure are created using ANSYS Mesh [59, 66]. Each part consists of a single homogeneous material and of a single type of element.

The generation of the UM model to be used in MCNP6 is performed using ANSYS Finite Element Modeler. It allows the translation of the UM in ABAQUS/CAE format that is subsequently accepted as input file by MCNP6 [54]. Each part defines also the pseudocells that are used as universe to fill the so called “fill-cells”. With “fill-cell” is intended the traditional MCNP card, defined using the CSG representation, that contains the universe (i.e. the “fill” parameter) [54]. In this way, the UM is embedded in the legacy CSG model that is created by means of ANSYS DesignModeler.

Therefore, the Hybrid Modelling allows the geometry nodalisation using both the CSG and the UM.

This representation is versatile and can be adapted to each layout. The user can also decide which geometric parts have to be nodalised with the CSG representation and which parts with the UM providing, in this way, an important flexibility according to the investigation needs.

On this regard, in Figure 3.3, two examples of Hybrid Modelling are reported. One model has been realised using a CSG box that is completely filled with UM (Figure 3.3 a and b). In other words, all the components like stiffening plates, FW, cooling channels, tubes, PbLi region, are modelled by means of the UM. This model reproduces the WCLL BU with 12 serpentine tubes routed in radial-toroidal direction already shown in [68]. The serpentine tubes could not be represented by means of CSG because they would require complex intersection between torus and cylinder while, using the UM, they can be nodalised without particular issues.

In the second model (Figure 3.3 c and d), the UM is, instead, used only for the water representation within the FW and the BZ while all the other parts are represented using the CSG Modelling. This model reproduces the WCLL BU already described in paragraph 1.2.2 and it will be used for the water activation analysis reported in paragraph 6.3.2.

Therefore, in Figure 3.3 left, the CAD models of the two WCLL configurations are shown while the corresponding Hybrid neutronic model are reported in Figure 3.3 right, respectively. As it is possible to observe, the CAD and neutronic models reproduce the same geometric detail avoiding any simplification as well as homogenisation of the materials.

For the WCLL with serpentine tubes, 18 parts or pseudo-cells have been created with an overall amount of $\sim 9.28E+05$ elements [68] while 36 parts and $\sim 1.18E+06$ for the WCLL BU with radial-toroidal tubes.

As done for the CSG Modelling of HCPB slice, the geometry verification has been pursued also for the Hybrid modelling on the two WCLL configurations.

Regarding the WCLL BU with serpentine tubes, the maximum volume variation for each cell and pseudo cell is comprised between +0.0021%/-0.0068% with an overall volume deviation of -0.0005% [68].

Concerning the WCLL BU with radial-toroidal tubes, the volume range variation is comprised between +0.15%/-0.43% with an overall volume deviation of -0.27%. The detailed comparison cell by cell is reported in Appendix 9.1, Table A.3 and Table A.4.

As for the CSG Modelling, the variation in the volume estimation of the Hybrid representation with respect to the BRep reference models are limited to less than 1% both for a complete UM and UM+CSG neutronic models. Furthermore, tuning the number and type of elements and area of application, the Hybrid Modelling allows a higher flexibility in terms of layout nodalisation as well as degree of detail representation. Moreover, it is also possible to change parts of the geometry without to affect the definition of the other parts. This feature is particularly suitable for scoping and design optimisation analyses.

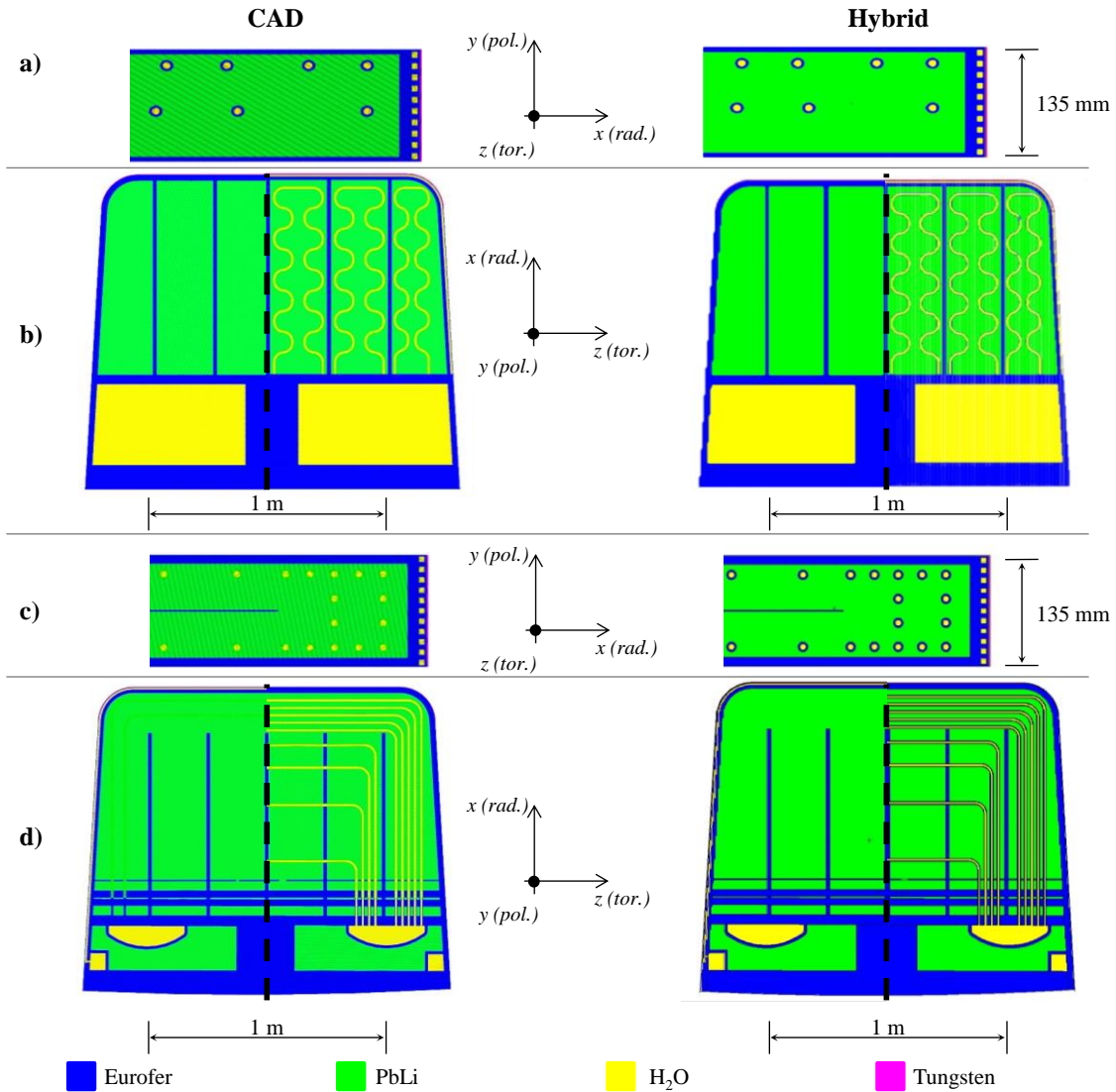


Figure 3.3. CAD and Hybrid neutronic models of WCLL BU with different BZ tube layout: serpentine (a and b) and radial-toroidal (c and d) configurations. Top (a): radial-poloidal cut detail of the WCLL BU CAD and Hybrid models with serpentine tubes. Centre (b): radial-toroidal cut of WCLL BU CAD and Hybrid models with serpentine tubes at PbLi and at BZ tubes level. Centre (c): radial-poloidal cut detail of the WCLL BU CAD and Hybrid models with radial-toroidal tubes. Bottom (d): radial-toroidal cut of WCLL BU CAD and Hybrid models with radial-toroidal tubes at PbLi and at BZ tube level.

3.3 Neutronic Analysis in MAIA Procedure

After the preparation of the neutronic model using the CSG and Hybrid Modelling, the next step of the MAIA procedure is to perform a neutronic/photonic calculation (step (c) of Figure 3.1).

For the neutron/photon radiation transport analysis, it is suggested in [71] to use the Fusion-Evaluated

Data Library (FENDL) [72]. This library has been used for all the neutron/photon transport analysis reported in this dissertation.

Considering that the detailed neutronic models represent only a portion of DEMO reactor, particular attention has been given to the definition of a local neutron and photon source as well as to the implementation of boundary conditions in order to correctly investigate the interactions between the sub-models under study and the universe around them. Indeed, the neutrons and photons can enter in the sub-model directly from the plasma or due to the interactions with other modules into the reactor and, then, by means of subsequently scattering, interact again with the sub-model. This second effect is also known as albedo effect [73, 74].

Therefore, it is possible to identify two ways of interaction of neutron and photons with the sub-model.

One is due to the direct or scattered neutrons/photons that enter the sub-model from the FW (this contribution is accounted by means of the neutron and photon local source definition, paragraph 3.3.1). This contribution has been assessed taken inspiration from the ‘‘tally source’’ method reported in [75].

The second one is due to the neutrons and photons that after interaction enter the sub-model from its boundaries (this contribution is taken into account by means of boundary conditions, paragraph 3.3.2).

3.3.1 Neutron and Photon Local Source Definition

In order to estimate the neutrons and photons that enter the sub-model from the FW and to sample both of them for the local source definition, the surface neutron and photon currents (i.e. F1:N and F1:P tallies, see paragraph 2.1.2) are calculated in the DEMO global neutronic model [76, 77].

Using a dedicated global neutron source model to simulate the actual neutron volumetric source of DEMO reactor, a surface (A_{TALLY}) is identified for biasing neutrons and photons in cosine and energy (in Figure 3.4 is reported a possible location of the surface A_{TALLY} for the equatorial region of the OB segment). The cosine (μ) distribution is ranged in 10 subdivisions from 0 to $|1|$.

According to the Vitamin J+ energy data structures [78] and for the relevance energy range of a fusion reactor, the neutron energy bins are sampled from 0.111 MeV to 14.2 MeV subdivided in 98 energy bins, whilst the photon energy bins are sampled from 0.001 MeV to 50 MeV subdivided in 43 energy bins.

The calculated data sets for local models, thus, includes 990 tally values each for neutronic surface flux and 430 tally values each for photonic surface flux.

In general, the probability p_{ij} that a particle starts from surface A_{TALLY} with a cosine comprised between $[\mu_i, \mu_{i+1}]$ and between the energy bin $[E_j, E_{j+1}]$, $i=1, \dots, I, j=1, \dots, J$ is given by:

$$p_{ij} = \frac{\int_{A_{TALLY}} dA \int_{E_j}^{E_{j+1}} dE \int_{\mu_i}^{\mu_{i+1}} \varphi(\mathbf{R}_s, E, \mu) \mu d\mu}{\int_{A_{TALLY}} dA \int_E dE \int_0^1 \varphi(\mathbf{R}_s, E, \mu) \mu d\mu}, \quad (3.1)$$

where \mathbf{n} is the unit vector of source surface A_{TALLY} , μ is the cosine and is equal to $\mathbf{\Omega} \cdot \mathbf{n}$ and $\varphi(\mathbf{R}_s, E, \mu)$ is the particle flux.

The probability p_{ij} is calculated starting from results of a dedicated neutron and photon transport analysis. The results of this analysis are herein indicated with $S_{i,j}$, with i representing the cosine bin and ranging from 1 to 10 and j representing the energy bin and ranging from 1 to 99 for neutronic surface flux and from 1 to 43 for photonic surface flux.

In order to estimate the probability and, so, to calculate the $S_{i,j}$, the same procedure is used both for the neutronic and photonic source definition taking care to change the number of considered energy bins that

are herewith indicated with EB . The tally score per cosine bin R_i can be calculated as:

$$R_i = \sum_{j=1}^{EB} S_{i,j} \quad \text{with } i=1, \dots, 10. \quad (3.2)$$

Furthermore, the net surface flux entering the surface from the plasma is

$$F1_{NET} = \sum_{i=1}^{10} R_i. \quad (3.3)$$

Therefore, the cosine emission probability C_i and the energy emission probability $E_{i,j}$ for each cosine bin can be calculated as follows:

$$C_i = \frac{R_i}{F1_{NET}} \quad \text{with } i=1, \dots, 10, \quad (3.4)$$

$$E_{i,j} = \frac{S_{i,j}}{R_i} \quad \text{with } i=1, \dots, 10 \quad j=1, \dots, EB.$$

The obtained C_i and $E_{i,j}$ values are used to define the local neutron and photon source for the nuclear investigation of the neutronic sub models. In this way, the definition of the local source takes into account not only the direct neutrons coming from the plasma but, also, the neutrons and photons subjected to the albedo effect and entering the sub-model from the FW.

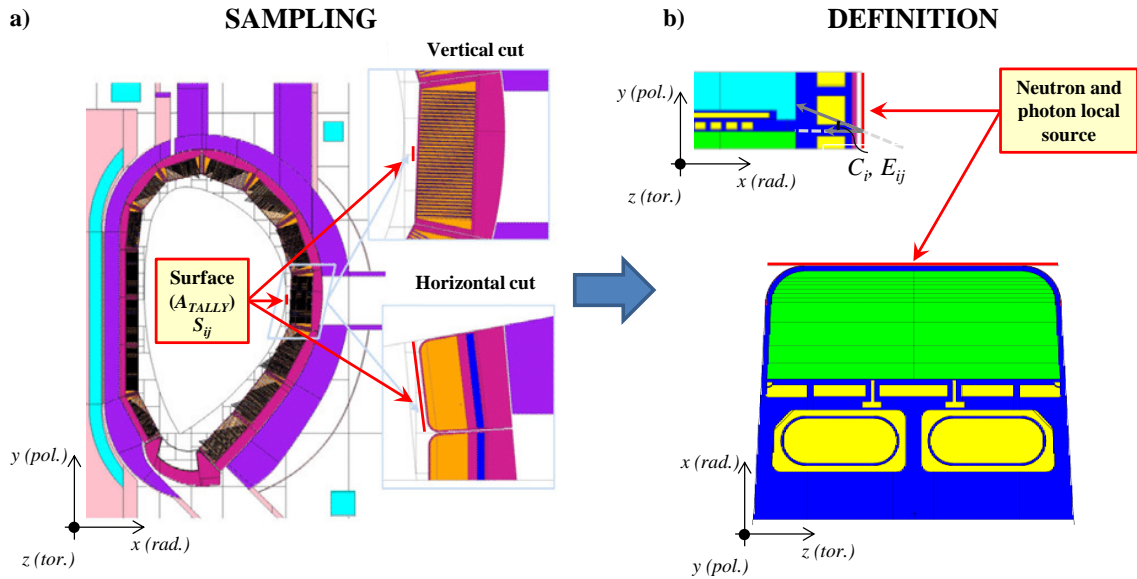


Figure 3.4. Local source sampling in the global neutronic model of DEMO 2015 [79] with HCPB BB and local source definition in the neutronic sub-model. Left (a): example of A_{TALLY} surface in the overall reactor. Left-top (a): vertical cut with radial-poloidal view of the OB4 module in which is highlighted in red the A_{TALLY} surface. Left-bottom (a): horizontal cut with radial-toroidal view of the OB4 module in which is highlighted in red the A_{TALLY} surface. Right-top (b): radial/poloidal view of the local source definition. Right-bottom (b): radial/toroidal view of local source definition. Figure (a) reproduced according to [79]. Figure (b) reproduced according to [70].

3.3.2 Boundary Conditions for Local Neutronic Models

As introduced before, the neutrons and photon entering in the sub-model are not only coming from the surfaces exposed to the plasma but, also, from the interactions with the adjacent materials.

Two different contributions could be identified:

- (i) the neutrons and photons produced/scattered in the neighbouring zones and entering the investigated domain from the poloidal and toroidal direction;

- (ii) the neutrons and photons that interacting with the VV are back-scattered within the sub-model.

The first contribution can be taken into account by a set of reflecting (e.g. mirror or albedo) boundary conditions under the assumptions that: the neutrons generated within the plasma are slowed down without deeply penetrate in the BB (i.e high scattering medium) and the neighbouring zones have a similar behaviour to the area under study.

The second contribution, although not significant, can be taken into account nodalising simply the VV in the neutronic model.

With reference to Figure 3.5 (a), the locations of the reflecting boundary condition in the poloidal and toroidal direction as well as the VV neutronic model are reported.

As explained in paragraph 2.1.2, the reflecting conditions can act as a mirror (Figure 3.5-b) or as a boundary with an infinite scatter (white condition, Figure 3.5-c). These two conditions can be applied in the toroidal and poloidal directions. The selection as well as the consistency verification of these conditions is reported in paragraph 4.1.1.

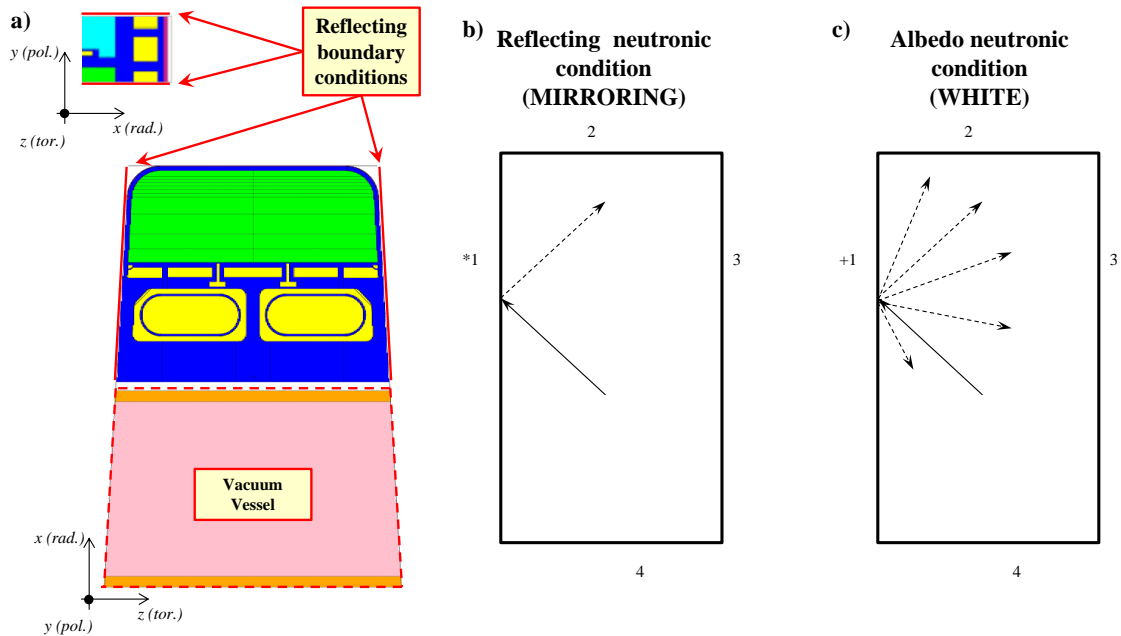


Figure 3.5. Boundary condition for the local neutronic model. Left (a): location of reflecting (e.g. mirroring or white) boundary conditions as well as of VV for back scattering. Centre (b): mirroring neutronic boundary condition. Right (c): MCNP white condition for taking into account the albedo effect. Note: the number in the figures b) and c) as well as the +/* signs refer to MCNP CSG language reported in [53]. Figure (a) is reproduced according to [70]. Figures (b) and (c) reproduced according to [53].

3.4 CFD Analysis in MAIA Procedure

From the neutron/photon radiation transport analysis, by means of tallies F6, modified FMESH or EMBEE (see paragraph 2.1.2), the power deposition in the corresponding sub-models is calculated.

Using ad-hoc scripts, the energy deposition per unit source emitted particle is converted to the deposited power required by thermal-hydraulic calculation (Figure 3.1 step (e) of the MAIA procedure).

For rescaling the local data according to the overall source, first of all, the DEMO neutron yield Y_{DEMO} is calculated as follows:

$$Y_{DEMO} = \frac{P_{fus}}{C_0 E_{fus}}, \quad (3.5)$$

where P_{fus} is the fusion power (e.g. 2037 MW), E_{fus} is the energy associated to the neutrons emitted for each fusion reaction that is equal to 17.6 MeV and, C_0 is an energy unit conversion constant equal to $1.602 \cdot 10^{-13}$

J/MeV. The neutron yield for DEMO2015 is 7.2238E+20 neutron/s.

Knowing the DEMO neutron yield, it is possible to estimate the local yield for neutron and photon sources defined for the sub-models.

Remembering that the F1 tally is the surface particle flux normalised per starting source particle (i.e. F1 measure the number of particles crossing the tallied area in DEMO per starting neutron), it is possible to multiply the DEMO neutron yield for the number of particles coming from the plasma side and used to define the local neutron and photon source.

It can occur that the tallied surface and the local source area are slightly different, in this case a scaling factor equal to the ratio between the source area and the tallied area has to be used. In conclusion, the local neutron or photon yield can be calculated as follows:

$$Y_{LOCAL} = Y_{DEMO} \frac{A_{SOURCE}}{A_{TALLY}} F1_{NET} , \quad (3.6)$$

where the A_{SOURCE} and A_{TALLY} are the local source and tally surfaces, respectively, while the $F1_{NET}$ represents the neutron or photon net surface flux.

Indicating with H_i ' the total energy deposition for each cell per unit source emitted particle calculated by means of F6, modified FMESH or EMBEE cards, the power deposited for each cell is calculated as follows:

$$Q_{dep} = C_0 Y_{LOCAL} H_i ' . \quad (3.7)$$

The Q_{dep} can be decomposed into two different contributes Q_{np} and $Q_{p,albedo}$ according to the neutron and photon sample source. Indeed, Q_{np} represents the power deposited per cell by neutrons generated in the plasma, neutrons scattered from other modules and neutron and photons produced in the sub-model due to the neutronic interaction with the materials. Furthermore, $Q_{p,albedo}$ represents the power deposited by photons produced due to neutronic interactions and scattered into the sub-model.

These two contributions are calculated separately in dedicated neutronic and photonic transport analysis and then, using the superposition, they are summed for obtaining the total deposited power.

3.4.1 Mapping of Heat Generation

Once the neutron and photon transport analyses are performed, the calculated distributions of power densities are mapped into ANSYS CFX (Figure 3.1 step (d) of the MAIA procedure).

From MCNP, with ad-hoc scripts, a file is produced containing the data in the profile data format (X, Y, and Z coordinates and the power density associated with them) [59]. It can then be imported in Profile Boundary Conditions [59] using a three dimensional interpolation function.

This function is created by interpolating values from a “cloud of points” using a distance weighted average based on the closest three points.

The system of coordinates and values is interpreted by CFX-Pre in the local coordinate frame and they are interpolated using a trilinear interpolation method.

In other words, a multivariate interpolation is used on a 3D grid by means of polynomials of first order. This provides an accuracy of the second order and requires 8 adjacent values surrounding the interpolation point. However, in case 8 neighbouring values are not available, the accuracy collapses to a bilinear one which is only 1st order and problematic at positions with large gradients. This issue is solved increasing the mesh nearby step gradient positions.

As examples, the mapping of the power densities for HCPB slice and WCLL BU are reported in Figure 3.6 and Figure 3.7, respectively.

The 3D power density profiles, reproduced within ANSYS CFX-Pre, are in good agreement with the outcomes of neutron and photon transport analysis. Furthermore, the interpolated integral data match with the original neutronic one ensuring power/energy conservation.

Indeed, considering that the neutronic and the CFD models are identical from a geometric point of view,

the only error associated to the heating interpolation is due to the different meshes. The necessity to use different meshes derives from the specific calculation requirements. For instance, a very fine mesh cannot be used for neutronic analysis because it would require a huge computational effort for obtaining a good statistics in each mesh element. On the other side, for instance for thermal-hydraulic calculations, some requirements in terms of inflation layer or mesh conformity are unavoidable.

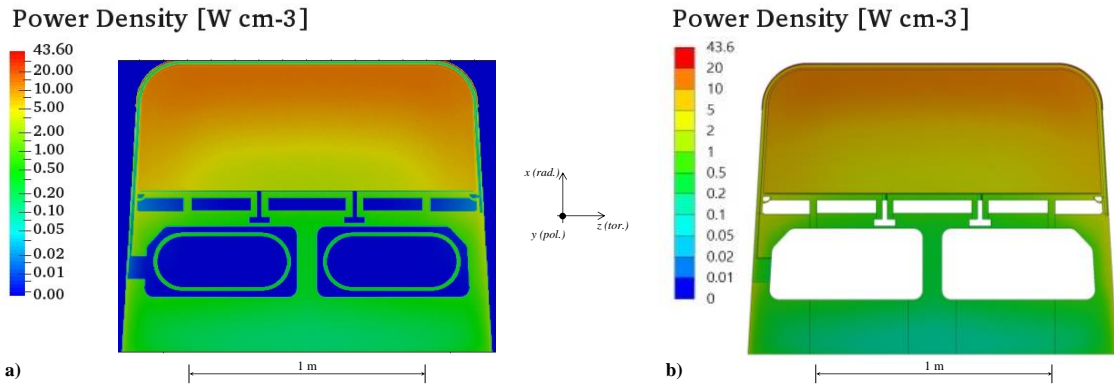


Figure 3.6. Mapping of 3D power density profile in ANSYS CFX. Left (a): outcome of HCPB slice neutronic and photonic calculations in terms of power density. Right (b): neutronic plus photonic power density mapped into ANSYS CFX.

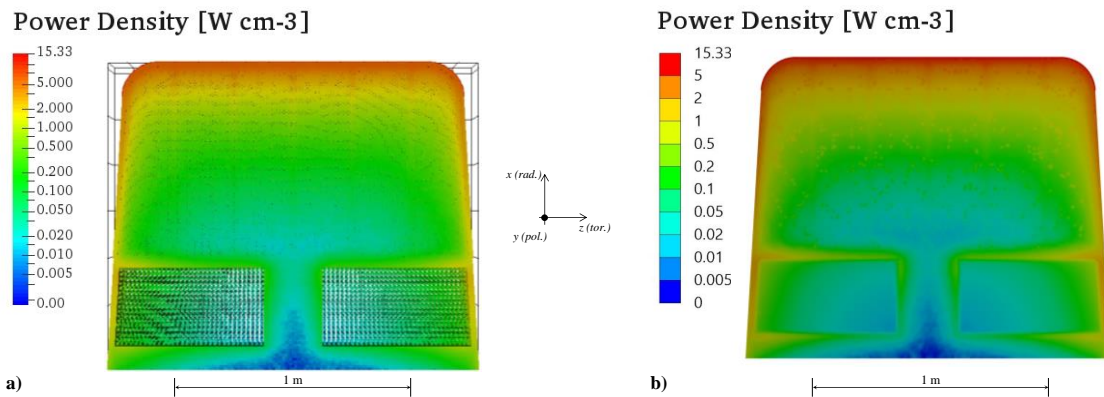


Figure 3.7. Mapping of 3D power density profile in ANSYS CFX. Left (a): outcome of WCLL BU neutronic calculation in terms of power density. Right (b): neutronic + photonic power density mapped into ANSYS CFX.

3.4.2 Thermal-hydraulic Boundary Conditions for Local Models

The thermal-hydraulic calculation is performed implementing the material properties by means of CFX Expression Language (CEL) functions [59] and a set of boundary conditions like the heat flux and the deposited power, the temperature and mass flow rate of the working fluid, and specific conditions (e.g. symmetry and adiabatic surfaces) for simulating the interaction with the universe around the sub-model. As explained, the power density is calculated and mapped in CFX in order to have a 3D distribution.

Regarding the heat flux coming from the plasma, the FW surface is subjected to a power deposition due to particles and radiations arising from plasma. This is modelled with a non-uniform heat flux imposed on the external surface. Each element of the FW surface has a normal heat flux calculated by multiplying the nominal heat flux value of 0.5 MW/m^2 [26, 30] for the cosine of the angle between the radial and the surface normal directions. In this way, the reduction of heat flux on the FW bends is taken into account.

From the power balance and according to the pressure and inlet temperature requirements (see paragraphs 1.2.1 and 1.2.2), the mass flow rate, the operating pressure and the temperature are applied to the inlet of the sub-models. Symmetry boundary conditions are imposed on the radial-toroidal surfaces in order to take into account the rest of the blanket that is not simulated with the sub-model [26, 30]. The

consistency verification of these symmetry conditions is reported in paragraph 4.2. Moreover, adiabatic conditions are set to the lateral surfaces of the FW and BSS (where, as conservative assumption, the radiation Towards the VV is neglected) of the sub-models with the exception of the FW plasma side.

For the thermal contact conductance (TCC) between the EUROFER97 steel structures and both Li_4SiO_4 and Be, the expression derived from the Yagi and Kunii model [80] applying the constants of Reimann et al. [81] are used.

3.5 Thermo-Mechanical Analysis in MAIA Procedure

From the CFD calculation (Figure 3.1 step (e) of the MAIA procedure), the temperature field $T(x,y,z)$ is calculated and, then, used to assess the stress, strain and displacement spatial fields (Figure 3.1 step (g) of the MAIA procedure). At this point, the application of the MAIA procedure is straightforward. If all the thermal-hydraulic limits (pressure drop, maximum structural temperature, etc.) are within the limits, it is possible to proceed with the mapping of the temperature field and, then, with the structural analysis to verify the compliance with C&S like SDC-IC [37] and RCC-MRx [82]. For this analysis, boundary conditions are used for simulating the mechanical actions of the rest of the BB.

3.5.1 Mapping of Temperature Field

The mapping of the temperature field obtained with CFD calculation is performed directly within ANSYS Workbench using the profile preserving option. Using this option, the profile of the variable (for example, temperature) on the CFD mesh is mapped into the structural mesh. When a profile preserving mapping is used, each target/receiver node is mapped onto an element on the source/sender side. Weights for each source node are calculated and assigned based on the location of the target node and the shape function of the element [66]. The interpolation algorithm is based on the Distance Based Average that, after finding the closest points contributing to the map of each target point, triangulates the data creating temporary elements (4-node tetrahedrons for 3D meshes) and iterates over all possible combinations of the source points [66]. An example of temperature data transfer is reported in Figure 3.8.

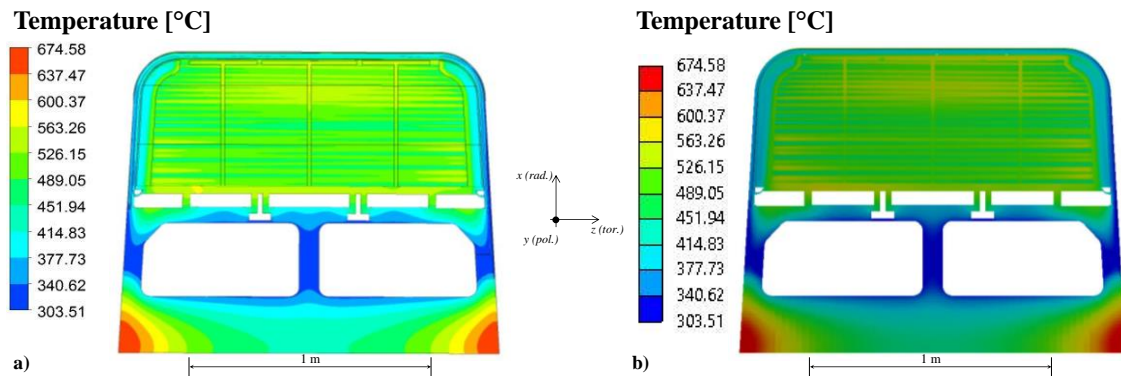


Figure 3.8. Mapping of 3D temperature field profile in ANSYS Mechanical. Left (a): outcome of HCPB slice CFD calculation in terms of structure temperature. Right (b): temperature field mapped in ANSYS Mechanical for thermo-mechanical calculation.

3.5.2 Boundary Conditions for Local Models

Regarding the mechanical restraints, a symmetry condition is applied at the lower cut surface of the model allowing here only displacements on the radial-toroidal plane (Figure 3.9-a). As for the upper cut surface boundary condition, there are 2 possible options [28]:

- a. Plane Strain (PS). Poloidal coordinate coupling of the nodes, i.e. nodes at this boundary can move to allow the thermal expansion of the slice, but in parallel to the cut surface (see schematic drawing in the top detail 1 in Figure 3.9-a);
- b. Generalised Plane Strain (GPS). Plane constraining of the nodes, i.e. nodes at this boundary can

move to allow the thermal expansion of the slice model, but only contained in a plane (see schematic drawing in the top detail 2 in Figure 3.9-a).

The implementation in ANSYS Mechanical [66] of PS and GPS conditions is reported in Appendix 9.2.

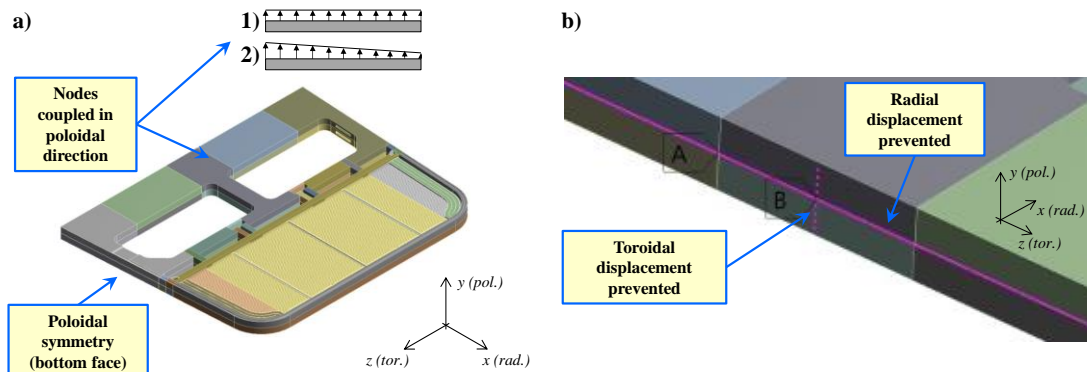


Figure 3.9. Mechanical restraints for thermo-mechanical analysis on a submodel. Left (a): poloidal boundary conditions applied to the sub-model. Right: node restraints applied to the sub-model for realistically simulate the mechanical action of the attachment system.

In order to realistically simulate the mechanical action of the attachment system on the module BSS and devoted to connect the module to the vacuum vessel, the following set of boundary conditions is assumed. Displacement along the radial direction is prevented to the nodes lying on the toroidal direction shown in Figure 3.9-b, as well as toroidal displacements are prevented to nodes lying along poloidal direction [83, 84]. The consistency verification of this set of boundary conditions is reported in paragraph 4.3.

4 Validation of MAIA Procedure Applied to the Breeding Blanket and Sensitivity Analysis

In this Chapter, the consistency verification of the three main pillars of the coupling is reported. The consistency of boundary conditions and the loads used for the neutronic, thermal-hydraulic and thermo-mechanical analyses is verified against the reference model identifying the strength and the weakness points of their application.

For the sake of brevity and clearness, all the consistency studies, herewith reported, are performed on the HCPB slice but the outcomes are valid also for the WCLL BU. Furthermore, regarding the neutronic model, the consistency check has been performed using the CSG representation that results more suitable for the integration in the reference DEMO neutronic model currently used for the design of the BB. Moreover, the outcomes are still valid for the Hybrid representation and do not affect the goodness of the approach.

4.1 Consistency Check of Local Source and Boundary Conditions for Neutronic Analysis

For the consistency check of the local model and, in particular, of the local source and boundary conditions used in MAIA procedure for neutron/photon transport analysis, three neutronic models have been created: (i) the HCPB slice, (ii) the HCPB module and (iii) the HCPB DEMO models [85]. In particular, the first two local neutronic models have been used to demonstrate the consistency of the MAIA results versus the latter that has been selected as reference.

The HCPB slice together with the cap model (already introduced and described in paragraph 3.2.1) have been used to create the CSG full heterogeneous model of the OB4 HCPB module (Figure 1.4 – a) using the repeated structures capabilities of MCNP5 [53]. It has been decided to focus on OB4 because, having the highest Neutron Wall Load (NWL) [86-88], it is usually taken as reference by the designers.

The HCPB module has been then implemented in a full DEMO HCPB neutronic model realised at KIT [79] and it has been used as reference for results comparison.

The DEMO HCPB neutronic model represents a 10° torus sector model that includes the plasma chamber, one full inboard and one and half outboard blanket modules, divertor, VV and ports, thermal shield, toroidal and poloidal magnetic field coils.

The VV structural elements are in stainless steel SS316 and the interior is filled with a mixture of homogenised material composed of 60% SS316 and 40% water.

This model, used as reference for the design analysis of HCPB, is filled with slice units of two beds of Be and Li_4SiO_4 enclosing a CP [79].

For taking into account the cooling channels within the FW, CP and Caps as well as the helium manifolds in the BSS, an effective Eurofer density has been set (i.e. 4.49 g/cm^3 for the CP and 1.89 g/cm^3 for the Caps [79]). The original HCPB Demo model is shown in Figure 4.1.

With the aim to verify the consistency the MAIA procedure, the HCPB module and DEMO HCPB models have been joined together. The HCPB DEMO model, equipped with the full heterogeneous OB4 module and with the plasma neutron source representative of plasma emission conditions in DEMO, has been employed for the definition of the local neutronic and photonic sources to be used for the local HCPB module and slice models according to the approach described in paragraph 3.3.1.

In Figure 4.2, the three models are reported and they will be recalled in the following for the consistency verification of the neutron and photon transport analysis of MAIA procedure.

In Figure 4.2 b) and c), the computing domains corresponding to the equatorial slice of the OB4 module are highlighted. On these domains, the preliminary studies are focused and, in the following, the results on module and DEMO will refer unless differently specified.

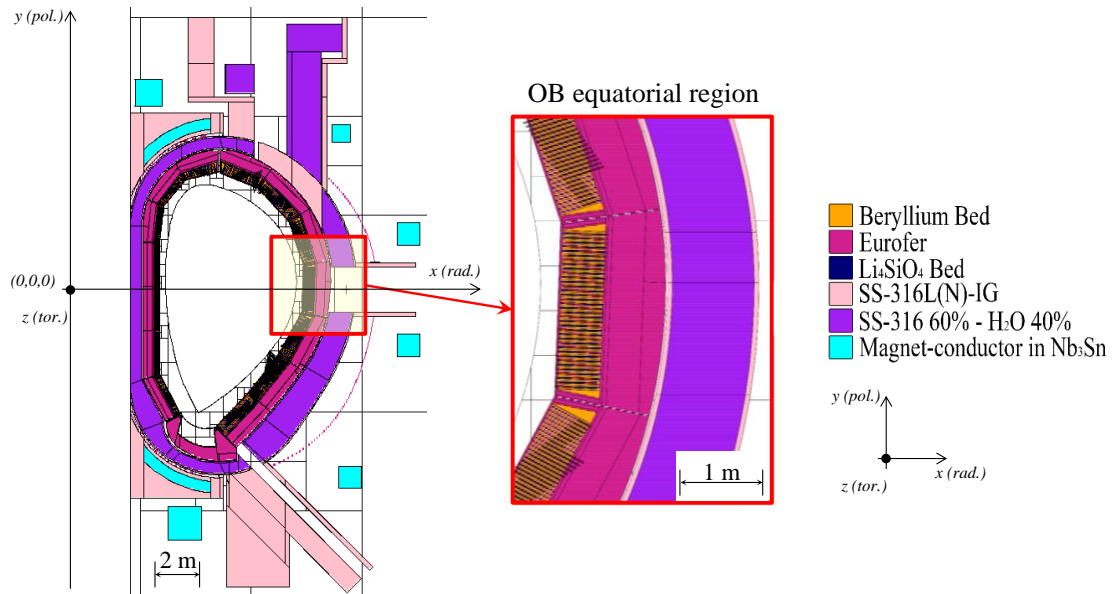


Figure 4.1. Reference DEMO HCPB neutronic model used for the design analysis. This figure is reproduced according to [86].

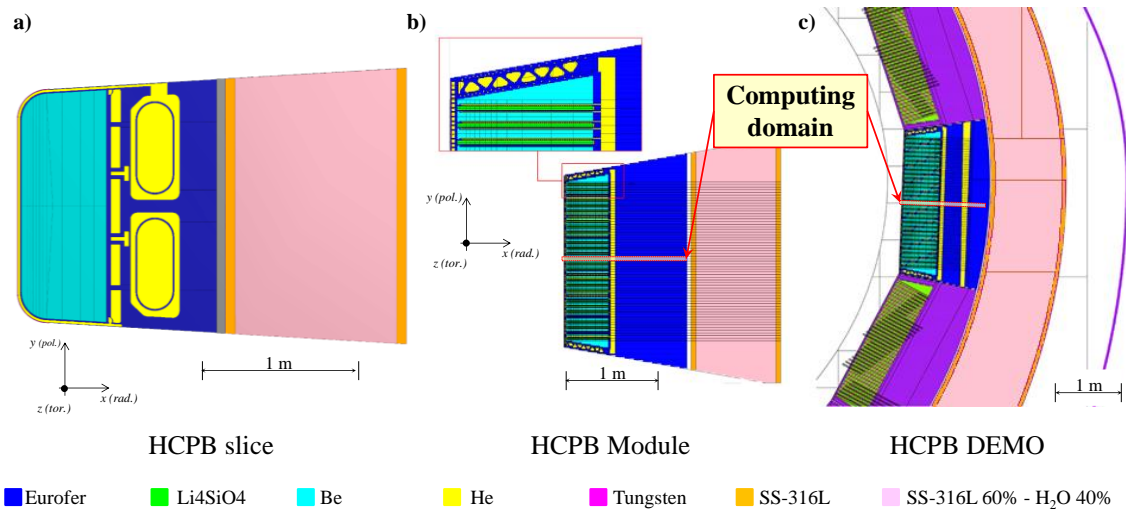


Figure 4.2. Neutronic models used for the consistency verification of the boundary conditions. Left (a): local neutronic models of HCPB slice with VV. Centre (b): local neutronic model of HCPB module representing the full heterogeneous OB4. Right (c): reference neutronic model of HCPB DEMO equipped with full heterogeneous OB4. Figure b) and c) are reproduced according to [85].

4.1.1 Boundary Conditions Consistency Verification

Once the two local models, on which the MAIA procedure has been applied, and the reference DEMO HCPB model have been set up, analyses have been performed in order to identify the correct set of boundary conditions and to validate the results in terms of deposited power on the sub-models.

The MAIA procedure step c) (Figure 3.1) has been followed for the sampling of local neutron and photon source to be used with HCPB slice and module sub-models. The neutron and photon source intensity parameters are reported in Table 4.1.

Several combinations of reflecting and white conditions applied to the toroidal and poloidal boundary surfaces have been studied according to the case study matrix reported in Appendix 9.3, Table A.5.

Eight analyses (4, number of combinations of boundary conditions, multiplied by 2, number of particles type, n and p) both for the HCPB slice and module local models (numbered from 3A-3A to 3D-4D) have been carried out with a relevant number of particle histories (i.e. all tally results relative errors have been

maintained below 5%). Using the above-mentioned models, boundary conditions and local neutron source, the total neutron fluxes for the two local models and for the DEMO reference model have been evaluated and compared as reported in Figure 4.3 and Figure 4.4. In particular, in Figure 4.3 for the case 3A-4A (mirroring conditions in both poloidal and toroidal directions), it is possible to see that the neutron fluxes calculated in the local models are in good agreement in the first centimetres but, then, the deviation with respect to the reference DEMO model diverge up to ~17% for the module and ~42% for the slice. In general, the module local model approximates better the behaviour of the reference DEMO model. However, the deviations obtained in the BSS result to be too high and clearly indicate that the set of boundary conditions do not represent adequately the physics of the problem. Practically, the mirror conditions in the toroidal direction increase the neutron fluxes in the BSS.

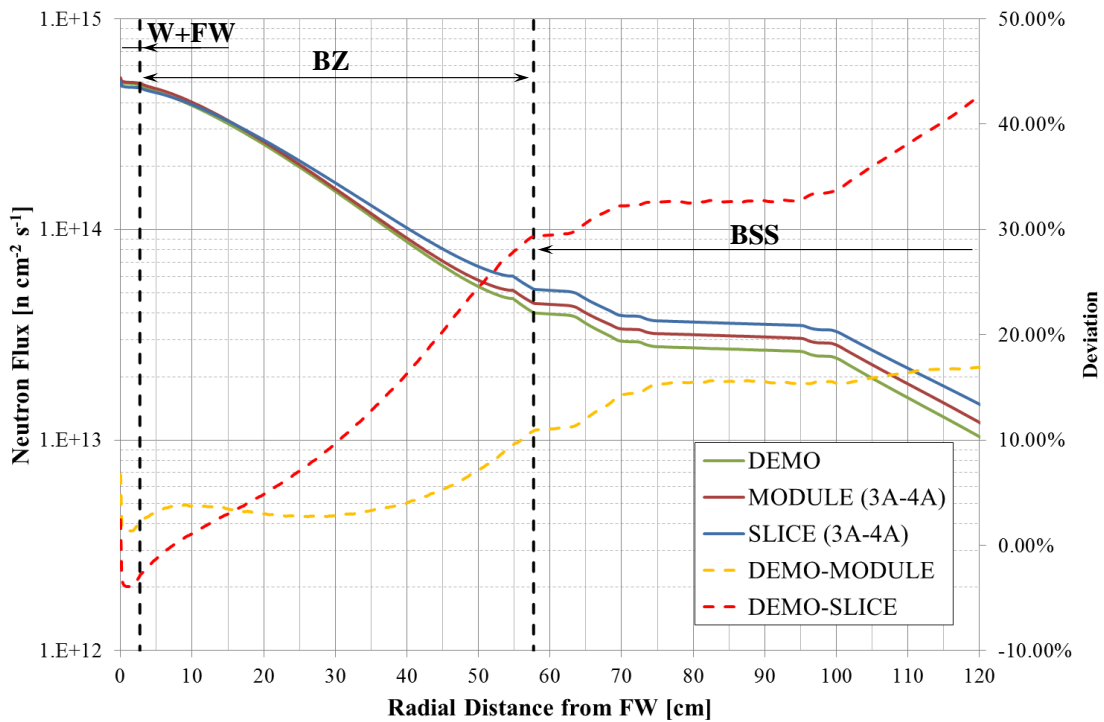


Figure 4.3. Radial neutron flux profile and deviations for the reference DEMO model and for the two (module and slice) local models for the case 3A-4A.

For the case 3D-4D (mirroring and white conditions in poloidal and toroidal directions, respectively), instead, it is possible to note that the two local models approximate better the total neutron flux calculated in the reference DEMO one. Indeed, the maximum deviations are ~4% for the module and ~20% for the slice (Figure 4.4). In particular, the neutron fluxes calculated in the DEMO and module models are practically overlapping, while for the slice one a larger deviation is found. This effect can be explained considering the poorer statistics (although with a relative error below of 5%) that is obtained in the bigger models (e.g. DEMO and module) at the deeper radial direction. However, with respect to the case 3A-4A, the deviations in the local models have been reduced by a factor of two for the case 3D-4D providing, already, an important indication on the set of boundary conditions to be applied in the local models. Therefore, in order to better evaluate the impact of the boundary conditions on the local models and their consistency with respect to the reference model, it has been decided to investigate the deviations occurring in the deposited power. For this reason, using the above-mentioned models, boundary conditions and local neutron source, the power released Q_{dep} has been estimated (see eq. (3.7)) and the results, in terms of error with respect to the HCPB DEMO reference model (Q_{dep} equal to $7.5526E+04$ W), are summarised in Table 4.2. The detailed data of the power released in each cell are reported in Appendix 9.3, from Table A.6 to Table A.9.

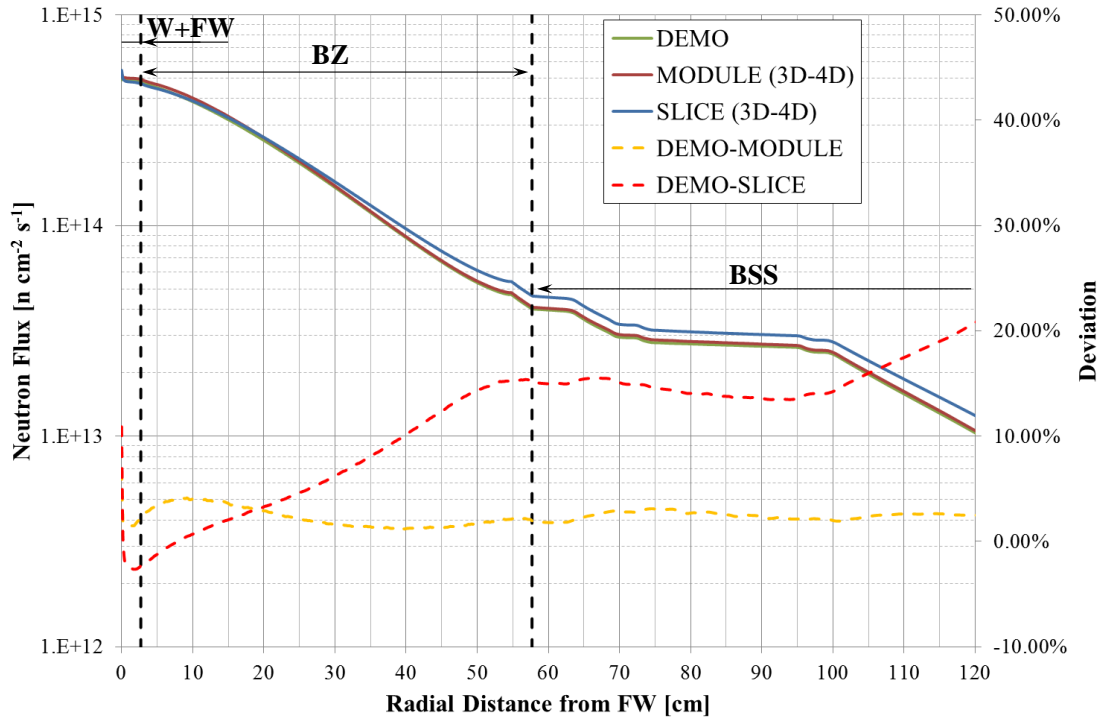


Figure 4.4. Radial neutron flux profile and deviations for the reference DEMO model and for the two (module and slice) local models for the case 3D-4D.

Table 4.1. Neutron and photon source parameters for the normalization of the HCPB equatorial outboard slice and module.

| | HCPB OB4 slice | | HCPB OB4 module | |
|--|----------------|---------------|-----------------|---------------|
| | Neutron source | Photon source | Neutron source | Photon source |
| P [W] | | | 2.03700E+09 | |
| E_f [J] | | | 2.81827E-12 | |
| Y_{DEMO} [part/s] | | | 7.22784E+20 | |
| F1 | 2.96784E-04 | 4.97275E-05 | 6.41637E-03 | 1.08446E-03 |
| A_{SOURCE} [cm²] | 1.39268E+03 | | 3.03025E+04 | |
| A_{TALLY} [cm²] | 4.64292E+02 | | 3.03215E+04 | |
| Y_{LOCAL} [part/s] | 1.1451E+04 | 1.91873E+03 | 7.42157E+05 | 1.25435E+05 |

From the acquired data emerges a congruence between the local models and the HCPB DEMO reference model when reflecting conditions are applied both on the poloidal and toroidal direction (case 3A-4A) or when reflecting condition are applied in the poloidal direction and white condition in the toroidal one (case 3D-4D). In particular, concerning the case 3A-4A, it is possible to note that both the local models predict a deposited power slightly overestimated with respect to the one calculated in HCPB DEMO. This could represent an advantage, from an engineering point of view, since the load conditions calculated with local models are more severe. Practically, with the sub-models, highest safety factors are assumed which advantage the safety of innovative design like BB where the uncertainties on loads could be very high.

It is important to note that a better power deposition estimation has been obtained in the module for the case 3A-4A. This effect can be explained considering the nature of the slice model which reproduces a reduced poloidal extension with respect to the HCPB module model.

Looking to the case 3D-4D, it is possible to note the beneficial effect of the white condition on the toroidal boundaries if compared with the results of case 3A-4A (i.e. the deviation is reduced from -3.4 % to

the -0.48%, for instance). Therefore, the white conditions in the toroidal direction provide a better approximation of the deposited power with respect to the mirroring one. This result can be explained taking into account the influence of the adjacent components that are not completely symmetric with respect to the single segment. Just thinking to the presence of the equatorial ports (same region of investigation) as well as to the poloidal variation of the BB toroidal thickness, it is possible to explain the better response of white conditions that, as explained in paragraphs 2.1.2 and 3.3.2, approximate an infinite scatterer surface with a cosine distribution. Different conclusions can be derived, instead, from case 3B-4B and 3C-4C where white conditions are applied in the poloidal direction. Indeed, it is possible to note two outcomes: (i) the slice model underestimates considerably the power deposited, (ii) there is a big discrepancy between the two local models (slice and module). Naturally, these two effects are linked together but it is possible to provide a separated explanation.

For the first effect, the underestimation is due to the random cosine distribution applied when the white conditions are used. Indeed, a big fraction of the neutrons and photons are sent back in the direction of the local source and, then, they are lost. This produces an underestimation of about 35% of power deposited in Beryllium, Orthosilicate and CP arriving to over the 90% in the BSS and an over estimation in the FW of about 6% because it is subjected to an additional flux from these back scattered neutrons (Table A.7 and Table A.8 in Appendix 9.3).

The second effect is, instead, due to the presence of the other slices in the HCPB module model that mitigate up to cancel the effect of the white boundary conditions on the equatorial slice. This allows to derive other two conclusions:

- (i) the effect of boundary conditions is reduced increasing the size of the model under investigation;
- (ii) symmetry conditions are envisaged in the poloidal direction.

Table 4.2. Variation of power deposited for each case study with respect to the HCPB DEMO reference model.

| Cases | Boundary Condition | Comparison | Comparison |
|-------|--|-----------------------|-----------------------|
| | | DEMO vs Slice | DEMO vs Module |
| | | ϵ_{Qdep} [%] | ϵ_{Qdep} [%] |
| 3A-4A | Reflect. (pol.-tor. dir.) | -3.40% | -1.61% |
| 3B-4B | White (pol.-tor. dir.) | 31.84% | 0.23% |
| 3C-4C | Reflect. (tor. dir.) – White (pol. dir.) | 31.33% | -1.60% |
| 3D-4D | Reflect. (pol. dir.) – White (tor. dir.) | -0.48% | 0.23% |

From this study on the deposited power, the case 3D-4D with reflecting and white conditions in poloidal and toroidal directions, respectively, is assumed as reference for the investigation of the BB sub-models in MAIA procedure. However, this calculation provides only indications on the overall power released and says nothing on its distribution. As introduced in paragraph 1.3, it is important for the design to determine correctly the gradients. This represents also one of the goals of MAIA procedure to use the sub-modelling techniques for simulating the real geometry. It is also important in a multi-physics design cycle to obtain a power density distribution to be used for thermal-hydraulic and thermo-mechanical calculations.

As introduced in paragraph 2.1.2, MCNP provides the possibility to map a physical quantity like the power density by means of a mesh tally (i.e UM or FMESH). For the comparison of power distribution on the three models, a three-dimensional Cartesian mesh has been superimposed on the HCPB slice, module and DEMO space of interest using an identical mesh in terms of boundaries and sizing. In particular, for the HCPB module and DEMO, it has been applied to the 31st slice counting from top to bottom in the BZ stack corresponding to the equatorial slice of OB4.

The mesh size has been defined imposing number of divisions in the direction x,y and z, $n_{div_{ij}}$, as summarised in Table 4.3 while it is shown in Figure 4.5.

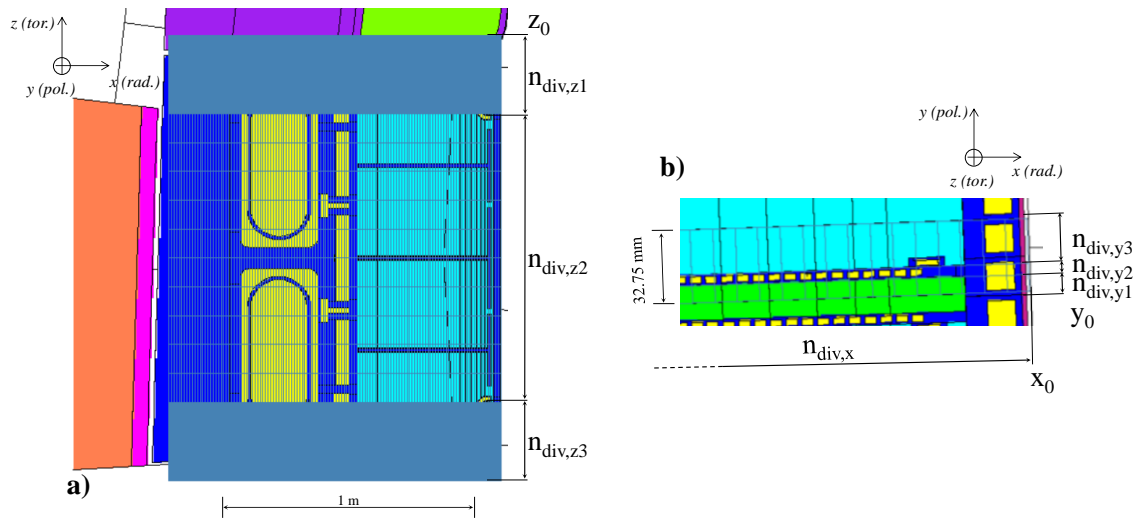


Figure 4.5. FMESH visualization on HCPB DEMO MCNP model;. Left (a): radial-toroidal view. Right (b): radial-poloidal view.

The mesh sizing has been chosen following a trade-off between two counteracting criteria. The small size of mesh element/voxel avoids extensive averaging of the release power over different materials. On the other hand, a fine mesh increases the computational time and makes difficult to obtain a good statistical behaviour. For these reasons, the selected mesh allows having a finer resolution (3 mm in toroidal direction) in the side wall where the geometry presents more features that, otherwise, would be hidden if biggest sizing is applied.

Table 4.3. FMESH card parameters.

| FMESH variable | x (radial) | y1 | y2 (poloidal) | y3 | z1 | z2 (toroidal) | z3 |
|---|---------------|---------|------------------|---------|---------|------------------|--------|
| Origin (x ₀ ,y ₀ ,z ₀) [cm] | -43.100 | | -99.025 | | | -85.000 | |
| Mesh limit [cm] | 83.650 | -98.250 | -97.750 | -95.750 | -55.000 | 55.000 | 85.000 |
| $n_{div_{ij}}$ [cm] | 127 | 1 | 1 | 1 | 100 | 10 | 100 |
| Size [cm] | 0.998 | 0.775 | 0.500 | 2.000 | 0.300 | 11.000 | 0.300 |

The power density distribution is calculated combining the F4 tally (i.e. FMESH), introduced in paragraph 2.1.2, eq. (2.18), with the FM card for the neutrons and photons energy release. In general, the FM card multiplies the tallied quantities for a given constant C and the continuous-energy reaction cross section $R(E) = \sigma_i(E)H(E)$.

From the previous calculations, it emerged again that the case 3D-4D better approximate the overall power deposition. For this reason, it has been used for the calculation and comparison of the power density distribution among the three models as reported in Figure 4.6.

The results are in good agreement between the three models concerning the local power density deposition. In particular, a good agreement in the 3D distributions has been acknowledged in all the regions. In order to better evaluate the discrepancies between the reference results of HCPB DEMO model and the two sub-models a statistical distribution of the error associated to the power density has been evaluated as reported in Figure 4.7.

In Figure 4.7-a), the comparison between the power density distribution calculated in the reference HCPB DEMO model and in the module one is reported.

Power Density [W cm⁻³]

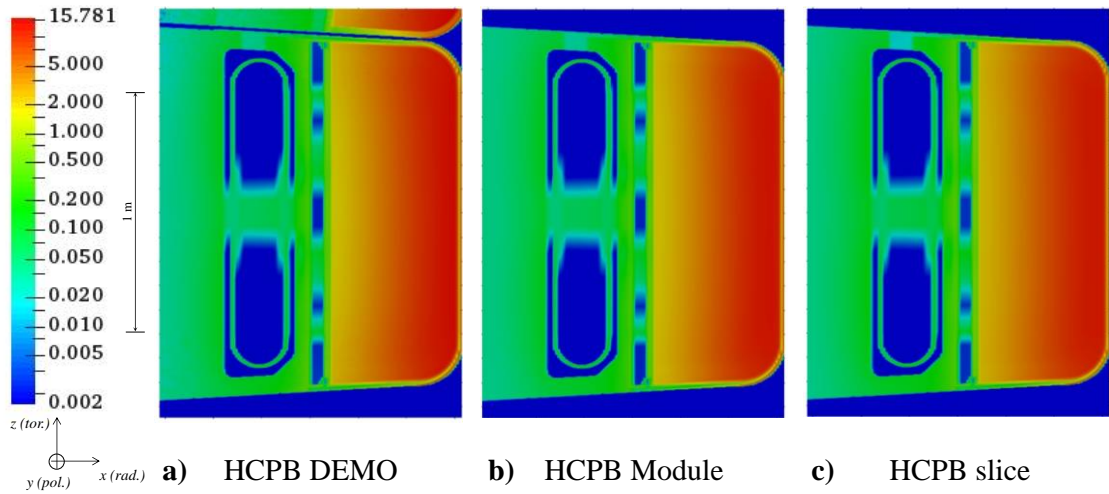


Figure 4.6. Spatial distribution of nuclear power density in the equatorial region of OB4 (see computing domain in Figure 4.2) for the case 3D-4D. Left (a): HCPB DEMO reference power density. Centre (b): HCPB module. Right (c): HCPB slice.

Considering the relative difference between the DEMO full scale model and the local ones, the mean value of the power density deviation error is 5.17 % with a standard deviation of 14.74 % and a median of 6.75%. In Figure 4.7-b), the comparison between the power density distribution calculated in the reference HCPB DEMO model and in the slice one is reported.

The mean value of the power density error is -3.97 % with a standard deviation of 18.71 % and a median of -1.60%. From a post-processing of the obtained results, it has been possible to note that the biggest variations occur when the power density values are small (e.g. helium channels and BSS) and far from the local source (e.g. back of BSS).

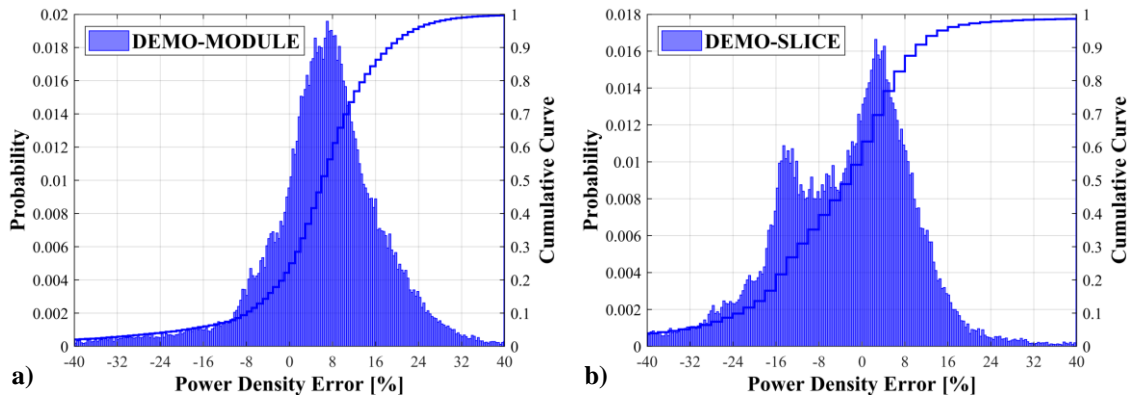


Figure 4.7. Statistical distribution of the error on power density for the case 3D-4D. Left (a): histogram of power density error between the DEMO and module models and cumulative curve. Right (b): histogram of power density error between the DEMO and slice models and cumulative curve.

This behaviour can be appreciated in Figure 4.8 where it is reported the 3D contour map power density error for the HCPB slice with respect to the HCPB DEMO model for the case 3D-4D. As it is possible to see in Figure 4.8-a), the most of the error (about the 45%) is comprised between ± 4 % in the central part where the mesh elements are big and the statistical behaviour is good in both HCPB slice and DEMO models. In the range ± 10 % would account for about the 75 % of the total. It is interesting to note the highest discrepancies between the slice and DEMO are encountered in the BSS near the equatorial port and in the sidewall near the manifolds for coolant and purge gas, as highlighted in Figure 4.6-a).

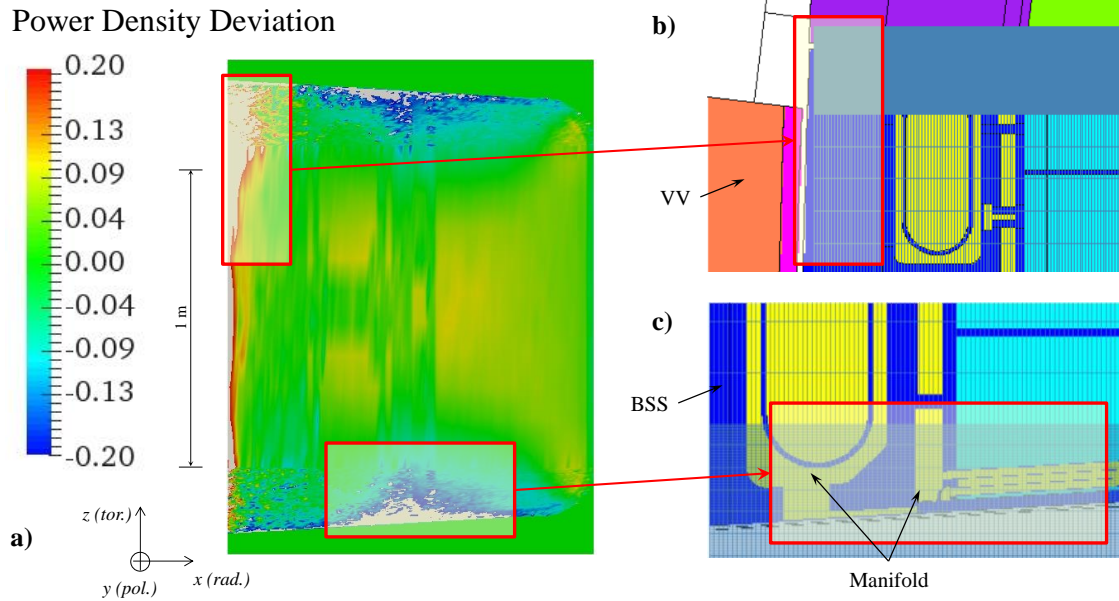


Figure 4.8. Computed 3D power density deviation between HCPB slice model and DEMO and details of FMESH. Left (a): contour map of power density error distribution in the range of ± 0.2 . Right-top (b): BSS mesh with detail of the VV equatorial port. Right-bottom (c): detail of mesh in side wall and manifold region.

Regarding the first spot (Figure 4.8-b), it is possible to note that the big error is mainly due to the coaction of a fine mesh and the missing back scattering due to the presence of the equatorial port. Indeed, in the HCPB slice as well as in the HCPB module, the presence of the VV equatorial port has not been taken into account and the VV is continuous for all the toroidal direction following the BSS extension.

The second spot occurs in the sidewalls where the finer mesh encounters the purge gas and coolant manifolds. The presence of He means few interaction due to his low density and a finer mesh means an extremely low statistic in the big models like HCPB DEMO.

However, although the presence of these localised zones, if the Figure 4.8 is read together with Figure 4.6-a, it is immediately clear that the highest errors are related to low power density values (between 0.002 and 0.1 W/cm^3).

The same considerations have been found also for the comparison between the HCPB module and DEMO. So it is possible to conclude that the set of boundary conditions selected (white and reflecting in toroidal and poloidal direction, respectively) for the local models reproduce the environment around them providing a satisfactory estimation both on the deposited power and its distribution.

A better local estimation of the released power in the aforementioned zones and a more reliable assessment of relative differences among the models could be achieved using variance reduction techniques and increasing the number of particle histories in the reference model.

The consistency verification of the boundary conditions has been continued with particular reference to the reflecting conditions applied in the poloidal direction of the local models.

Indeed, in order to better evaluate the contribution of neutrons and photons that are scattered in the neighbouring zones and are entering the investigated domain from the poloidal surfaces, two different studies have been carried out.

The first one has been aimed to the verification that the neighbouring zones (i.e. the adjacent slices) have a similar behaviours to the area of study. This study allows checking the poloidal symmetry in terms of power deposition and so the consistency of poloidal reflecting conditions.

The second study is devoted to demonstrate that the neutrons are mostly scattered in the poloidal direction and the contribution of neutrons emitted directly from the plasma is negligible after few

centimetres of BB.

Regarding the first point, a dedicated power deposition calculation on different levels of the full heterogeneous OB4 module of the HCPB DEMO reference model has been carried out in order to verify the consistency in the entire module and near the discontinuities (e.g. caps).

However, a first demonstration of the correct definition of symmetry conditions has been already envisaged in the previous calculation on reflecting and white condition reported in Table 4.2. Indeed, the results on the equatorial region of the HCPB module have already shown a similar behaviour of neighbouring slices independently of the poloidal condition applied.

For verifying the subsistence of symmetry conditions in all the modules, eleven slices have been identified (four near the cap on the top, three in the middle area of the module and four near the cap on the bottom, Figure 4.9) and the power deposition for each cell of the slices has been calculated following the approach already described at the beginning of this paragraph.

The detailed results for each slice and for each cell are reported in Appendix 9.3, from Table A.10 to Table A.12. In this way, it has been possible to calculate the variation of the deposited power cell by cell between a i -th slice and the i -th±1 slice as reported in Table 4.4 for the equatorial slice and Table 4.5 for the slices near the top and bottom caps. The up and down variation are defined with respect to the i -th slice.

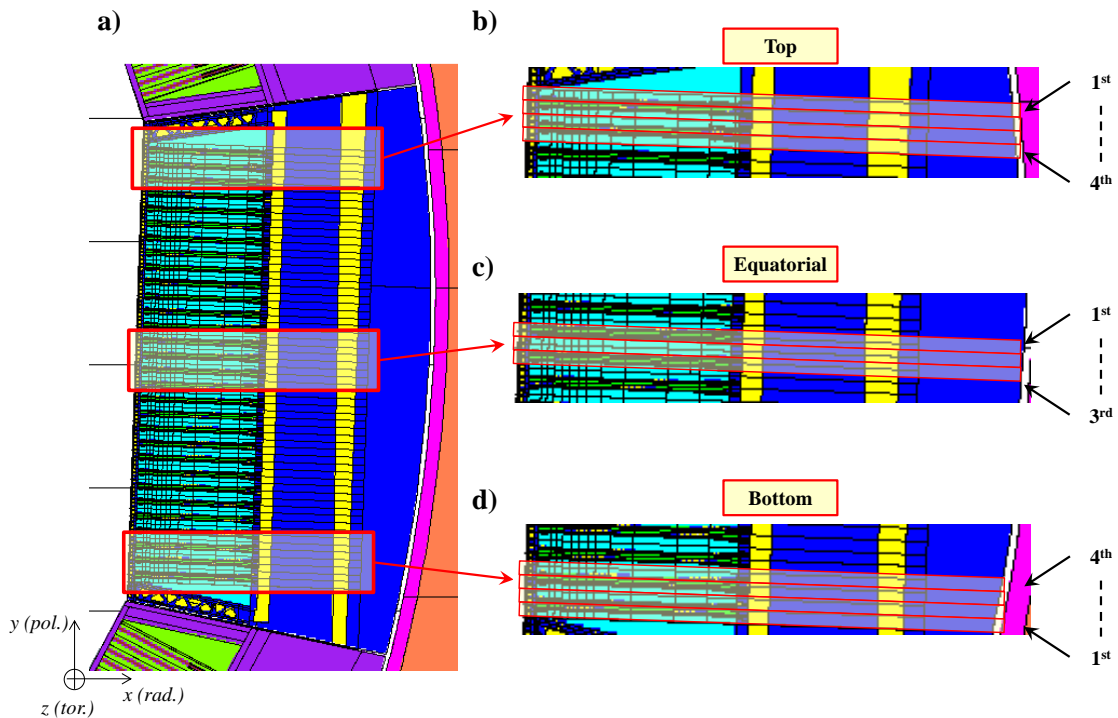


Figure 4.9. Slices zone identification in the full heterogeneous OB4 module of the HCPB DEMO reference model. Left (a): full heterogeneous OB4 module with evidence of the three zones of investigation. Right-top (b): slices identified near the top cap. Right-centre (c): slices identified in the OB4 middle area. Right-bottom (c): slices identified near the bottom cap. Figures a), b) and c) are reproduced according to [85].

As it is possible to note, in the equatorial region (Table 4.4) the variation in the power deposition for each cell are very low and the overall mismatch is at most the -0.11%.

These results are in agreement with the one encountered during the previous calculation and demonstrate that the neighbouring slices have the same behaviour as the one under study and therefore, also the applicability of the reflecting conditions in the poloidal direction is recommended.

Looking to Table 4.5, the same trend is found up to the third to last slice both near the top and bottom cap. Therefore, small variations occur and the effect of the discontinuities (i.e. the caps) does not produce any effect except for the last near slice.

Table 4.4. Power deposition variation of the middle slice with respect to the adjacent ones.

| Region | DEMO | |
|--------------------------------------|------------------------------------|------------------------------|
| | Equatorial (2 nd slice) | |
| | Up (1 st slice) | Down (3 rd slice) |
| Armour | -0.36% | -0.44% |
| Be Bed | -0.07% | -0.22% |
| BSS | -0.23% | -0.28% |
| CP | -0.07% | -0.14% |
| FW | -0.08% | -0.17% |
| He BSS | -0.11% | -0.06% |
| He CP | -0.12% | -0.22% |
| He Dummy Channels | -0.07% | -0.24% |
| He FW | -0.19% | -0.33% |
| He Manifold | -0.15% | -0.05% |
| He Purge BSS | -0.01% | -0.34% |
| Li ₄ SiO ₄ Bed | 0.09% | 0.00% |
| Manifold | -0.45% | -0.26% |
| Grand Total | -0.01% | -0.11% |

Indeed, it is possible to observe in Table 4.5 that the biggest variation on the power deposition is located in the last Li₄SiO₄ beds (-11.84% near the top cap and -11.34% near the bottom cap, respectively).

This produces an overall power production variation of -5.95% and -5.63% (Table 4.5). The highest power released in the Orthosilicate is due to the highest neutron multiplication that occurs in the cap which are filled with Be. This asymmetry produced by the caps is already attenuated after the first slice and demonstrates the applicability of reflecting conditions except for the last slice.

Table 4.5. Power deposition variation of *i-th* slice near the top and bottom caps with respect to the adjacent ones.

| Region | DEMO 2 nd Top | | DEMO 3 rd Top | | DEMO 3 rd Bottom | | DEMO 2 nd Bottom | |
|--------------------------------------|-----------------------------|----------------------------|-----------------------------|----------------------------|--------------------------------|----------------------------|--------------------------------|----------------------------|
| | Up (1 st) | Down (3 rd) | Up (2 nd) | Down (4 th) | Up (4 th) | Down (2 nd) | Up (3 rd) | Down (1 st) |
| | Armour | 0.00% | 0.02% | -0.02% | 0.11% | 0.44% | -0.58% | 0.57% |
| Be Bed | 0.11% | -0.90% | 0.89% | -0.14% | -0.27% | 0.90% | -0.90% | 0.29% |
| BSS | -2.19% | 1.36% | -1.38% | 0.62% | 0.65% | -0.99% | 0.98% | -1.95% |
| CP | -0.78% | 0.25% | -0.25% | 0.15% | 0.11% | -0.33% | 0.33% | -0.76% |
| FW | -0.13% | -0.64% | 0.63% | 0.12% | 1.26% | -0.54% | 0.53% | -0.25% |
| He BSS | 1.11% | -0.79% | 0.78% | -1.16% | -1.53% | 1.32% | -1.34% | 1.81% |
| He CP | 0.31% | -0.57% | 0.57% | -0.36% | -0.59% | 0.58% | -0.59% | 0.60% |
| He Dummy Channels | 1.07% | -0.64% | 0.63% | -1.10% | -1.27% | 0.82% | -0.83% | 1.47% |
| He FW | 0.04% | 0.06% | -0.06% | -0.25% | 0.09% | -0.19% | 0.19% | -0.20% |
| He Manifold | 0.45% | -0.43% | 0.42% | -0.53% | -0.82% | 0.87% | -0.88% | 0.81% |
| He Purge BSS | 0.18% | -0.92% | 0.91% | -0.71% | -0.86% | 1.22% | -1.23% | 0.46% |
| Li ₄ SiO ₄ Bed | -11.84% | 1.61% | -1.63% | 2.91% | 2.53% | -1.54% | 1.52% | -11.34% |
| Manifold | 0.01% | 0.53% | -0.53% | 0.06% | 0.45% | -0.49% | 0.49% | 0.22% |
| Grand Total | -5.95% | 0.56% | -0.56% | 1.43% | 1.33% | -0.65% | 0.64% | -5.63% |

Therefore, the set of boundary conditions used in MAIA and the applicability of the procedure itself can

be spread for the entire module with the exception of the cap regions. Further investigations would have to be performed for the application of MAIA procedure where geometry discontinuities appear.

Moreover, the power deposition variations reported in Table 4.4 and Table 4.5 represent a range of investigation for the consistency verification of thermal-hydraulic as well as thermo-mechanical conditions in order to evaluate the impact on temperature and stress fields.

As anticipated, a second study has been also carried out in order to verify that only scattered neutrons pass through the poloidal reflecting boundary conditions.

Indeed, it is possible that neutrons emitted by plasma go through the adjacent slices without scattering and then they interact with the domain under study. These neutrons, which have not collided before and have crossed the blanket in the poloidal direction, represent a neutron flux term that is not accounted both by local neutron source and by boundary conditions. In particular, in Figure 4.10, the schematic view of this case for three slices is reported.

As verified before, the neighbouring slices have similar power deposition and then they experience similar neutron fluxes. This characteristic is schematically expressed by the green arrows that represent the neutron flux passing through the surface tally (orange dashed line) and sampled in the local source.

The sampled neutron flux is similar in the neighbouring slices and, for this reason, the use of reflecting boundary condition (red dashed line) allows the simulation of the environment around the local model under investigation. However, some neutrons could neither cross the source surface tally nor interact with adjacent slices (blue arrows).

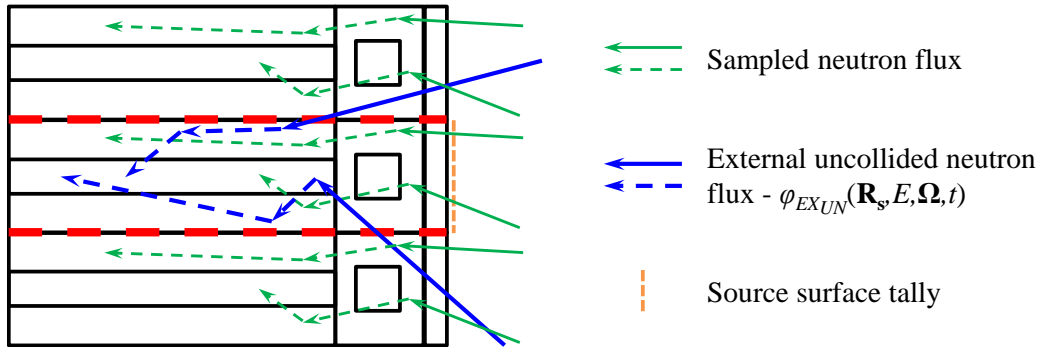


Figure 4.10. Schematic view of neutron interactions with the investigated domain. Details on collided neutron flux taken into account with local source and boundary conditions and contribution of external uncollided neutron flux.

This external uncollided neutron flux $\varphi_{EXUN}(\mathbf{R}_s, E, \Omega, t)$ (the term “uncollided” is here used for specifying the neutrons that come from the plasma and have not scattered before to reach the slice under study) could pass through the neighbouring slices, cross the boundaries and interact for the first time with the investigated domain.

It is immediately clear that this contribution can have an impact on the correctness of the results obtained when sub-models are used. In order to take into account this contribution in the OB4 and successively in all the other modules, it has been identified a figure of merit (FoM) η defined as the ratio between the number of neutrons crossing the boundary poloidal surface coming directly from the plasma and the number of the overall neutrons crossing the same radial-toroidal surface S as reported in eq. (4.1)

$$\eta = \frac{\int_S dS \int_{E_{th}}^{+\infty} dE \int_{2\pi} \varphi(\mathbf{R}_s, E, \mu) \mathbf{\Omega} \cdot \mathbf{n} d\Omega}{\int_S dS \int_0^{+\infty} dE \int_{2\pi} \varphi(\mathbf{R}_s, E, \mu) \mathbf{\Omega} \cdot \mathbf{n} d\Omega}, \quad (4.1)$$

where E_{th} is lower plasma emitted neutron energy.

This FoM is calculated starting from the full heterogeneous OB4 module inserted in HCPB DEMO reference model on which previous analyses demonstrated a poloidal symmetry behaviour.

In order to evaluate correctly the $\varphi_{EX_{UN}}(\mathbf{R}_s, E, \Omega, t)$, it is necessary to identify the energy bin associated with “uncollided” neutrons. As reported in [89-91], the D-T energy spectrum can be represented by a Gaussian energy distribution strongly peaked around 14.1 MeV with an isotropic angular distribution [92, 93]. According to the energy neutron spectrum measurements reported in [94], it has been assumed that all the neutrons in the region of interest ($E_{th} > 13.2$ MeV) come directly from the plasma inducing the external “uncollided” flux.

This assumption is not completely true for one main reason: some neutrons, after a scatter, could lose only a small fraction of energy falling again within the range considered. However, as preliminary investigation, this effect has been assumed negligible.

On the other side, the wide energy range selected for the external uncollided flux estimation represents a conservative assumption as shown in the following.

For determining η , a dedicated analysis has been performed on the reference DEMO HCPB model equipped with the full heterogeneous OB4 module.

Three radial-toroidal surfaces have been identified in the equatorial zone (Figure 4.11-a, red line) and near the top and bottom cap (Figure 4.11-a, green lines) subdivided in the radial direction according to the incremental dimensions reported Figure 4.11-a.

On these regions, the FoM η for “uncollided” neutron with energy above 13.2 MeV (Figure 4.11-b) and above 13.95 MeV (Figure 4.11-c) has been evaluated. This second value has been selected to narrowing the energy bin assumed for the external “uncollided” flux $\varphi_{EX_{UN}}$.

It is possible to note that, for both cases, the FoM η reduces strongly with the radial direction (less than 5 % after the FW) and no appreciable differences are encountered between the equatorial zone and the regions near the caps. This represents another confirmation of the poloidal symmetry and means that the middle zone is, from a neutronic point of view, representative of the entire module.

The main values of η are localised in Armour and FW regions, as expected. The external “uncollided” flux counted in these two regions is composed both of the uncollided flux perpendicular to the tally area and of uncollided flux passing through the sampling source surface that cannot be neglected due to the angle of incidence of neutrons coming from plasma.

However, considering that the FoM η , estimated on the OB4, is also used as reference and the same overestimation on uncollided flux in the first centimetres of the BB is encountered also in the other modules, it does not affect the conclusion of the study.

The same approach, for the calculation of FoM η , has been followed for the other modules on which an equatorial radial-toroidal surface for 7 selected modules between the IB and OB has been identified (Figure 4.11-a, red lines).

The results are shown in Figure 4.12. It is possible to note that the results and trends calculated for the OB4 are similarly obtained in all the analysed modules with a small exception for the OB7 where a higher η , with respect to the one assessed in OB4, is found (Figure 4.12 – a).

Indeed, this module, due to the D-shape of the plasma, is more exposed to a direct poloidal flux in particular in the Armour and FW zones. However, this does not affect the behaviour found in the other module and, more specifically, in the OB4 used as reference in this evaluation.

In conclusion, starting from the consistency verification of boundary conditions mainly performed on OB4 module and using a FoM for weighting the effect of external uncollided flux with respect to the total flux, it has been possible to extrapolate the considerations done on the equatorial outboard region to all the BB modules. This provides a preliminary indication about the applicability of MAIA procedure to all the modules both for IB and OB.

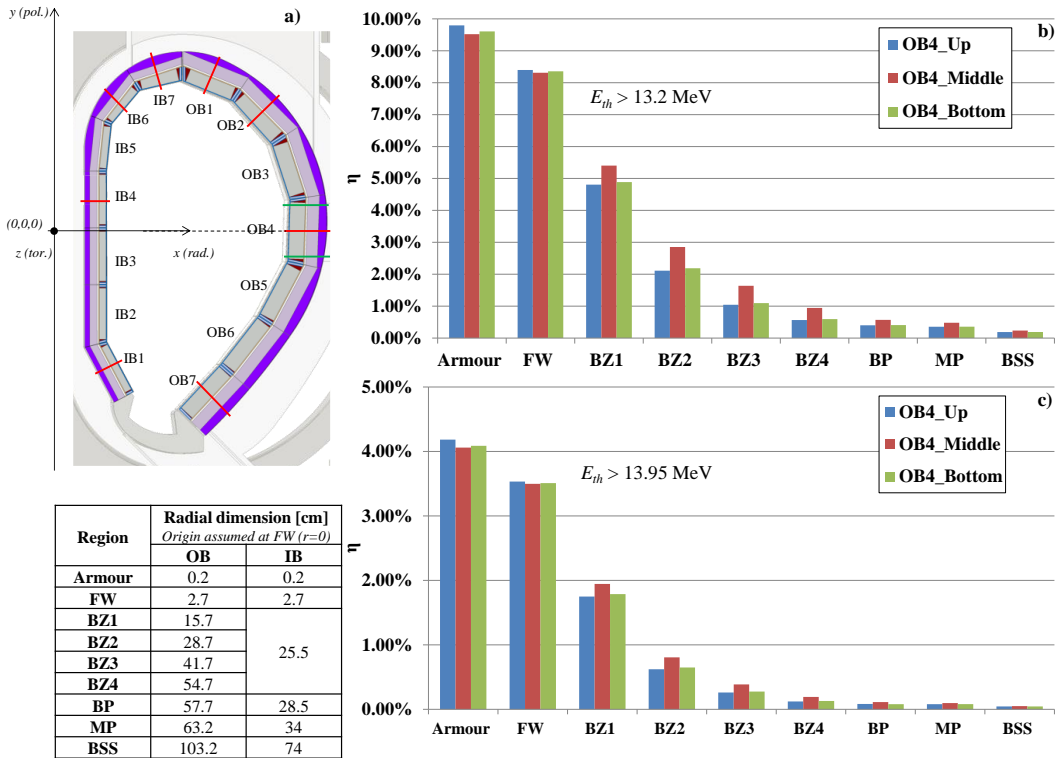


Figure 4.11. Schematic view of DEMO model with identification of sampled surfaces and estimation of external uncollided flux at different levels for the OB4 module. Left (a): sampled surfaces for the IB and OB modules and incremental radial subdivision. Right-top (b): estimation of FoM η at different radial position considering energy of “uncollided” neutrons above 13.2 MeV. Right-bottom (c): estimation of FoM η at different radial position considering energy range of “uncollided” neutrons above 13.95 MeV. Figure (a) reproduced according to [26].

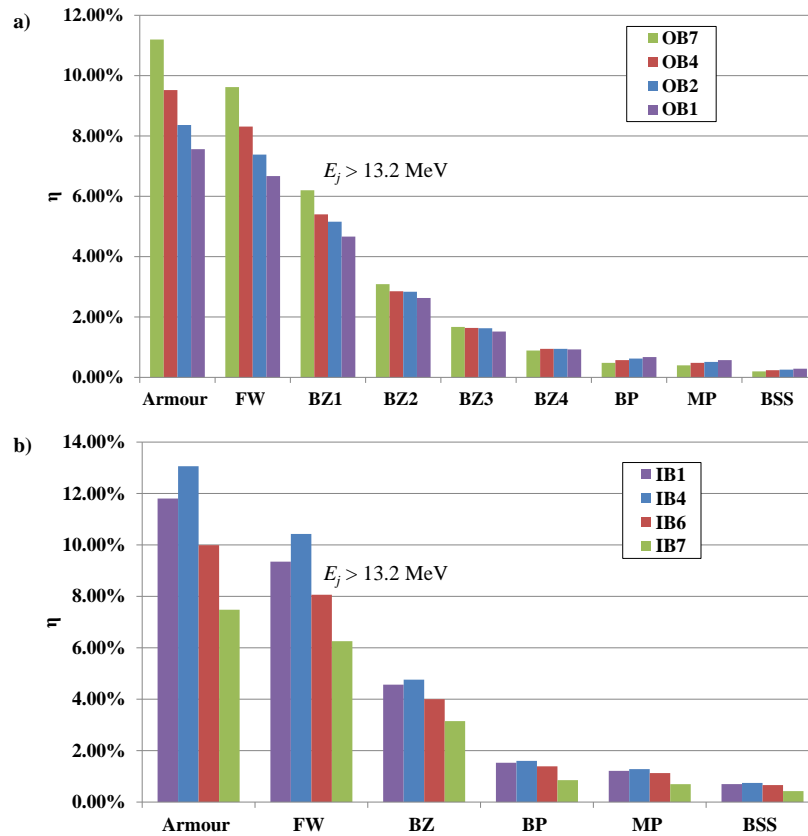


Figure 4.12. Estimation of FoM η for different modules at the blanket modules equatorial zone. Top (a): FoM η for OB. Bottom (b): FoM η for IB.

4.1.2 Local Source Representation and Sensitivity Analysis

Once the consistency of the boundary conditions has been demonstrated, the last step is to investigate the impact of local neutron and photon sources on the results in order to assess the best representative cosine bin discretisation.

In Figure 4.13, with reference to the OB4 module of HCPB DEMO model, it is shown for each cosine bin (cosine defined with respect to the normal to the source surface A_{TALLY} , see Figure 3.4), the energy probability for the neutrons passing through the source surface tally. Similar graph with different probability distributions can be obtained for the photon local source.

Two contributions can be easily identified: (i) one due to the neutrons at high energies emitted by the plasma; and (ii) another due to the neutrons that have interacted with the materials present within the VV (e.g. blanket and divertor) and are scattered towards the domain of investigation.

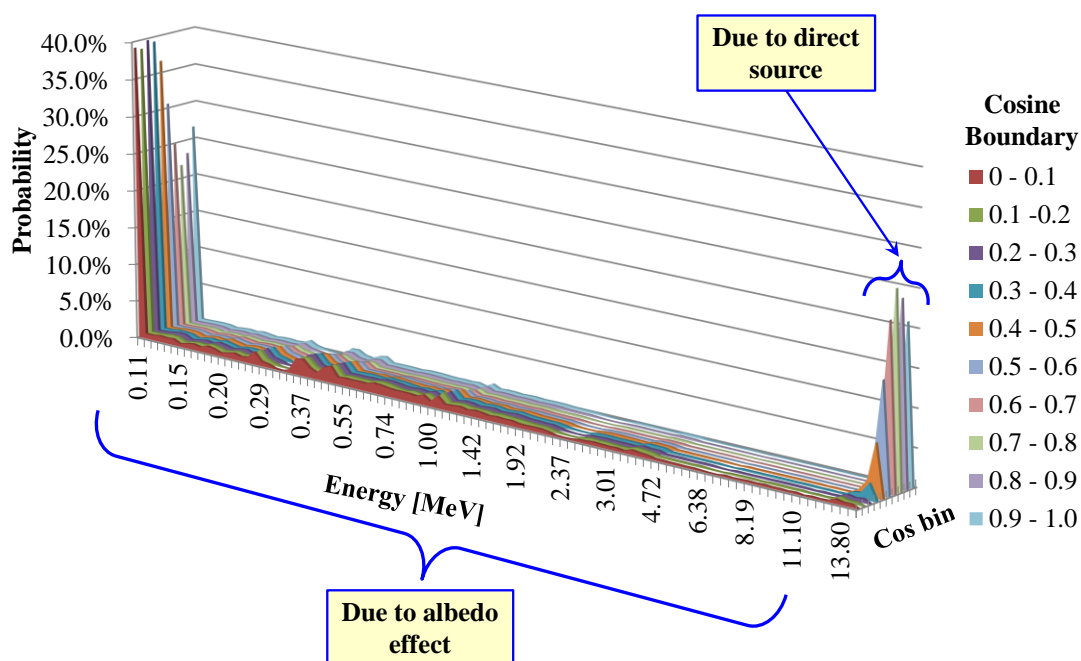


Figure 4.13. Neutron energy probability function for each cosine bin sampled in front of the equatorial slice of HCPB DEMO OB4 module.

As already explained, the definition of local source depends on the energy and cosine bin selected that are strictly connected on the computational effort. Indeed, narrow bins require long calculation using the global model in order to minimise statistical errors. On the other side, large bins average the distributions impacting on the results of the local models.

Regarding the selection of the energy bins, as said, the energy data structure of Vitamin J+ [78] have been used. These data are applied for the definition of nuclear libraries used in neutron and photon transport calculations and represent a fine and broad group energy structures. In particular, the use of the same energy bins applied for the creation of nuclear libraries does not introduce any approximation. For these reasons, the sensitivity analysis has been focused only on the cosine subdivision.

Furthermore, a first investigation has been carried out comparing the distribution obtained when an identical number of angle or cosine subdivision is used for the sampling of the local source in the global model. Therefore, using the methodology described in paragraph 3.3.1, two source sampling analysis on surface A_{TALLY} (see Figure 3.4) with 10 angles subdivisions in the range from 0° to 90° and 10 cosine subdivisions in the range from 1 to 0 have been performed.

The results for two energy bins at 13.8-14.2 MeV and 0-0.111 MeV are reported in Figure 4.14.

It is interesting to note that, for the same number of bins, the cosine and angle distributions present discrepancies that can reach 20% in particular for the energy bin at 13.8-14.2 MeV (Figure 4.14-a).

This is due to (i) the cosine distribution that is sparser for small angles and more concentrated at angles around 90° while the angle distribution results equally spaced for all the angles and (ii) to the poor statistics at large angles.

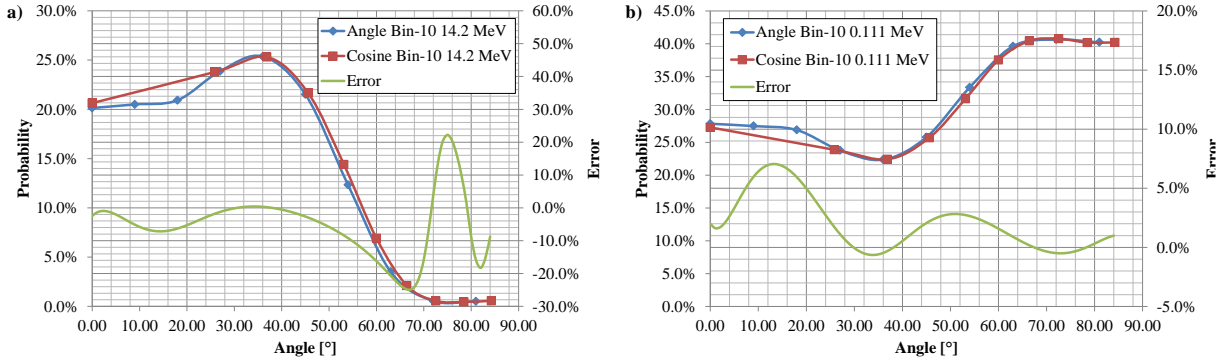


Figure 4.14. Neutron cosine and angle probability distribution considering 10 subdivisions and for given energy bins at 13.8-14.2 MeV and 0-0.111 MeV. Left (a): neutron cosine and angle probability at 14.2 MeV and error among them. Right (b): neutron cosine and angle probability at 14.2 MeV and error among them.

In order to minimise the error between the angle and cosine distributions, it is necessary to reach a number of divisions equal to 30. In Figure 4.15, it is possible to note that the two probabilities function approximate each other better and the error is limited between -13% and 7% for the energy bin 13.8-14.2 MeV and between the -0.3% and 1.9% for the energy bin 0-0.111 MeV.

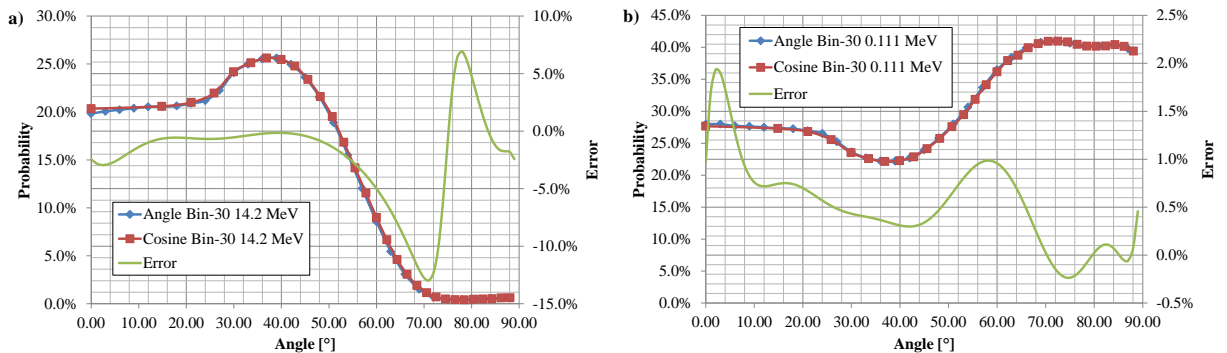


Figure 4.15. Neutron cosine and angle probability distribution considering 30 subdivisions and for given energy bins at 13.8-14.2 MeV and 0-0.111 MeV. Left (a): neutron cosine and angle probability at 14.2 MeV and error among them. Right (b): neutron cosine and angle probability at 14.2 MeV and error among them.

The study so far conducted, demonstrates as expected that a finer subdivision reduces the differences between an angle and cosine distribution, but does not indicate the best cosine bin discretisation to be used.

For these reason, dedicated analysis have been carried out using a bin subdivision from 0 to 30 ranged according to the Table 4.6.

The derived neutron and photon local sources have been then used on the HCPB slice model for evaluating the deposited power. Furthermore, the results have been compared with the power deposition calculated in HCPB DEMO reference model.

As it is possible to see in Table 4.6 and in Figure 4.16, the released power depends on the number of cosine or angle bins selected. For instance, for a single bin the difference between the power in HCPB DEMO reference model and HCPB slice can reach $\sim 20\%$ with a strong underestimation of the local model.

Increasing the number of bin divisions, the error reduces considerably reaching a flat to at 10 subdivisions. Practically, after 10 bins, no differences can be appreciated between the angle and cosine

distributions. This is a clear indication that the subdivision in 10 cosine bins, already used in the previous analyses, represents a good choice in terms of discretisation, fidelity of the results obtained for the reference model and computational effort. Indeed, although with 20 or 30 bin division, the error slightly reduces, the calculation time of the source sample increases considerably.

Table 4.6. Power deposition on HCPB slice and error with respect to the OB4 HCPB DEMO reference model as function of angle and cosine bin discretisation.

| Bin N° | HCPB DEMO Power [W] | Cos. Distribution Power [W] | Ang. Distribution Power [W] | Cos. Distribution Error | Ang. Distribution Error |
|--------|---------------------|-----------------------------|-----------------------------|-------------------------|-------------------------|
| 1 | | 63022.8 | | -19.84% | |
| 2 | 75526.10 | 73503.68 | 71769.7 | -2.68% | -4.97% |
| 5 | | 74929.07 | 74712.73 | -0.79% | -1.08% |
| 10 | | 75157.27 | 75101.38 | -0.49% | -0.56% |
| 20 | | 75211.71 | 75189.52 | -0.42% | -0.45% |
| 30 | | 75221.30 | 75219.13 | -0.40% | -0.41% |

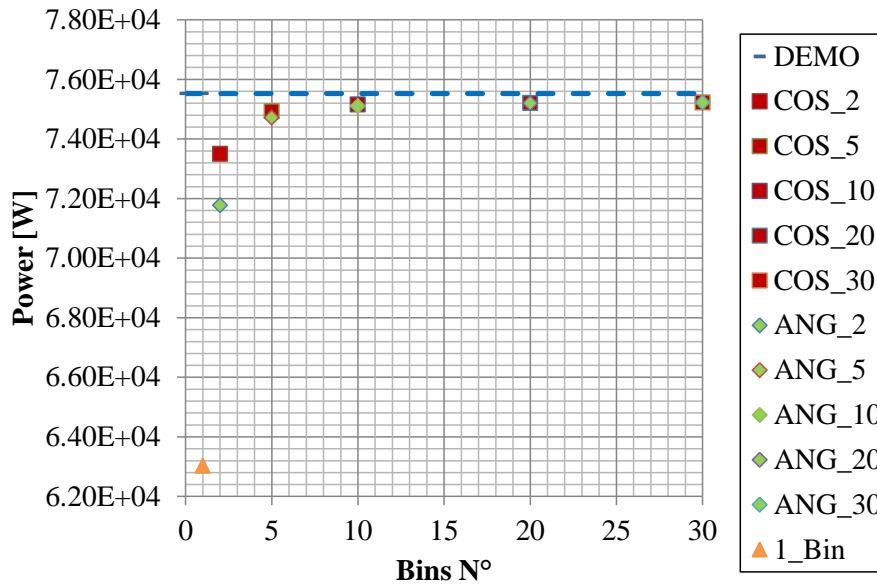


Figure 4.16. Power deposition on HCPB slice as function of angle and cosine bin discretisation.

4.2 Consistency Verification of MAIA Thermal-Hydraulic Model

After the consistency verification of the neutronic boundary conditions and local sources of MAIA procedure, the attention has been focused to thermal symmetry conditions used in thermal-hydraulic calculations.

The parameters affecting the applicability of these conditions are:

- (i) geometric asymmetry of the adjacent slice with respect to the one under investigation;
- (ii) asymmetries in the power deposition nearby; and
- (iii) anomalous mass flow rate distributions due to the asymmetries in the released power or due to not optimised thermal-hydraulic circuit.

The first contribution can be neglected by design. Indeed, each unit (e.g. slice, BU) within a module is conceived equal to the others and no differences are expected nearby.

The second contribution has been already estimated in the previous paragraph and the power deposition variation can be found in Table 4.4 for the equatorial slice and **Table 4.5** for the slices near the top and bottom caps.

The third contribution can be assessed considering two aspects:

- (i) if an optimised design is already achieved, the mass flow rates in the neighbouring slices follow the variations related to the deposited power. In general, marginal power differences could also lead to different gas/fluid expansions and, hence, modify the flow distribution among the channels. However, this last effect can be neglected and assume integrated in the variations related to the deposited power;
- (ii) if the design has not been optimised, the mass flow rate distributions are those assessed by isothermal hydraulic analyses and related to the thermal hydraulic resistances of the circuits.

This last aspect has not been assessed as far and, for this reason, it will be addressed in the following.

The approach, used for the determination of the mass flow rate distribution due to the hydraulic resistances, takes inspirations from the methodology used to perform thermal-hydraulic analysis in fission reactors with the use of System Code such as RELAP [95].

Indeed, it is common for the system analysis of fission reactors to nodalise part of the circuit with few control volumes on which an ad-hoc thermal-hydraulic characteristic is applied for simulating the behaviour of more complex components and for saving calculation time.

Practically, by means of a function (usually referred to the pressure drop vs mass flow rate), the average behaviour of a complex component is taken into account and the overall system can be studied in a simplified and reliable way. Therefore, for estimating the mass flow rate distribution in a HCPB BB segment, the following steps have been performed:

1. Investigation of the characteristic function $\Delta p(G)$ of the HCPB slice coolant circuit which expresses the functional dependence of the pressure drop across the circuit, Δp , from the flow rate G that crosses it.
2. Study of mass flow rate distribution in a full segment of HCPB using the real model of inlet and outlet manifolds as well as a porous media model for simulating each HCPB slice in which the hydraulic characteristic function is applied [96].

For the first step, the following procedure is adopted:

- a) The thermodynamic conditions of the component's incoming coolant p^{in} and T^{in} are set (the T^{in} used in this analysis corresponds to the mean of the HCPB operational temperatures, namely 400 °C).
- b) A series of outlet pressures is defined, p_i^{out} with $i = 1..N$, such that $p_i^{out} < p^{in} \forall i = 1..N$.
- c) The total mass flow G_i , induced by the pressure difference considered, is determined by means of suitable theoretical and computational analyses, $\Delta p_i = p^{in} - p_i^{out} \forall i = 1..N$.
- d) The characteristic function $\Delta p(G)$ is deduced, by means of the numerical interpolation of the obtained N pairs $(G_i, \Delta p_i)$.
- e) The pressure resistance loss coefficient $K(v)$ calculated as a function of the velocity (v) is, then, deduced by means of numerical interpolation of the obtained N pairs (v_i, K_i) .

The characteristic curves are approximated by means of the following functional expression

$$\Delta p(G) = aG^b, \quad (4.2)$$

where a and b are coefficients determined according to the fourth step d).

From (4.2) the linear resistance loss coefficient is easily obtained as follows:

$$\frac{K}{L} = \frac{2\rho A^2 a G^{b-2}}{L}, \quad (4.3)$$

where ρ is the fluid density, A is the area on which the variables are evaluated and L is the characteristic length of circuit on which the thermal-hydraulic characteristic $\Delta p(G)$ is calculated.

Eq. (4.3), with few passages, can be written as

$$\frac{K}{L} = \alpha v^\beta, \quad (4.4)$$

where α and β are the coefficients determined according to the fifth step e) and equal to $\frac{2a\rho^{b-1}A^b}{L}$ and $2-b$, respectively.

In order to perform the first step for the determination of the thermal-hydraulic characteristics reported in eq. (4.2) and eq. (4.4), a dedicated model of HCPB slice cooling circuit has been set up (Figure 4.17 - a).

Tetrahedral elements are adopted taking into account the geometrical features of the domains to be meshed and the required optimization of the number of nodes and mesh quality. The mesh is composed of $\sim 17.1E+06$ nodes linked in $\sim 7.5E+06$ elements with an orthogonal quality average of 0.643 and skewness average of 0.356. A number of 10 inflation layers has been used with first layer height of $5.5E-05$ m and a growth rate of 1.2. The mesh is shown in Figure 4.17 - a. For the calculation of hydraulic characteristic, an average temperature of 400°C has been assumed and the mass flow rate has been ranged from 0.01 kg/s to 0.1 kg/s subdivided in 10 bins (the nominal mass flow rate for each HCPB slice loop is 0.046072 kg/s [28]). The surfaces on which the pressure drops have been calculated are shown in Figure 4.17 - b and c, while the characteristic functions $\Delta p(G)$ and $K(v)$ are reported in Figure 4.18 and Figure 4.19.

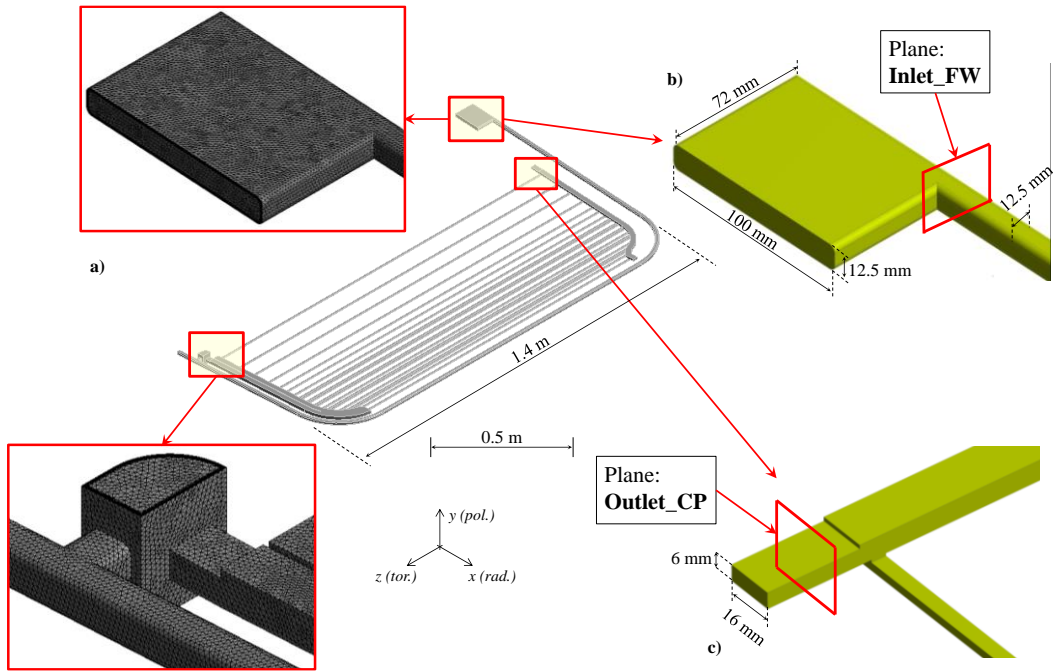


Figure 4.17. HCPB slice cooling circuit with detail of mesh and planes for the determination of pressure drops. Left (a): HCPB slice cooling circuit and detail of mesh inflation layers. Right-top (b): inlet FW circuit plane. Right-bottom (c): outlet CP circuit plane.

After the assessment of thermal-hydraulic characteristic on the HCPB slice cooling circuit, the second step has been aimed to the calculation of the mass flow rates in each CP. For investigating the variation that occurs between neighbouring slices, it has been decided to study the overall behaviour of the HCPB OB segment loop as shown in Figure 4.20.

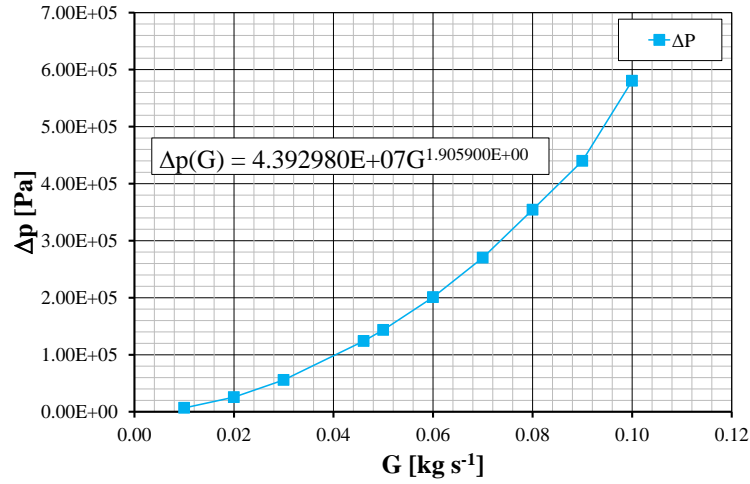


Figure 4.18. $\Delta p(G)$ characteristic function and interpolation equation.

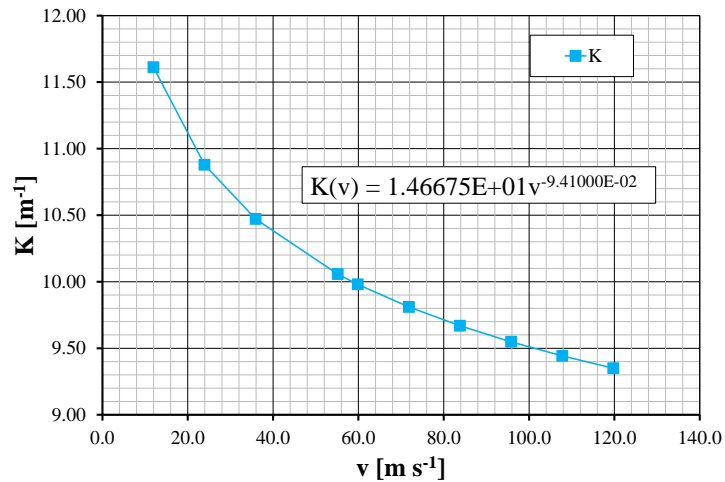


Figure 4.19. $K(v)$ characteristic function and interpolation equation.

The model consists of the inlet and outlet manifold fluid domains (details 1-b and 1-c of Figure 4.20) and the porous model representing the slices of each OB module (details 1-a, 2-a and 3-a of Figure 4.20). Practically, the C-shaped porous domain is a simplification of the CP cooling circuit shown Figure 1.4 – d on which the $K(v)$ characteristic function has been applied for reproducing the hydraulic behaviour of a complete slice (FW + CPs). The dependency of the resistance loss coefficient allows to estimate the pressure drop according to the local velocity field and taking into account the effect of the adjacent slices. Using this technique, the overall OB segment can be studied as a unique cooling circuit considering the impact of the 419 slices. A mesh independency analysis has been performed for the finite volume model to select optimized spatial discretization allowing accurate results and saving calculation time. Three meshes with 30, 60 and 90 millions of elements have been set-up. The conditions to assess the achievement of convergence, which allows to interrupt the steady state calculation, are three:

- residual RMS error values are below an acceptable value, i.e. 10^{-5} ;
- monitor points for selected parameters of interest (e.g. pressure drop, channel mass flow

distributions) achieve steady solutions;

- mass, momentum and energy imbalances are less than 1% in the entire domain.

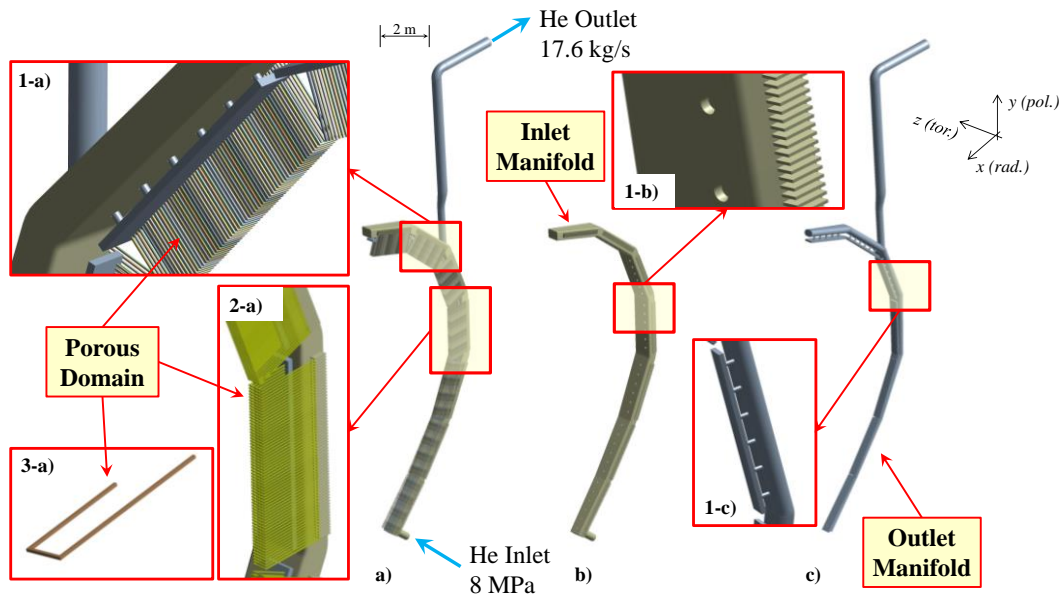


Figure 4.20. Model of a parallel coolant loop of the HCPB BSS manifold piping with the entire CP represented by means of the porous model. Left (a): inlet and outlet manifold with porous model simulating the FW and CP channels. Left-top (1-a, 2-a and 3-a): details of the porous domain. Centre (b): inlet manifold domain. Centre-top (1-b): detail of the inlet manifold and FW inlet channels. Right (c): outlet manifold domain. Right-bottom (1-c): detail of CP outlet manifold.

The pressure drop has been used as parameter for the mesh independence grid. The pressure drop reduces going from 30 to 90 million of elements reaching a minimum variation of 2.3% when the number is increased from 60 to 90 million. In order to better estimate the pressure drop, the latter has been selected. In particular, tetrahedral elements are adopted taking into account the geometrical features of the domains to be meshed and the required optimization of the number of nodes and mesh quality. A conformal mesh (i.e. each node on the interface side matches with the nodes on the other side) between the different domains has been set-up. The mesh is composed of $32.7E+06$ nodes linked in $91.9E+06$ elements with an orthogonal quality average of 0.701 and skewness average of 0.287. A number of 8 inflation layers has been used with first layer height of $2.0E-05$ m and a growth rate of 1.6. The mesh is shown in Figure 4.21.

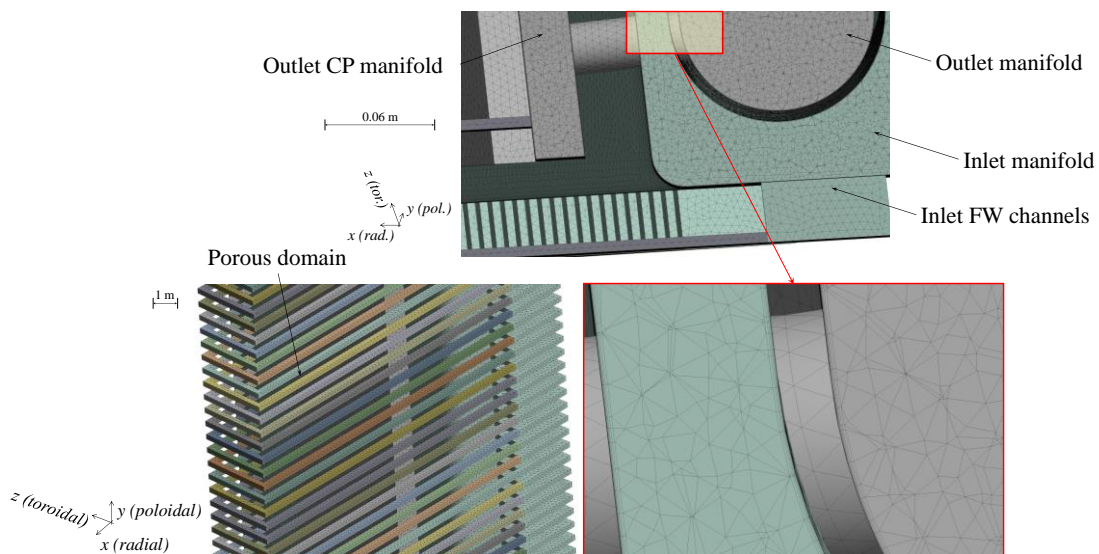


Figure 4.21. Mesh of a parallel coolant loop of the HCPB BSS manifold piping with all the CP represented by means of the porous model.

The coolant flow has been simulated as an isothermal fluid domain with a reference pressure of 8 MPa and a domain temperature of 400 °C. At the inlet boundary of this fluid domain (Figure 4.20), which corresponds to the DN250 OB segment inlet pipe, a relative pressure of 0 Pa has been set. At the outlet, a total mass flow of 17.6 kg/s, corresponding to the half of the total OB segment mass flow has been set [28].

The resistance loss coefficient function has been applied to the porous domain and He gas properties have been given to the fluid domain. The mass flow rate distribution is shown in Figure 4.22. The maximum mass flow rate (0.04242 kg/s) is reached in the first slice of OB3 (the numeration of slices goes from the top to the bottom). While the minimum mass flow rate (0.04105 kg/s) is obtained in slice 52 and 53 of OB7.

The maximum and minimum variation of the mass flow rate of adjacent slices has been calculated as the error between the mass flow rate in a slice and the next one. It has been found a variation ranged between -1.295 % and the 0.553 %. An overall pressure drop of 1.58 bar has been also evaluated.

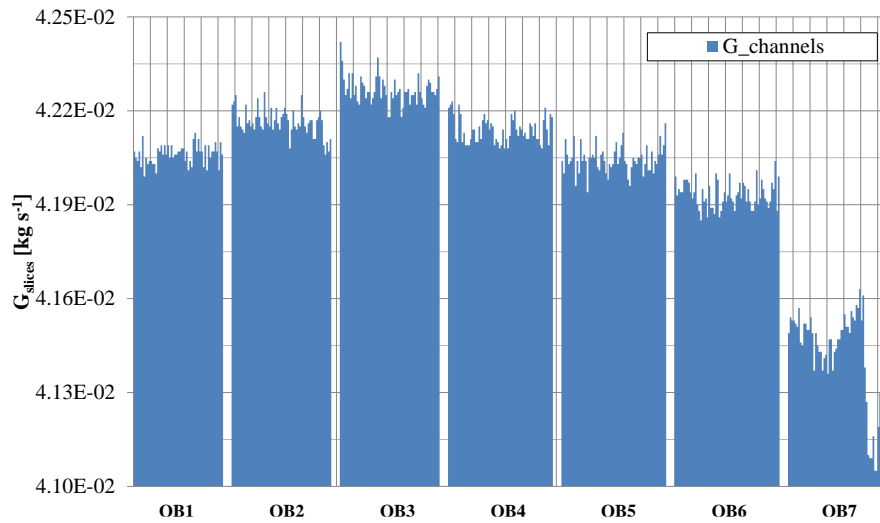


Figure 4.22. Mass flow rate distribution for each module of the OB segment.

The calculated mass flow distribution variation together with the deposited power ones are used for the adequateness verification of the symmetry conditions as discussed in the following.

4.2.1 Adequateness of Boundary Conditions

The variations, encountered on the power deposition as well as on the mass flow rate distribution, define the ranges that a slice within the HCPB BB may face with respect to the neighbouring ones. Therefore, they can be used to define study cases for the consistency verification of the symmetry conditions. For this reason, two CFD models have been set-up. One composed of three adjacent HCPB slices entirely simulated, and one composed of only one HCPB slice where the symmetry conditions are applied on the radial-toroidal surfaces located to the top and bottom of the domain. The scope is to test that the temperature field calculated on the central domain of the 3-slices model is similar to the one calculated in the more simplified model, verifying the applicability of the symmetry conditions (Figure 4.23).

For the model with 3-slices, hexahedral and tetrahedral elements are adopted taking into account the geometrical features of the domains to be meshed and the required optimization of the number of nodes and mesh quality. A conformal mesh between the different domains has been set-up. The mesh is composed of 16.3E+06 nodes linked in 56.7E+06 of elements with an orthogonal quality average of 0.711 and skewness average of 0.281. A number of 8 inflation layers has been used with first layer height of 2.0E-05 m and a growth rate of 1.2. The mesh is shown in Figure 4.23.

The 1-slice model on which symmetry conditions are applied has the same mesh of the central slice (5.4E+06 of nodes and 18.6E+06 of element) in order to allow a comparison node-by-node of the temperature field between the two models.

From the power deposition variation reported in Table 4.4 and Table 4.5 and from the mass flow rate distribution fluctuation calculated on the HCPB segment, 7 cases have been identified for the verification of symmetry conditions:

- Case 0. The three slices experience the same nominal power density and mass flow rates;
- Case 1. It is assumed that the 3 slices are located in the equatorial region of the OB4, therefore the fluctuations reported in Table 4.4 are applied to the up and down slice with respect to the central one where nominal power density is assumed. The mass flow rate in each slice, imposed as an outlet flow, is derived by the local power balance.
- Case 2. Same fluctuations on nuclear heating of Case 1. Minimum variation (-1.295 %) of mass flow rate applied to the up-slice and maximum (0.553 %) on the down-slice.
- Case 3. Same fluctuations on nuclear heating of Case 1. Minimum variation (-1.295 %) of mass flow rate applied to the down-slice and maximum (0.553 %) on the up-slice.
- Case 4. It is assumed that the 3 slices are located near the cap of the OB4, therefore the fluctuations reported in Table 4.5 are applied to the up and down slice with respect to the central one where nominal power density is assumed. The mass flow rate in each slice, imposed as an outlet flow, is derived by the local power balance.
- Case 5. Same fluctuations on nuclear heating of Case 3. Minimum variation (-1.295 %) of mass flow rate applied to the up-slice and maximum (0.553 %) on the down-slice.
- Case 6. Same fluctuations on nuclear heating of Case 3. Minimum variation (-1.295 %) of mass flow rate applied to the down-slice and maximum (0.553 %) on the up-slice.

According to the identified cases, a uniform average power density, calculated from neutronic calculations (paragraph 4.1), has been set-up for each slice region as reported in Appendix 9.4.

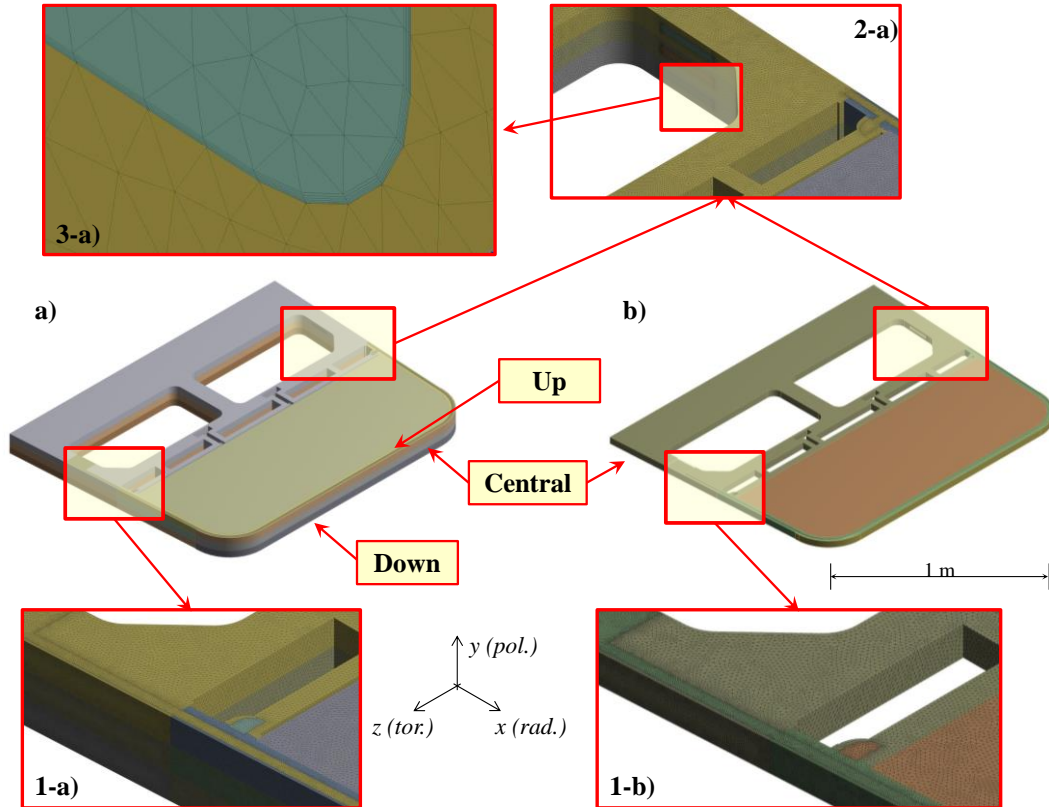


Figure 4.23. Geometry and mesh details of the 3-slice HCPB model and of the 1-slice HCPB used for the consistency verification of symmetry boundary conditions. Central (a): 3-slice HCPB model. Bottom (1-a): mesh detail of the BSS and FW side wall. Top (2-a): mesh detail of the BSS and inlet/outlet channels. Top (3-a): conformal mesh detail between inlet FW channel and BSS structure. Central (b): 1-slice HCPB model. Bottom (1-b): mesh detail of the BSS and FW side wall for 1-slice HCPB model.

A normal heat flux calculated by multiplying the nominal heat flux value of 0.5 MW/m^2 [26, 30] for the cosine of the angle between the radial and the surface normal directions for the OB4 has been also applied.

The 7 cases have been compared with the 1-slice model with symmetry conditions where the nominal power density and mass flow rate is set-up.

The first comparison has been conducted with the Case 0 (Figure 4.24). The deviation in the temperature field between the central slice of the 3-slice model and the 1-slice model with thermal symmetry conditions has been calculated.

The node-by-node error temperature is limited between $\pm 1.2 \%$ with a peak around 0. As expected, this is a demonstration that the symmetry conditions work properly when a symmetric load is applied nearby the domain of investigation. More in general, this outcome provides a reference for the comparison of the other 6 cases.

Indeed, analysing all the results, the cases 4 and 5 have shown the maximum error on temperature fields as reported in Figure 4.25. Even if the variation of the local power density can reach the $\sim 11\%$ (in the Li_4SiO_4 according to the Table 4.5), the maximum temperature error between the single slice with symmetry conditions and the cases 4 and 5 does not exceed the 2.4 % and the 2.0 %, respectively.

Case 4, although the mass flow rate from the local power balance is applied, shows a biggest deviation spread with respect to the reference case 0 as confirmed by the different slope of the cumulative curves (in blue for the Case 0 and green for the Case 4, Figure 4.25). This effect is due to the maximisation of heat flux toward the coolant that produces biggest gradients as it is possible to see in the left tail of the green probability distribution reported in Figure 4.25.

In the case 5, the highest power deposition (up-slice with 5.95% higher power than the central one, Table 4.5) together with the minim variation of the mass flow rate (-1.295 %) produce an asymmetric error with the tail of the distribution shifted towards the 2 %.

In conclusion, the results show a limited variation to few percent of the temperature field when variation on power and mass flow rate are considered.

From a thermal-hydraulic point of view, these fluctuations seem to be acceptable and the applicability of symmetry condition guaranteed also when an overall power deposition variation of 5.95 % is assumed. However, from a thermo-mechanical point of view, the temperature fluctuation could produce the creation of secondary stresses. For this reason, the conclusions on the impact of these variations are postponed to the mechanical analysis.

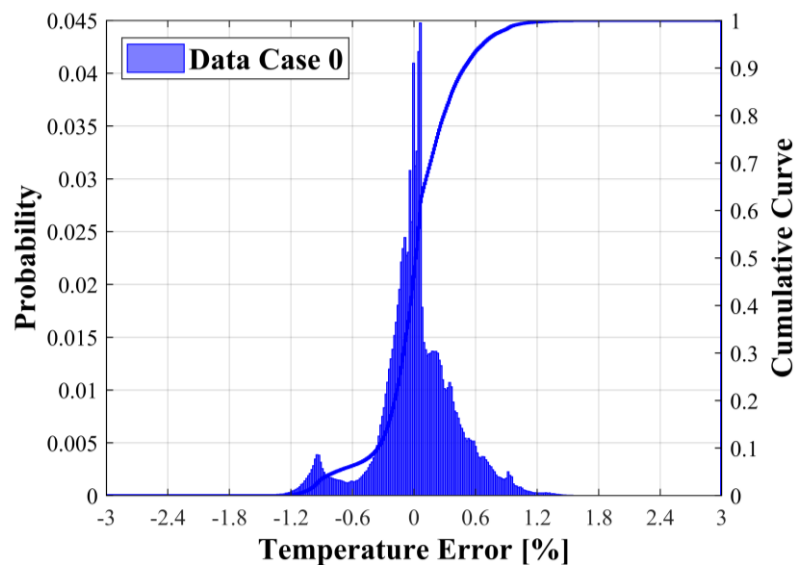


Figure 4.24. Statistical distribution of the error on temperature field between the Case 0 and the slice with symmetry boundary conditions.

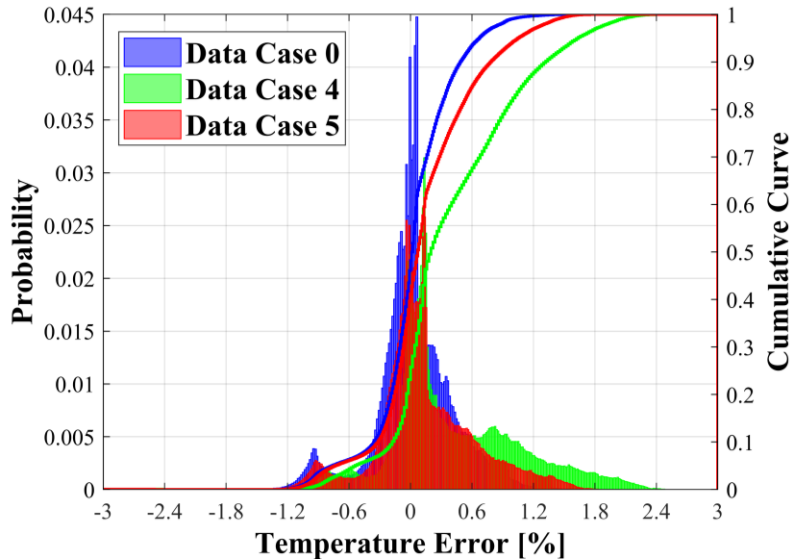


Figure 4.25. Statistical distribution of the errors on temperature fields between the Case 0, 4 and 5 in comparison to the single slice with symmetry boundary conditions.

4.2.2 Sensitivity Analysis of Symmetry Conditions

Once the adequateness of symmetry conditions have been demonstrated from a thermal-hydraulic point of view, some efforts have been dedicated to the sensitivity analysis of symmetry conditions due to statistical variation of power density and mass flow rate.

The scope is to investigate the maximum statistical variation of volumetric heating and mass flow rate such that the null hypothesis of null heat flux to the boundaries (i.e. symmetry) is respected. Indeed, the significance of an input parameter with respect to the output one can be determined by means of statistical hypothesis test.

In this test, it is assumed a null hypothesis of insignificance and it is verified whether, from a statistical point of view, it is true with respect to significance level selected by the user. In order to perform this hypothesis test, a probability value (p-value) has to be calculated and compared with the significance level. If it is greater than the significance level, it means that the null hypothesis is true and the input and output parameters are insignificant to each other.

In order to perform this study, the CFD model with 3 adjacent slices has been used (Figure 4.26 - a).

On this thermal fluid dynamic system composed of three slices, different mass flow rates and power densities have been applied.

In particular, the nominal volumetric heating and mass flow rate have been applied to the central slice. While, on the neighbouring up and down slices, four coefficients (a_{UP} , b_{DOWN} , c_{UP} and d_{DOWN}), distributed following a normal distribution with a standard deviation of 0.06 (Figure 4.26 - b) have been multiplied to the nominal power density and mass flow (Figure 4.26). In this way, it has been possible to variate independently according to a normal distribution all the main parameters that affect the thermal symmetry condition. The value of the standard deviation has been selected in accordance to the overall power deposition variation calculated in Table 4.5 with the aim to test the null hypothesis on the heat flux through the boundary conditions. The coefficients a_{UP} , b_{DOWN} , c_{UP} and d_{DOWN} have been introduced in ANSYS CFX as parameters [59] and their distribution ranged in 201 bins.

Varying these coefficients according to their distribution, a probabilistic analysis by means of Design of Experiments (DoE) has been carried out for each stochastic input to obtain a set of design points used for building a response surface.

This probabilistic approach replaces the finite volume model and allows the estimation of user defined outcomes using an appropriate response function.

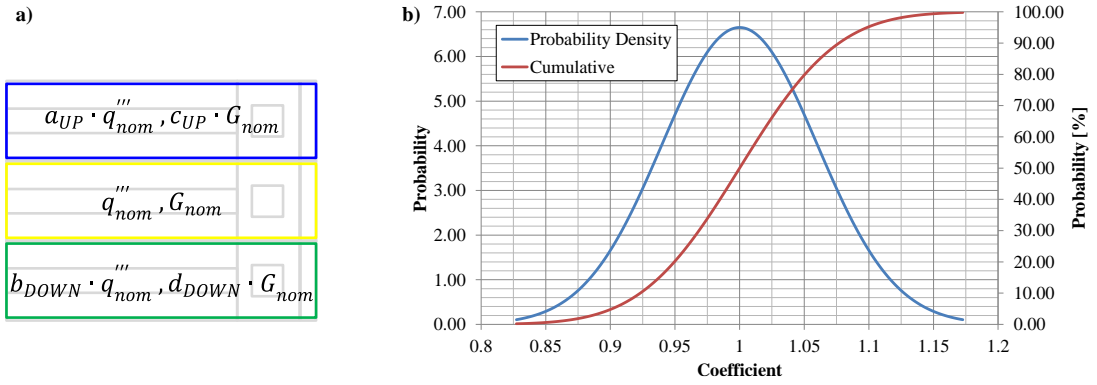


Figure 4.26. Normal distribution applied to the coefficients multiplying the nominal values for the up and down slices. Left (a): schematic view of three adjacent slices and loads applied. Right (b): normal distribution of multiplying coefficients.

In this way, it has been possible to assess the statistical distributions of the heat flux at the boundaries of the central slice according to the variations imposed to the neighbouring slices. The probabilistic functions of the heat fluxes in different regions of the central slice boundaries are reported in Appendix 9.5.

It has to be noted that the use of different coefficients both for the power densities and mass flow rates and both for the up and down slices represent a more stringent condition because of the magnitude of the variation and the contingency of their application that could occur in with different combinations.

In order to verify that the symmetry conditions are valid for variation of volumetric heating and mass flow rates following a normal distribution with a standard deviation of 0.06, it has been decided to apply the t-test for one sample. The t-test is used here to compare the mean of sample data with a known value in order to verify if the mean is significantly different or not from a hypothesized value [97, 98], which in this case is 0, meaning that the sample data is hypothesized (so-called null hypothesis) to belong to an original population of mean 0 and standard deviation 0.06. In this way, if the p-value of the t-test is statistically not-significant, it will be inferred that the symmetry conditions are valid. This procedure works for spaces (e.g., in our case, power and mass flow rate), which have steady, differentiable and smooth solutions, containing no bifurcations or instability. The matching of t-test confirms that there is not any response amplification showing the robustness of the hypothesis.

The application of the t-test involves four steps:

1. Definition of null (μ_0) and alternative (μ_a) hypotheses;
2. Calculation of the t-value according to the following formula:

$$t = \frac{\bar{x} - \mu_0}{\frac{\sigma}{\sqrt{n}}}, \quad (4.5)$$

where \bar{x} is the mean value of the sample, σ is the sample standard deviation and n is the size of the samples.

3. Identification of the p-value for given confidence and degree of freedom (DOF). The DOF are defined as $n-1$;
4. Comparison between the t-value and p-value for the accepting ($-p < t < p$) or rejecting ($t < -p$ or $t > p$) the null hypothesis.

Concerning the first step, for the symmetry conditions, the null hypothesis correspond to the null heat flux at the boundaries, so $q'' = 0$ and then $\mu_0 = 0$. Regarding the second step, the sample mean and standard deviation have been calculated as reported in Appendix 9.5 while the size of samples corresponds to the number of design points (real CFD calculations) used to build the response surface and it is equal to 15. For a selected confidence level of 95 % and DOF of 14, the corresponded p-value is 2.145 according to [99]. Therefore, the results of the t-test application can be found in Table 4.7

Table 4.7. T-test for symmetry condition sensitivity analysis.

| Output Parameters | Mean | Standard Deviation | Null Hypothesis | T-Value | T-Test |
|---|-----------|--------------------|-----------------|---------|--------|
| P23 - Flux BSS DOWN [W m⁻²] | -1.27E+00 | 4.84E+02 | 0 | -0.01 | TRUE |
| P24 - Flux BSS UP [W m⁻²] | 7.82E-01 | 4.66E+02 | 0 | 0.01 | TRUE |
| P25 - Flux Be [W m⁻²] | 1.50E-08 | 8.50E-08 | 0 | 0.66 | TRUE |
| P26 - Flux FW DOWN [W m⁻²] | 1.26E+03 | 3.70E+03 | 0 | 1.27 | TRUE |
| P27 - Flux FW UP [W m⁻²] | 7.11E+01 | 3.36E+03 | 0 | 0.08 | TRUE |
| P28 - Flux Li [W m⁻²] | 5.72E-08 | 1.02E-07 | 0 | 2.10 | TRUE |
| P29 - Flux W DOWN [W m⁻²] | -3.55E+03 | 1.84E+04 | 0 | -0.72 | TRUE |
| P30 - Flux W UP [W m⁻²] | 1.38E+03 | 1.82E+04 | 0 | 0.28 | TRUE |

The results of the t-test reveal that symmetry conditions, for applied loads on the adjacent slices with a standard variation of 6 %, are substantially valid on a confidence level of 95%.

4.3 Consistency Verification of MAIA Thermo-Mechanical Model

The last consistency verification carried out regards to the MAIA thermo-mechanical boundary conditions to be applied in the local models for the simulation of the missing BB parts.

The aim is to find a set of boundary conditions that well approximate the mechanical behaviour of a BB segment and that are able to provide a sufficiently correct estimation of the displacements as well as of stresses. For these reasons, two main methodologies have been followed. The first aimed to the determination of the correct poloidal condition (Plane Strain, PS, or Generalised Plane Strain, GPS) taking into account different domain nodalisations (uniform or castellated tungsten) as well as different temperature fields (uniform or radial gradient temperature). The detailed explanation can be found in paragraph 4.3.1. The second aimed to the investigation of the sensitivity to variations of temperature fields. This last step continues the study of the propagation of uncertainties on power densities and mass flow rates calculated in the preceding paragraphs. The detailed explanation is reported in paragraph 4.3.2.

4.3.1 Consistency Check of Boundary Conditions

In order to perform the consistency verification of boundary conditions described in paragraphs 2.3.1 and 3.5.2, two models have been created. One represents the entire module of the HCPB BB and it is assumed as reference model for comparison. The second one is the local model of an equatorial slice on which the boundary conditions are applied. In Figure 4.27, the two models used in this consistency check are shown.

The module of HCPB has been selected as reference for two main reasons:

- (i) in the multi-module approach, it represents a mechanical unit repeated to form a segment, and
- (ii) it minimises the computational effort maintaining a quasi-heterogeneous nodalisation.

Regarding the second aspect, the selection of HCPB module as reference allows to have a full model where the main characteristics such as the FW and armour structure (their feature have been maintained except for the channel within the FW), the 62 CPs [28] (the cooling and purge gas channels have been homogenised within the each CP) and the real structure of caps (Figure 4.27-a), BP and BSS are represented. In this way, the main features of the HCPB module have been nodalised without increasing excessively the computational effort. The tungsten armour has been also included in the models because of the stress that can arise due to the different thermal expansion with respect to the Eurofer. The materials have been considered homogeneous, uniform and isotropic and their thermo-mechanical properties have been assumed to depend uniquely on the temperature as indicated in [100, 101].

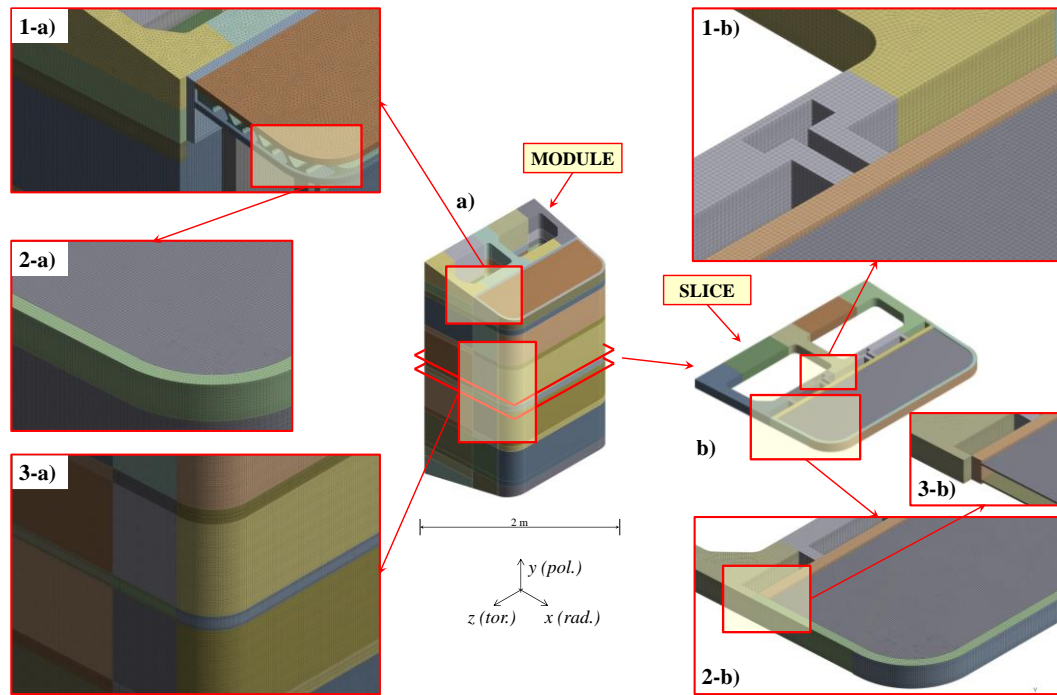


Figure 4.27. HCPB module and slice thermo-mechanical models. Centre (a): thermo-mechanical reference model of HCPB OB4 module. Left-top (1-a): internal Cap mesh detail. Left-centre (2-a): CAP mesh detail. Left-bottom (3-a): FW mesh detail. Centre (b): thermo-mechanical local model of HCPB slice used for consistency check of boundary conditions. Right-top (1-b): BP and BSS mesh detail. Right-bottom (2-b): FW mesh detail. Right-centre (3-b): CPs mesh detail.

Due to the geometrical features of the domains to be meshed, in order to optimise number of nodes and mesh quality, both tetrahedral (for the cap regions) and hexahedral elements have been adopted and, in particular, as to HCPB module model (Figure 4.27-a), a mesh composed of $\sim 24.6E+06$ nodes connected in $\sim 6.7E+06$ elements has been selected, while, concerning the HCPB slice model (Figure 4.27-b), a mesh composed of $\sim 2.5E+06$ nodes connected in $\sim 5.4E+05$ elements has been taken into account.

In order to simulate the mechanical action of the attachment system of both models, the displacements in the radial and toroidal direction have been constrained for those nodes lying on the B-C and A-D edges of Figure 4.28, respectively.

A symmetry condition is applied at the lower cut surface of both models allowing here only displacements on the radial-toroidal plane (Figure 4.28). In the upper cut surface, for the HCPB reference module model, a PS has been imposed on the BSS (red surface of Figure 4.28-a) in order to simulate the rest of segment that has not been simulated.

The PS condition can be applied to the HCPB module because of the uniform temperature and, thus, uniform plane deformation to which the BSS is subjected according to the design calculations [26, 28]. For the HCPB slice, the application of PS or GPS has been investigated (yellow surface of Figure 4.28-b). In order to better understand the impact on the displacements, a uniform temperature of $550\text{ }^{\circ}\text{C}$ has been assumed as first approximation.

In this way, it has been possible to simplify the problem considering a thermal expansion mainly driven by the thermo-physical properties of materials as well as of geometric characteristics. In the second set of analysis, this assumption has been changed and a radial profile of temperature has been used as described in the following.

Once the reference model has been set up, several combinations of boundary conditions have been investigated. In particular, for the first set of analyses, it has been assumed:

- uniform armour plate for the reference HCPB module model (i.e. armour is not castellated);
- uniform temperature of $550\text{ }^{\circ}\text{C}$ for both HCPB module and slice;

- PS applied to the structure and armour (Figure 4.29-a) and only to the structure (Figure 4.29-b);
- GPS applied to the structure and armour (Figure 4.29-c) and two different for structure and armour (Figure 4.29-d);

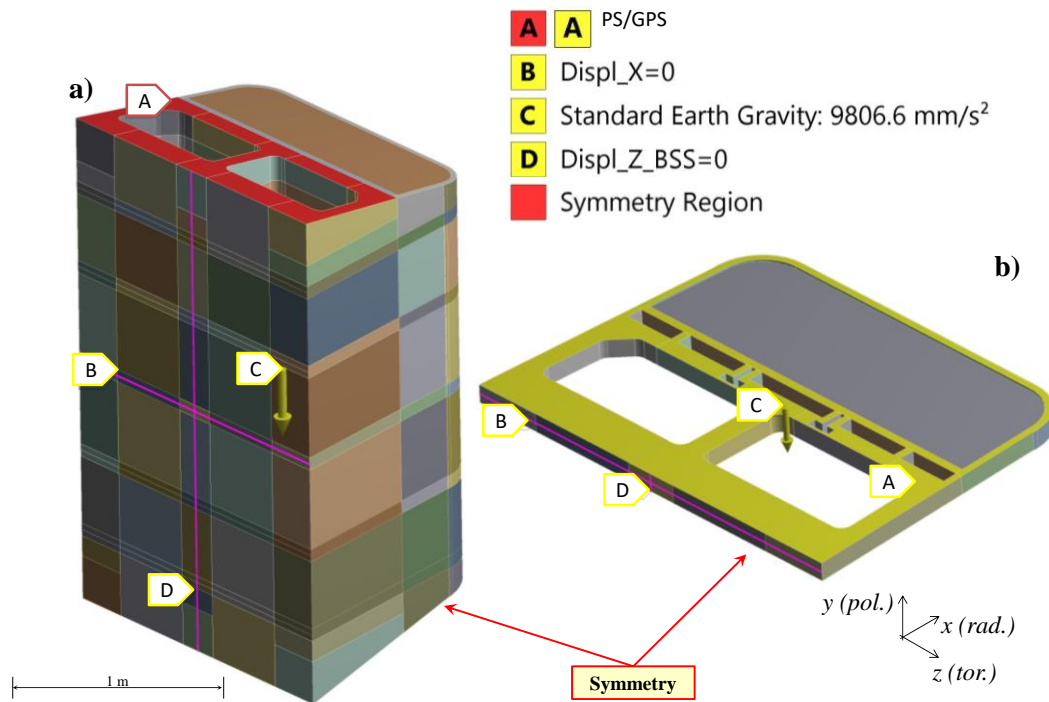


Figure 4.28. Thermo-mechanical boundary conditions for the HCPB module and slice. Left (a): HCPB reference module model with conditions on nodes lying on the BSS and on the top and bottom surfaces. Right (b): HCPB slice model with conditions on poloidal and toroidal nodes of the BSS and in the bottom and up surfaces.

It has to be noted that two PS condition cannot be applied on the same nodes, and, for this reason, the armour of Figure 4.29-b) is without boundary conditions and free to expand according to its thermo-physical properties.

Using the conditions introduced above and for the cases identified, the effects of PS and GPS on the displacements of the local model (i.e. HCPB slice) have been investigated and compared with the ones calculated in the reference model (i.e. HCPB module).

The variables investigated are the deformations that allow an "immediate" feedback on the response to the different constraints. The results for each case, in terms of percentage deviation of the local model with respect to the reference one, are collected in the histograms shown in Figure 4.30 and Figure 4.31.

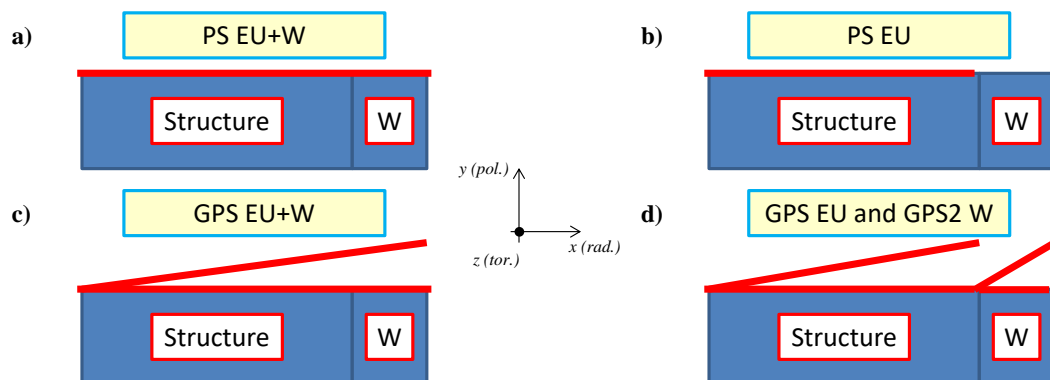


Figure 4.29. Boundary conditions applied to the local model of HCPB slice. Left-top (a): PS on the whole structure and armour. Right-top (b): PS on the structure. Left-bottom (c): GPS condition on structure and armour. Right-bottom (d): different GPS for structure and armour.

Looking to the deviations on radial and toroidal directions (i.e. X and Z, respectively) (Figure 4.30), it seems that no particular differences can be highlighted between the four cases. Indeed, concerning the two cases with PS conditions, the errors are mostly concentrated between $\pm 3\%$ while for the two cases with GPS condition between $\pm 2\%$. For all the cases, only a minority (less than 5% of the total number of nodes) shows errors up to -10% . This effect is localised in the BSS nearby the restraint conditions on the nodes. In this zone, indeed, the displacements are very low (approaching to zero), due to the prevention of the movements in the radial and toroidal direction, and so the errors are higher.

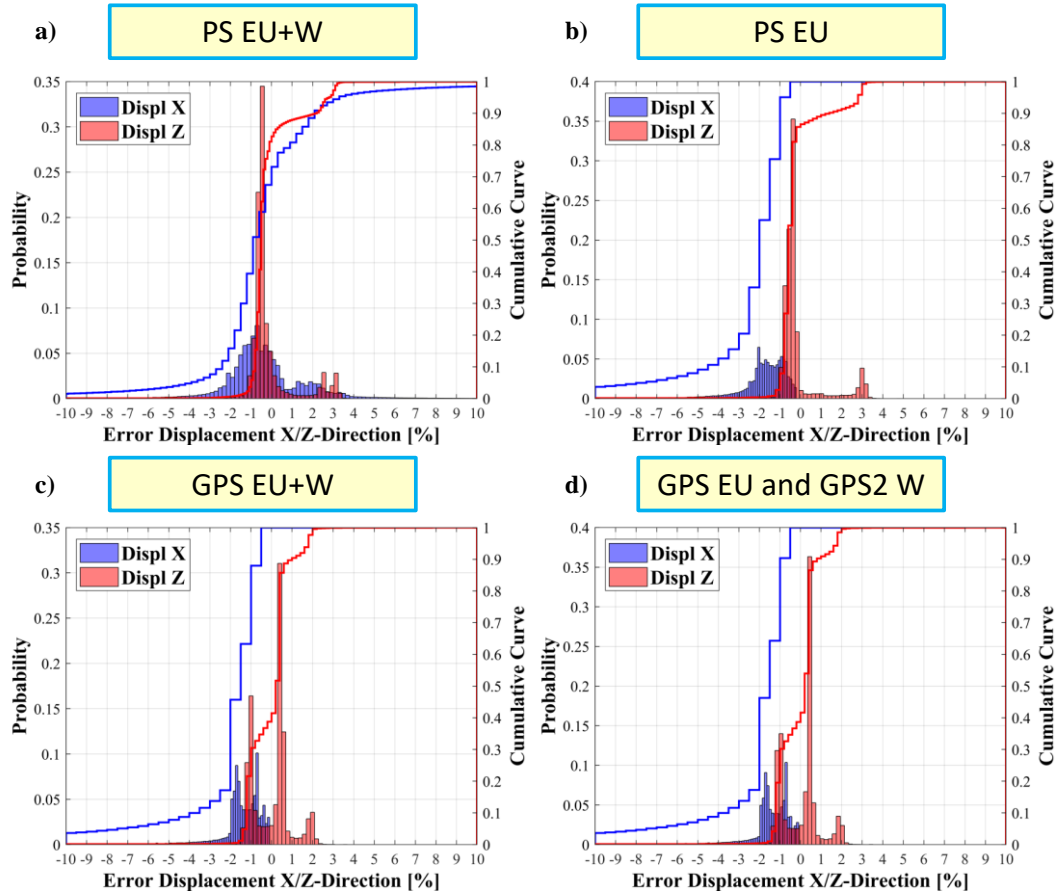


Figure 4.30. Error density distribution and cumulative curve for the displacement along the radial (X) and toroidal (Z) directions for the four local models with different PS and GPS conditions.

However, analysing the errors obtained along the poloidal (Y) direction (Figure 4.31), it is possible to observe that the PS conditions produce errors higher than 10% (Figure 4.31-a and b), while the two cases with GPS embed the errors between the -6% and the 4% (Figure 4.31-c and d). In Figure 4.32, the contour map of the error on the poloidal displacement, for the four cases analysed, is reported.

From Figure 4.32 – a) and b), it is possible to note that the PS produces high errors in the FW zone. This is due to the presence of tungsten that imposes to the first centimetres of FW a different displacement driven by its thermal expansion.

In other words, the PS conditions do not reproduce correctly the displacements given by the differential thermal expansion between Eurofer and tungsten. Indeed, due to the uniform temperature, the most massive BSS drives the dilatation of the entire module and the applicability of PS conditions on the local HCPB slice model seems controversial. On the other side, the GPS conditions allow a better estimation of the poloidal displacement in the local models with respect to the reference one (Figure 4.32 – c and d). Moreover, the error on the poloidal displacement is almost completely enveloped between $\pm 5\%$ demonstrating the better applicability of GPS with respect to the PS conditions.

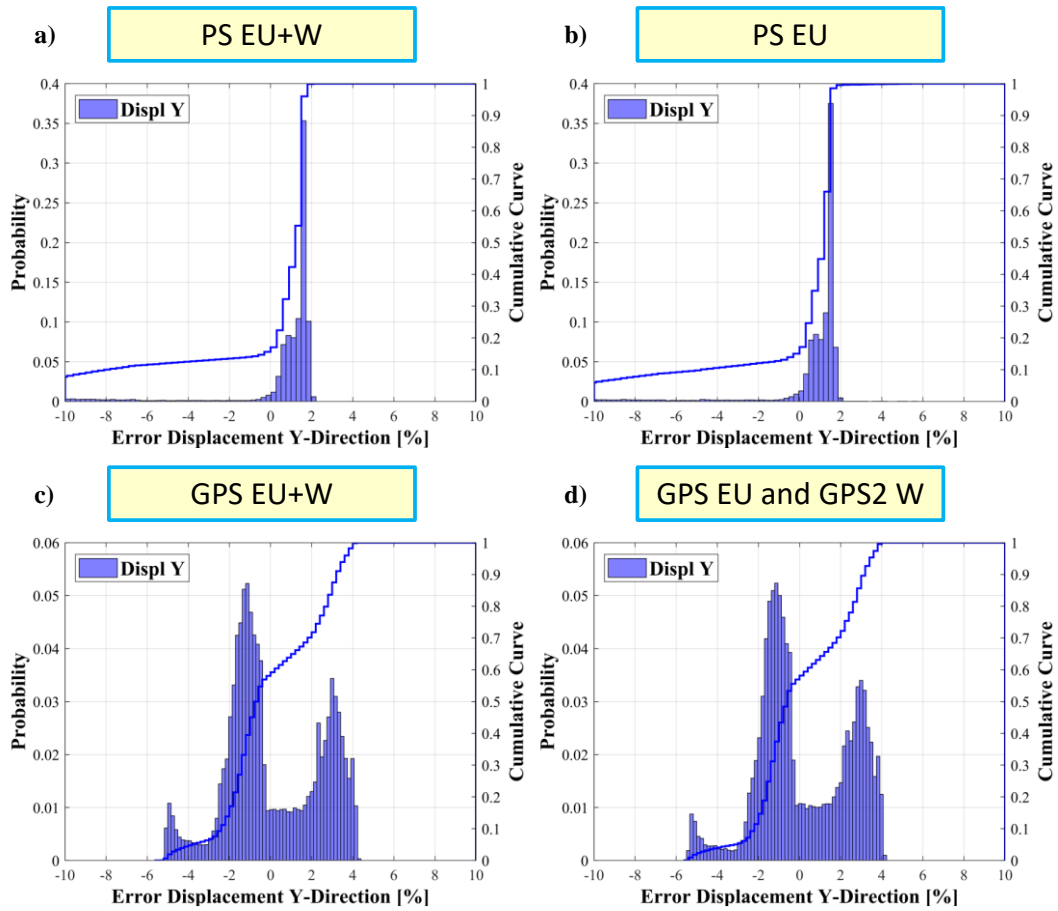


Figure 4.31. Error density distribution and cumulative curve for the displacement along the poloidal (Y) direction for the four local models with different PS and GPS conditions.

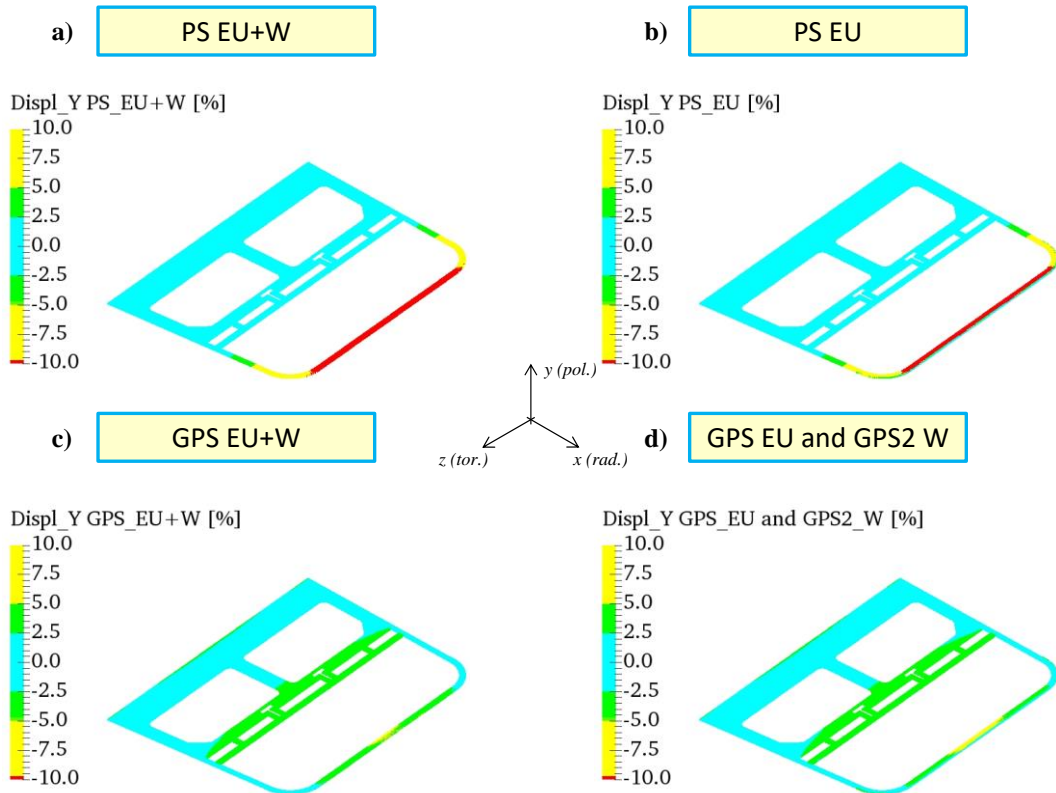


Figure 4.32. Error contour map of the errors on the poloidal displacements for the four cases with different PS and GPS conditions.

In general, this first set of analysis demonstrate also that the presence of tungsten in the thermo-mechanical model produce local effects on the displacements that could affect the correctness of results according to the boundary conditions applied. For this reason, it has been decided to further investigate the answer of the local model on which a GPS is applied with respect to reference HCPB module model with castellated armour.

The assumption of castellated tungsten is justified by the inherent unstable nature of armour surface that, for the temperatures and loads faced under operation, goes to deep cracking (i.e. due to the brittle nature of tungsten is unlikely to have a unique mono-block layer and for this reason a castellation is also taken in account in the design of BB) [102].

A dedicated model has been created to take into account a castellated armour surface (Figure 4.33-a). In this model, the tungsten has not been bonded in the poloidal direction as shown in Figure 4.33-b.

In the local model, the GPS condition has been applied only to the structure as reported in Figure 4.33-c.

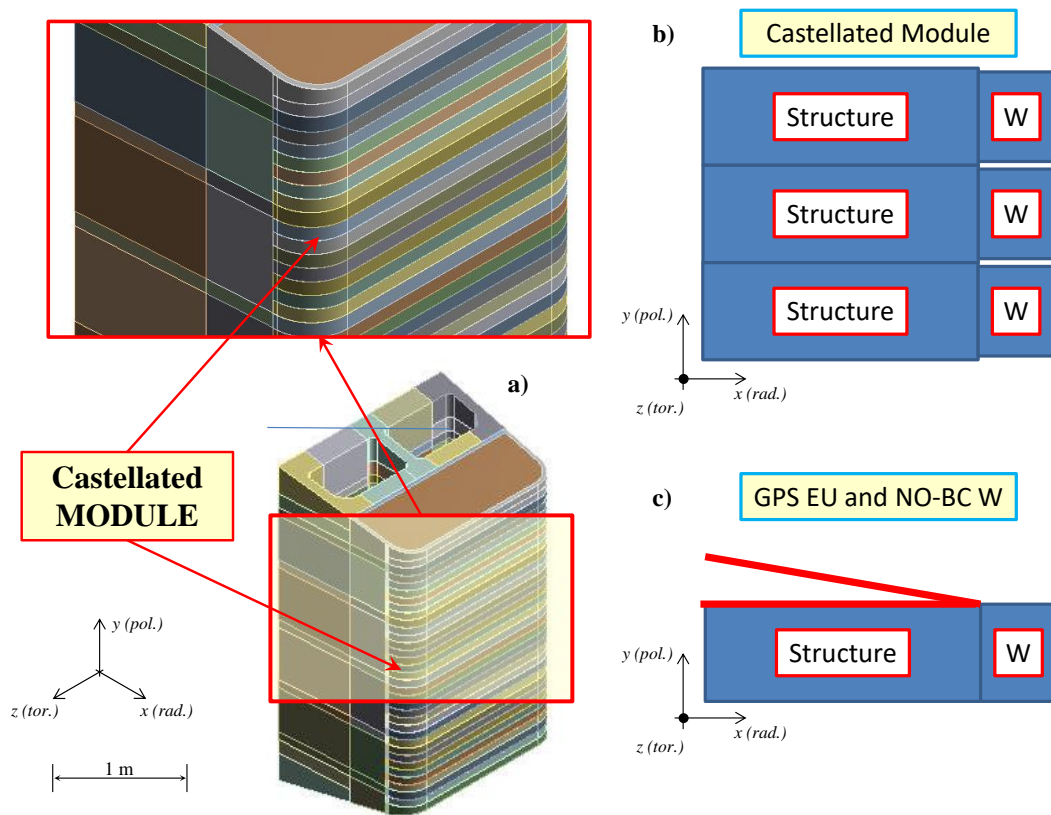


Figure 4.33. HCPB reference module model with castellated tungsten and schematic representation of the reference and local model. Left (a): poloidal castellation of the reference model. Right (b): schematic view of reference HCPB module model with tungsten not bonded in the poloidal direction. Right (c): local HCPB slice model with GPS applied on the structure.

Using the model reported in Figure 4.33-b and c, a comparison between the local model with GPS on the structure and the reference model with castellated tungsten has been carried out.

The results, shown in Figure 4.34, demonstrate that also in this configuration the boundary conditions applied on the local model reproduce faithfully the displacement encountered in the reference module model. It is interesting to note that errors higher than 10 % (Figure 4.34-b) are met at the nodes between the tungsten and Eurofer where a discontinuity in the boundary conditions as well as in the thermal expansions occurs (Figure 4.34-d).

However, these variations are negligible and localised to the interfacing nodes between the tungsten and Eurofer. Therefore, it is possible to conclude that a good agreement in terms of displacements is achieved when the GPS condition is applied to the local models also in case of castellated tungsten of the armour surface.

GPS EU and NO-BC W

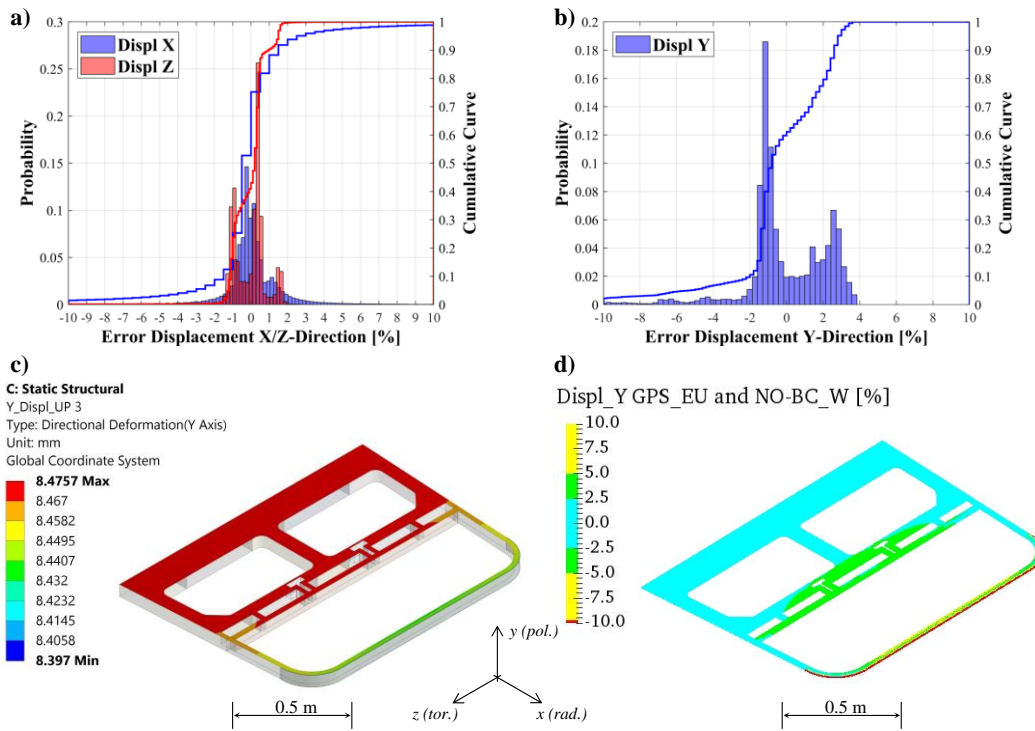


Figure 4.34. Error density distributions and cumulative curves of displacement in X, Y and Z directions. Left-top (a): error histogram of local model with respect to the reference one with castellated tungsten for X and Z directions. Right-top (b): error distribution of local model with respect to the reference one with castellated tungsten for Y direction. Left-bottom (c): poloidal relative displacement in the reference HCPB module model with castellated tungsten. Right-bottom (d): contour map of the poloidal displacement error between the local model with GPS condition on structure and reference model.

Until now, all the investigations have considered a uniform temperature distribution both for the reference and local models and the GPS have been selected as the best condition for approximating the behaviour of reference model with a local one. However, the BB, during its operation, experiences temperature gradients that, as first assumption, are mainly distributed along the radial direction.

For this reason, the applicability of the GPS condition has been also tested when a radial temperature distribution is applied both in the reference and local models.

Therefore, a castellated module model with linear temperature profile that from the FW at 550 °C goes down to 300 °C at the BP and remains constant at 300 °C in the BSS has been set-up. The same temperature distribution has been applied to the HCPB slice model with GPS only on the structure. This profile has been selected in accordance to the design calculations reported in [26, 28] that show a BSS at the uniform temperature of 300 °C and almost linear increment up to 550 °C at the FW.

The displacement error results are reported in Figure 4.35. It is possible to note that, when a temperature profile is applied, the errors on the local model near the node restraints increase up to $\pm 20\%$ in the radial direction (Figure 4.35 – a and d). Indeed, the displacements of the nodes on the BSS lying in the toroidal direction are prevented with respect to the radial direction. This means that the neighbouring nodes are strongly affected by the constraints and the displacements are very small. This produces big oscillation around zero and so highest errors. In general, it is possible to see that the errors in the entire slice are comprised between $\pm 5\%$ (Figure 4.35 – d). Regarding the toroidal direction, the displacements are completely enveloped between $\pm 4\%$ with tails up to $\pm 12\%$ in the middle where the displacements approach to zero (Figure 4.35 – a). Concerning the poloidal displacements, the variation between the reference and local model are comprised between -16% and 20% (Figure 4.35 – b). The highest errors are near the FW bends and in the centre-back of the BSS where the restraints are applied.

In general, also when a temperature profile is considered, the GPS condition is able to approximate the behaviour of the reference model in terms of displacement although largest variations are encountered.

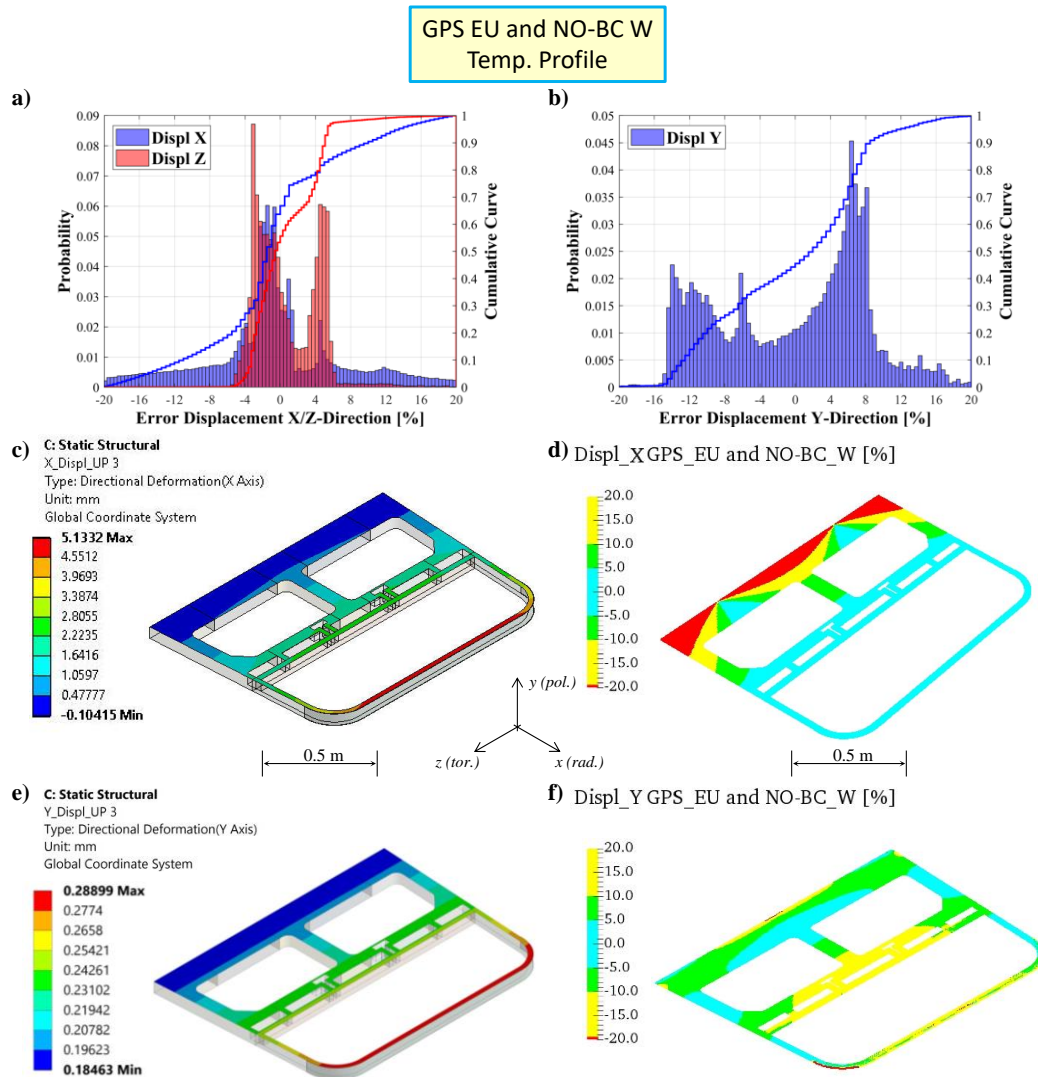


Figure 4.35. Displacement error comparison when a temperature profile is applied. Left-top (a): error density and cumulative curve for displacements along X and Z directions. Right-top (b): error density and cumulative curve for displacement along Y direction. Left-centre (c): reference displacements along X direction. Right-centre (d): contour map of the error along X direction. Left-bottom (e): reference displacements along Y direction. Right-bottom (f): contour map of the error along Y direction.

Until now, all the studies have been devoted to the verification of displacements comparing the results of the local model with the ones of the reference model. This approach has been justified also by the selection of the boundary conditions under investigation that, practically, act directly on the displacements of the nodes on the boundaries.

However, in thermo-mechanical analysis, in addition to the displacements, the stresses are also calculated and they are, then, compared with the design criteria of C&S.

Furthermore, it is possible to identify two “classes” of stress, namely primary and secondary.

Primary stresses (indicated with P) arise from the application of mechanical loads (e.g. pressure) and satisfy the force and moment equilibrium. They are not self-limiting and usually are also defined as load controlled stresses because, for an increasing mechanical load, they will continue to increase in direct proportion to the applied mechanical load until the failure of the component. Secondary stresses (indicated with Q) arise from geometric discontinuities due to the application of thermal loads (e.g. temperature) or, more in general, due to loads inducing volumetric deformations (e.g. swelling). They are also defined as

self-limiting stresses, because, once the yield point is reached locally, there is not anymore a direct relationship between the load and the stress [103].

For both primary and secondary stress, it is possible to evaluate a stress tensor as function of space and time (see eq. (2.41)) and define the normal and shear stresses.

In the next, the discussion will focus on the secondary stress because, so far, only thermal loads in terms of temperatures have been taken into account for the consistency check of MAIA thermo-mechanical boundary conditions. Later on, the primary stress will be also investigated.

Using the castellated reference model with a radial temperature profile of the HCPB module and the local model of the HCPB slice with GPS on the structure, it has been calculated the unaveraged (i.e. assessed on ipn without to apply any interpolation as well as shape function) stress field for each normal and shear tensor component for both models. These have then been compared one-by-one with the stress tensor component evaluated on the reference HCPB module and the results, in terms of errors, have been reported on histograms of Figure 4.36.

It has to be noted that each stress tensor component presents a wide number of nodes where the values approach to zero (see Appendix 9.6, from Figure A.10 to Figure A.12). This produces big variation on small values hiding the errors related to the biggest stress value that, of course, are of highest interest.

For this reason, in order to minimise the background noise given by big variation on small values, it has been decided to neglect the stresses comprised between ± 10 MPa.

The results, shown in Figure 4.36 for error of normal and shear stress tensor component, demonstrate a general agreement between the local and reference model with peaks almost comprised between $\pm 20\%$. However, looking better to the cumulative curve, it is possible to see that a not negligible fraction of variation reach higher errors.

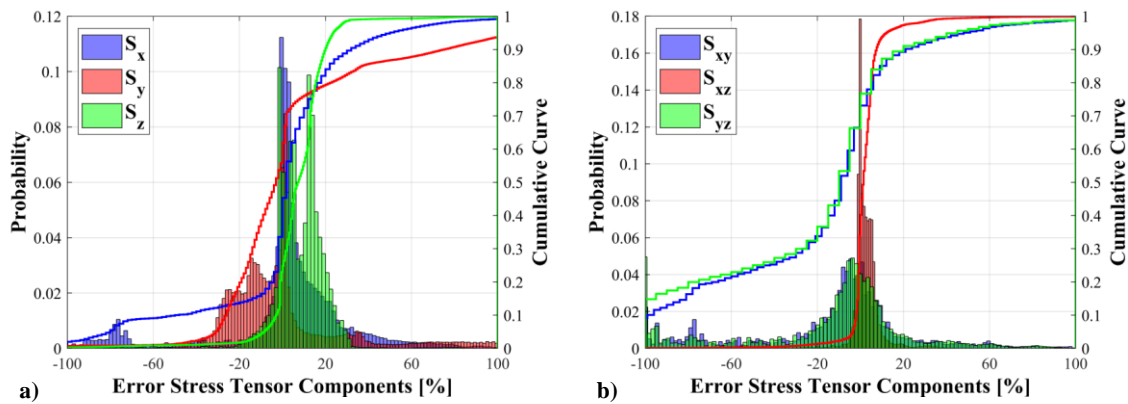


Figure 4.36. Error densities of normal and shear stress tensor components and cumulative curves. Left (a): histograms and cumulative curves of normal stress tensor. Right (b): histograms and cumulative curves of shear stress tensor.

This aspect seems in contrast with the most promising results obtained on the displacements (see Figure 4.35). However, two main arguments can be carried on for the understanding of these results:

- (i) the GPS conditions act directly on the displacements of the nodes lying on the boundaries; and
- (ii) the variation on the displacements along the three directions, although small, are summed through the strain-displacement equations (see (2.45)) and averaged through the Poisson module (see eq. (2.46) and (2.47)) producing a propagation of the error and, consequently, high errors on the stresses.

For these reason, the histograms and contour map of the stress component errors provide only a rough estimation of the adequateness of the GPS conditions as well as of the conservatism of the obtained results with the local model. In order to exit from the *impasse*, it has been decided to use the procedure of stress

verification reported in C&S like RCC-MRx [104] and SDC-IC [105] currently used for the design of BB [106, 107].

Indeed, the data obtained from the resolution of the thermo-mechanical problem cannot be directly used for the verification or design of the various components, due to the triaxial tension state that is established. To overcome this problem, the various regulations have used the so-called equivalent stress, determined by means of a resistance criterion (e.g. Von Mises, Tresca), and a procedure for classifying the stresses. The Von Mises formula for calculating the equivalent stress σ_{eq} is reported in eq. (4.6) [104, 105] as follows

$$\sigma_{eq} = \sqrt{\frac{(\sigma_{xx} - \sigma_{yy})^2 + (\sigma_{yy} - \sigma_{zz})^2 + (\sigma_{zz} - \sigma_{xx})^2 + 6(\sigma_{xy}^2 + \sigma_{yz}^2 + \sigma_{zx}^2)}{2}}. \quad (4.6)$$

Moreover, regarding the stress classification, the C&S subdivides the primary and secondary stresses as follows [104, 105]:

- General Membrane stress (P_m or Q_m). They represent the average value in the stress section caused by loads in areas distant from discontinuity.
- Local Membrane stress (P_L or Q_L). They represent the average value in the section of the stresses always caused by external loads, but in correspondence with a discontinuity of the structure.
- Bending stress (P_b or Q_b). They are the variable component, in the section, of the stresses caused by external loads in areas far from discontinuities.
- Peak stress (F). They are additional to the primary and secondary stresses and represent the stress concentration due to local discontinuities or localized thermal gradients. They do not cause significant structure distortions but are the most likely cause of fatigue failure.

In order to calculate the above mentioned stresses, a line integration through the thickness of the single layer homogeneous structure is used. This line is defined as supporting line segment and it is perpendicular to the mid-surface of the structure and the length equals to the wall thickness (l).

In Figure 4.37, the five supporting lines (i.e. paths), for the determination of the membrane and bending equivalent stresses, are shown.

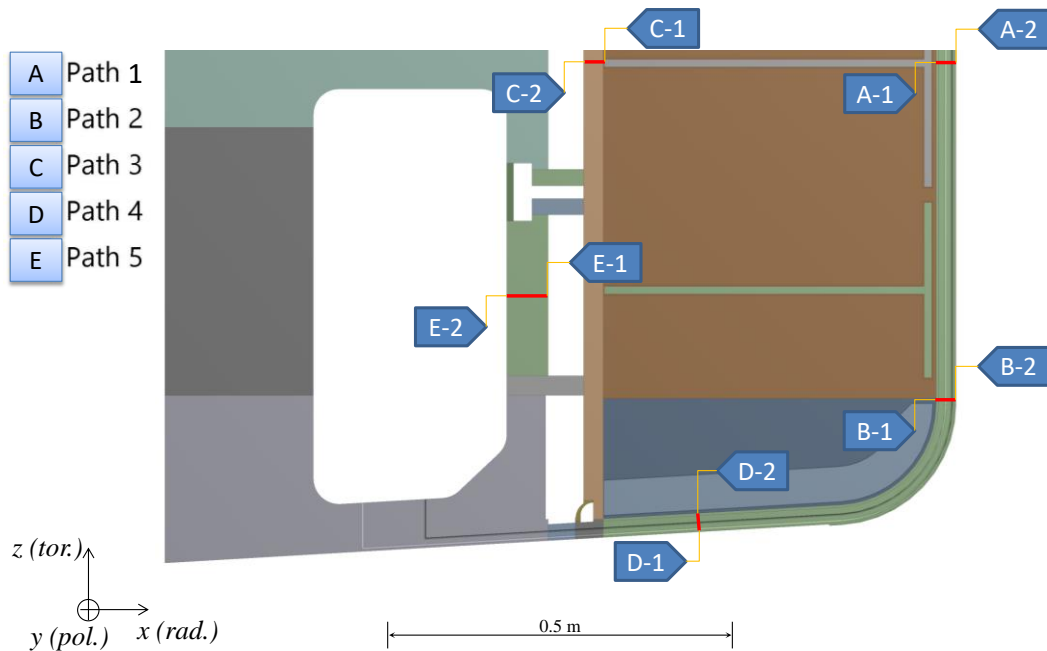


Figure 4.37. Supporting lines of paths identified for the determination of membrane and bending equivalent stresses in the reference and local models.

On those paths, the components of membrane and bending stress tensor have been calculated.

The components of the membrane stress tensor, $(\sigma_{ij})_m$, are defined as the mean value of the σ_{ij} stresses, introduced in (2.41), along the path (l) considered [105]

$$(\sigma_{ij})_m = \frac{1}{l} \int_{-\frac{l}{2}}^{\frac{l}{2}} \sigma_{ij} dx. \quad (4.7)$$

The components of the bending stress tensor, $(\sigma_{ij})_b$, are defined as components varying linearly along the path and having the same bending moment of the stress tensor σ_{ij} [105]

$$(\sigma_{ij})_b = \frac{12x}{l^3} \int_{-\frac{l}{2}}^{\frac{l}{2}} \sigma_{ij} x dx. \quad (4.8)$$

Using the path identified in Figure 4.37 and the definition of membrane and bending stresses reported in eq. (4.7) and (4.8), it has been possible to estimate the general membrane and bending secondary stress both for the reference HCPB module and for the local HCPB slice models.

The membrane and bending component values for each path are reported in Appendix 9.6, from Table A.15 to Table A.19. In Table 4.8, the equivalent membrane and bending stresses, calculated according to eq. (4.6) for each path of HCPB module and slice, are shown.

The equivalent membrane and bending stress calculated on the local model are over conservative except for the path4 where the stresses are slightly below the one calculated in the reference model. It is important to underline that, where the stress are very high (e.g. path1 and path2) the local model with GPS boundary conditions is always conservative with respect to the reference one.

Furthermore, the equivalent stresses calculated in the BSS (path5) are several times higher in the HCPB slice with respect to the module. This is due to the proximity of boundary conditions in the back (restrained nodes) and in the bottom and top surface of the BSS (symmetry and GPS conditions).

Moreover, it is important to note that the trends, in terms of variation from one path to another, are coherently reproduced in the local model. This means that MAIA can be used as a preliminary thermo-mechanical design tool because it allows to find the differences, in a reliable way, between different layouts and/or different load scenarios and, therefore, to be able to choose some solutions over others.

In general, considering that the equivalent stresses are used for the verification of the design criteria reported in C&S, it is important to demonstrate that the results obtained with local model are conservative and the verification, then, of the local model ensure the verification of biggest models.

The Table 4.8 provides also a first estimation of the accuracy on secondary equivalent membrane and bending stresses calculated in local models.

Table 4.8. Equivalent membrane and bending secondary stress for each path of HCPB module and slice.

| Equiv. Stress (Von Mises) | Module_Slice | | Slice_GPS_EU | | Membrane Error | Bending Error |
|------------------------------|-------------------|------------------|-------------------|------------------|-------------------|------------------|
| | Membrane [MPa] | Bending [MPa] | Membrane [MPa] | Bending [MPa] | | |
| Path1 | 286.93 | 48.65 | 382.23 | 50.06 | -33.21% | -2.90% |
| Path2 | 305.16 | 49.32 | 363.59 | 49.93 | -19.15% | -1.24% |
| Path3 | 78.28 | 9.98 | 116.39 | 13.05 | -48.69% | -30.82% |
| Path4 | 66.31 | 4.75 | 59.88 | 4.57 | 9.69% | 3.84% |
| Path5 | 16.38 | 13.26 | 97.15 | 17.78 | -493.08% | -34.05% |

The consistency verification, until now discussed, has demonstrated that the use of local model with the set of boundary conditions is conservative in terms of secondary equivalent stresses.

The last step, for completing a consistency check of the thermo-mechanical boundary conditions and for providing a complete overview of all the aspects, involves the primary stresses.

For the determination of this last contribution, a dedicated analysis has been carried out considering the over pressurisation load case [26]. In this load combination, it is assumed that, as a consequence of In-box LOCA (Loss Of Coolant Accident), the module BZ, where usually there is the purge gas at low pressure, is pressurised at 8 MPa. The decision to investigate this case is based on two considerations:

- (i) the module used until now as reference has homogenised CP so it is not possible to consider the internal pressure during a normal operation scenario; and
- (ii) the In-box LOCA represents one of the design driving load case currently used for the conception of BB.

A dedicated reference model has been created imposing the boundary condition already used in the previous calculation and a pressure of 8 MPa for all the internal surfaces of the box (Figure 4.38-a).

Regarding the local HCPB slice model, it has been used the set of boundary condition already verified for the secondary stresses (GPS on the up structure surface, symmetry on the bottom surface and node restraints at BSS) with the addition of two pressure load contributions.

One pressure load (highlighted in red in Figure 4.38-b) is intended for simulating the In-box pressure that directly acts on the internal surfaces of the slices.

The second one (highlighted in green in Figure 4.38-b) is applied in order to take into account the presence of closed surfaces in the caps region that produce a normal component on the equatorial slice. Indeed, considering that the sub-model cut in the middle two beds, it is missing a force component in the poloidal direction derived by the closure of these surfaces and by the application of the pressure. This contribution can be considered imposing a pressure load of ~51 MPa on the resistant section (S_{res}) highlighted in green in Figure 4.38-b. It has been calculated multiplying the in-box pressure of 8 MPa for the ratio between the internal surface of cap, S_{cap} , and the resistant section surface ($6.33E+05 \text{ mm}^2$ for S_{cap} and $9.90E+04 \text{ mm}^2$ for S_{res}). This load has to be applied as two tensile pressure acting in the opposite direction on the two resistant sections (Figure 4.38-b).

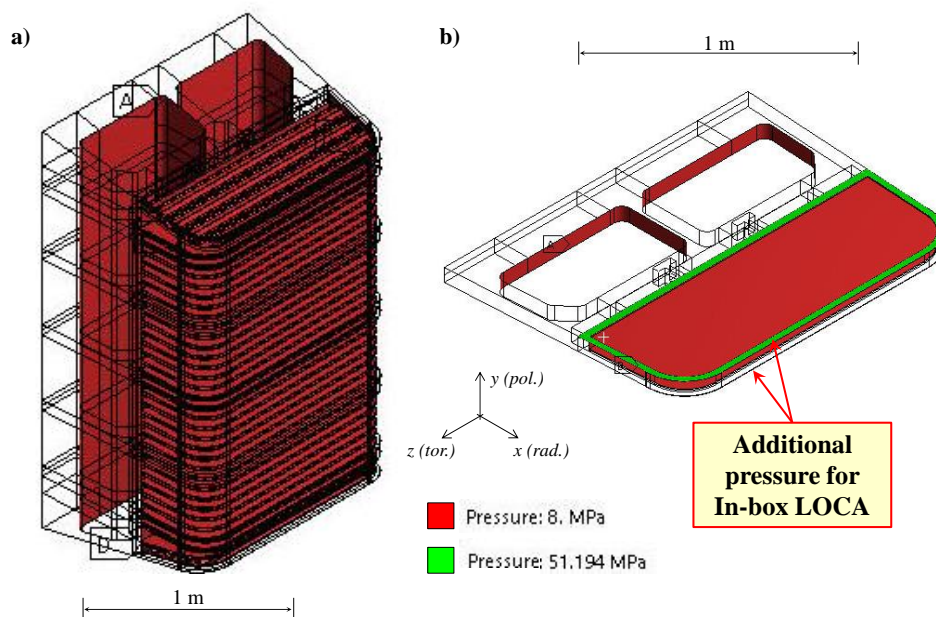


Figure 4.38. HCPB reference module and slice models for the over pressurisation scenario with details of pressure loads. Left (a): pressure load of 8 MPa applied to the internal surfaces of the HCPB module. Right (b): pressure loads due to the internal pressurisation and closed cap surfaces.

Therefore, the primary stress tensor for both reference and local models has been calculated and a comparison component by component has been performed. As done for the secondary stresses tensor components, the stresses comprised between ± 10 MPa have been neglected in order to improve the readability of the histograms removing the background noise due to big variations on small values. Furthermore, filtering the data considering a threshold of ± 30 MPa, the peaks on the tail disappear completely and the errors concentrate around zero.

The results are shown in Figure 4.39 while the reference values for each tensor component and the error contour maps are reported in Appendix 9.6 from Table A.25 to Table A.29.

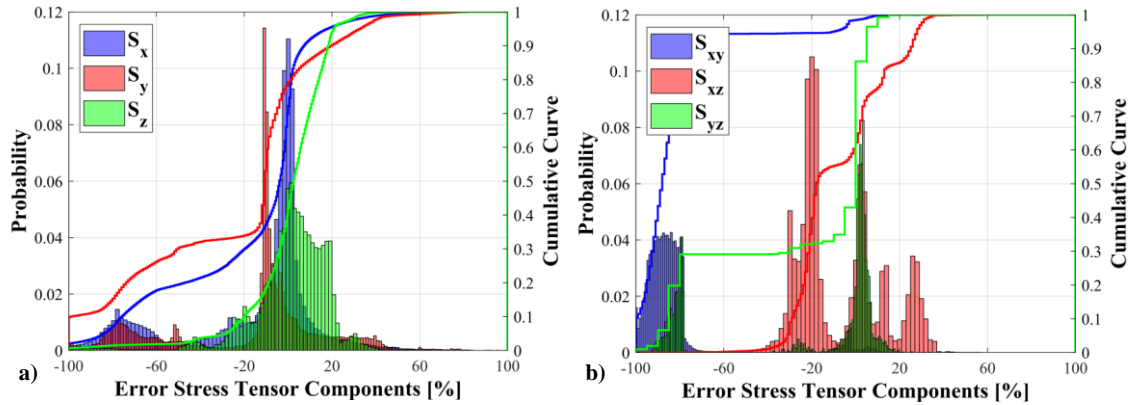


Figure 4.39. Error densities of normal and shear primary stress tensor components and cumulative curves. Left (a): histograms and cumulative curves of normal primary stress tensor. Right (b): histograms and cumulative curves of shear primary stress tensor.

It is possible to see that the variations are very big also for the primary stresses due to the big scatter of relatively small values. As for the secondary stress, the histograms and contour maps of the stress component errors cannot be used for fine assessment of the result quality of the local model. For this reason, the stress linearization has been performed following the procedure already explained for the secondary stress. The results are reported in Table 4.9. The membrane and bending component values for each path are reported in Appendix 9.6, from Table A.20 to Table A.24.

Table 4.9. Equivalent membrane and bending primary stress for each path of HCPB module and slice.

| Equiv. Stress (Von Mises) | Module_Slice | | Slice_GPS_EU | | Membrane Error | Bending Error |
|------------------------------|-------------------|------------------|-------------------|------------------|-------------------|------------------|
| | Membrane [MPa] | Bending [MPa] | Membrane [MPa] | Bending [MPa] | | |
| Path1 | 51.06 | 1.70 | 51.42 | 1.39 | -0.71% | 18.14% |
| Path2 | 43.71 | 4.43 | 41.68 | 4.74 | 4.64% | -6.80% |
| Path3 | 12.66 | 1.90 | 19.77 | 1.55 | -56.09% | 18.32% |
| Path4 | 47.63 | 4.93 | 49.35 | 4.94 | -3.62% | -0.33% |
| Path5 | 8.42 | 49.71 | 14.00 | 49.31 | -66.38% | 0.81% |

The analysis of Table 4.9 shows that also for the primary equivalent stresses, the local model is almost always over conservative with respect to the reference HCPB module model. Only few equivalent stress results are lower in the HCPB slice. Namely, the membrane stress on path2 that is 41.68 MPa compared to 43.71 MPa of the module and bending stresses of path1, 3 and 5 that are 1.39, 1.55 and 49.31 MPa compared to 1.70, 1.90 and 49.71 MPa of reference model. These variations are limited and negligible, therefore it is possible to conclude that regarding the primary stresses the local model imposing the chosen boundary conditions approximates the reference model with credible reliability.

In conclusion, the set of boundary conditions (GPS on the up structure surface, symmetry on the bottom

surface and node restraints at BSS), defined for the thermo-mechanical analysis of local model, reproduce faithfully the behaviour of reference model in terms of displacements and, albeit to a lesser extent, stresses.

Furthermore, the local models result more conservative than reference one providing a highest safety factor for the designers.

4.3.2 Sensitivity Analysis of Deformation and Stress Fields

In the paragraph 4.2.1, it was analysed the variation of temperature field fluctuations on power densities and mass flow rates in the adjacent slices. Using a power density variation comprised between 0.01 % and 0.11 % for the equatorial slice and between -5.95 % and 0.56 % for the slice near the cap (Table 4.4 and Table 4.5) and considering the mass flow rate distribution fluctuation (-1.295 % and 0.553 %) calculated on the HCPB segment, 7 cases have been identified (paragraph 4.2.1). They have been then compared with the 1-slice model with symmetry conditions where the nominal power density and mass flow rate have been set-up. Therefore, considering the highest temperature fluctuations, four temperature fields have been derived: one from the 1-slice model with symmetry conditions, one for the Case 0 that represent the reference for the other 6 cases, and two for Case 4 and 5, respectively, where the biggest temperature variations occur.

These four temperature fields have been used as thermal load for sensitivity analysis on deformation and stress fields. The model used for performing this study represents the real geometry of HCPB slice.

Due to the geometrical features of the domains to be meshed, in order to optimise number of nodes and mesh quality tetrahedral elements have been adopted and, in particular, as to HCPB slice model, a mesh composed of $\sim 7.1E+06$ nodes connected in $\sim 4.4E+06$ elements has been selected.

In order to simulate the mechanical action of the attachment system, the displacements along the radial direction are prevented to the nodes lying on the toroidal direction as well as toroidal displacements are prevented to nodes lying along poloidal direction (Figure 4.28). A symmetry condition is applied at the lower cut surface of both models allowing here only displacements on the radial-toroidal plane (Figure 4.28). In the upper cut surface, a GPS has been imposed as discussed in the previous paragraphs.

Four different thermal analyses have been performed and the results both in terms of total displacements and equivalent stresses have been calculated and compared. The results are shown in Figure 4.40.

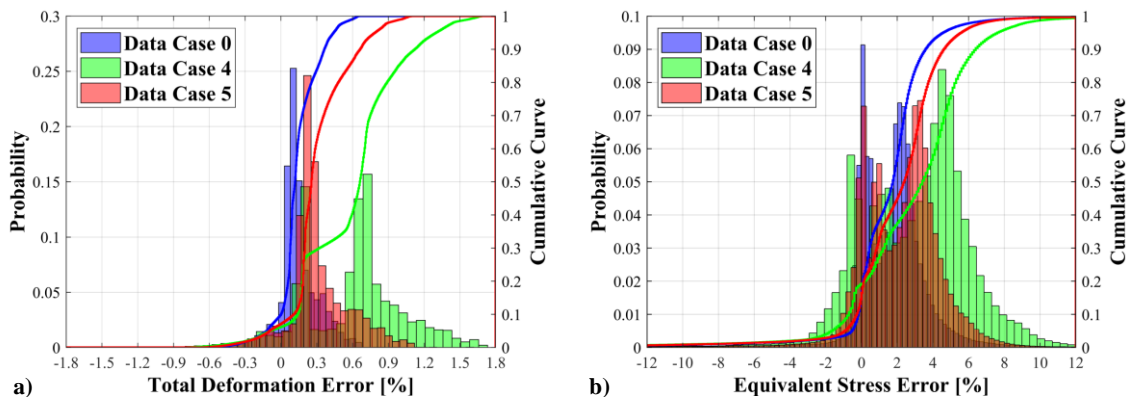


Figure 4.40. Error densities of total deformation and equivalent Von Mises secondary stress tensor and cumulative curves. Left (a): histograms and cumulative curves of total deformation vector. Right (b): histograms and cumulative curves of equivalent Von Mises secondary stress tensor.

The small variations on temperature field, like found in Figure 4.25, produce relatively low variations on total deformation. Indeed for the reference scenario (Case 0), on which the deformation derived from the temperature field of 1-slice model is compared with the deformation obtained applying the temperature field of Case 0, it is possible to see that the total variation on the deformation are comprised between -0.3 % and 0.6 % (blue histogram of Figure 4.40-a). It is interesting to note that the Case 4, in addition to have

larger variations (from the -0.3 % to the 1.7 %, green histogram of Figure 4.40-a), presents a second peak at 0.6 % that is fully in agreement with the temperature peak shown in Figure 4.25.

As expected the temperature fluctuation are directly proportional to the deformation.

Looking to the equivalent stress variations reported in Figure 4.40 – b, it is possible to observe that in 90% of the cases the error associated is comprised between -3 % and 7 % with a small protruding tail for the Case 4.

As done previously and with reference to the Figure 4.37, the stress linearization has been applied also to this sensitivity study.

In Table 4.10, the comparison of equivalent membrane and bending stresses for each identified path is reported.

Table 4.10. Equivalent membrane and bending stress for each case study.

| Equiv. Stress (Von Mises) | Case0 | | Case4 | | Case5 | |
|------------------------------|-------------------|------------------|-------------------|------------------|-------------------|------------------|
| | Membrane Error | Bending Error | Membrane Error | Bending Error | Membrane Error | Bending Error |
| Path1 | -10.71% | 4.89% | -15.15% | 4.62% | -11.86% | 4.62% |
| Path2 | -2.20% | 4.54% | -2.44% | 4.20% | -2.83% | 4.27% |
| Path3 | -1.81% | -1.42% | -5.00% | -3.93% | -3.47% | -2.64% |
| Path4 | -1.90% | -2.14% | -3.81% | -2.93% | -2.47% | -2.80% |
| Path5 | -0.43% | -2.70% | -1.23% | -7.00% | -0.90% | -4.69% |

The Case 0 represents the comparison between the stress field derived by the 1-slice model with symmetry conditions where the nominal power density and mass flow rate is set-up and the one obtained when three slices experience the same nominal power density and mass flow rates.

This case indicates that the application of thermal-symmetry conditions produce variations on equivalent membrane secondary stress up to -10.71% of the FW where the highest fluctuation occur.

Regarding the equivalent bending secondary stress the maximum error is 4.89 %. For the Case 0, relatively small variations are encountered in all the other paths.

The Case 0 can be used as reference scenario for comparing the Case 4 and 5 (these cases take into account the power fluctuation calculated in the neutronic analysis and mass flow rate variation on the BSS).

It is possible to note that the equivalent membrane stresses increase lightly with a maximum increment of ~4.5 % with respect to the Case 0 (membrane error of Case 4 path1, Table 4.10). For all the other paths of Case 4 and 5, very limited fluctuations have been found.

In conclusion, from the sensitivity analysis, it is possible to argue that the variation of the temperature fields produces fluctuations on total deformation comprised between -0.3 % and the 1.7 %, on equivalent membrane stress up to 15 % while on equivalent bending stress between the -7 % and the 5 %. These deviations, if compared to the ones calculated on the primary and secondary stresses, put an additional factor of ~10%, which is marginal.

5 Application of the MAIA Procedure for the HCPB Breeding Blanket Test Case

In this Chapter, the application of MAIA procedure to the HCPB slice is reported. The three main pillar analyses have been conducted according to the procedure described in Chapter 3 applying the boundary conditions already validated in Chapter 4. The aim of this Chapter is to demonstrate the applicability of MAIA procedure as well as to show the impact on the design when CAD-centric models are used and the high resolution loosely-coupling analyses are performed. For the sake of brevity and clearness, the application of the MAIA is limited to the HCPB slice. The geometric features have been already introduced in paragraph 1.2.1, but, when more detailed information is needed, it is reported within the text.

5.1 Neutronic Analysis HCPB Breeding Blanket Slice Test Case

In this section, the first three steps of the MAIA procedure are applied to the HCPB concept. Starting from a generic CAD of the HCPB slice (Figure 3.1 step (a)), a model suitable for MCNP is created (Figure 3.1 step (b)) and the neutron and photon transport analyses are carried out (Figure 3.1 step (c)).

5.1.1 Neutron/Photon Radiation Transport Model Setup

The neutronic analyses on the HCPB have been carried out in order to assess the nuclear response, focusing the attention on such quantities as neutron flux, the deposited nuclear power and the spatial distribution of its volumetric density. To this purpose, it has been used the completely heterogeneous HCPB slice CSG model (Figure 5.1 – a and b), described in paragraph 3.2.1, along with FENDL3.1 [72] neutron cross section library and MCLIB04 [108] photon cross section library. The neutronic analyses of the HCPB slice comprise the assessment of main nuclear performances such as nuclear power generation and its distribution. The calculations have been carried out using the completely heterogeneous CSG HCPB slice model (Figure 5.1 – a and b), described in paragraph 3.2.1, with the use of nuclear data from FENDL [72].

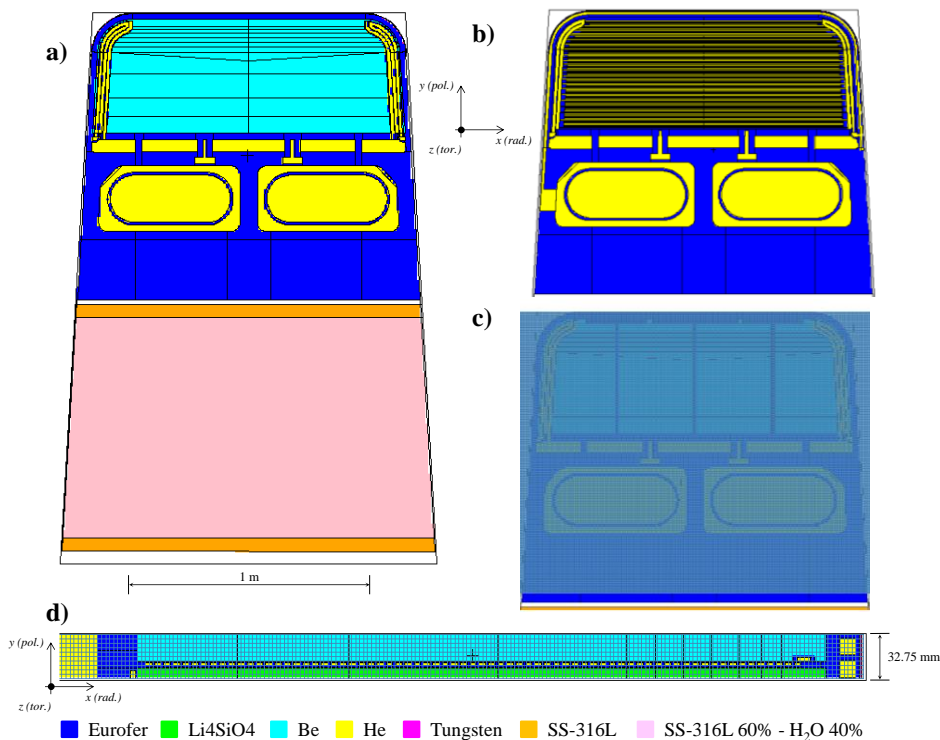


Figure 5.1. The MCNP model of HCPB slice. Left (a): to view of the entire CSG neutronic model. Right-top (b): detail of the CP neutronic model. Right-centre (c): radial-toroidal view of the HCPB slice with superimposed Cartesian mesh. Bottom (d): radial-poloidal view of the superimposed mesh on HCPB slice neutronic model.

The neutron and photon sources, used for the analysis of the sub-model, are simulated according to the methodology reported in paragraph 3.3.1 and validated in paragraph 4.1.2.

Reflecting and white boundary conditions have been applied in the poloidal and toroidal directions as validated in paragraph 4.1.1.

About 270 heterogeneous cells have been identified for the discretisation of the domain on which a Cartesian mesh (namely FMESH) of $\sim 2.4 \text{ E}+06$ elements/voxels has been superimposed. The resolution of the mesh is: ~ 3 mm in x-direction, ~ 3.3 mm in y-direction and ~ 3 mm in z-direction. Some details of the FMESH are reported in Figure 5.1 – c and d.

For the normalisation of the results described in the following paragraphs, the neutron and photon source intensity parameters reported in Table 4.1 have been used.

5.1.2 Nuclear Heating

Using the above mentioned setup, boundary conditions and local neutron source, the power deposited per cell by neutrons and photons Q_{np} and the power deposited by photons produced due to neutronic interaction outside the domain of interest and scattered into the sub-model $Q_{p,albedo}$ (see eq. (3.7)) have been calculated and reported in Table 5.1. The highest power deposition occurs in the Li_4SiO_4 ($\sim 46\%$) where the tritium production reactions happen (due to the enrichment of 60% in ${}^6\text{Li}$, the exothermic reaction (1.6) prevails on the endothermic reaction (1.7)). About the 28% of the power is released in the Be bed while about the $\sim 22\%$ on the Eurofer present in the FW, CP, BSS and manifolds.

Table 5.1. Computed power deposition in each OB4 HCPB slice region for DEMO 2015.

| HCPB Slice Regions | Volume [cm ³] | Q_{np} [W] | $Q_{p,albedo}$ [W] | Q_{dep} [W] | Percentage deposited power |
|--|---------------------------|--------------|--------------------|---------------|----------------------------|
| Armour | 1.0888E+02 | 1.4982E+03 | 7.9606E+02 | 2.2942E+03 | 3.023% |
| Be Bed | 1.3595E+04 | 2.1183E+04 | 3.7581E+02 | 2.1559E+04 | 28.409% |
| BSS | 8.0780E+03 | 1.9339E+03 | 4.3325E+01 | 1.9772E+03 | 2.605% |
| CP | 2.6998E+03 | 6.6674E+03 | 5.6457E+02 | 7.2319E+03 | 9.530% |
| FW | 1.3058E+03 | 6.4280E+03 | 9.7320E+02 | 7.4011E+03 | 9.753% |
| He BSS | 9.8587E+02 | 2.1918E+00 | 5.2575E-03 | 2.1971E+00 | 0.003% |
| He CP | 1.1551E+03 | 2.7346E+01 | 1.9026E-01 | 2.7537E+01 | 0.036% |
| He Dummy Channels | 7.3723E+02 | 1.0397E+01 | 6.5727E-02 | 1.0463E+01 | 0.014% |
| He FW | 8.2504E+02 | 3.2855E+01 | 4.3099E-01 | 3.3286E+01 | 0.044% |
| He Manifold | 1.1167E+04 | 1.2822E+01 | 1.3680E-02 | 1.2835E+01 | 0.017% |
| He Purge BSS | 1.8858E+03 | 6.8594E+00 | 3.3448E-02 | 6.8929E+00 | 0.009% |
| Li₄SiO₄ Bed | 5.5335E+03 | 3.4929E+04 | 2.1802E+02 | 3.5147E+04 | 46.316% |
| Manifold | 1.0847E+03 | 1.8054E+02 | 2.0903E+00 | 1.8263E+02 | 0.241% |
| Grand Total | 4.9162E+04 | 7.2912E+04 | 2.9738E+03 | 7.5886E+04 | - |

However, this calculation provides only indications on the overall power released that are used for the estimation of mass flow rate but it does not provide information on power distribution. As already stated in the previous paragraphs, the determination of the gradients represents one of the main goals of MAIA procedure. Furthermore, the power density distribution is an important input for the thermal-hydraulic and thermo-mechanical calculations.

Using the FMESH already introduced in paragraph 4.1.1, the power density distribution has been calculated. The spatial distributions of the nuclear power volumetric density together with the related statistic errors are reported in the following figures. In particular, Figure 5.2 and Figure 5.3 show the nuclear heating due to neutrons and related photons respectively, Figure 5.4 that due to albedo photons and Figure 5.5 shows the total power density spatial distribution.

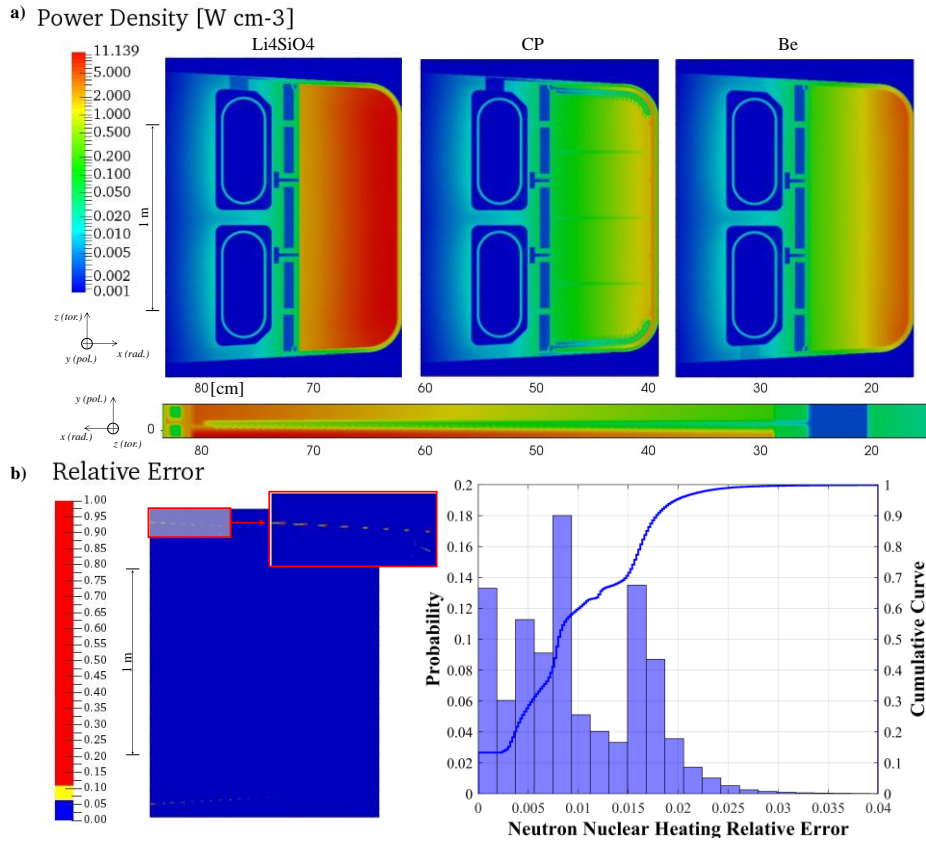


Figure 5.2. Neutron power density deposited in neutron/photon transport analysis. Top (a): volumetric heating distribution in Li4SiO4, Be and CP. Bottom (b): relative error counter map (left) voxel relative error distribution and cumulative curve (right).

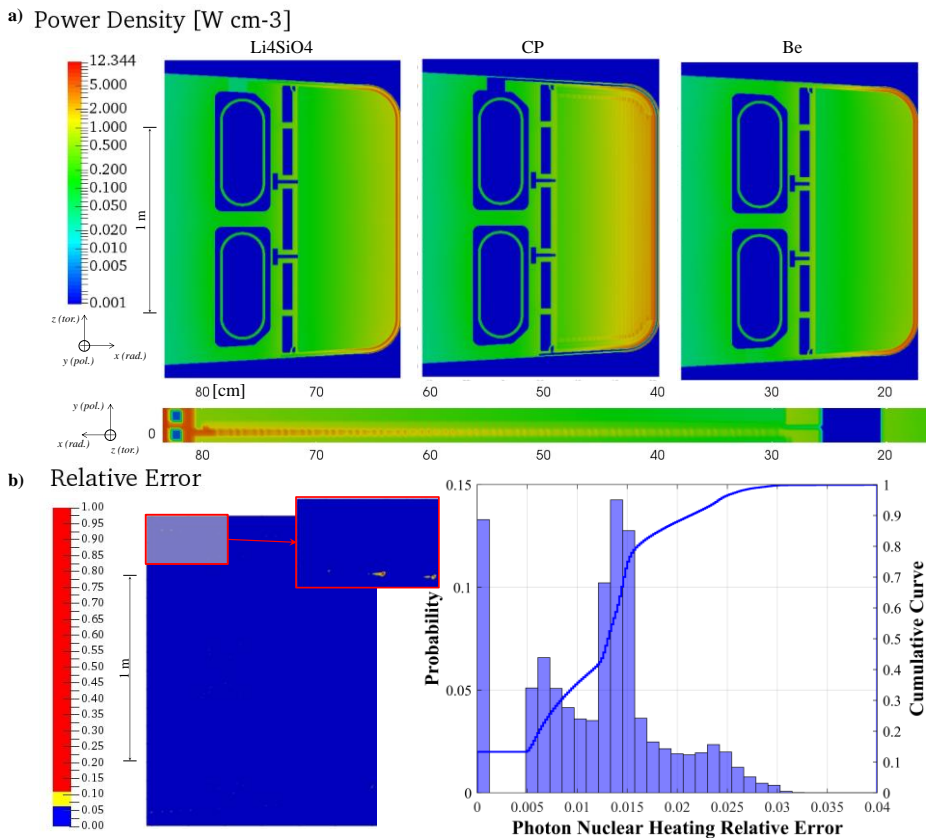


Figure 5.3. Photon power density deposited in neutron/photon transport analysis. Top (a): volumetric heating distribution in Li4SiO4, Be and CP. Bottom (b): relative error counter map (left) voxel relative error distribution and cumulative curve (right).

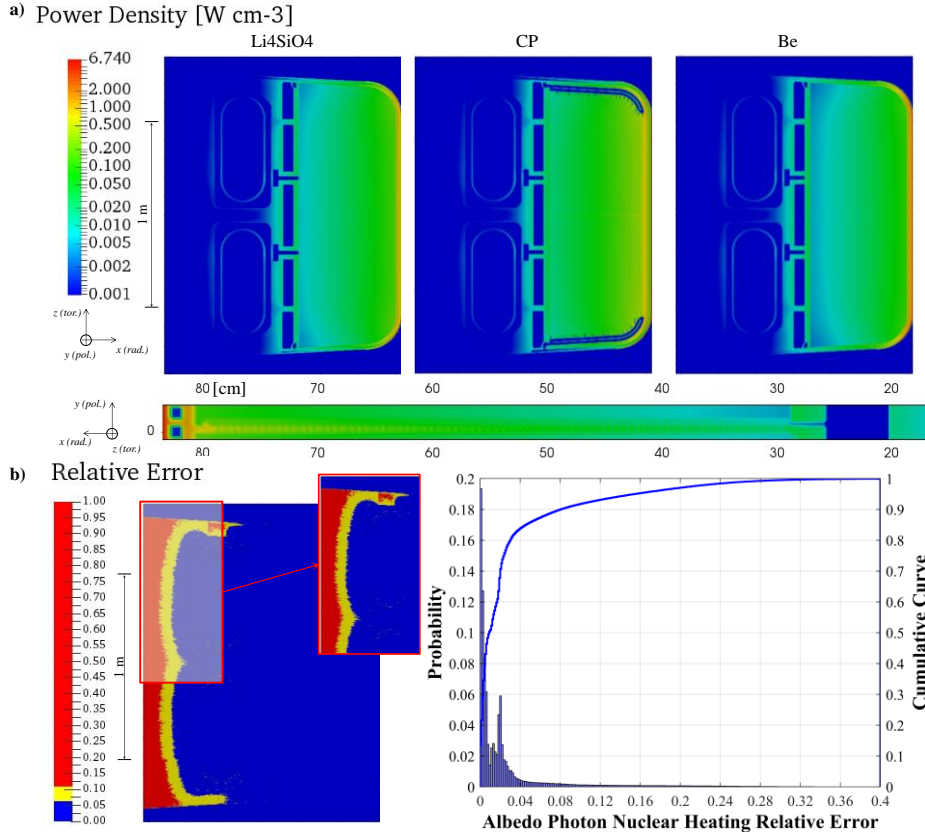


Figure 5.4. Albedo photons power density deposited in photon transport analysis. Top (a): volumetric heating distribution in Li_4SiO_4 , Be and CP. Bottom (b): relative error counter map (left) voxel relative error distribution and cumulative curve (right).

As it is possible to note, the maximum value for the three contributions does not occur in the same regions. Indeed, regarding the power deposited by neutrons, the maximum volumetric heating of $\sim 11.1 \text{ W cm}^{-3}$ is reached in the Li_4SiO_4 (Figure 5.2 – a).

Concerning the photon power density, the maximum ($\sim 12.3 \text{ W cm}^{-3}$) is obtained on the Eurofer of FW where the interactions of incident neutrons with material and, then, the related photon production start to play an important role (Figure 5.3 –a).

As expected, the maximum contribution ($\sim 6.7 \text{ W cm}^{-3}$) of the albedo effect is reached on the armour material where the photons release big part of their energy (Figure 5.4 –a).

These results show the presence of a pronounced radial gradient of the power density but also the presence of not negligible gradients along the toroidal and poloidal directions. This aspect is really important considering that, in the actual analysis for the design of the BB, a pure radial profile of the nuclear heating [26, 30] is usually assumed.

Looking in detail to the power released by neutrons (Figure 5.2 – a), it is possible to note that the volumetric heating drops down of about four orders of magnitude going from the FW to the back of the BSS. Moreover, the presence of He channels produce local alternating power density as it is possible to see in the radial-poloidal cross section of the HCPB neutronic power density (Figure 5.2 – a). This effect is better highlighted in the following when a pure radial profile is calculated.

It is interesting to note that the use of sub-models allows a detailed estimation of the released power with good statistic as demonstrated by the relative error distribution reported in Figure 5.2 – b. Indeed, only the 0.075% of the voxels has a relative error higher of 0.05 and they are located on the side walls of the BSS at the interface between the Eurofer and void.

The probabilities reported in Figure 5.2 – b demonstrate that the relative errors associated with the neutronic power density are well below the statistical limit of 0.05 (see paragraph 2.1.2).

The same behaviour, in terms of reliability of results, is encountered for the photon power density (Figure 5.3 –b). Indeed, only 0.045% of voxels shows a relative error higher than 0.05.

Different discussion has to be done for the photon power density due to the albedo effect. First of all, it is possible to see that its contribution is negligible in the BSS (e.g. power density lower than 0.005 W cm^{-3} , Figure 5.4). It means that the photons, born from the interaction of neutrons in other reactor locations, penetrate the BB just up to the BP. This behaviour produces a good statistical error in the first 80 cm of HCPB slice and a consequently increase over the 0.05 in the remaining part (Figure 5.4 –b). Indeed, 14.306% of voxels show a relative error higher than 0.05.

Summing the three contributions, the total power density distribution is obtained as shown in Figure 5.5.

The maximum power density is reached at the armour ($\sim 18.7 \text{ W cm}^{-3}$) while a value of $\sim 12 \text{ W cm}^{-3}$ is obtained in the Li_4SiO_4 and $\sim 8.5 \text{ W cm}^{-3}$ in the Be.

The analysis of the data shows that the power density deposited on the side walls of the HCPB slice is higher, due to the neutron streaming effect, with respect to the centre that is shielded by the surrounding material. The neutron streaming issues are well known in fusion community but their investigation is usually limited to the VV as described in [109]. However, a precise estimation of this effect could provide important feedback on the BB design (e.g. modification of the cooling circuit near the side walls as well as identification of hot spot hidden when an average radial profile is used). Other improvements could be achieved in the evaluation of the Eurofer damage (e.g. assessment of displacement per atom (dpa) along the sides) that has a direct effect on the Ductile-Brittle Transition Temperature (DBTT) [110].

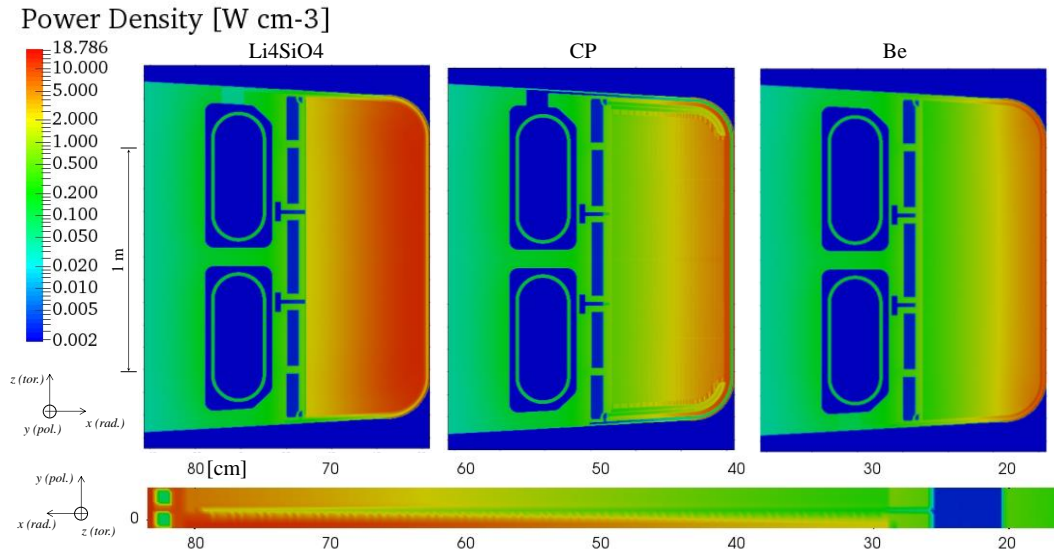


Figure 5.5. Total power density deposited in Orthosilicate, CP, Be bed and on radial-poloidal cross section of HCPB slice.

In addition to the 3D power density distribution calculations, it has been performed also the assessment of its radial profiles for Eurofer, Orthosilicate and Beryllium averaging the volumetric heating along the poloidal and toroidal direction. The results are shown in Figure 5.6.

From the acquired data, it is possible to observe that the geometry heterogeneities (i.e. presence of He cooling and purge gas channels) produce oscillations (see detail on radial power density reported in Figure 5.6) in the Eurofer nuclear heating both in the FW and CP.

Moreover, looking to the detail on the Li_4SiO_4 radial profile of the power density reported in Figure 5.6, it is possible to note small peak at around 7 cm from the plasma facing surface. This effect is probably due to the neutron multiplication that occurs in the Be bed that, after few centimetres, becomes predominant producing the increment of the power density in Orthosilicate. In that area the neutron flux is still very hard and, therefore, the multiplication rate has a maximum. It must also be said that Be bed acts as a sort of

diffuse reflector that spreads the interacting neutrons in all the directions.

In Figure 5.7, the radial profile of the total neutron flux is reported. The neutron flux varies slightly, less than one order of magnitude, in the FW and BZ. A greater variation is reached in the BSS where more massive Eurofer is present. However, the highest reduction of the neutron flux is deployed entirely within the VV where the presence of water and stain steel 316L moderates and shields the neutrons, respectively. Two features can be underlined: (i) at ~55 cm, the neutron flux changes its derivative according to the small peak visible in radial profile of the power density (in that region there is the crossing from the beds to the BP) and (ii) from ~58 cm to ~63 (corresponding to the purge gas manifold behind the BP), the neutron flux is flat according to the zero power density shown in Figure 5.6 (cross section of He is small, therefore no power is released and the neutrons propagate unmoderated).

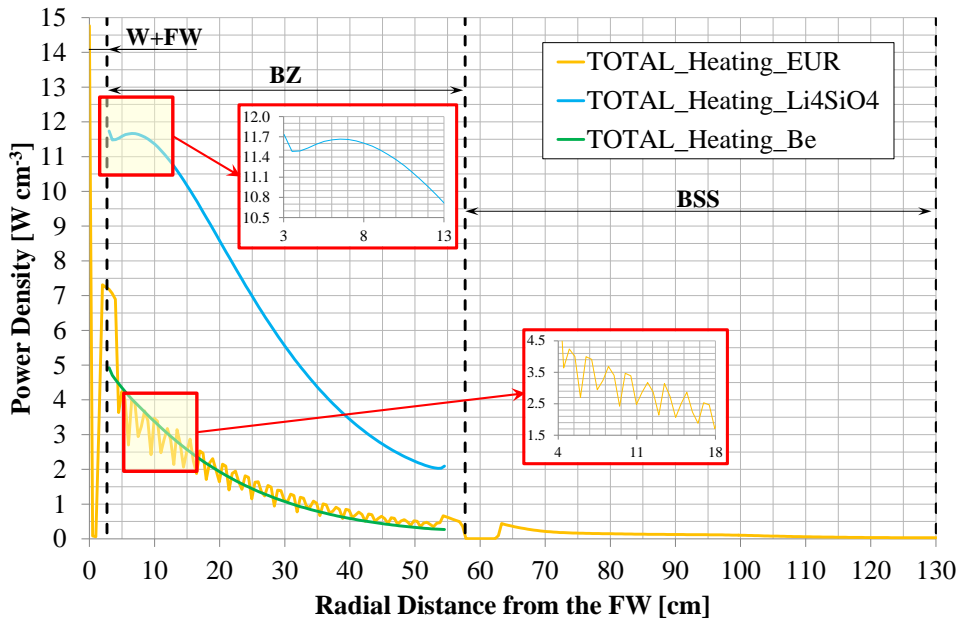


Figure 5.6. Radial power density profiles in different materials of HCPB slice homogenised in the poloidal and toroidal directions.

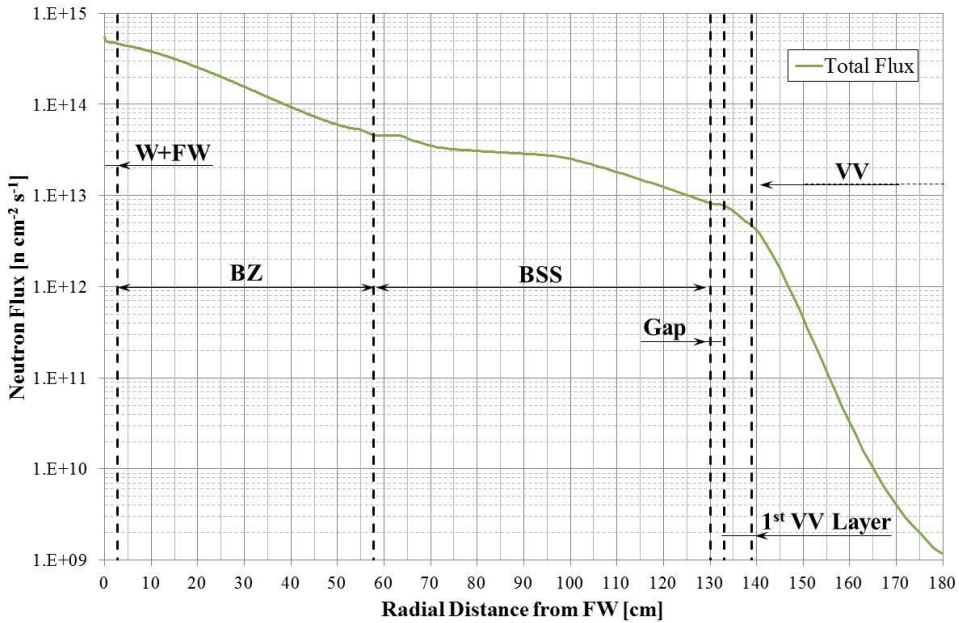


Figure 5.7. Radial neutron flux profile for the HCPB slice.

5.2 Computational Fluid Dynamics Analysis of HCPB Breeding Blanket Slice Test Case

In this section, the steps (d) and (e) of the MAIA procedure (see paragraph 3.1) are applied to the HCPB slice. Indeed, the power density calculated in neutronic analysis is mapped in ANSYS CFX (Figure 3.1 step (d)) and a thermal fluid dynamic analysis is carried out (Figure 3.1 step (e)).

5.2.1 Computational Domain

In order to perform the thermal-hydraulic analysis on HCPB slice, a fluid-dynamic computational domain has been set up.

Hexahedral and tetrahedral elements have been adopted taking into account the geometrical features of the domains to be meshed and the required optimization of the number of nodes and mesh quality. A conformal mesh between the different domains has been set-up.

The mesh, both on the fluid and on the structure, is composed of $5.4E+06$ nodes linked in $18.6E+06$ elements with an orthogonal quality average of 0.710 and skewness average of 0.253. 8 inflation layers have been used with first layer height of $2.0E-05$ m and a growth rate of 1.2. The mesh is shown in Figure 5.8.

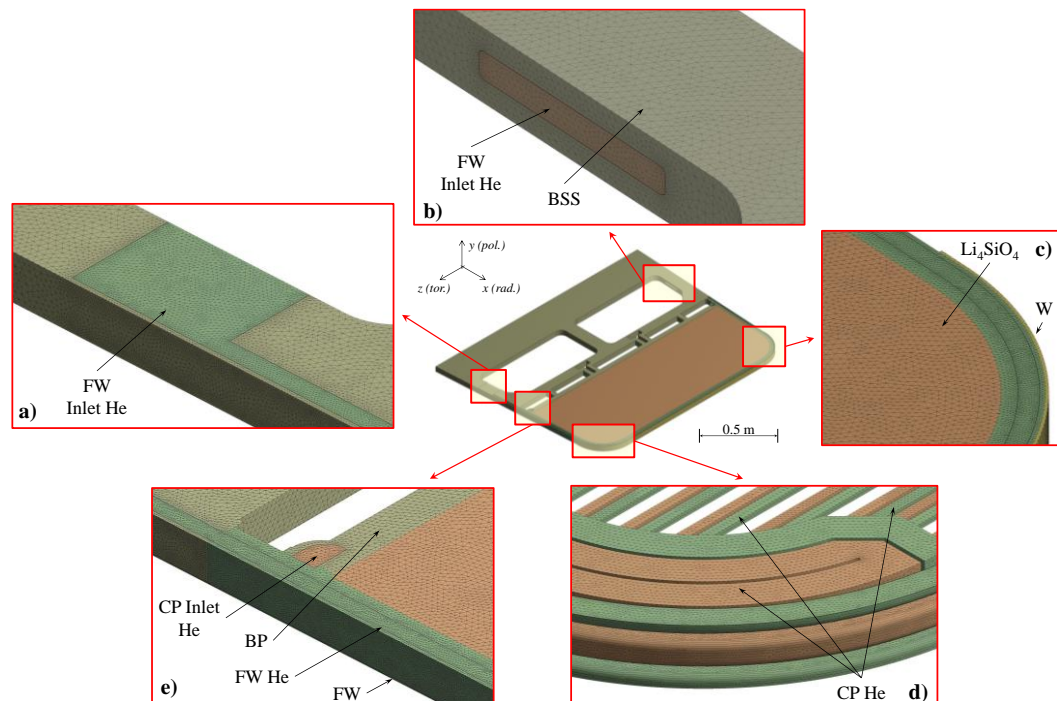


Figure 5.8. HCPB slice thermal-hydraulic model setup. Left (a): mesh detail of FW Inlet He channel. Top (b): mesh detail of FW Inlet He channel and BSS. Right (c): mesh detail of Li_4SiO_4 and FW with W. Bottom (d): mesh detail of He CP cooling circuit. Bottom (e): mesh detail of FW side wall, BP and He CP Inlet channel.

Symmetry conditions have been set to the top and bottom surfaces of the unit slice and adiabatic conditions have been set to the lateral surfaces of the slice with the exception of the FW plasma side. A normal heat flux calculated by multiplying the nominal heat flux value of 0.5 MW/m^2 [26, 30] for the cosine of the angle between the radial and the surface normal directions has been also applied.

The power density calculated in neutron and photon transport analysis and reported in Figure 5.9 has been mapped into CFX and used for the thermal-hydraulic calculation.

Due to the fact that such a slice model cannot model the transversal flow in the BSS inlet manifold, a heat transfer coefficient (HTC) of $\sim 1200 \text{ W/m}^2\text{K}$ has been set to the wetted surfaces of the BSS inlet manifold. It has been estimated calculating the Nusselt number by means of Gnielinski correlation and

assuming an average cumulative mass flow at the point of the unit slice of 10.3 kg/s (total OB segment mass flow minus flow diverted to OB7, OB6 and OB5), a fluid temperature of 300 °C at a pressure of 8 MPa [28].

The application of Gnielinski correlation represents a very conservative assumption since it is used for full thermal and hydraulic developed flows which are not present at the BSS inlet where turbulence phenomena are predominant. Therefore, the estimated HTC is lower with respect to the real one and, consequently, the calculated temperatures will be higher.

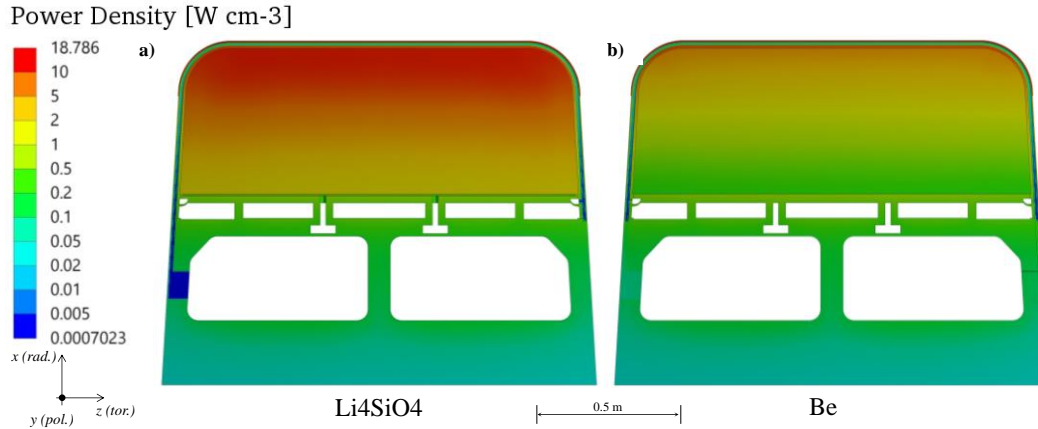


Figure 5.9. 3D power density profile on Orthosilicate (left) and Be (right) side calculated in neutronic analysis and mapped in ANSYS CFX.

As a conservative assumption for the cooling in the BZ at the rear side of the BB, adiabatic surfaces have been considered at the purge gas chambers. This assumption is justified by low velocity of the purge gas flow that results in a negligible HTC. A mass flow rate of 0.046072 kg/s has been derived by the power balance assuming a ΔT of 200 °C according to the operational performances of HCPB BB. It has been applied at the inlet of the parallel cooling loops while a relative pressure of 0 Pa has been imposed to the outlets. The material properties have been implemented by means of CEL functions [59]. The TCC between the EUROFER97 steel structures and both Li₄SiO₄ and Be, are derived from the Yagi and Kunii model [80] applying the constants of Reimann et al. [81].

5.2.2 Thermal-Hydraulic Analysis

Using the above mentioned setup, boundary conditions and power density distribution, a thermal-hydraulic analysis has been performed and the temperature limits verified.

It is important to remember that the temperature design limit window established for the EUROFER97 is from 300 °C to 550 °C. The lower design temperature limit is dictated by the shift of the DBTT under neutron irradiation and the subsequent risk of embrittlement and fast fracture of the components for irradiation temperatures lower than 300 °C. The upper design temperature limit is given by the abrupt loss of creep strength at temperatures higher than 550 °C [111]. The commonly accepted temperature restriction for the ternary ceramic breeder compound Li₄SiO₄ is <920 °C and it is selected for having a certain margin before the phase change takes place. The temperature limit for the metallic beryllium is 650 °C due to swelling, material properties degradation at higher temperatures under neutron irradiation and safety considerations (steam reaction with Be giving H₂ in case of water ingress to the blanket, e.g. due to a breakage of the BB together with the water-cooled divertor) [111].

The main thermal-hydraulic results obtained on HCPB slice using the MAIA procedure are summarised in Table 5.2. The maximum temperature (~940 °C) is reached in the Li₄SiO₄ domain and it is over the acceptable temperature limit. The Be maximum temperature is ~760 °C and it represents another violation of the temperature limit selected for the material. Also the Eurofer temperature exceeds the limit of 550 °C in the CP domain while it is below in the FW and BSS.

The maximum He temperature reaches ~ 600 °C in the same zone (CP centre) where the maximum Eurofer temperature (~ 630 °C) is achieved. This means that the coolant heats up part of the structure if a temperature of 500 °C is reached at the outlet demonstrating a not-optimal configuration of the cooling circuit with respect to the power density distribution considered.

Regarding the pressure drop within the two parallel cooling loops, a value of 1.49 bar and 1.45 bar is obtained for the loop1 and 2, respectively. This light asymmetry is indicative of not completely optimised cooling layout.

Table 5.2. Thermal-hydraulic results for each HCPB slice region.

| Regions | Mean Temp. [°C] | Min Temp. [°C] | Max Temp. [°C] | Δp [bar] |
|--------------------------------------|----------------------------|---------------------------|---------------------------|--|
| Armour | 495.60 | 344.30 | 554.10 | |
| FW | 396.70 | 308.60 | 547.00 | |
| CP | 478.80 | 358.80 | 632.80 | |
| BSS | 353.40 | 300.20 | 497.40 | n.a |
| Be | 531.10 | 349.10 | 757.90 | |
| Li₄SiO₄ | 614.70 | 314.60 | 942.00 | |
| He_Loop1 | 395.10 | 299.40 | 596.90 | 1.49 |
| He_Loop2 | 392.50 | 299.50 | 598.30 | 1.45 |

The temperature distributions for each domain are reported in Figure 5.10 and Figure 5.11.

The maximum temperature in the CP is reached to the centre near the FW (Figure 5.10 – c) where both the maximum of Be and Li₄SiO₄ occur (Figure 5.11 – a and b). This means that cooling layout has to be optimised in that area in order to reduce the temperature of Eurofer. It is important to note that the CP sides are strongly cooled down by the radial He distributors producing high temperature gradients in the toroidal direction. On the BSS ((Figure 5.10 – d), it is possible to observe that the highest temperature occurs in the BP nearby the purge gas manifolds where adiabatic conditions are considered. On the BSS back a temperature of ~ 360 °C is obtained. Usually the design calculations [26, 28] show a uniform BSS temperature of 300 °C that is mainly driven by the low power density and by the heat sink represented by the manifolds. These differences are due to the geometry and load homogenisations introduced in the neutronic calculations that strongly reduce the power released in the BSS producing a not realistic load scenario.

The effect of the CP He radial distributors as well as of the FW inlet is also visible on the Be bed where the temperature drops down to ~ 350 °C (Figure 5.11 – a) and on the Orthosilicate bed where the minimum temperature is ~ 300 °C.

The application of MAIA procedure has highlighted some warning on the HCPB BB that have not been discovered using the conventional coupling process based on the simplification of geometry features and loads [26, 28]. Moreover, the results show a violation of the thermal hydraulic requirement limits that have not been solved introducing design solutions.

Indeed, the outcomes of the thermal-hydraulic analysis suggest a modification of the cooling layout in order to reduce the temperature in structural and functional materials.

According to the MAIA procedure reported in paragraph 3.1, Figure 3.1, when the thermal-hydraulic requirements are not respected, it is necessary to introduce a design modification and to restart the process. However, it is important to underline that the optimisation of the design is not the objective of this work. For this reason, it has been decided to prosecute with thermo-mechanical analysis and with the application of the MAIA procedure in order to highlight the effects of 3D detailed investigations on the final evaluation when integrated multi-physics calculations are carried out.

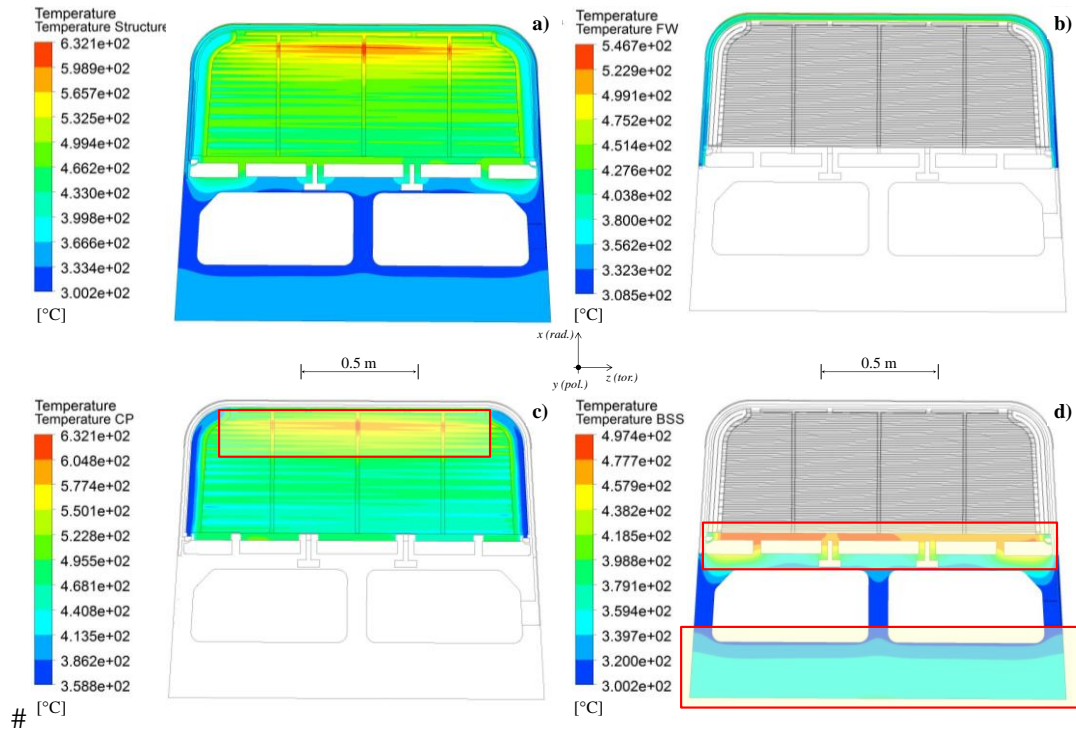


Figure 5.10. Temperature field on structural material of HCPB slice. Left-top (a): overall temperature distribution in Eurofer. Right-top (b): FW temperature field. Left-bottom (c): CP temperature field. Right-bottom (d): BSS temperature field.

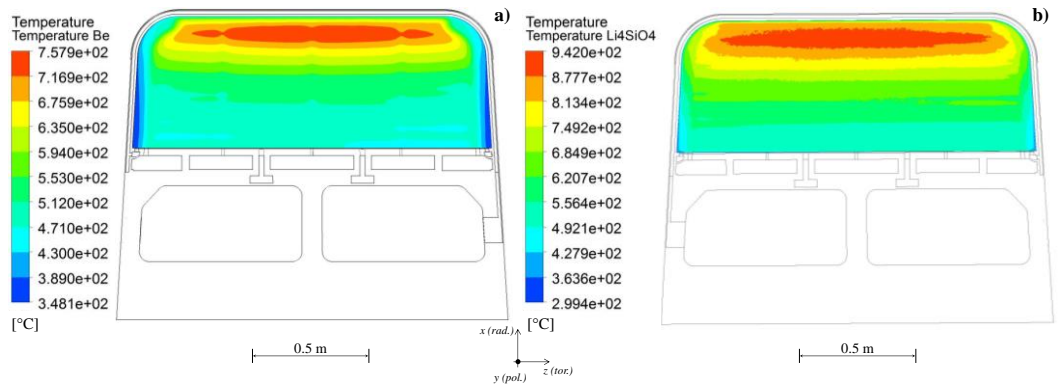


Figure 5.11. Temperature field on functional material of HCPB slice. Left (a): Be bed temperature field. Right (b): Li_4SiO_4 temperature field.

5.3 Structural Assessment of HCPB Breeding Blanket Slice Test Case

In this paragraph, the steps (f) and (g) of the MAIA procedure (see paragraph 3.1) are applied to the HCPB slice. Once the thermal-hydraulic analysis is performed, the temperature field is mapped (Figure 3.1 step (f)) into Finite Element Method (FEM) tool like ANSYS Mechanical [66] and a structural analysis is performed (Figure 3.1 step (g)).

5.3.1 Finite Element Model

In order to perform the thermo-mechanic analysis on HCPB slice, an FEM computational domain has been set up.

The materials have been considered homogeneous, uniform and isotropic and their thermo-mechanical properties have been assumed to depend uniquely on the temperature as indicated in [100, 101].

Due to the geometrical features of the domains to be meshed, in order to optimise number of nodes and

mesh quality both tetrahedral elements have been adopted and, in particular, as to HCPB slice model (Figure 5.12), a mesh composed of $\sim 7.1E+06$ nodes connected in $\sim 4.4E+06$ elements has been selected.

Helium coolant mechanical interaction with the module has been simulated according to the investigated scenario. In particular, under normal operation scenario, it has been modelled imposing 8 MPa pressure to cooling channels walls as well as to rear manifolds and back-plates internal surfaces.

Breeder pebble bed mechanical interactions with module internal walls as well as the purge gas pressure have not been taken into account and, for this reason, no pressure has been imposed along the internal surfaces of each breeder cell. This assumption is conservative because it maximises the pressure gradient between the cooling channels and the BZ. Finally, the non-uniformly distributed temperature field, calculated by the previous thermal-hydraulic analysis, has been applied.

The temperature field produces a non-uniformly distributed thermal deformation field, arising within the slice as a consequence of both its thermal field and its isotropic thermal expansion tensor, and it is applied as an equivalent mechanical load.

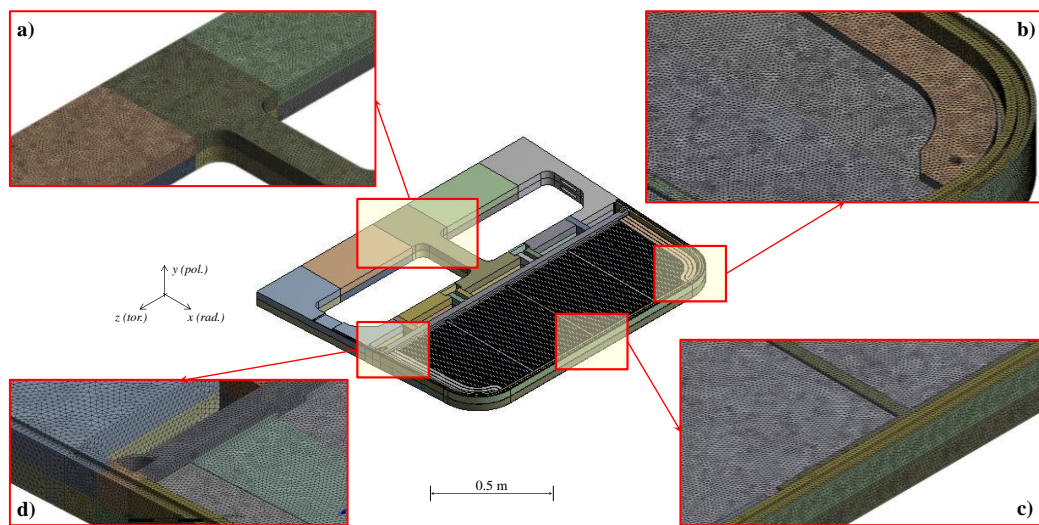


Figure 5.12. HCPB slice thermo-mechanical model. Top-left (a): mesh detail of the BSS. Top-right (b): mesh detail of the FW bend and CP. Bottom-right (c): mesh detail of FW and CP at the front. Bottom-left (d): mesh detail of FW side wall and BP.

Concerning mechanical constraints, poloidal symmetry has been imposed to nodes lying on the bottom of the toroidal-radial boundary surface of the model, while nodes lying on the top toroidal-radial surface have been assumed to undergo poloidal generalised plane strain. Moreover, displacements along the radial direction are prevented to the nodes lying on the toroidal direction, as well as toroidal displacements are prevented to nodes lying along poloidal direction (Figure 3.9-b) [83, 84].

5.3.2 Structural Analysis

Thermo-mechanical steady state analyses have been carried out to assess the potential aptitude of the HCPB slice to safely withstand the loads it undergoes under flat-top plasma operational state without incurring in significant deformations or yielding-induced structural crisis. Normal operation scenario arises when the module undergoes both thermal deformations due to the thermal field distribution typical of flat-top plasma operational state and 8 MPa Helium coolant pressure on its cooling channel walls.

As to the nominal operation loading scenario, on the basis of the thermal field distribution obtained, a specific steady state mechanical analysis has been performed to assess the spatial distribution of total stresses by means of ANSYS Mechanical [66].

Furthermore, a separate steady state mechanical analysis has been carried out, considering uniquely thermal loads, in order to directly assess secondary stress distribution. Finally, primary stress spatial distribution has been derived as the difference between those already obtained with regard to total and

secondary stresses. In Figure 5.13, the total deformation and the equivalent Von Mises stress field for the radial toroidal section are reported. With respect to the displacement field (Figure 5.13 – a), attention has been paid to radial, poloidal and toroidal displacements (respectively u_x , u_y and u_z) within the model, in order to check that no excessive displacements take place during flat-top operation plasma state.

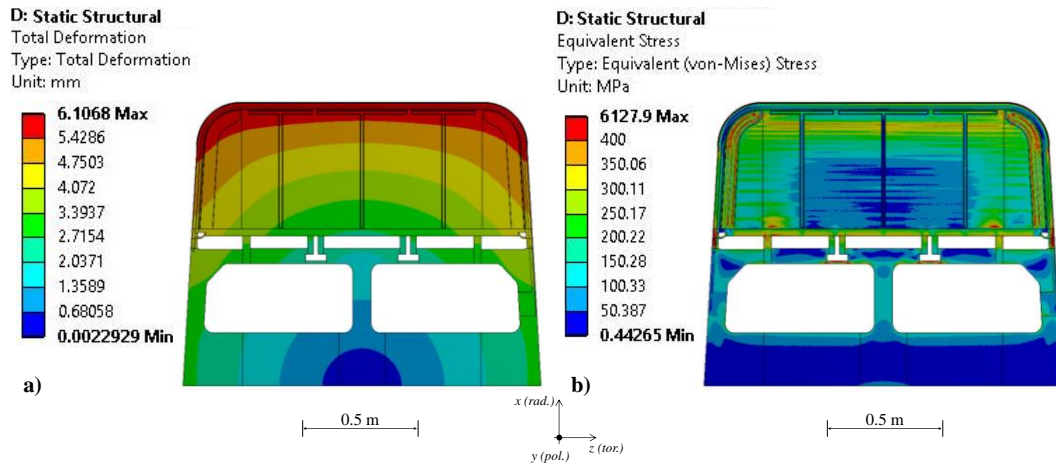


Figure 5.13. Thermo-mechanical results on HCPB slice model. Left (a): total deformation. Right (b): Von Mises stress field.

The obtained results indicate that displacements predicted within FW, CP, PB and BSS are acceptable from a qualitative point of view even if physically meaningful. In particular, the highest displacement value in radial direction for these components is about 5.9 mm, maximum displacement in poloidal direction is about 0.5 mm, while in the toroidal direction it is about 3.8 mm.

A summary of the most significant results in terms of displacements obtained is reported in Table 5.3.

With respect to the thermal behaviour predicted under the Normal operation scenario for the HCPB slice, results obtained (Figure 5.13 – b) indicate that a significant stress is localised:

- (i) at the junction with the armour,
- (ii) in the caps of the CP Helium distributors and
- (iii) at the connection between the BP and the CP.

The very intense values of Von Mises equivalent stress (~ 2000 MPa) obtained at the boundary between the Eurofer and tungsten are probably due to the combined effect of particular high temperature predicted in these areas, where hot spots higher than 500 °C have been estimated, and the different thermal expansion of the two materials. This is an important outcome of this analysis and demonstrates the huge effect on local stress created by the presence of tungsten. Also in the caps of the CP distributors, intense Von Mises stresses are obtained (~ 1900 MPa). This is due to the combined action of high temperatures and small thickness. Analogous behaviour has been encountered at the bound between the BP and BSS.

Moreover, as far as the HCPB slice system is concerned, it may be observed (Figure 5.13 – b) that the Von Mises equivalent stress field is somehow lower than 400 MPa reaching maximum values in very small regions located where dedicated design actions should be taken.

Table 5.3. Summary of computed displacements for each region for DEMO2015 at normal operation conditions.

| Region | Displacements [mm] | | | | | |
|--------|--------------------|-----------|-----------|-----------|-----------|-----------|
| | u_x Max | u_x Min | u_y Max | u_y Min | u_z Max | u_z Min |
| FW | 5.948 | 2.101 | 0.279 | 0.000 | 3.765 | -3.799 |
| CP | 5.737 | 2.534 | 0.510 | -0.226 | 3.665 | -3.699 |
| PB | 2.860 | 2.450 | 0.267 | 0.000 | 3.658 | -3.696 |
| BSS | 2.691 | 0.000 | 0.266 | 0.000 | 3.384 | -3.389 |

According to the methodology for stress linearization reported in paragraph 4.3.1 and with reference to the paths on the FW, BP and BSS identified in Figure 4.37, the equivalent Von Mises stresses, induced by primary and secondary loads, have been calculated and are reported in Table 5.4.

The membrane and bending component values for each path are reported in Appendix 9.7, from Table A.30 to Table A.34.

Table 5.4. Computed equivalent membrane and bending for primary and secondary stress of HCPB slice for DEMO2015 at normal operation conditions.

| Equiv. Stress (Von Mises) | Primary Stresses | | Secondary Stresses | |
|--------------------------------------|---------------------------|--------------------------|---------------------------|--------------------------|
| | Membrane [MPa] | Bending [MPa] | Membrane [MPa] | Bending [MPa] |
| Path1 | 22.43 | 5.55 | 115.63 | 95.60 |
| Path2 | 17.17 | 5.20 | 92.58 | 81.27 |
| Path3 | 3.07 | 1.39 | 212.34 | 40.09 |
| Path4 | 30.51 | 8.48 | 171.17 | 51.55 |
| Path5 | 6.31 | 64.49 | 64.61 | 95.16 |

The combination of primary and secondary stresses in terms of membrane and bending can be used to verify the design criteria reported in C&S such as RCC-MRx [104] and SDC-IC [105] although this comparison, for this specific case, is meaningless due to the thermal failure of the requirements for the structure, Orthosilicate and Beryllium beds.

6 Application of MAIA Procedure for Nuclear Safety Assessment

In this Chapter, the enhancement of MAIA procedure for application on particular problems connected to safety analysis is described.

The first aim of this Chapter is to describe the use of MAIA procedure for the study of water activation in WCLL BB providing indications about the methodology used and the outcomes that can be obtained.

Second aim of this Chapter is also to provide a demonstration of the versatility and adaptability of the MAIA procedure for the investigation of specific phenomena.

6.1 General Introduction to Nuclear Safety Analysis for Fusion

In a fusion reactor, or more general in a Nuclear Power Plant (NPP), the technological development is strictly linked to the safety one. For this reason, it is nowadays a common practice to take into account, since the early design phase, all the aspects related to the safety. They are, thus, developed according to the maturity of the conception driving the design itself.

In particular, for a fusion reactor, the main safety issues are related to the confinement of tritium and activated material [112].

Therefore, the tritium, used as fuel and produced in the BB, is a β - emitter that can easily permeate through the confinement jeopardising the workers and the population in case of any release.

Concerning the activated materials, they are produced due to the interaction of functional and structural materials and high energy neutrons. They can be subdivided in mobilised and immobilised materials.

In the first group, there are all the activated dust and gases, water activation products and activated corrosion products (ACPs) that can escape during an accident and contaminate the environment for a long period. In the second group there are all the structural and functional materials that, for their physical state, cannot be released in case of an accident and their treatment is more a concern for the waste management.

A particular safety issue, not only during an accidental scenario but also during normal operation, is related to the activated products (e.g. ^3H , ^{19}O , ^{16}N and ^{17}N) in water coolant of DEMO reactor when equipped with WCLL BB. Indeed, the activated water represents a distributed radiation photon and neutron source that can jeopardise the sensible equipment (e.g. valves) to which a safety function is associated. It also limits the human intervention. The water activation poses also issues to the design of the PHTS that has to be properly shielded and carefully routed within the confinement.

The major contribution is given by nitrogen isotopes produced by neutron-induced reactions with the oxygen isotopes present in the water. They emit gamma rays (e.g. ^{16}N) and neutrons (e.g. ^{17}N produces delayed neutrons) and, flowing together with the water in the piping, affect the dose sustained by the PHTS components compromising their structural integrity.

In the following paragraphs, the enhancement of MAIA procedure for the study of this particular phenomenon is described.

6.2 Water Activation in Fusion Nuclear Reactors

In DEMO reactor, the neutrons coming from plasma with high energy produce several nuclear reactions with the hydrogen and oxygen isotopes of water.

The main water isotopes composition, reported as relative percentage abundance of isotopes, of nuclear reactor is: 99.985% of ^1H ; 0.015% of ^2H , 99.762% of ^{16}O ; 0.038% of ^{17}O and 0.200% of ^{18}O [113].

These isotopes, for neutron energy lower than 15 MeV, produce radioisotopes like ^3H , ^{14}C , ^{15}C , ^{16}N , ^{17}N , ^{18}N , ^{19}O . In Table 6.1, the main reactions and radioisotopes decay modes are reported [113]. Some isotopes

like ^{15}C , ^{18}N , and ^{19}O are not produced in abundance due to the limited presence of the parent isotope ^{18}O .

The tritium production in water is negligible with respect to the one that diffuses from the BZ [113]. Considering the big half-life, some concerns in terms of waste treatment could be represented by ^{14}C but, taking into account that it is a β -emitter and is confined within the primary circuit, it does not produce any issue to the equipment and workers (the β -rays are shielded by water itself and by the structure) unless an accident with loosing of confinement function occurs. The main contributions are given by ^{16}N and ^{17}N produced by reactions with ^{16}O and ^{17}O , respectively. These radionuclides produce gamma ray and, in case of ^{17}N , delayed neutrons that can induce the activation of the main PHTS components.

Table 6.1. Reactions of pure water isotopes with neutrons having energies lower than 15 MeV and radioactivities induced by these interactions [113].

| Nuclide | Reaction | Q-value [MeV] | Decay | Half-life | Gamma rays [MeV] |
|-----------------|--|------------------|-----------------------------|-----------|---|
| ^3H | $^2\text{H}(n,\gamma)^3\text{H}$ | 6.257 | β^- | 12.33 y | Not applicable |
| | $^{17}\text{O}(n,t)^{15}\text{N}$ | -7.789 | | | |
| | $^{18}\text{O}(n,t)^{16}\text{N}$ | -13.343 | | | |
| ^{14}C | $^{17}\text{O}(n,\alpha)^{14}\text{C}$ | 1.818 | β^- | 5730 y | None |
| | $^{18}\text{O}(n,\alpha)^{14}\text{C}$ | -6.226 | | | |
| ^{15}C | $^{18}\text{O}(n,\alpha)^{15}\text{C}$ | -5.008 | β^- | 2.449 s | 5.298 |
| ^{16}N | $^{16}\text{O}(n,p)^{16}\text{N}$ | -9.637 | β^- | 7.13 s | 6.129, 7.115 |
| | $^{17}\text{O}(n,np+d)^{16}\text{N}$ | -11.556, -13.780 | | | |
| | $^{18}\text{O}(n,t)^{16}\text{N}$ | -13.343 | | | |
| ^{17}N | $^{17}\text{O}(n,p)^{17}\text{N}$ | -7.898 | $\beta^- + n^{**}$ | 4.173 s | 0.871 |
| ^{18}N | $^{18}\text{O}(n,p)^{18}\text{N}$ | -13.117 | $\beta^- + \alpha + n^{**}$ | 0.630 s | 0.535, 0.822 1.651, 1.938 1.981, 2.425 2.429, 2.473 2.673, 3.548 5.788, 6.197 7.128 |
| | | | | | 0.110, 0.197 |
| | | | | | 1.357, 1.444 |
| | | | | | 1.554 |
| | | | | | |
| | | | | | |
| ^{19}O | $^{18}\text{O}(n,\gamma)^{19}\text{O}$ | 3.957 | β^- | 26.91 s | 0.110, 0.197 1.357, 1.444 1.554 |

The threshold energies for the ^{16}N and ^{17}N production reactions are 10.24 MeV and 8.55 MeV [72], respectively. With reference to their cross sections reported in Figure 6.1, it is possible to observe that the ^{16}N exhibits a peak at 11.65 MeV while the maximum value for the ^{17}N is at 14.00 MeV [72].

^{16}N is a β -emitter and it decays back to ^{16}O with a half-life of 7.13 s and a branching ratio of 99.99%. The ^{16}O is produced in excited state that undergoes to the ground state emitting prompt energetic γ rays.

^{17}N is a β -emitter and it decays back to ^{16}O followed by delayed neutron emission with a half-life of 4.17 s and a branching ratio of 94.99%. The delayed neutrons could activate the structural material of the piping lines outside the VV and produce a further distributed photonic source.

The emission probabilities for each γ ray line emitted by ^{16}N decay and for each delayed neutrons energy are reported in Table 6.2. For the ^{16}N , the most relevant energy of γ -rays is 6.129 and 7.115 MeV that represent ~74% of emission probability. These rays contribute mostly to the dose rate calculations to the workers and equipment due to their high energy and intensity. They are also responsible of the main radiation damages to the components. For the ^{17}N , the most relevant delayed neutron energies are 1.171, 0.383 and 1.700 MeV that represent the ~94.63% of emission probability.

In general, the impact of ^{16}N is higher with respect to the one of ^{17}N because of (i) the large amount of ^{16}O in comparison with ^{17}O , (ii) higher cross section and (iii) higher energy associated to the emitted particle. However, the ^{17}N contribution cannot be neglected because it produces further material activation.

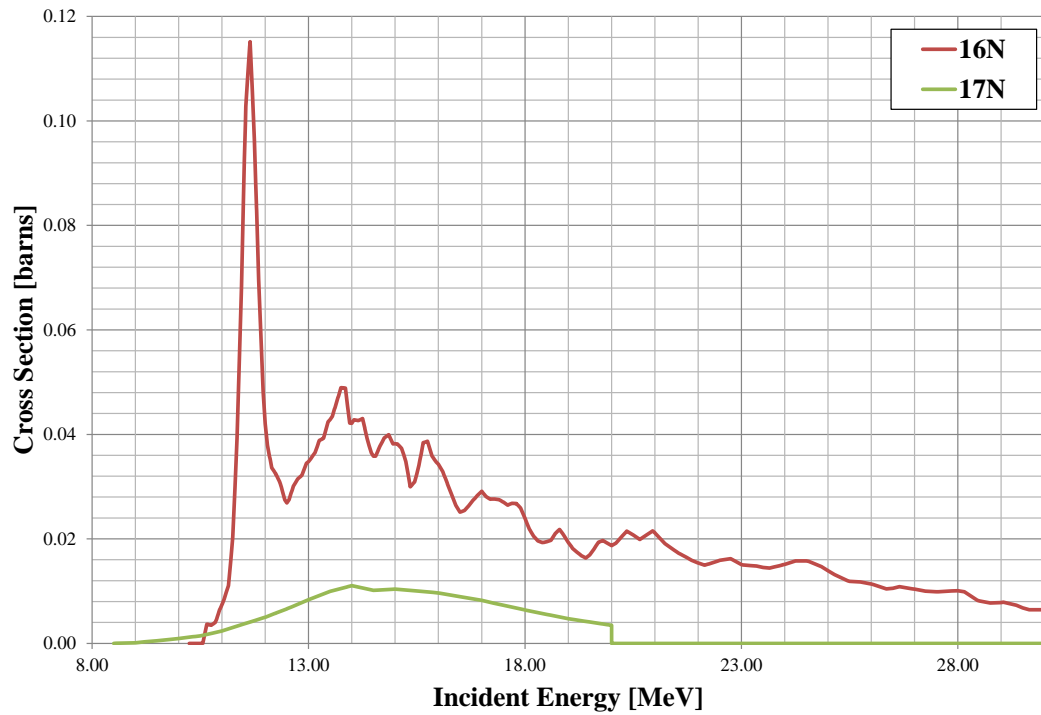


Figure 6.1. Cross section for $^{16}\text{O}(n,p)^{16}\text{N}$ and $^{17}\text{O}(n,p)^{17}\text{N}$ reactions as function of the incident neutron energy from NEA / Incident neutron data / FENDL-3.1b data libraries [72].

Table 6.2. Energy and emission probabilities of delayed γ rays and neutrons following β - decay of ^{16}N and ^{17}N isotopes [114].

| ^{16}N | | ^{17}N | |
|-----------------------|--------------------------|----------------------|--------------------------|
| γ energy [MeV] | Emission Probability [%] | Neutron energy [MeV] | Emission Probability [%] |
| 6.129 | 68.800 | 1.171 | 52.781 |
| 7.115 | 4.999 | 0.383 | 34.807 |
| 2.742 | 0.839 | 1.700 | 7.037 |
| 1.755 | 0.139 | 0.884 | 0.571 |
| 8.869 | 0.079 | - | - |
| 1.955 | 0.039 | - | - |
| 6.916 | 0.039 | - | - |
| 6.048 | 0.013 | - | - |
| 0.987 | 0.004 | - | - |
| 2.823 | 0.001 | - | - |

In order to compute the concentration of ^{16}N and ^{17}N in the WCLL cooling system, it is necessary to solve a coupled neutronic/fluid-dynamic problem. Indeed, for a given control volume, it has to be considered the balance between the production of nitrogen isotopes generated by neutron interaction or the nitrogen that enters the volume, and the reduction due to isotopes decay and to the isotope flow exiting from the same volume. This problem can be represented by means of a differential transport equation of a passive

scalar nitrogen (^{16}N or ^{17}N) volumetric density variable n_N , as reported in eq. (6.1)

$$\underbrace{\frac{\partial n_N}{\partial t}}_{\text{time dependent}} + \underbrace{u_i \frac{\partial n_N}{\partial x_i}}_{\text{advection}} - \underbrace{\Gamma \frac{\partial^2 n_N}{\partial x_i^2}}_{\text{diffusion}} = \underbrace{R^N - \lambda n_N}_{\text{sources}}, \quad (6.1)$$

where u_i is the flow velocity, Γ is the nitrogen isotope scalar diffusivity, R^N is the volumetric production rate and λ is the nitrogen isotope decay constant.

Eq. (6.1) takes into account the time variation and the advection and diffusion nitrogen transport (left hand side of the equation), the nitrogen production and decay losses (right hand side of the equation).

In other words, eq. (6.1) couples (i) the neutronic calculation of the nitrogen production rate with (ii) the fluid-dynamic transport of a passive scalar represented by nitrogen concentration.

The resolution of the flow velocity field has been already introduced by means of the mass balance and Navier-Stokes equation reported in paragraph 2.2 equations (2.28) and (2.33), respectively.

Concerning the source term, the volumetric density of nitrogen production rate can be calculated as follows:

$$R^N(x_i, t) = \int_0^{+\infty} \int_{4\pi} \sum_{(n,p)}^{O_k} (x_i, E) \psi(x_i, E, \Omega_i, t) d\Omega_i dE, \quad (6.2)$$

where $\Sigma_{(n,p)}^{O_k}$ is the macroscopic cross section for the (n,p) reaction, ψ is neutron flux angular energy density as a function of the space x_i , energy E , neutron motion direction Ω_i and time t .

The coupling resolution of the nitrogen isotope production and transport has been achieved within MAIA procedure demonstrating also the flexibility of the approach.

6.3 Enhanced Use of MAIA Procedure for Water Activation Analysis on WCLL BB

As demonstrated in the previous sections, MAIA provides a powerful means for the analysis and design of the BB. Furthermore, the MAIA procedure can also be adapted to the study of particular phenomena, like the water activation, demonstrating also its flexibility to satisfy the needs of designers.

In this paragraph, the enhancement use of MAIA procedure for the water activation analysis is described.

6.3.1 Adaptation of MAIA Procedure for Water Activation Studies on WCLL BB

The basic structure of MAIA procedure is articulated in 8 steps, as shown in paragraph 3.1 and Figure 3.1, that are executed in sequence. Starting from this logical structure and in particular from neutronic calculations, it is possible to spread the BB investigation in two flow paths. One path, represented by steps from d to g of Figure 6.2, is used for the transport of the scalar power density used as a load for the estimation of the temperature, stress and strain fields.

The other path (steps i and l of Figure 6.2) is used for the transport of the scalar nitrogen concentration applying the ^{16}N and ^{17}N production rate as loads. Once again, the neutronic calculation demonstrates its centrality in the design of the BB. Indeed, the main forcing loads, which are afterwards used in the other calculations, derive from the interaction between the neutron and the BB materials. For this reason, it is even more important to have a detailed discretisation of the geometry in the neutron/photon transport model in order to calculate the magnitude and the spatial distribution of the quantity under study like, for instance, the nitrogen production. In particular, the second point assumes a considerable importance because, as it is shown in the following paragraphs, the production of the ^{16}N and ^{17}N has an energy threshold that triggers a particular spatial distribution in the first centimetres of the BB. In other words, the oxygen activation does not involve all the water present in the BB but only a portion according to the neutrons slow-down.

For these reasons, the water activation studies are performed calculating the 3D profile of the nitrogen production using a complete heterogeneous neutronic model with a neutron source and of boundary conditions (c), mapping it into an FVM code like CFX (i) and calculating the concentration by means of a set of equations for the transport of passive scalar (l).

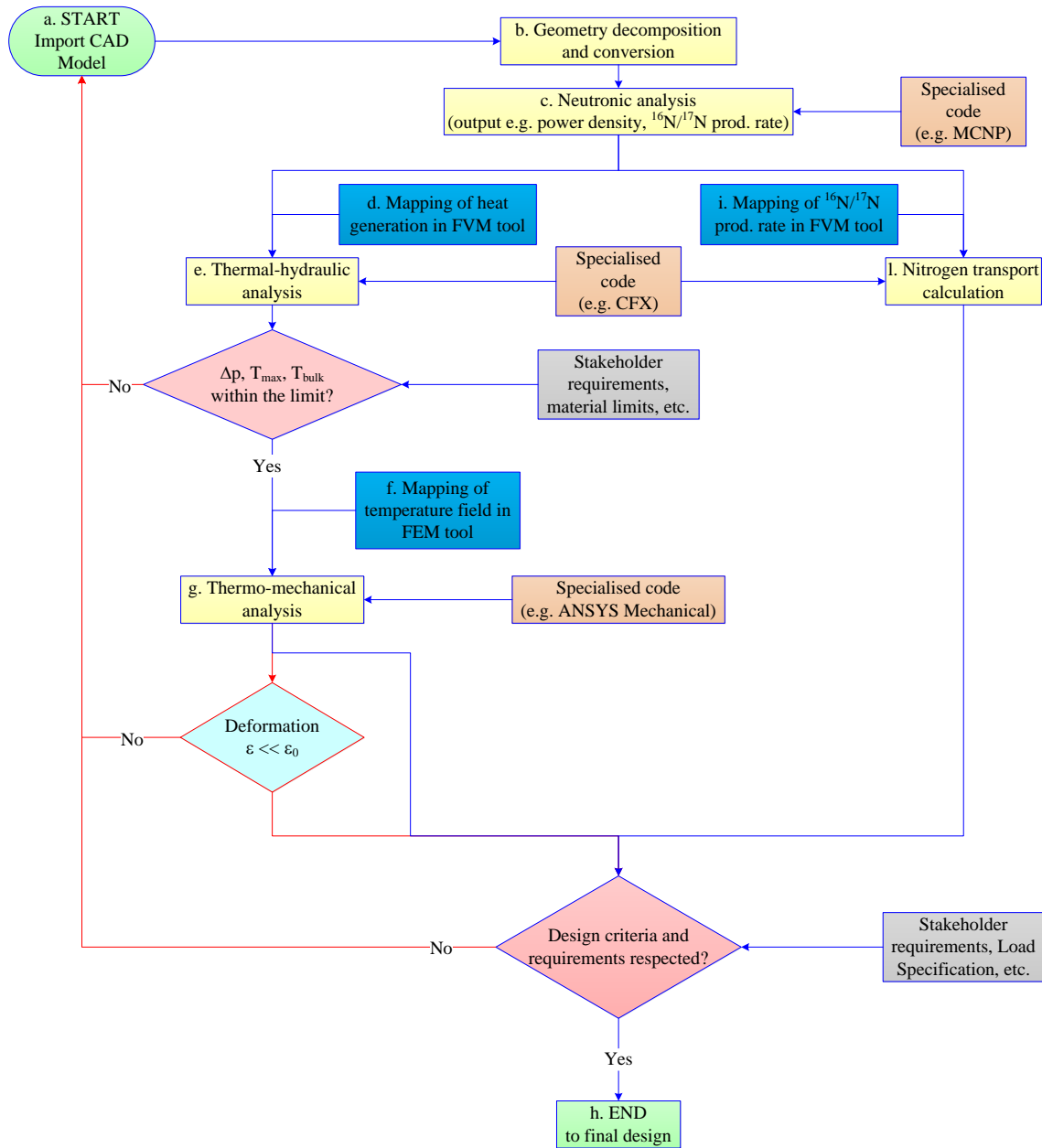


Figure 6.2. Enhanced MAIA procedure flow diagram for water activation studies.

The neutronic calculation (step c of Figure 6.2), for the water activation studies in MAIA procedure, is conducted in accordance to the local neutron source and boundary condition defined in paragraph 3.3 and validated in paragraph 4.1. The nitrogen production rate is calculated combining the F4 tally, introduced in paragraph 2.1.2, eq. (2.18), with the FM card for the ^{16}N and ^{17}N . The modification of the standard tally can be applied also to the EMBEE cards in case the hybrid representation is used, following the instructions reported in MCNP6 manual [54]. In general, the FM card multiplies the tallied quantities for a given constant C and the continuous-energy reaction cross section,

$$C \int \phi(E)R(E)dE, \quad (6.3)$$

where $\phi(E)$ is the energy-dependent fluence and $R(E)$ is the energy dependent reaction cross section.

In case of water activation, C is obtained by means of ^{16}O and ^{17}O atomic density and neutron source intensity, and $R(E)$ is the cross section of (n,p) oxygen isotopes reaction. Once the neutron transport analysis is performed, the calculated distributions of nitrogen production rates are mapped into ANSYS CFX (Figure 6.2 step (i) of the MAIA procedure) according to the procedure already described in paragraph 3.4.1. The nitrogen transport is then solved (Figure 6.2 step (l) of the MAIA procedure) implementing the eq. (6.1) in ANSYS CFX [59]. The following boundary condition at the inlet channels is applied:

$$n_{N,Inlet} = n_{N,Outlet} e^{-\lambda_k \tilde{t}}, \quad (6.4)$$

where $n_{N,Inlet}$ and $n_{N,Outlet}$ are the ^{16}N and ^{17}N concentrations at inlet and outlet of the BB domain, λ_k represents the nitrogen isotope decay constant for ^{16}N or ^{17}N and \tilde{t} is the transit time of water outside the BB in the PHTS cooling circuit.

Using this boundary condition, it is possible to simulate the residence time of water outside the reactor and, then, to calculate the amount of nitrogen that decays within the PHTS circuit and comes back to the BB. The validation of the enhanced MAIA procedure for a simplified model is reported in Appendix 9.8.

6.3.2 ^{16}N and ^{17}N Volumetric Density Distributions of WCLL Breeder Unit

The application of the enhanced MAIA procedure has been pursued on the WCLL BU already described in paragraph 1.2.2. Its neutronic input has been created using the Hybrid representation (see paragraph 3.2.2) where the water within the channels and tube is represented by means of UM while all the other geometric features are reproduced using the CSG representation. This strategy allows:

- (i) to perform less onerous neutronic analyses from a computational point of view;
- (ii) to have, in the domain of interest, more precise results in terms of source distribution. In this way, it is possible to have a precise spatial definition of nitrogen production rate.

In Figure 6.3, a detail of the UM used for the neutronic model is reported. The resulting neutronic model has been already described in paragraph 3.2.2 and it is shown in Figure 3.3 – d.

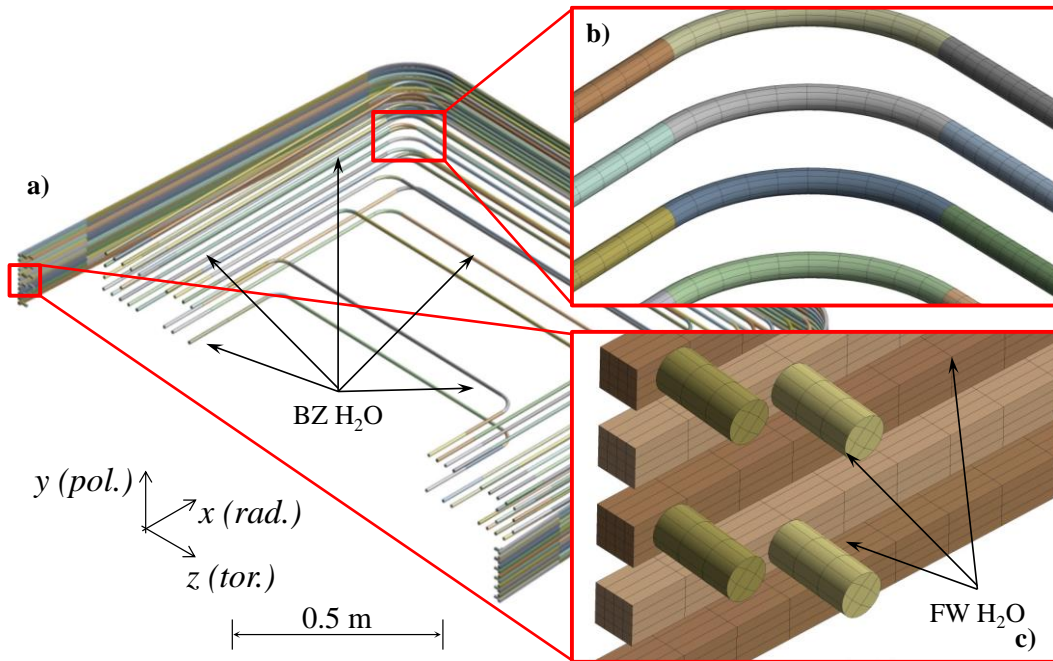


Figure 6.3. UM of WCLL BU. Left (a): FW and BZ coolant water in the BU of WCLL2015. Right-top (b): detail of the UM for the BZ coolant water. Right-bottom (c): detail of the UM for the FW coolant water.

The definition of boundary conditions (reflecting condition in the poloidal direction and white in the toroidal direction) as well as local neutron source (cosine and energy distribution) has followed the procedures already described in paragraph 3.3 and validated in paragraph 4.1. In particular, for the sampling of the local source particle, the MCNP DEMO global model of WCLL 2015 has been used [77].

The chemical composition of water as well as the main thermo-physical properties, used in the neutron transport analysis, have been selected in accordance with the expected WCLL coolant conditions and are reported in Table 6.3.

For the density assessment, the average temperature of 311.5°C has been selected. Indeed, considering that between 295°C and 328°C the water density variation is about 10%, the average density minimises the deviations in the hot and cold water channels.

Nevertheless, the influence of temperature on volumetric distribution of nitrogen isotopes might be further investigated in future works.

Table 6.3. Chemical composition and thermo-physical properties of coolant water.

| Isotope | Isotopic fraction [%] | Physical properties | Value |
|-----------------|-----------------------|-------------------------------|--------|
| ¹ H | 66.6567 | Pressure [MPa] | 15.5 |
| ² H | 0.01000 | Temperature [°C] | 311.5 |
| ¹⁶ O | 33.2540 | Density [kg m ⁻³] | 701.28 |
| ¹⁷ O | 0.01267 | - | - |
| ¹⁸ O | 0.06667 | - | - |

In order to minimise the statistical errors on the results, a statistical relevant number of particle histories has been run (i.e. 2.0E+9).

As described in paragraph 3.4, the results have been normalised to the total neutron source intensity (see eq. (3.6)) using the parameters reported in Table 6.4 and assuming that the WCLL BU was positioned at the equatorial outboard segment. Indeed, the outboard equatorial module is usually used as reference because it is the one with the highest peak values in terms of neutron wall loading. For the same reason it has been selected for these studies.

Table 6.4. Neutron source parameters for the normalization of the WCLL equatorial outboard BU.

| WCLL OB BU | |
|--|--------------|
| Neutron source | |
| P [W] | 2.037000E+09 |
| E_f [J] | 2.818270E-12 |
| Y_{DEMO} [part/s] | 7.227839E+20 |
| F_{1N} | 3.869127E-04 |
| A_{SOURCE} [cm²] | 2.060800E+03 |
| A_{TALLY} [cm²] | 1.576580E+03 |
| Y_{LOCAL} [part/s] | 5.057464E-04 |

Using the above mentioned models, boundary conditions and local neutron source, it has been carried out the neutronic analysis for the evaluation of ¹⁶N and ¹⁷N production rate using the reaction (n,p) identified by reaction rate 103 in MCNP input [53].

In Figure 6.4 and Figure 6.5, the concentration production rates for ¹⁶N and ¹⁷N, the relative errors and the radial profile of neutron flux above 10 MeV and 8 MeV, on the ten FW cooling channels and on the 21 BZ cooling tubes of the WCLL BU, are reported.

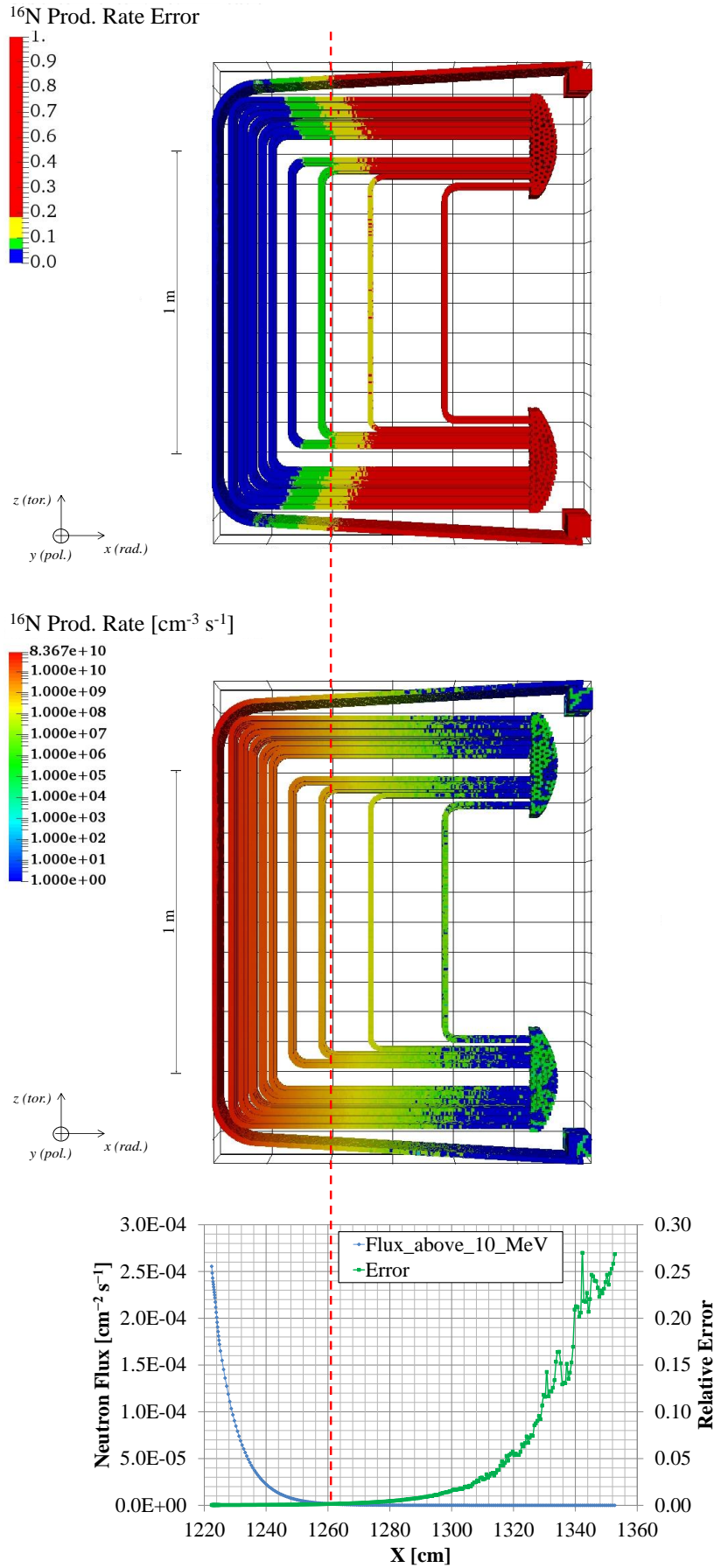


Figure 6.4. ^{16}N production rate 3D distribution of WCLL BU with detail of radial neutron flux above 10 MeV. Top: UM relative error of ^{16}N production rate 3D distribution. Centre: 3D ^{16}N production rate. Bottom: radial neutron flux, averaged in toroidal and poloidal directions, above 10 MeV.

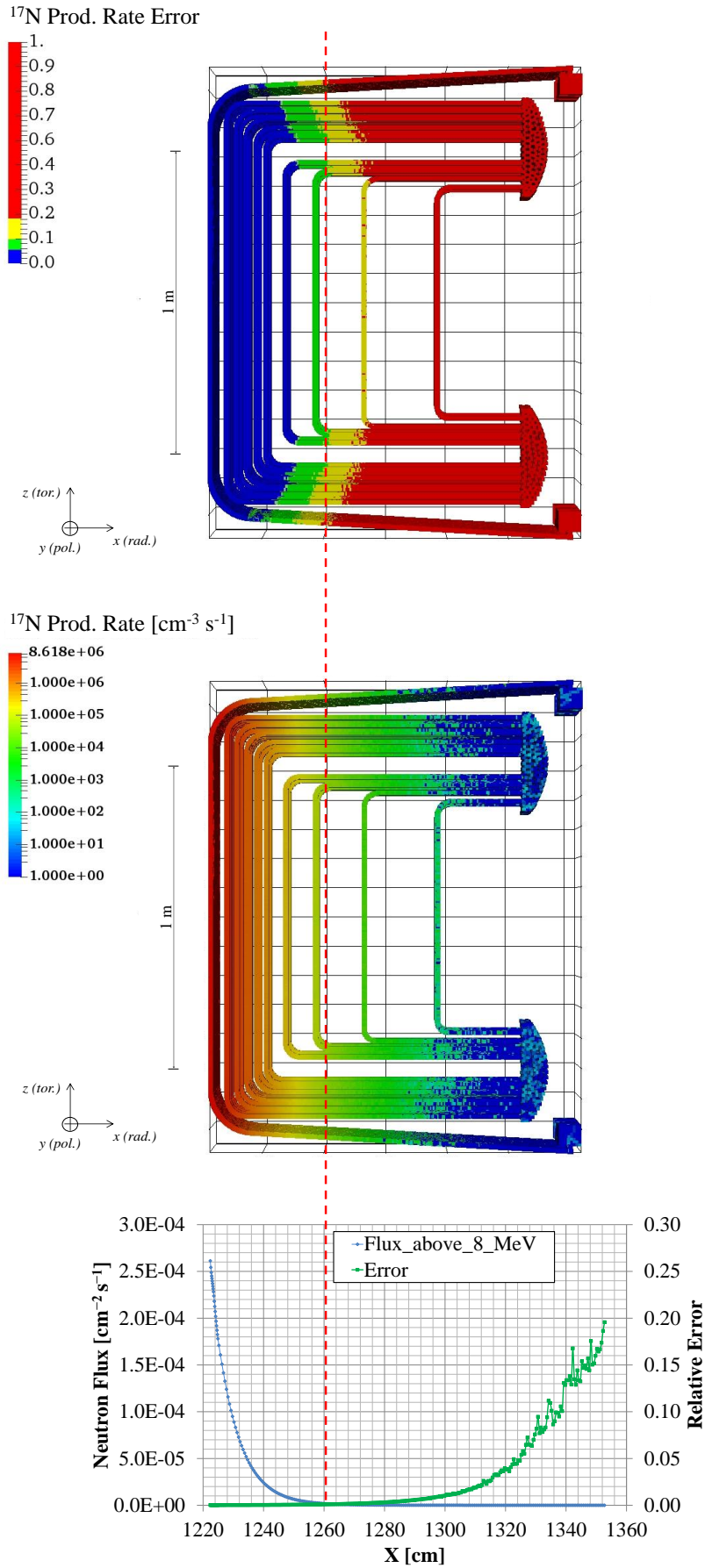


Figure 6.5. ^{17}N production rate 3D distribution of WCLL BU with detail of radial neutron flux above 8 MeV. Top: UM relative error of ^{17}N production rate 3D distribution. Centre: 3D ^{17}N production rate. Bottom: radial neutron flux, averaged in toroidal and poloidal directions, above 8 MeV.

With reference to Figure 6.4, it is possible to observe that a significant production of ^{16}N occurs in the first 40 cm from the plasma facing area. After this distance, the production rate falls down by more than two orders of magnitude going rapidly to zero at the BSS (Figure 6.4- Centre). This behaviour is in line with the radial profile of the neutron flux above 10 MeV. Indeed, as mentioned in paragraph 6.2, the (n,p) reaction of ^{16}O to produce ^{16}N occurs only with neutrons that have an energy higher than 10.24 MeV. Therefore, all the neutrons with energy lower than this threshold are not able to induce any activation reaction with ^{16}O except tunnel phenomena occur.

Moreover, due to the presence of water as well as the light elements used in the WCLL BB for tritium production, the high energy neutrons are rapidly slowed down and the neutron flux above 10 MeV approaches zero practically after 40 cm in accordance with the nitrogen production.

This phenomenon is also highlighted by the special distribution of production rate relative error (Figure 6.4- Top). Furthermore, around the same radial coordinate, the relative error increases to values greater than 10% that, in accordance to the guidelines for the estimation of result goodness, can be questionable or even meaningless.

With reference to Figure 6.5, the same consideration done for the ^{16}N concentration production can be made for the ^{17}N . Indeed, also in this case the ^{17}O (n,p) ^{17}N reaction is subjected to an energy threshold of about 8.55 MeV. The ^{17}N concentration production rate is four orders of magnitude lower than ^{16}N one. This is due mainly to the different concentration between the ^{16}O and ^{17}O (about three orders of magnitude, see Table 6.3) and to the lower cross section of the latter (about one order of magnitude, see Figure 6.1). The neutron flux above 8 MeV goes rapidly down after also ~40 cm producing a drop of ^{17}N production with the consequent increase of the relative error at the same distance (Figure 6.5 - Top and Bottom) as seen for the ^{16}N . Both analyses show a strong dependence of the nitrogen production by the position. Indeed, only the first 40 cm considerably contribute to the final concentration while the rest of the volume dilutes the produced nitrogen. Dedicated studies have been performed in order to assess the impact of homogenisation on the concentration production estimation. It has been found that the FW homogenisation produces an underestimation of the final nitrogen production rate of about 14% with respect to the complete heterogeneous model. This is mainly due to the modification of the water atom distribution in the first centimetres of the FW that cause a modification of the high neutron fluxes reducing the number of reactions. In other words, when the FW is homogenised, the high energy neutrons are slowed down before to interact with water producing a considerable reduction of the nitrogen concentration production rate.

As it was expected, the fully heterogeneous 3D representation of the neutronic domain allows a better calculation of nitrogen production. A comparison between the nitrogen production rate calculated on the pseudo-cells by means of conventional tally F4, modified by FM cards, and the EMBEE card used for the UM is reported in Appendix 9.9.

6.3.3 Fluid-Dynamic Analysis of WCLL Breeder Unit ^{16}N and ^{17}N Concentrations

Once the neutronic transport calculations are performed, the nitrogen concentration production rate is mapped in ANSYS CFX [59] following the same procedure described in paragraph 3.4.1 for the power density.

A numerical model is created for the transport of nitrogen produced within the WCLL coolant and for assessing the final concentration within the BB. Following a 3D FVM for the nitrogen concentration transport, a steady state analysis has been performed for solving the eq. (6.1) together with the boundary conditions (6.4). Dedicated studies have been performed on the effect of diffusion term of eq. (6.1). Indeed, its effect is negligible with respect to the convective and source terms and affects slightly only the concentration distribution on the flow path cross section when a huge diffusive coefficient is used. For this reason, the diffusive term can be neglected from the resolution without losing any information or to compromise the final nitrogen concentration assessment.

The FW and BZ cooling channel fluid domains have been meshed applying a set of local control like sizing, sweep method and inflation layer.

For the FW channel an element size of 2 mm has been used while 4 mm for the BZ cooling tubes. Inflation with 8 layers and a growth rate of 1.15 has been used both for the FW and BZ cooling channels. Elements of the second order like 10-noded tetrahedral (Tet10), 20-noded hexahedral (Hex20) or 15-noded prism (Wed15) elements have been used. An overall amount of about $24E+06$ nodes linked to form about $7.7E+06$ elements has been used. Some details on the mesh are reported in Figure 6.6.

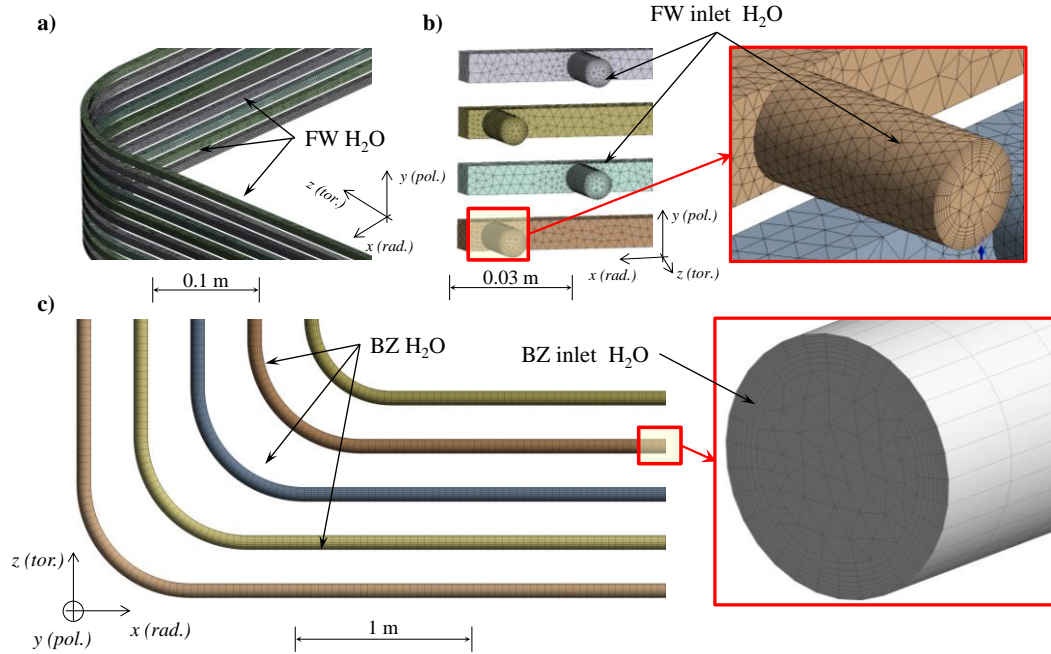


Figure 6.6. FW and BZ coolant water mesh. Top-left (a): details of FW mesh. Top-centre (b): mesh detail of FW inlet channels. Bottom (c): details of BZ mesh.

An isothermal analysis with a reference pressure of 155 bar and an average temperature of $311.5\text{ }^{\circ}\text{C}$ has been carried out. The mass flow rates, 0.38 kg/s for FW and 1.19 kg/s for the BZ, have been derived by the power balance taking into account the operational temperature variation of $33\text{ }^{\circ}\text{C}$ [30, 32]. It is important to underline the importance of the mass flow rate in concentration transport calculations. Indeed, the residence time of water and consequently the amount of oxygen that is activated is strongly depended of the mass flow rate/velocity considered.

Taking into account that one of the main functions of the BB is to transfer the thermal power to the PHTS in thermal-hydraulic condition suitable for the electricity generation, it is clear that the mass flow rate, to be used in the analyses, has to be derived by the local power balance. For this reason, the average heat flux on the FW has been taken into account and not the design value of 0.5 MW/m^2 .

For the implementation of the boundary condition expressed by eq. (6.4), it is necessary to define as input the transit time \tilde{t} of water outside the BB in the PHTS cooling circuit.

According to [115, 116], taking into account the lengths of piping systems and components, and the average velocity of water coolant, the transit time outside the VV has been estimated to be 33.336 s for FW and BZ cooling circuits. Naturally, this is a rough estimation that could be refined when the PHTS cooling circuit design will be more developed and precise. Using the numerical model and the boundary conditions introduced above, the concentration transport calculation both for ^{16}N and ^{17}N have been carried out. The results in terms of ^{16}N and ^{17}N concentration are shown in Figure 6.7. In Figure 6.8, the FW and BZ outlet channels are identified and in Table 6.5 the outlet nitrogen concentrations for both FW and BZ are reported.

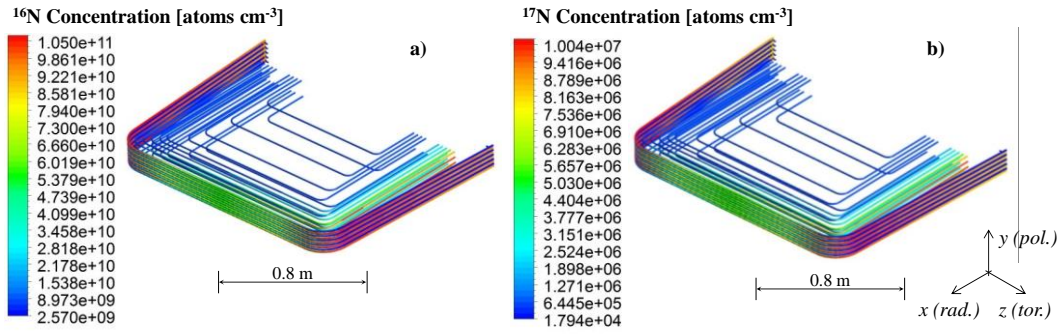


Figure 6.7. ^{16}N and ^{17}N concentrations for the FW and BZ water cooling channel for the OB4 of DEMO 2015.

Table 6.5. Outlet nitrogen concentration.

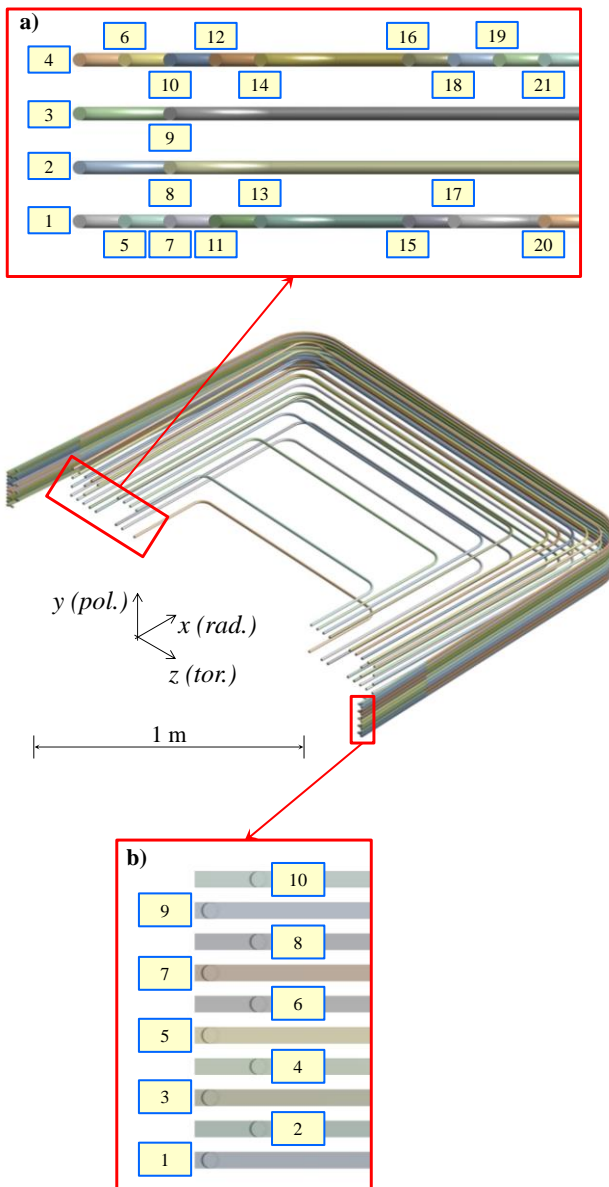


Figure 6.8. Outlet FW channels and BZ tubes. Top (a): 21 outlet cooling tubes of WCLL BZ. Bottom (b): 10 outlet cooling channels of WCLL FW.

| Region | ^{16}N Conc. [cm^{-3}] | ^{17}N Conc. [cm^{-3}] |
|---------------|--|--|
| BZ_1 | 2.846E+10 | 2.694E+06 |
| BZ_2 | 3.126E+10 | 2.965E+06 |
| BZ_3 | 3.128E+10 | 2.967E+06 |
| BZ_4 | 2.849E+10 | 2.697E+06 |
| BZ_5 | 1.782E+10 | 1.674E+06 |
| BZ_6 | 1.784E+10 | 1.676E+06 |
| BZ_7 | 1.123E+10 | 1.044E+06 |
| BZ_8 | 1.186E+10 | 1.105E+06 |
| BZ_9 | 1.187E+10 | 1.106E+06 |
| BZ_10 | 1.123E+10 | 1.044E+06 |
| BZ_11 | 7.118E+09 | 6.504E+05 |
| BZ_12 | 7.114E+09 | 6.505E+05 |
| BZ_13 | 4.630E+09 | 4.126E+05 |
| BZ_14 | 4.621E+09 | 4.122E+05 |
| BZ_15 | 1.922E+09 | 1.540E+05 |
| BZ_16 | 1.922E+09 | 1.542E+05 |
| BZ_17 | 7.820E+08 | 4.465E+04 |
| BZ_18 | 7.820E+08 | 4.473E+04 |
| BZ_19 | 4.087E+08 | 8.324E+03 |
| BZ_20 | 3.651E+08 | 3.264E+03 |
| BZ_21 | 3.655E+08 | 3.274E+03 |
| BZ_Ave | 1.102E+10 | 1.024E+06 |
| FW_1 | 9.259E+10 | 8.221E+06 |
| FW_2 | 9.726E+10 | 8.651E+06 |
| FW_3 | 9.533E+10 | 8.472E+06 |
| FW_4 | 9.416E+10 | 8.366E+06 |
| FW_5 | 9.357E+10 | 8.311E+06 |
| FW_6 | 9.363E+10 | 8.315E+06 |
| FW_7 | 9.421E+10 | 8.372E+06 |
| FW_8 | 9.536E+10 | 8.476E+06 |
| FW_9 | 9.719E+10 | 8.645E+06 |
| FW_10 | 9.257E+10 | 8.217E+06 |
| FW_Ave | 9.459E+10 | 8.405E+06 |

With reference to Figure 6.7, it is important to highlight that the maximum peak in term of ^{16}N and ^{17}N is reached just after the bends in the FW and in the BZ. This effect is due mainly to two factors:

- (i) the source term (i.e. the nitrogen concentration production rate) decreases rapidly after the first centimetres;
- (ii) the decay of nitrogen starts to play a role in the isotope balance.

In particular, the maximum ^{16}N concentration achieved in the FW is $1.05\text{E}+11\text{ cm}^{-3}$ and $3.28\text{E}+10$ in the BZ tubes. With reference to Table 6.5, the average value at the FW outlet is, instead, $9.46\text{E}+10\text{ cm}^{-3}$ and $1.10\text{E}+10\text{ cm}^{-3}$ for the FW and BZ, respectively. Regarding the ^{17}N , the maximum concentration achieved is $1.00\text{E}+07\text{ cm}^{-3}$ in the FW and $3.22\text{E}+06\text{ cm}^{-3}$ in the BZ. The average value at the FW outlet is, instead, $8.41\text{E}+6\text{ cm}^{-3}$ and $1.02\text{E}+6\text{ cm}^{-3}$ for the FW and BZ, respectively.

In terms of specific activity, the average nitrogen isotopes concentrations correspond to $9.195\text{E}+03\text{ MBq cm}^{-3}$ and $1.071\text{E}+03\text{ MBq cm}^{-3}$ for the ^{16}N , and $1.397\text{E}+00\text{ MBq cm}^{-3}$ and $1.703\text{E}-01\text{ MBq cm}^{-3}$ for the ^{17}N at the outlet of FW and BZ, respectively.

From the peak values in the FW, it is possible to argue that the variation with respect to the average concentration at the outlet is about -11% and -19% for ^{16}N and ^{17}N , respectively. This difference is strictly linked and in accordance to the dissimilar half-life of the two isotopes.

Different situation is registered in the BZ. Therefore, the variations of the averages values for ^{16}N and ^{17}N are about three times lower than the maximum one and this effect cannot be explained only with the half-life of the isotopes analysing the spatial distribution of the nitrogen production rate. Actually, the tubes located in the rear of the BZ do not experience a big production of activated isotopes and, then, their outlet concentrations is two or three orders of magnitude lower with respect to the other tubes (see ^{16}N and ^{17}N concentrations for the tubes from 17 to 21 in Table 6.5). Practically, they act as dilutors towards the other tubes with higher concentration.

These effects have been discovered by means of MAIA procedure and, in particular, of the possibility to use a heterogeneous neutronic model as well as a fully 3D transport analysis.

The MAIA procedure takes into account in a "precise" manner the effects of the flow. Indeed, the higher the water velocity is, the less irradiated it becomes and, thus, the lower the production of nitrogen is. This results then in a lower outlet concentration. It should also be pointed out that outside the effective flow zone a smaller flow (e.g. enlarging the outlet WCLL manifold) is more convenient because the transit time and, therefore, the nitrogen decay increase.

The outcomes of MAIA procedure for water activation analysis, in terms of ^{16}N and ^{17}N outlet concentration, can be used as input for safety analysis or dose rate estimation to the PHTS equipment.

7 Summary and Outlook

7.1 Summary

The objective of this work is the creation of multi-physics design approach aimed to the coupling of the three main pillar analyses used for the BB design, namely the neutron and photon transport analysis, the thermal fluid-dynamic calculation and the structural stress exploration. Moreover, such an approach has also to supply to the designers an adequate accurateness and flexibility guaranteeing a relatively short computational time.

The strategy, followed for the achievement of this challenge, consists of creating a CAD-centric and loosely-coupled procedure for the design of the BB concepts based on the coupling of the neutronic, thermal-hydraulic and thermo-mechanic calculations adopting a sub-modelling technique, named MAIA. The MAIA procedure bases its architecture on the use of validated codes and on the minimisation of their number. It is articulated in 10 main steps that go from the decomposition of generic CAD in a format suitable for neutron/photon transport analysis to the nuclear analysis for the assessment of volumetric heating, from the assessment of temperature and velocity fields to the evaluation of deformation and stress field, from the evaluation of nitrogen isotopes production rates to the calculation of the nitrogen concentration taking into account the effects of the flow. All the steps share the same geometry details and the consistency between the input and output parameters. The new MAIA procedure differs from the conventional coupling approach with respect to three key aspects.

First, it does not introduce homogenisations of models and loads. Indeed, the computational needs and the scope of some analyses (e.g. neutronic calculation), conventionally performed for the design of the BB, are more related to the investigation of the overall reactor performances with the aim to have an integral overview of the main design parameters of DEMO reactor like TBR, shielding performances, dpa assessment, etc. From these investigations, some inputs are usually derived for driving the BB design (e.g. power density). However, this approach brings to the introduction of some simplification both in the model nodalisation and in the calculated loads that might hide specific design issue created by strong gradients in the loads and responses. These issues are solved in MAIA by means of detailed nodalisation of geometry features using both CSG and Hybrid representations for what concerns the neutronic input. These methodologies allow a representation of the geometry that deviates from the real CAD for less than 0.01 % in terms of volume.

Second, MAIA can capture load gradients at high resolution in the three directions for all the analysis involved without to require prohibitive computational performances. Indeed, usually in the conventional coupling approach, the resolution, used among the neutronic, thermal-hydraulic and thermo-mechanic calculations, differs according to the analysis that is carried out.

And third, MAIA keeps the consistency between the three analyses maintaining the congruence between the inputs and outputs. Usually, the conventional coupling approach is shared among several teams and the transfer of data is not always coherent because of different level of model developments or sensibility shown by designers.

However, the computational effort required by the CAD-centric feature of MAIA procedure imposes the representation of BB portions if a high geometric detail has to be maintained. For this reason, a research campaign has been dedicated for the definition and validation of a set of boundary conditions for each performed calculation. As far as the neutron and photon radiation transport analyses are concerned, it has been found that the set of reflecting and white conditions in the poloidal toroidal directions, together with

the presence of VV and the definition of local neutron and photon source, produces a mismatch of 0.23 % and -0.48 % in terms of power deposition between the DEMO and the local (e.g. module and slice) models with a mean value of the power density error of 5.17 % and -3.97 %, respectively. These errors, although negligible and driven by the presence of localised zones where small power density values are assessed, represent confidence interval when neutron/photon transport analysis are carried out using MAIA procedure. On the other side, it has been demonstrated that the neutronic symmetry conditions are valid in the entire module up to the last slices nearby the caps. Therefore, the set of boundary conditions used in MAIA and the applicability of the procedure itself can be spread for the entire module with the exception of the cap regions. Furthermore, a sensitivity analysis on cosine subdivision of local neutron and photon source has been performed indicating in 10 bins the best subdivision number in terms of discretisation, fidelity of the results obtained with respect to the reference model and computational effort.

Concerning the analysis of thermal-hydraulic boundary conditions, it has been found that the variation on mass flow rates (comprised between ~ -1.3 % and ~ -0.6 %) as well as power density fluctuation (up to ~ 6 % in the neighbouring domains) affect the temperature distribution for less than ± 2.4 % demonstrating the applicability of poloidal symmetry conditions. This has also been verified using a statistical check (t-test) showing that symmetry conditions, for applied loads on the adjacent slices with a standard deviation of 6 %, can be considered valid at a 95% confidence level.

Furthermore, it has to be highlighted that, for the validation of the thermal-hydraulic boundary conditions, a well-known procedure for fission applications has been newly introduced in the design cycle of breeding blankets in fusion, which is based on the use of porous media and thermal-hydraulic characteristic of local circuits. This represents an additional and positive side-effect contribution to the methodologies that can be applied to the BB design. Indeed, this new application of porous media model is used for the investigation of mass flow rate distribution as well as for the estimation of the overall segment pressure drop but also for the optimisation of the segment hydraulic layout without requiring huge computational efforts.

As far as the thermo-mechanical analyses are concerned, it has been identified the set of boundary conditions (e.g. radial and toroidal displacements prevented to the nodes lying along the toroidal and poloidal direction, symmetry at the lower cut surface and GPS to the top one) that produce a discrepancy in terms of displacement in the sub-model comprised between the -6 % and the 4 % and conservative assessment of membrane and bending stresses both for primary and secondary stresses. The impact of the temperature variation has also been investigated showing that the fluctuations on total deformation are comprised between -0.3 % and the 1.7 %, on equivalent membrane stress up to 15 % while on equivalent bending stress between the -7 % and the 5 %.

As a proof-of-concept, the MAIA procedure and the consistency verification of the boundary conditions have then been used to discern and evaluate the impact on the BB design. So, it has been demonstrated that some criticalities are present in the design. Indeed, the application of MAIA procedure has highlighted problematic regions on the HCPB BB that have not been discovered using the conventional coupling process based on the simplification of geometry features and loads. In particular, the fluid-dynamic results show a violation of the temperature requirement limits that have not been solved introducing design solutions. Furthermore, these violations of thermal-hydraulic requirements produce very intense values of Von Mises stresses at the junction with the armour, in the caps of the CP Helium distributors and at the connections between the BP and the CP. In this way, the benefits that can be derived from the use of coupling procedures, based on CAD-centric and adopting sub-modelling techniques have been demonstrated among each analysis field. It has also been demonstrated the positive effect of the synergistic interactions study that, avoiding excessive simplifications in the geometry and load representation, show the presence of driving design gradients.

In order to further demonstrate the versatility and adaptability of the MAIA procedure to the investigation of specific phenomena, the safety related issue of water activation in fusion reactors has been also approached. The activated water represents a distributed radiation photon and neutron source that can jeopardise the sensible equipment (e.g. valves) to which a safety function is associated and limit the human intervention. Using MAIA procedure, it has been possible to take into account the effects of the flow on the nitrogen concentration and to provide useful information for the development of WCLL design and its PHTS. Indeed, the lower the water velocity in not-irradiated zones (e.g. BSS), the highest is the decay and, consequently, lower the radioactivity of Nitrogen isotopes. This allowed providing indication on the WCLL design for the minimisation of water activation as well as on the ^{16}N and ^{17}N concentration that can be used as input for safety analysis or dose rate estimation to the PHTS equipment.

However, the applicability of MAIA procedure is currently limited to the BB and cannot be directly exported to other In-Vessel components without a revalidation of the boundary conditions. Additionally, a more stringent uncertainty analysis has to be carried out on thermo-mechanical boundary conditions if MAIA procedure has to be used for more advanced design phase. In particular, it has to demonstrate that, for all the load combinations, the use of sub-models produce an over estimation of the stress and deformations that, in this work, has been proved only for the normal and for the over pressurisation scenarios.

7.2 Outlook and Future Work

With the positive development coupling procedure, with the consistency verification of the boundary conditions to be used for the study of the BB, with the demonstration of the benefit for the design and with the evident flexibility to adapt to the study of new phenomena, the natural continuation of the present work is the enhancement of MAIA procedure including the tritium transport analysis and the magnetohydrodynamic (MHD) calculations for liquid metal BBs. Their integration will open the door to an accurate and precise representation of the BB and to the holistic study of these phenomena and their impact of BB performances. Indeed, the tritium permeation through the BB structure represents one of the main safety related issues in terms of inventories and releases. It is driven mainly by the interaction of neutrons with breeder material and by the temperature field in structures and fluids as well as by the velocity of coolant. All these aspects have been already addressed in this work and the basement for the tritium permeation analysis has been established already. Therefore, starting from the present work, following the approach already used for the transport of nitrogen isotopes, it would be possible to enhance the MAIA procedure for the study of tritium permeation.

Another important aspect, which could be addressed in future works, refers to the impact of MHD effects on heat transfer and tritium transport in liquid metal BBs. Indeed, the flow of LiPb in WCLL is strongly affected by magnetic field and, in particular, by the magnetic field gradients that can arise within the BB. Therefore, the MHD could trigger unexpected buoyancy effects on LiPb and, then, the heat transfer with the cooling circuit but also could have an impact on the tritium permeation that, as explained, is driven by temperatures and fluid velocities. It represents another coupling problem that, for its own nature, must be studied by a multi-physics approach. Moreover, the automatization of all the MAIA steps, using dedicated scripts for the creation of models and running of analyses, can be introduced with the aim to perform parametric studies of geometry. This improvement could provide to the designers a fully integrated tool able to investigate a wide range of configurations in order to find optimum and integrated solutions for all the three analyses. In this context, the integration with system codes like MIRA could be pursued. This will allow taking into account in both directions the impact of reactor parameters and of detailed BB design solutions.

8 References

- [1] International Energy Agency, "Global Energy & CO₂ Status Report 2018", 2019 Accessed on: 06.11.2019, Available: <https://webstore.iea.org/global-energy-co2-status-report-2018>.
- [2] International Energy Agency, "World Energy Outlook 2018", 2018 Accessed on: 06.11.2019, Available: <https://webstore.iea.org/download/summary/190?fileName=English-WEO-2018-ES.pdf>.
- [3] International Renewable Energy Agency, "Global energy transformation: A roadmap to 2050 (2019 edition)", 2019 Accessed on: 06.11.2019, Available: <https://irena.org/publications/2019/Apr/Global-energy-transformation-A-roadmap-to-2050-2019Edition>.
- [4] Wikipedia. (2019, Accessed on: 03.05.2019). https://de.wikipedia.org/wiki/Fridays_for_Future.
- [5] Directorate General for Energy, "Energy roadmap 2050", European Commission, 2012 Accessed on: 06.11.2019, Available: https://ec.europa.eu/energy/sites/ener/files/documents/2012_energy_roadmap_2050_en_0.pdf.
- [6] Directorate General for Research and Innovation, "A new horizon for Europe", European Commission, 2018 Accessed on: 06.11.2019, Available: https://ec.europa.eu/info/sites/info/files/research_and_innovation/contact/documents/horizon_europe_impact_assessment_book_web_version.pdf.
- [7] EUROfusion Programme Manager, "European Research Roadmap to the Realisation of Fusion Energy", EUROfusion, 978-3-00-061152-0, 2018 Accessed on: 06.11.2019, Available: https://www.euro-fusion.org/fileadmin/user_upload/EUROfusion/Documents/2018_Research_roadmap_long_version_01.pdf.
- [8] M. Keilhacker, A. Gibson, C. Gormezano, P. J. Lomas, P. R. Thomas, M. L. Watkins, P. Andrew, B. Balet, D. Borba, C. D. Challis *et al.*, "High fusion performance from deuterium-tritium plasmas in JET", *Nuclear Fusion*, vol. 39, no. 2, pp. 209-234, 1999.
- [9] G. Federici, W. Biel, M. R. Gilbert, R. Kemp, N. Taylor and R. Wenninger, "European DEMO design strategy and consequences for materials", *Nuclear Fusion*, vol. 57, no. 9, p. 092002, 2017.
- [10] A. A. Harms, K. F. Schoepf, G. H. Miley and D. R. Kingdon, *Principles of Fusion Energy: An Introduction to Fusion Energy for Students of Science and Engineering*. Hackensack, New York, US: World Scientific, 2000, ISBN: 978-981-238-0335-7.
- [11] Wikipedia. (2019, Accessed on: 10.01.2019). https://en.wikipedia.org/wiki/Nuclear_binding_energy.
- [12] National-Physical-Laboratory. (2017, Accessed on: 03.05.2019). www.kayelaby.npl.co.uk/atomic_and_nuclear_physics.
- [13] W. M. Stacey, *Fusion: An Introduction to the Physics and Technology of Magnetic Confinement Fusion*. Darmstadt, Germany: 2010 WILEY-VCH Verlag GmbH & Co. KGaA, 2010, ISBN: 978-3-527-40967-9.
- [14] L. Jr. Spitzer, "The Stellarator Concept", *The Physics of Fluids*, vol. 1, no. 4, pp. 253-264, 1958.
- [15] E. A. Azizov, "Tokamaks: from A D Sakharov to the present (the 60-year history of tokamaks)", *Physics-Uspekhi*, vol. 55, no. 2, pp. 190-203, 2012.
- [16] P. H. Rebut, "ITER: the first experimental fusion reactor", *Fusion Engineering and Design*, vol. 30, no. 1, pp. 85-118, 1995.
- [17] C. Bachmann, "DEMO Plant Description Document v1.4", EUROfusion, EFDA D 2KVVQZ, 2015.
- [18] G. Federici, C. Bachmann, W. Biel, L. Boccaccini, F. Cismondi, S. Ciattaglia, M. Coleman, C. Day, E. Diegele, T. Franke *et al.*, "Overview of the design approach and prioritization of R&D activities towards an EU DEMO", *Fusion Engineering and Design*, vol. 109-111, Pt. B, pp. 1464 - 1474, 2016.
- [19] M. Abdou, Neil B. Morley, Sergey Smolentsev, Alice Ying, Siegfried Malang, Arthur Rowcliffe and Mike Ulrickson, "Blanket/first wall challenges and required R&D on the pathway to DEMO", *Fusion Engineering and Design*, vol. 100, pp. 2-43, 2015.
- [20] M. Kovari, R. Kemp, H. Lux, P. Knight, J. Morris and D. J. Ward, "'PROCESS': A systems code for fusion power plants—Part 1: Physics", *Fusion Engineering and Design*, vol. 89, no. 12, pp. 3054-3069, 2014.

-
- [21] C. Reux, L. Di Gallo, F. Imbeaux, J. F. Artaud, P. Bernardi, J. Bucalossi, G. Ciraolo, J. L. Duchateau, C. Fausser, D. Galassi *et al.*, "DEMO reactor design using the new modular system code SYCOMORE", *Nuclear Fusion*, vol. 55, no. 7, p. 073011, 2015.
- [22] F. Franza, "Development and Validation of a Computational Tool for Fusion Reactors' System Analysis", Doctoral thesis, Karlsruhe Institut für Technologie (KIT), 2019.
- [23] R. Wenninger, "Reference Design - 2015 April (EU DEMO1 2015) PROCESS Full Output", EUROfusion, EFDA D 2MDKFH, 2015.
- [24] B. Meszaros, "EU DEMO1 2015 DEMO-Tokamak-Complex (CAD Model)", EUROfusion, EFDA D 2M9AJJ, 2015.
- [25] R. Wenninger, "DEMO1 Reference Design - 2015 April ("EU DEMO1 2015") - Initial Geometry Based on PROCESS Output (v1.0)", EUROfusion, EFDA D 2MG46D, 2015.
- [26] F. Hernández, P. Pereslavtsev, Q. Kang, P. Norajitra, B. Kiss, G. Nádas and O. Bitz, "A new HCPB breeding blanket for the EU DEMO: Evolution, rationale and preliminary performances", *Fusion Engineering and Design*, vol. 124, pp. 882-886, 2017.
- [27] L. V. Boccaccini, G. Aiello, J. Aubert, C. Bachmann, T. Barrett, A. Del Nevo, D. Demange, L. Forest, F. Hernandez, P. Norajitra *et al.*, "Objectives and status of EUROfusion DEMO blanket studies", *Fusion Engineering and Design*, vol. 109-111, no. PartB, pp. 1199-1206, 2016.
- [28] F. Hernandez, "HCPB Design Report", EUROfusion, EFDA D 2MNBH9, 2016.
- [29] A. Tassone, A. Del Nevo, P. Arena, G. Bongiovi, G. Caruso, P. A. di Maio, G. di Gironimo, M. Eboli, N. Forgone, R. Forte *et al.*, "Recent Progress in the WCLL Breeding Blanket Design for the DEMO Fusion Reactor", *IEEE Transactions on Plasma Science*, vol. 46, no. 5, pp. 1446-1457, 2018.
- [30] A. Del Nevo, E. Martelli, P. Agostini, P. Arena, G. Bongiovi, G. Caruso, G. Di Gironimo, P. A. Di Maio, M. Eboli, R. Giammusso *et al.*, "WCLL breeding blanket design and integration for DEMO 2015: status and perspectives", *Fusion Engineering and Design*, vol. 124, pp. 682-686, 2017.
- [31] P. A. Di Maio, P. Arena, G. Bongiovi, P. Chiovaro, A. Del Nevo and M. L. Richiusa, "On the thermo-mechanical behaviour of DEMO water-cooled lithium lead equatorial outboard blanket module", *Fusion Engineering and Design*, vol. 124, pp. 725-729, 2017.
- [32] A. Del-Nevo, "WCLL Design Report 2015", EUROfusion, EFDA D 2N6WLQ, 2016.
- [33] Günter Kessler, Anke Vesper, Franz-Hermann Schlüter, Wolfgang Raskob, Claudia Landman and Jürgen Päsler-Sauer, *The Risks of Nuclear Energy Technology*. Karlsruhe Institut für Technologie (KIT), Eggenstein-Leopoldshafen, Germany: Springer, 2014, ISBN: 9783642551161.
- [34] G. Grasso, M. Adorni, W. Ambrosini, D. Araneo, M. Aufiero, S. Bortot, A. Cammi, M. Cherubini, P. Console Camprini, E. Coscarelli *et al.*, "Studio di fattibilità per lo sviluppo di un modello multi-fisica (neutronica, termoidraulica e termomeccanica) di dinamica spaziale di nocciolo: rapporto di analisi della codicistica esistente a supporto dello sviluppo di uno strumento di dinamica spaziale di nocciolo", ENEA, RdS/2011/364, 2011.
- [35] V. Seker, J. W. Thomas and T. J. Downar, "Reactor physics simulations with coupled Monte Carlo calculation and computational fluid dynamics", American Nuclear Society, United States, ANL/NE/CP--58661, 2007 Accessed on: 06.11.2019, Available: http://inis.iaea.org/search/search.aspx?orig_q=RN:41133373.
- [36] M. Calleja Reyna, "Improvements in Multi-physics and Multi-scale Methodologies for Safety-related Investigations of Pressurized Water Reactors within the NURESIM Platform", Doctoral thesis, Karlsruhe Institut für Technologie (KIT), 2013.
- [37] P. J. Turinsky, "Advances in multi-physics and high performance computing in support of nuclear reactor power systems modelling and simulation", *Nuclear Engineering and Technology*, vol. 44, 2012.
- [38] Jerome Serp, Michel Allibert, Veronique Ghetta, Daniel Heuer, Elsa Merle-Lucotte, Ondrej Benes, Sylvie Delpech, Olga Feynberg, Victor Ignatiev, David Holcomb *et al.*, "The molten salt reactor (MSR) in generation IV: Overview and perspectives", *Progress in Nuclear Energy*, vol. 77, pp. 308-319, 2014.
- [39] T. J. Tautges, R. Meyers, K. Merkley, C. Stimpson and C. Erns, "MOAB : a mesh-oriented database", U.S. Department of Energy, Sandia Report SAND2004-1592, 2004.
- [40] T. J. Tautges, Alvaro Caceres, Rajeev Jain, Hong-Jun Kim, Jason A. Kraftcheck and Brandon M. Smith, "Coupled multi-physics simulation frameworks for reactor simulation: A bottom-up approach", in *International Conference on Mathematics and Computational Methods Applied to*
-

-
- Nuclear Science and Engineering (M&C 2011)*, Brazil, 2011, http://inis.iaea.org/search/search.aspx?orig_q=RN:47073022, ISBN: 978-85-63688-00-2.
- [41] A. M. Garofalo, V. S. Chan, R. D. Stambaugh, J. P. Smith and C. P. C. Wong, "Mission and Overview of a Fusion Development Facility", *IEEE Transactions on Plasma Science*, vol. 38, no. 3, pp. 461-467, 2010.
- [42] M. R. Gilbert, S. L. Dudarev, S. Zheng, L. W. Packer and J. Ch Sublet, "An integrated model for materials in a fusion power plant: transmutation, gas production, and helium embrittlement under neutron irradiation", *Nuclear Fusion*, vol. 52, no. 8, p. 083019, 2012.
- [43] B. Smith, P. P. H. Wilson and M. E. Sawan, "Three Dimensional Neutronics Analysis of the ITER First Wall/Shield Module 13", in *2007 IEEE 22nd Symposium on Fusion Engineering*, New Mexico, 2007, pp. 1-4, <http://ieeexplore.ieee.org/stamp/stamp.jsp?tp=&arnumber=4337910&isnumber=4337855>, ISBN: 1078-8891.
- [44] A. Ying, M. Abdou, H. Zhang, R. Munipalli, M. Ulrickson, M. Sawan and B. Merrill, "Progress on an integrated multi-physics simulation predictive capability for plasma chamber nuclear components", *Fusion Engineering and Design*, vol. 85, no. 7-9, pp. 1681-1688, 2010.
- [45] K. Jiang, Weiqiang Ding, Xiaokang Zhang, Jia Li, Xuebin Ma, Kai Huang, Yuetong Luo and Songlin Liu, "Development of neutronic-thermal hydraulic-mechanic-coupled platform for WCCB blanket design for CFETR", *Fusion Engineering and Design*, vol. 137, pp. 312-324, 2018.
- [46] Y. Qiu, "Development of a coupling approach for multi-physics analyses of fusion reactors", Doctoral thesis, Karlsruhe Institut für Technologie (KIT), 2016.
- [47] Salome. (2019, Accessed on: 07.05.2019). <http://www.salome-platform.org/>.
- [48] Y. Huang, Fabio Cismonti, Eberhard Diegele, Giafranco Federici, Alessandro Del Nevo, Fabio Moro and Nasr Ghoniem, "Thermo-structural design of the European DEMO water-cooled blanket with a multiscale-multiphysics framework", *Fusion Engineering and Design*, vol. 135, pp. 31-41, 2018.
- [49] J. Shimwell, Rémi Delaporte-Mathurin, Jean-Charles Jaboulay, Julien Aubert, Chris Richardson, Chris Bowman, Andrew Davis, Andrew Lahiff, James Bernardi, Sikander Yasin *et al.*, "Multiphysics analysis with CAD-based parametric breeding blanket creation for rapid design iteration", *Nuclear Fusion*, vol. 59, no. 4, p. 046019, 2019.
- [50] J. J. Duderstadt and W. Russell Martin, *Transport theory*. New York, US: Wiley, 1979, ISBN: 047104492X, 9780471044925.
- [51] John R. Lamarsh, *Introduction to Nuclear Reactor Theory*. University of Michigan, US: American Nuclear Society, 2002, ISBN: 0894480405, 9780894480409.
- [52] Weston M. Stacey, *Nuclear Reactor Physics, 2nd, Completely Revised and Enlarged Edition*. Darmstadt, Germany: John Wiley & Sons, 2007, ISBN: 3527611053, 9783527611058.
- [53] X-5-Monte-Carlo-Team, "MCNP - Version 5, Vol. I: Overview and Theory", Los Alamos National Laboratory, LA-UR-03-1987, 2003.
- [54] C.J. Werner, "MCNP Users Manual - Code Version 6.2", Los Alamos National Laboratory, LA-UR-17-29981, 2017.
- [55] Bastian E. Rapp, "Chapter 13 - Continuity and Navier-Stokes Equations in Different Coordinate Systems", in *Microfluidics: Modelling, Mechanics and Mathematics*, B. E. Rapp, Ed. Oxford, United Kingdom: Elsevier, 2017, pp. 303-308.
- [56] David P. Kessler and Robert A. Greenkorn, *Momentum, heat, and mass transfer fundamentals*. Bosa Roca, US: Taylor & Francis Inc, 1999, ISBN: 978-0824719722.
- [57] J. R. Welty, Charles E. Wicks, Robert E. Wilson and Gregory L. Rorrer, *Fundamentals of Momentum, Heat, and Mass Transfer*. Chichester, United Kingdom: John Wiley and Sons Ltd, 2008, ISBN: 0470128688, 978-0470128688.
- [58] Joel H. Ferziger and Milovan Peric, *Computational Methods for Fluid Dynamics 3rd Edition*. Berlin Heidelberg, Germany: Springer 2001, ISBN: 3540420746.
- [59] ANSYS CFX, "https://www.sharcnet.ca/Software/Ansys/17.2/en-us/help/cfx_thry/cfx_thry.html", ed: ANSYS, 2019, Accessed on: 11.03.2019.
- [60] H. S. Carslaw and J. C. Jaeger, *Conduction of Heat in Solids*. Oxford, United Kingdom: Clarendon Press, 1959, ISBN: 0198533683, 9780198533689.
- [61] R. J. Atkin and N. Fox, *An Introduction to the Theory of Elasticity*. Mineola, New York, US: Courier Corporation, 2013, ISBN: 0486150992, 9780486150994.
-

-
- [62] S. P. Timoshenko and J. N. Goodier, *Theory of Elasticity*. University of Michigan, US: McGraw-Hill Education, 1969, ISBN: 0070642702, 9780070642706.
- [63] A. Kotousov and C. Hui Wang, "Fundamental solutions for the generalised plane strain theory", *International Journal of Engineering Science*, vol. 40, no. 15, pp. 1775-1790, 2002.
- [64] S. M. Kamal, U. S. Dixit, A. Roy, Q. Liu and Vadim V. Silberschmidt, "Comparison of plane-stress, generalized-plane-strain and 3D FEM elastic-plastic analyses of thick-walled cylinders subjected to radial thermal gradient", *International Journal of Mechanical Sciences*, vol. 131-132, pp. 744-752, 2017.
- [65] G. R. Liu and S. S. Quek, *The Finite Element Method (Finite Element Method)*. Oxford, United Kingdom: Butterworth-Heinemann, 2014, p. 464, ISBN: 978-0-08-098356-1.
- [66] ANSYS Mechanical, "Academic Research Mechanical - Release 19.0", ed: ANSYS, 2019.
- [67] L. N. Topilski, D. A. Petti, B. J. Merrill, S. T. Polkinghorne, R. Moore, T. Inabe, Y. Seki, R. Kurihara, W. Gulden, J. M. Gay *et al.*, "Validation and verification of ITER safety computer codes", in *17th IEEE/NPSS Symposium Fusion Engineering (Cat. No.97CH36131)*, California, 1997, vol. 1, pp. 188-191, DOI: 10.1109/FUSION.1997.687017.
- [68] G. A. Spagnuolo, P. Chiovaro, P. A. Di Maio and R. Favetti, "A multi-physics integrated approach to breeding blanket modelling and design", *Fusion Engineering and Design*, vol. 143, pp. 35-40, 2019.
- [69] DesignModeler, "ANSYS Academic Research DesignModeler, Release 19.1", ed: ANSYS, 2019.
- [70] G. A. Spagnuolo, F. Franza, U. Fischer and L. V. Boccaccini, "Identification of blanket design points using an integrated multi-physics approach", *Fusion Engineering and Design*, vol. 124, pp. 582-586, 2017.
- [71] U. Fischer, M. Angelone, T. Bohm, K. Kondo, C. Konno, M. Sawan, R. Villari and B. Walker, "Benchmarking of the FENDL-3 Neutron Cross-section Data Starter Library for Fusion Applications", *Nuclear Data Sheets*, vol. 120, pp. 230-234, 2014.
- [72] International Atomic Energy Agency Nuclear Data Service. (Accessed on: 27.05.2019). *FENDL-3.1d: Fusion Evaluated Nuclear Data Library Ver.3.1d*. Available: <https://www-nds.iaea.org/fendl/index.html>.
- [73] A. H. Dhaba'an and T. D. Beynon, "Albedo calculations for candidate fusion reactor materials used in the inboard side of a compact tokamak reactor and the effects of using such materials on the tritium breeding", *Progress in Nuclear Energy*, vol. 28, no. 4, pp. 391-403, 1994.
- [74] A. Khanouchi, A. Sabir, M. Boulkheir, R. Ichaoui, J. Ghassoun and A. Jehouani, "The Albedo effect on neutron transmission probability", *Applied Radiation and Isotopes*, vol. 48, no. 10, pp. 1667-1671, 1997.
- [75] F. Wasastjerna, "Calculating streaming with the "tally source" method, as applied to IFMIF", *Annals of Nuclear Energy*, vol. 35, no. 3, pp. 438-445, 2008.
- [76] P. Pereslvtsev, "2016 DEMO HCPB MCNP model", EUROfusion, EFDA D 2MK7GG, 2016.
- [77] Fabio Moro, "2016_DEMO_WCLL_MCNP_model.txt", EUROfusion, EFDA D 2L5U6W, 2016.
- [78] E. Sartori, "VITAMIN-J, A 175 group neutron cross section library based on JEF-1 for shielding Benchmark calculations", vol. JEF-1/Dot-100, 1985.
- [79] P. Pereslvtsev, "2015 DEMO HCPB MCNP model", EUROfusion, EFDA D 2M5J2G, 2016.
- [80] Sakae Yagi and Daizo Kunii, "Studies on heat transfer near wall surface in packed beds", *AIChE Journal*, vol. 6, no. 1, pp. 97-104, 1960.
- [81] J. Reimann, G. Piazza and H. Harsch, "Thermal conductivity of compressed beryllium pebble beds", *Fusion Engineering and Design*, vol. 81, no. 1, pp. 449-454, 2006.
- [82] *RCC-MRx - Appendix A. Materials properties data support document for Eurofer steel*, DMR 10-115 A3-19AS, 2012.
- [83] P. A. Di Maio, P. Arena, G. Bongiovì, I. Catanzaro, A. Del Nevo and R. Forte, "On the effect of stiffening plates configuration on the DEMO Water Cooled Lithium Lead Breeding Blanket module thermo-mechanical behaviour", *Fusion Engineering and Design*, vol. 146, pp. 2247-2250, 2019.
- [84] P. Chiovaro, P. Arena, J. Aubert, G. Bongiovì, P. A. Di Maio, R. Giammusso and A. Li Puma, "Assessment of the Thermo-mechanical Performances of a DEMO Water-Cooled Liquid Metal Blanket Module", *Journal of Fusion Energy*, vol. 34, no. 2, pp. 277-292, 2015.
- [85] R. Favetti, P. Chiovaro, P. A. Di Maio and G. A. Spagnuolo, "Validation of Multi-Physics Integrated Procedure for the HCPB Breeding Blanket", *International Journal of Computational*
-

-
- Methods*, vol. 17, no. 6, p. 1950009, 2020.
- [86] F. A. Hernández and P. Pereslavytsev, "First principles review of options for tritium breeder and neutron multiplier materials for breeding blankets in fusion reactors", *Fusion Engineering and Design*, vol. 137, pp. 243-256, 2018.
- [87] P. Pereslavytsev, "2016 DEMO HCPB MCNP model", EUROfusion, 2016, vol. EFDA D 2MK7GG.
- [88] P. Pereslavytsev, Ulrich Fischer, Francisco Hernandez and Lei Lu, "Neutronic analyses for the optimization of the advanced HCPB breeder blanket design for DEMO", *Fusion Engineering and Design*, vol. 124, pp. 910-914, 2017.
- [89] H. Brysk, "Fusion neutron energies and spectra", *Plasma Physics*, vol. 15, no. 7, pp. 611-617, 1973.
- [90] C. Fausser, A. Li Puma, F. Gabriel and R. Villari, "Tokamak D-T neutron source models for different plasma physics confinement modes", *Fusion Engineering and Design*, vol. 87, no. 5, pp. 787-792, 2012.
- [91] H. A. Hussain, "Mean neutron energy and the neutron spectra from T(d,n)4He reaction", *The International Journal of Applied Radiation and Isotopes*, vol. 35, no. 3, pp. 201-207, 1984.
- [92] Y. Wu, Y. Chen, Q. Huang, B. Liu, X. Zhu and M. Kong, "Analysis on nuclear heating in the superconducting coils of HT-7U tokamak fusion device", *Fusion Engineering and Design*, vol. 66-68, pp. 1013-1017, 2003.
- [93] C. Yi-xue and Wu Yi-can, "Effect of Fusion Neutron Source Numerical Models on Neutron Wall Loading in a D-D Tokamak Device", *Plasma Science and Technology*, vol. 5, no. 2, pp. 1749-1754, 2003.
- [94] P. Bilski, J. Blomgren, F. D'Errico, A. Esposito and G. Fehrenbacher, "Complex workplace radiation fields at European high-energy accelerators and thermonuclear fusion facilities", in "CERN Yellow Reports: Monographs", CERN, Geneva, 2006, DOI: 10.5170/CERN-2006-007, Accessed on: 26.06.2019.
- [95] C. D. Fletcher and R. R. Schultz, "RELAP5/MOD3 Code Manual ", vol. 5, NUREG/CR-5535 INEL-95/0174 ed: Idaho National Engineering Laboratory 1995.
- [96] R. Chen, Maolin Tian, Sen Chen, Wenxi Tian, G. H. Su and Suizheng Qiu, "Three dimensional thermal hydraulic characteristic analysis of reactor core based on porous media method", *Annals of Nuclear Energy*, vol. 104, pp. 178-190, 2017.
- [97] J. I. E. Hoffman, "Chapter 23 - t-Test Variants: Cross-Over Tests, Equivalence Tests", in *Basic Biostatistics for Medical and Biomedical Practitioners (Second Edition)*, J. I. E. Hoffman, Ed. London, United Kingdom: Academic Press, an imprint of Elsevier, 2019, pp. 367-374.
- [98] T. K. Kim, "T test as a parametric statistic", (in eng), *Korean journal of anesthesiology*, vol. 68, no. 6, pp. 540-546, 2015.
- [99] Statistics How To. (Accessed on: 30.06.2019). *T-Distribution Table (One Tail and Two-Tails)* Available: <https://www.statisticshowto.datasciencecentral.com/tables/t-distribution-table/>.
- [100] F. Tavassoli, "Fusion Demo Interim Structural Design Criteria (DISDC)/Appendix A Material Design Limit DATA/A3.S18E Eurofer Steel", CEA, EFDA_TASK_TW4-TTMS-005-D01, 2004.
- [101] E. Zolti, "Interim structural design criteria for fusion reactor components", *International Journal of Pressure Vessels and Piping*, vol. 37, no. 1, pp. 53-66, 1989.
- [102] M. Li and Jeong-Ha You, "Design options to mitigate deep cracking of tungsten armor", *Fusion Engineering and Design*, vol. 124, pp. 468-472, 2017.
- [103] M. R. Eslami and M. Shariyat, "A Technique to Distinguish the Primary and Secondary Stresses", *Journal of Pressure Vessel Technology*, vol. 117, no. 3, pp. 197-203, 1995.
- [104] *RCC-MRx Code - Section III - Règles Pour Les Matériels Mécaniques Des Installations Nucléaires*, Paris, France, 2012, www.afcen.com, ISBN 2-913638-39-2.
- [105] V. Barabash, "In-vessel Components, SDC-IC", ITER Organisation, G 74 MA 8 01-05-28 W 0.2, 2012.
- [106] G. Aiello, J. Aktaa, F. Cismondi, G. Rampal, J. F. Salavy and F. Tavassoli, "Assessment of design limits and criteria requirements for Eurofer structures in TBM components", *Journal of Nuclear Materials*, vol. 414, no. 1, pp. 53-68, 2011.
- [107] F. Cismondi, S. Kecskes and G. Aiello, "HCPB TBM thermo mechanical design: Assessment with respect codes and standards and DEMO relevancy", *Fusion Engineering and Design*, vol. 86, no. 9, pp. 2228-2232, 2011.
- [108] M. C. White, "Photoatomic Data Library MCPLIB04: A New Photoatomic Library Based On Data From ENDF/B-VI Release 8", LANL internal memorandum X-5:MCW-02-111 and
-

-
-
- LA-UR-03-1019, 2002.
- [109] T. D. Bohm and Laila El-Guebaly, "Novel Solution for the Problem of Neutron Streaming Through Inboard Assembly Gaps of ARIES Tokamak Power Plants", *Fusion Science and Technology*, vol. 60, no. 1, pp. 278-282, 2011.
- [110] E. Gaganidze and Jarir Aktaa, "Assessment of neutron irradiation effects on RAFM steels", *Fusion Engineering and Design*, vol. 88, no. 3, pp. 118-128, 2013.
- [111] L. V. Boccaccini, L. Giancarli, G. Janeschitz, S. Hermsmeyer, Y. Poitevin, A. Cardella and E. Diegele, "Materials and design of the European DEMO blankets", *Journal of Nuclear Materials*, vol. 329-333, pp. 148-155, 2004.
- [112] J. C. Niel, "Safety considerations for nuclear fusion reactors", in *IAEA GC62 Side Event on Fusion Energy for Peace and Sustainable Development Presentations*, International Atomic Energy Agency (IAEA), 2018, vol. INIS-XA--18M4147, Vienna, Austria, 2018, http://inis.iaea.org/search/search.aspx?orig_q=RN:49075937, ISBN: 49075937, Accessed on: 26.06.2019.
- [113] Y. Ikeda, Yoshitomo Uno, Fujio Maekawa, Donald L. Smith, Itacil C. Gomes, Robert C. Ward and Anatoly A. Filatenkov, "An investigation of the activation of water by D-T fusion neutrons and some implications for fusion reactor technology", *Fusion Engineering and Design*, vol. 37, no. 1, pp. 107-150, 1997.
- [114] R.B. Firestone, C.M. Baglin and S.Y.F. Chu, *Table of Isotopes: 1999 Update* (no. v. 4). University of Michigan, US: Wiley, 1999, ISBN: 9780471356332.
- [115] L. Barucca, S. Ciattaglia, M. Chantant, A. Del Nevo, W. Hering, E. Martelli and I. Moscato, "Status of EU DEMO heat transport and power conversion systems", *Fusion Engineering and Design*, vol. 136, pp. 1557-1566, 2018.
- [116] E. Martelli, A. Del Nevo, F. Giannetti and M. Polidori, "DEMO BoP –WCLL BB PHTS and PCS preliminary design", EFDA D 2MH7KC, 2017.

9 Appendix

9.1 Volume Comparison between ANSYS DesignModeler and CSG Modelling

In this Appendix, the volume estimation of CSG and UM neutronic models are reported. For comparison, it is reported also the reference volume calculated on the CAD model. The error is calculated with respect to the reference. In Table A.1, the comparison between the reference CAD model and the neutronic model based on CSG Modelling for the HCPB slice is shown. In Table A.2, the comparison between the reference CAD model and the neutronic model based on CSG Modelling for the HCPB cap is summarized. In Table A.3, the comparison between the reference CAD model and the neutronic model based on Hybrid Modelling for the WCLL BU with serpentine tubes is stated. In Table A.4, the and comparison between the reference CAD model and the neutronic model based on Hybrid Modelling for the WCLL BU with radial-toroidal tubes is reported.

Table A.1. Volume estimation and comparison between the reference CAD model and the neutronic model based on CSG Modelling for the HCPB slice.

| Cell Name | ANSYS DesignModeler | MCNP | Error [%] | Cell Name | ANSYS DesignModeler | MCNP | Error [%] |
|-----------|---------------------------|---------------------------|-----------|---------------|---------------------------|---------------------------|-----------|
| | Volume [cm ³] | Volume [cm ³] | | | Volume [cm ³] | Volume [cm ³] | |
| Be.10 | 2.63E+02 | 2.63E+02 | -0.10 | He_D-LS.6 | 8.94E+00 | 8.94E+00 | -0.02 |
| Be.11 | 2.08E+02 | 2.08E+02 | 0.03 | He_D-LS.7 | 9.66E+00 | 9.64E+00 | 0.25 |
| Be.12 | 1.02E+03 | 1.01E+03 | 0.25 | He_D-LS.8 | 9.19E+00 | 9.19E+00 | -0.06 |
| Be.13 | 1.03E+03 | 1.03E+03 | -0.02 | He_D-LS.9 | 9.65E+00 | 9.62E+00 | 0.26 |
| Be.14 | 1.13E+03 | 1.13E+03 | -0.04 | He_D-RS.40 | 4.53E+00 | 4.53E+00 | 0.10 |
| Be.15 | 1.50E+03 | 1.50E+03 | -0.02 | He_Manifold.1 | 3.55E+03 | 3.55E+03 | -0.03 |
| Be.16 | 1.78E+02 | 1.78E+02 | -0.02 | He_Manifold.2 | 3.55E+03 | 3.55E+03 | -0.07 |
| Be.17 | 3.58E+02 | 3.58E+02 | 0.06 | He_Manifold.3 | 4.40E+01 | 4.41E+01 | -0.19 |
| Be.18 | 2.86E+02 | 2.86E+02 | 0.07 | He_Manifold.4 | 1.99E+03 | 1.99E+03 | -0.08 |
| Be.19 | 2.74E+02 | 2.74E+02 | 0.10 | He_Manifold.5 | 4.40E+01 | 4.40E+01 | -0.06 |
| Be.2 | 1.03E+03 | 1.03E+03 | 0.07 | He_Manifold.6 | 1.99E+03 | 1.99E+03 | -0.06 |
| Be.20 | 2.70E+02 | 2.70E+02 | 0.23 | Li.10 | 8.68E+01 | 8.67E+01 | 0.16 |
| Be.21 | 2.63E+02 | 2.63E+02 | 0.09 | Li.11 | 1.56E+02 | 1.56E+02 | -0.04 |
| Be.22 | 2.08E+02 | 2.08E+02 | 0.04 | Li.12 | 7.44E+01 | 7.43E+01 | 0.17 |
| Be.23 | 1.02E+03 | 1.01E+03 | 0.25 | Li.13 | 4.17E+02 | 4.17E+02 | -0.01 |
| Be.24 | 2.73E+02 | 2.73E+02 | 0.05 | Li.14 | 4.58E+02 | 4.58E+02 | 0.08 |
| Be.3 | 1.13E+03 | 1.13E+03 | 0.16 | Li.15 | 6.06E+02 | 6.05E+02 | 0.10 |
| Be.4 | 1.50E+03 | 1.50E+03 | 0.16 | Li.16 | 5.21E+02 | 5.20E+02 | 0.28 |
| Be.5 | 1.78E+02 | 1.78E+02 | 0.17 | Li.17 | 1.16E+02 | 1.15E+02 | 0.21 |
| Be.6 | 3.58E+02 | 3.58E+02 | -0.08 | Li.18 | 1.11E+02 | 1.11E+02 | 0.20 |
| Be.7 | 2.86E+02 | 2.86E+02 | 0.06 | Li.19 | 1.10E+02 | 1.10E+02 | 0.19 |
| Be.8 | 2.74E+02 | 2.74E+02 | 0.02 | Li.2 | 4.17E+02 | 4.17E+02 | -0.11 |
| Be.9 | 2.70E+02 | 2.70E+02 | -0.08 | Li.20 | 1.08E+02 | 1.08E+02 | 0.32 |
| Eu_CP.10 | 6.15E+01 | 6.14E+01 | 0.21 | Li.21 | 8.68E+01 | 8.68E+01 | -0.01 |
| Eu_CP.11 | 5.82E+01 | 5.82E+01 | 0.04 | Li.22 | 1.56E+02 | 1.56E+02 | 0.06 |
| Eu_CP.12 | 1.29E+02 | 1.29E+02 | 0.12 | Li.3 | 4.58E+02 | 4.58E+02 | 0.01 |
| Eu_CP.13 | 9.63E+01 | 9.62E+01 | 0.15 | Li.4 | 6.06E+02 | 6.04E+02 | 0.20 |
| Eu_CP.14 | 1.71E+01 | 1.71E+01 | 0.01 | Li.5 | 5.21E+02 | 5.20E+02 | 0.20 |
| Eu_CP.15 | 6.16E+00 | 6.16E+00 | -0.03 | Li.6 | 1.16E+02 | 1.16E+02 | 0.05 |
| Eu_CP.16 | 1.14E+01 | 1.15E+01 | -0.13 | Li.7 | 1.11E+02 | 1.11E+02 | -0.08 |
| Eu_CP.17 | 5.49E+00 | 5.48E+00 | 0.04 | Li.8 | 1.10E+02 | 1.10E+02 | -0.07 |
| Eu_CP.18 | 2.40E+01 | 2.40E+01 | -0.01 | Li.9 | 1.08E+02 | 1.08E+02 | 0.08 |
| Eu_CP.19 | 1.55E+02 | 1.55E+02 | -0.04 | Be.1 | 2.73E+02 | 2.72E+02 | 0.20 |
| Eu_CP.20 | 1.75E+02 | 1.75E+02 | 0.15 | Eu.10 | 1.35E+03 | 1.35E+03 | 0.03 |
| Eu_CP.21 | 2.12E+02 | 2.11E+02 | 0.23 | Eu.11 | 8.12E+00 | 8.13E+00 | -0.16 |
| Eu_CP.22 | 1.61E+02 | 1.61E+02 | 0.14 | Eu.12 | 8.12E+00 | 8.13E+00 | -0.16 |
| Eu_CP.23 | 2.37E+01 | 2.37E+01 | 0.04 | Eu.13 | 9.47E+00 | 9.49E+00 | -0.30 |

| | | | | | | | |
|---------------|----------|----------|-------|------------|----------|----------|-------------|
| Eu_CP.24 | 3.99E+01 | 3.98E+01 | 0.19 | Eu_CP.2 | 1.06E+01 | 1.06E+01 | -0.13 |
| Eu_CP.25 | 4.89E+00 | 4.86E+00 | 0.51 | Eu_CP.3 | 2.97E+01 | 2.97E+01 | 0.01 |
| Eu_CP.26 | 3.99E+00 | 4.02E+00 | -0.69 | Eu_CP.4 | 9.21E+00 | 9.22E+00 | -0.14 |
| Eu_CP.27 | 2.69E+01 | 2.69E+01 | 0.00 | Eu_CP.5 | 9.21E+00 | 9.19E+00 | 0.16 |
| Eu_CP.28 | 6.36E+01 | 6.35E+01 | 0.15 | Eu_CP.6 | 2.97E+01 | 2.98E+01 | -0.07 |
| Eu_CP.29 | 6.36E+01 | 6.38E+01 | -0.23 | Eu_FW.1 | 1.40E+02 | 1.39E+02 | 0.28 |
| Eu_CP.30 | 2.36E+01 | 2.36E+01 | 0.12 | Eu_FW.2 | 5.73E+02 | 5.74E+02 | -0.05 |
| Eu_CP.31 | 3.30E+01 | 3.29E+01 | 0.22 | Eu_FW.3 | 1.40E+02 | 1.40E+02 | -0.13 |
| Eu_CP.32 | 2.68E+01 | 2.68E+01 | 0.07 | Eu_FW.4 | 2.46E+02 | 2.46E+02 | -0.04 |
| Eu_CP.33 | 3.30E+01 | 3.30E+01 | 0.14 | Eu_FW.5 | 2.46E+02 | 2.46E+02 | -0.06 |
| Eu_CP.34 | 3.30E+01 | 3.30E+01 | -0.03 | He_BSS.1 | 5.39E+01 | 5.39E+01 | 0.06 |
| Eu_CP.35 | 3.99E+01 | 3.98E+01 | 0.12 | He_BSS.2 | 1.20E+02 | 1.20E+02 | -0.03 |
| Eu_CP.36 | 1.75E+02 | 1.75E+02 | 0.29 | He_BSS.3 | 5.38E+01 | 5.37E+01 | 0.24 |
| Eu_CP.37 | 2.12E+02 | 2.12E+02 | 0.02 | He_BSS.4 | 3.74E+02 | 3.74E+02 | -0.26 |
| Eu_CP.38 | 1.61E+02 | 1.61E+02 | 0.01 | He_BSS.5 | 3.74E+02 | 3.74E+02 | -0.15 |
| Eu_CP.39 | 1.55E+02 | 1.55E+02 | 0.07 | He_CP1.1 | 6.66E+01 | 6.65E+01 | 0.22 |
| Eu_CP.40 | 1.14E+01 | 1.14E+01 | 0.01 | He_CP1.10 | 1.98E+01 | 1.97E+01 | 0.26 |
| Eu_CP.41 | 6.16E+00 | 6.16E+00 | -0.08 | He_CP1.11 | 1.97E+01 | 1.97E+01 | 0.04 |
| Eu_CP.42 | 7.09E+00 | 7.10E+00 | -0.15 | He_CP1.2 | 1.94E+01 | 1.93E+01 | 0.20 |
| Eu_CP.43 | 3.30E+01 | 3.30E+01 | -0.13 | He_CP1.3 | 1.96E+01 | 1.95E+01 | 0.37 |
| Eu_CP.44 | 3.30E+01 | 3.30E+01 | -0.09 | He_CP1.4 | 1.96E+01 | 1.95E+01 | 0.20 |
| Eu_CP.45 | 3.30E+01 | 3.30E+01 | 0.03 | He_CP1.5 | 1.95E+01 | 1.94E+01 | 0.39 |
| Eu_CP.46 | 7.09E+00 | 7.10E+00 | -0.24 | He_CP1.6 | 1.95E+01 | 1.94E+01 | 0.25 |
| Eu_CP.47 | 5.49E+00 | 5.48E+00 | 0.18 | He_CP1.7 | 1.94E+01 | 1.94E+01 | 0.24 |
| Eu_CP.48 | 4.89E+00 | 4.85E+00 | 0.78 | He_CP1.8 | 2.00E+01 | 1.99E+01 | 0.13 |
| Eu_CP.49 | 4.01E+00 | 4.00E+00 | 0.05 | He_CP1.9 | 1.98E+01 | 1.98E+01 | 0.20 |
| Eu_CP.7 | 9.63E+01 | 9.65E+01 | -0.18 | He_CP2.1 | 6.66E+01 | 6.66E+01 | 0.08 |
| Eu_CP.8 | 5.82E+01 | 5.82E+01 | 0.12 | He_D-RS.1 | 9.68E+00 | 9.67E+00 | 0.11 |
| Eu_CP.9 | 1.71E+01 | 1.71E+01 | 0.33 | He_D-RS.10 | 9.32E+00 | 9.29E+00 | 0.36 |
| Eu_Manifold.1 | 5.43E+02 | 5.43E+02 | -0.16 | He_D-RS.11 | 9.64E+00 | 9.65E+00 | -0.07 |
| Eu_Manifold.2 | 5.43E+02 | 5.43E+02 | -0.11 | He_D-RS.12 | 4.84E+00 | 4.84E+00 | 0.07 |
| He_CP1.12 | 1.65E+01 | 1.65E+01 | -0.14 | He_D-RS.13 | 9.63E+00 | 9.65E+00 | -0.19 |
| He_CP1.13 | 1.92E+01 | 1.91E+01 | 0.23 | He_D-RS.14 | 9.38E+00 | 9.41E+00 | -0.32 |
| He_CP1.14 | 1.89E+01 | 1.89E+01 | 0.04 | He_D-RS.15 | 9.63E+00 | 9.63E+00 | 0.02 |
| He_CP1.15 | 1.84E+01 | 1.84E+01 | 0.07 | He_D-RS.16 | 9.40E+00 | 9.39E+00 | 0.09 |
| He_CP1.16 | 1.75E+01 | 1.75E+01 | 0.12 | He_D-RS.17 | 9.62E+00 | 9.58E+00 | 0.36 |
| He_CP1.17 | 1.67E+01 | 1.67E+01 | 0.21 | He_D-RS.18 | 9.41E+00 | 9.38E+00 | 0.34 |
| He_CP1.18 | 6.94E+01 | 6.93E+01 | 0.13 | He_D-RS.19 | 9.61E+00 | 9.61E+00 | -0.01 |
| He_CP1.19 | 6.95E+01 | 6.94E+01 | 0.04 | He_D-RS.2 | 7.90E+00 | 7.92E+00 | -0.19 |
| He_CP1.20 | 6.78E+01 | 6.79E+01 | -0.15 | He_D-RS.20 | 9.42E+00 | 9.41E+00 | 0.07 |
| He_CP2.10 | 2.00E+01 | 2.00E+01 | 0.23 | He_D-RS.21 | 9.60E+00 | 9.59E+00 | 0.19 |
| He_CP2.11 | 1.93E+01 | 1.93E+01 | -0.28 | He_D-RS.22 | 9.43E+00 | 9.40E+00 | 0.39 |
| He_CP2.12 | 1.70E+01 | 1.70E+01 | 0.06 | He_D-RS.23 | 9.59E+00 | 9.59E+00 | 0.06 |
| He_CP2.13 | 1.79E+01 | 1.79E+01 | -0.03 | He_D-RS.24 | 9.45E+00 | 9.44E+00 | 0.03 |
| He_CP2.14 | 1.86E+01 | 1.85E+01 | 0.22 | He_D-RS.25 | 9.59E+00 | 9.58E+00 | 0.10 |
| He_CP2.15 | 1.90E+01 | 1.90E+01 | 0.18 | He_D-RS.26 | 9.46E+00 | 9.42E+00 | 0.43 |
| He_CP2.16 | 1.94E+01 | 1.94E+01 | 0.08 | He_D-RS.27 | 9.58E+00 | 9.57E+00 | 0.09 |
| He_CP2.17 | 1.65E+01 | 1.65E+01 | -0.16 | He_D-RS.28 | 9.47E+00 | 9.44E+00 | 0.36 |
| He_CP2.18 | 6.94E+01 | 6.93E+01 | 0.14 | He_D-RS.29 | 9.57E+00 | 9.56E+00 | 0.07 |
| He_CP2.19 | 6.95E+01 | 6.94E+01 | 0.06 | He_D-RS.3 | 9.67E+00 | 9.68E+00 | -0.07 |
| He_CP2.2 | 1.94E+01 | 1.94E+01 | 0.18 | He_D-RS.30 | 9.48E+00 | 9.47E+00 | 0.15 |
| He_CP2.20 | 6.78E+01 | 6.78E+01 | 0.03 | He_D-RS.31 | 9.56E+00 | 9.53E+00 | 0.32 |
| He_CP2.3 | 1.95E+01 | 1.94E+01 | 0.22 | He_D-RS.32 | 9.49E+00 | 9.44E+00 | 0.55 |
| He_CP2.4 | 1.95E+01 | 1.94E+01 | 0.54 | He_D-RS.33 | 9.56E+00 | 9.48E+00 | 0.81 |
| He_CP2.5 | 1.96E+01 | 1.95E+01 | 0.35 | He_D-RS.34 | 9.50E+00 | 9.49E+00 | 0.15 |
| He_CP2.6 | 1.96E+01 | 1.96E+01 | 0.13 | He_D-RS.35 | 9.54E+00 | 9.51E+00 | 0.32 |
| He_CP2.7 | 1.97E+01 | 1.97E+01 | 0.05 | He_D-RS.36 | 9.51E+00 | 9.49E+00 | 0.29 |
| He_CP2.8 | 1.98E+01 | 1.98E+01 | 0.17 | He_D-RS.37 | 9.54E+00 | 9.50E+00 | 0.35 |
| He_CP2.9 | 1.99E+01 | 1.99E+01 | 0.09 | He_D-RS.38 | 9.52E+00 | 9.53E+00 | -0.11 |
| He_D-LS.1 | 9.68E+00 | 9.66E+00 | 0.18 | He_D-RS.39 | 9.53E+00 | 9.51E+00 | 0.23 |
| He_D-LS.10 | 9.32E+00 | 9.31E+00 | 0.14 | He_D-RS.4 | 8.45E+00 | 8.45E+00 | -0.02 |
| He_D-LS.11 | 9.64E+00 | 9.63E+00 | 0.08 | He_D-RS.5 | 9.67E+00 | 9.66E+00 | 0.06 |
| He_D-LS.12 | 4.84E+00 | 4.82E+00 | 0.48 | He_D-RS.6 | 8.94E+00 | 8.93E+00 | 0.09 |
| He_D-LS.13 | 9.63E+00 | 9.63E+00 | 0.07 | He_D-RS.7 | 9.66E+00 | 9.65E+00 | 0.09 |
| He_D-LS.14 | 9.38E+00 | 9.36E+00 | 0.29 | He_D-RS.8 | 9.19E+00 | 9.19E+00 | -0.07 |

| | | | | | | | |
|------------|----------|----------|-------|--------------|-----------------|-----------------|--------------|
| He_D-LS.15 | 9.63E+00 | 9.63E+00 | -0.06 | He_D-RS.9 | 9.65E+00 | 9.63E+00 | 0.23 |
| He_D-LS.16 | 9.40E+00 | 9.42E+00 | -0.21 | He_FW.1 | 1.56E+00 | 1.57E+00 | -0.73 |
| He_D-LS.17 | 9.62E+00 | 9.63E+00 | -0.18 | He_FW.2 | 7.04E-01 | 7.04E-01 | -0.07 |
| He_D-LS.18 | 9.41E+00 | 9.36E+00 | 0.50 | He_FW.3 | 7.03E-01 | 7.02E-01 | 0.08 |
| He_D-LS.19 | 9.61E+00 | 9.58E+00 | 0.29 | He_FW.4 | 3.71E+02 | 3.71E+02 | -0.03 |
| He_D-LS.2 | 7.90E+00 | 7.88E+00 | 0.31 | He_FW.5 | 4.10E+02 | 4.10E+02 | -0.08 |
| He_D-LS.20 | 9.42E+00 | 9.39E+00 | 0.29 | He_Purge.2 | 5.94E+02 | 5.93E+02 | 0.17 |
| He_D-LS.21 | 9.60E+00 | 9.58E+00 | 0.22 | He_Purge.3 | 1.43E+02 | 1.42E+02 | 0.32 |
| He_D-LS.22 | 9.43E+00 | 9.41E+00 | 0.22 | He_Purge.4 | 1.43E+02 | 1.43E+02 | -0.41 |
| He_D-LS.23 | 9.59E+00 | 9.55E+00 | 0.41 | He_Purge.5 | 3.22E+01 | 3.23E+01 | -0.26 |
| He_D-LS.24 | 9.45E+00 | 9.41E+00 | 0.38 | He_Purge.6 | 2.39E+01 | 2.39E+01 | 0.25 |
| He_D-LS.25 | 9.59E+00 | 9.55E+00 | 0.34 | He_Purge.7 | 2.39E+01 | 2.40E+01 | -0.12 |
| He_D-LS.26 | 9.46E+00 | 9.45E+00 | 0.11 | He_Purge.8 | 2.29E+01 | 2.29E+01 | -0.09 |
| He_D-LS.27 | 9.58E+00 | 9.58E+00 | -0.02 | He_Purge.9 | 4.50E+02 | 4.51E+02 | -0.19 |
| He_D-LS.28 | 9.47E+00 | 9.43E+00 | 0.38 | Li.1 | 7.44E+01 | 7.44E+01 | 0.08 |
| He_D-LS.29 | 9.57E+00 | 9.58E+00 | -0.16 | W.1 | 1.97E+01 | 1.98E+01 | -0.38 |
| He_D-LS.3 | 9.67E+00 | 9.67E+00 | -0.02 | W.2 | 1.97E+01 | 1.97E+01 | 0.08 |
| He_D-LS.30 | 9.48E+00 | 9.51E+00 | -0.27 | W.3 | 6.93E+01 | 6.93E+01 | 0.00 |
| He_D-LS.31 | 9.56E+00 | 9.59E+00 | -0.34 | Eu.1 | 5.11E+02 | 5.11E+02 | 0.05 |
| He_D-LS.32 | 9.49E+00 | 9.48E+00 | 0.17 | Eu.2 | 5.11E+02 | 5.12E+02 | -0.21 |
| He_D-LS.33 | 9.56E+00 | 9.57E+00 | -0.12 | Eu.3 | 3.00E+03 | 3.00E+03 | -0.02 |
| He_D-LS.34 | 9.50E+00 | 9.49E+00 | 0.10 | Eu.4 | 3.09E+03 | 3.10E+03 | -0.06 |
| He_D-LS.35 | 9.54E+00 | 9.56E+00 | -0.19 | Eu.5 | 3.10E+03 | 3.10E+03 | 0.06 |
| He_D-LS.36 | 9.51E+00 | 9.53E+00 | -0.17 | Eu.6 | 3.13E+03 | 3.13E+03 | -0.04 |
| He_D-LS.37 | 9.54E+00 | 9.53E+00 | 0.09 | Eu.7 | 3.13E+03 | 3.13E+03 | -0.08 |
| He_D-LS.38 | 9.52E+00 | 9.51E+00 | 0.06 | Eu.8 | 2.95E+01 | 2.96E+01 | -0.47 |
| He_D-LS.39 | 9.53E+00 | 9.50E+00 | 0.29 | Eu.9 | 2.95E+01 | 2.95E+01 | -0.16 |
| He_D-LS.4 | 8.45E+00 | 8.46E+00 | -0.11 | Eu_CP.1 | 6.15E+01 | 6.15E+01 | 0.02 |
| He_D-LS.40 | 4.53E+00 | 4.51E+00 | 0.56 | He_Purge.1 | 4.50E+02 | 4.50E+02 | 0.15 |
| He_D-LS.5 | 9.67E+00 | 9.67E+00 | -0.01 | TOTAL | 5.89E+04 | 5.89E+04 | 0.01 |

Table A.2. Volume estimation and comparison between the reference CAD model and the neutronic model based on CSG Modelling for the HCPB cap.

| Cell Name | ANSYS DesignModeler | MCNP | Error [%] | Cell Name | ANSYS DesignModeler | MCNP | Error [%] |
|-----------|---------------------------|---------------------------|-----------|----------------------------|---------------------------|---------------------------|-----------|
| | Volume [cm ³] | Volume [cm ³] | | | Volume [cm ³] | Volume [cm ³] | |
| Be_Bed.1 | 1.90E+02 | 1.90E+02 | 0.14 | CP_Bottom_Left_Outlet_He.7 | 2.86E+01 | 2.85E+01 | 0.22 |
| Be_Bed.2 | 1.90E+02 | 1.90E+02 | 0.00 | CP_Bottom_Left_Outlet_He.8 | 2.77E+01 | 2.77E+01 | 0.11 |
| Be_Bed.3 | 4.57E+04 | 4.57E+04 | -0.02 | CP_Bottom_Left_Outlet_He.9 | 3.20E+00 | 3.24E+00 | -1.21 |
| BP.1 | 8.84E+01 | 8.85E+01 | -0.06 | CP_Top_Left_Inlet_He.1 | 5.77E-01 | 5.82E-01 | -0.74 |
| BP.2 | 8.84E+01 | 8.86E+01 | -0.23 | CP_Top_Left_Inlet_He.10 | 1.09E+00 | 1.08E+00 | 0.24 |
| BP.3 | 9.04E+03 | 9.04E+03 | 0.02 | CP_Top_Left_Inlet_He.11 | 2.71E+01 | 2.71E+01 | -0.13 |
| BP.4 | 6.17E+01 | 6.18E+01 | -0.05 | CP_Top_Left_Inlet_He.12 | 3.28E+00 | 3.28E+00 | 0.07 |
| BP.5 | 4.59E+01 | 4.59E+01 | -0.02 | CP_Top_Left_Inlet_He.13 | 2.74E+01 | 2.74E+01 | 0.06 |
| BP.6 | 4.59E+01 | 4.60E+01 | -0.06 | CP_Top_Left_Inlet_He.14 | 1.33E+01 | 1.33E+01 | -0.08 |
| BP.7 | 6.17E+01 | 6.18E+01 | -0.12 | CP_Top_Left_Inlet_He.15 | 4.68E-01 | 4.70E-01 | -0.30 |
| BSS.1 | 3.83E+04 | 3.83E+04 | -0.05 | CP_Top_Left_Inlet_He.16 | 3.08E+01 | 3.07E+01 | 0.10 |
| BSS.2 | 3.83E+04 | 3.83E+04 | 0.00 | CP_Top_Left_Inlet_He.17 | 4.03E-01 | 3.99E-01 | 0.90 |
| BSS.3 | 5.62E+03 | 5.62E+03 | -0.01 | CP_Top_Left_Inlet_He.18 | 3.27E+01 | 3.28E+01 | -0.18 |
| BSS.4 | 1.96E+04 | 1.96E+04 | -0.01 | CP_Top_Left_Inlet_He.19 | 3.29E+01 | 3.29E+01 | -0.06 |

| | | | | | | | |
|----------------|----------|----------|-------|------------------------------|----------|----------|--------------|
| BSS.5 | 5.62E+03 | 5.62E+03 | -0.01 | CP_Top_Left_I nlet_He.2 | 2.85E+01 | 2.85E+01 | -0.06 |
| BSS.6 | 1.22E+04 | 1.22E+04 | 0.00 | CP_Top_Left_I nlet_He.20 | 3.30E+01 | 3.29E+01 | 0.32 |
| BSS.7 | 5.75E+03 | 5.75E+03 | 0.03 | CP_Top_Left_I nlet_He.21 | 3.32E+01 | 3.32E+01 | -0.03 |
| BSS.8 | 5.72E+03 | 5.72E+03 | 0.02 | CP_Top_Left_I nlet_He.22 | 3.34E+01 | 3.34E+01 | -0.09 |
| BSS.9 | 1.21E+04 | 1.22E+04 | -0.02 | CP_Top_Left_I nlet_He.23 | 3.36E+01 | 3.35E+01 | 0.14 |
| BP.8 | 1.17E+02 | 1.17E+02 | 0.01 | CP_Top_Left_I nlet_He.24 | 3.82E+01 | 3.83E+01 | -0.04 |
| BP.9 | 1.17E+02 | 1.17E+02 | -0.14 | CP_Top_Left_I nlet_He.25 | 3.30E+01 | 3.30E+01 | 0.08 |
| CAP_Central.1 | 6.29E+02 | 6.29E+02 | 0.11 | CP_Top_Left_I nlet_He.26 | 1.78E+01 | 1.78E+01 | -0.13 |
| CAP_Central.10 | 1.77E+02 | 1.77E+02 | 0.09 | CP_Top_Left_I nlet_He.27 | 1.54E+01 | 1.54E+01 | 0.27 |
| CAP_Central.11 | 1.00E+02 | 1.00E+02 | 0.22 | CP_Top_Left_I nlet_He.28 | 4.00E+00 | 4.02E+00 | -0.38 |
| CAP_Central.12 | 2.31E+02 | 2.31E+02 | 0.00 | CP_Top_Left_I nlet_He.3 | 4.22E-01 | 4.19E-01 | 0.71 |
| CAP_Central.13 | 7.83E+02 | 7.83E+02 | -0.01 | CP_Top_Left_I nlet_He.4 | 3.18E+01 | 3.18E+01 | -0.08 |
| CAP_Central.14 | 1.02E+02 | 1.02E+02 | 0.11 | CP_Top_Left_I nlet_He.5 | 3.22E+01 | 3.22E+01 | -0.08 |
| CAP_Central.15 | 8.34E+02 | 8.34E+02 | -0.01 | CP_Top_Left_I nlet_He.6 | 1.99E+02 | 1.99E+02 | 0.00 |
| CAP_Central.16 | 1.83E+02 | 1.83E+02 | -0.16 | CP_Top_Left_I nlet_He.7 | 2.85E+00 | 2.85E+00 | 0.05 |
| CAP_Central.17 | 1.78E+03 | 1.78E+03 | 0.02 | CP_Top_Left_I nlet_He.8 | 4.37E+00 | 4.39E+00 | -0.34 |
| CAP_Central.18 | 1.31E+03 | 1.31E+03 | 0.05 | CP_Top_Left_I nlet_He.9 | 7.12E+00 | 7.16E+00 | -0.56 |
| CAP_Central.19 | 1.12E+03 | 1.12E+03 | -0.04 | CP_Top_Left_O utlet_He.1 | 6.66E+02 | 6.66E+02 | -0.01 |
| CAP_Central.2 | 6.44E+02 | 6.44E+02 | 0.03 | CP_Top_Left_O utlet_He.10 | 4.48E+00 | 4.48E+00 | 0.15 |
| CAP_Central.20 | 3.08E+03 | 3.09E+03 | -0.03 | CP_Top_Left_O utlet_He.11 | 7.14E+00 | 7.16E+00 | -0.29 |
| CAP_Central.21 | 1.81E+02 | 1.81E+02 | -0.14 | CP_Top_Left_O utlet_He.12 | 2.22E+00 | 2.23E+00 | -0.48 |
| CAP_Central.22 | 1.01E+03 | 1.01E+03 | 0.00 | CP_Top_Left_O utlet_He.13 | 6.28E+00 | 6.30E+00 | -0.26 |
| CAP_Central.23 | 2.34E+03 | 2.34E+03 | 0.00 | CP_Top_Left_O utlet_He.14 | 2.87E+01 | 2.87E+01 | -0.02 |
| CAP_Central.24 | 6.31E+01 | 6.33E+01 | -0.31 | CP_Top_Left_O utlet_He.15 | 3.12E+00 | 3.15E+00 | -1.07 |
| CAP_Central.25 | 2.98E+02 | 2.98E+02 | -0.04 | CP_Top_Left_O utlet_He.16 | 2.74E+01 | 2.75E+01 | -0.11 |
| CAP_Central.26 | 6.31E+01 | 6.31E+01 | -0.07 | CP_Top_Left_O utlet_He.17 | 1.33E+01 | 1.33E+01 | 0.12 |
| CAP_Central.27 | 2.98E+02 | 2.98E+02 | -0.05 | CP_Top_Left_O utlet_He.18 | 5.72E-04 | 5.94E-04 | -3.87 |
| CAP_Central.3 | 2.23E+02 | 2.23E+02 | 0.05 | CP_Top_Left_O utlet_He.19 | 3.35E+01 | 3.34E+01 | 0.06 |
| CAP_Central.4 | 1.36E+01 | 1.36E+01 | 0.26 | CP_Top_Left_O utlet_He.2 | 7.62E+00 | 7.61E+00 | 0.11 |
| CAP_Central.5 | 3.64E+02 | 3.64E+02 | 0.03 | CP_Top_Left_O utlet_He.20 | 3.27E+01 | 3.27E+01 | -0.11 |
| CAP_Central.6 | 1.03E+02 | 1.03E+02 | -0.07 | CP_Top_Left_O utlet_He.21 | 2.72E+01 | 2.71E+01 | 0.20 |
| CAP_Central.7 | 9.02E+02 | 9.03E+02 | -0.05 | CP_Top_Left_O utlet_He.22 | 3.33E+01 | 3.32E+01 | 0.27 |
| CAP_Central.8 | 1.01E+02 | 1.01E+02 | -0.15 | CP_Top_Left_O utlet_He.23 | 3.31E+01 | 3.30E+01 | 0.24 |

| | | | | | | | |
|----------------------------|----------|----------|-------|--------------------------|----------|----------|-------|
| CAP_Central.9 | 6.34E+02 | 6.33E+02 | 0.03 | CP_Top_Left_Outlet_He.24 | 3.30E+01 | 3.29E+01 | 0.16 |
| CAP_Lower_plate.1 | 4.27E+01 | 4.26E+01 | 0.17 | CP_Top_Left_Outlet_He.25 | 3.28E+01 | 3.27E+01 | 0.13 |
| CAP_Lower_plate.10 | 6.26E+00 | 6.25E+00 | 0.15 | CP_Top_Left_Outlet_He.26 | 4.41E+01 | 4.41E+01 | 0.02 |
| CAP_Lower_plate.11 | 7.21E-01 | 7.17E-01 | 0.56 | CP_Top_Left_Outlet_He.27 | 5.10E+01 | 5.10E+01 | -0.09 |
| CAP_Lower_plate.12 | 2.73E+00 | 2.74E+00 | -0.29 | CP_Top_Left_Outlet_He.28 | 5.34E+00 | 5.37E+00 | -0.54 |
| CAP_Lower_plate.13 | 6.26E+00 | 6.26E+00 | -0.06 | CP_Top_Left_Outlet_He.29 | 2.37E+01 | 2.37E+01 | -0.03 |
| CAP_Lower_plate.14 | 7.21E-01 | 7.22E-01 | -0.23 | CP_Top_Left_Outlet_He.3 | 1.09E+03 | 1.09E+03 | -0.02 |
| CAP_Lower_plate.15 | 2.73E+00 | 2.71E+00 | 0.66 | CP_Top_Left_Outlet_He.30 | 2.05E+01 | 2.06E+01 | -0.16 |
| CAP_Lower_plate.2 | 8.05E+01 | 8.06E+01 | -0.07 | CP_Top_Left_Outlet_He.4 | 2.46E+01 | 2.46E+01 | -0.08 |
| CAP_Lower_plate.3 | 4.87E+03 | 4.87E+03 | 0.00 | CP_Top_Left_Outlet_He.5 | 8.40E+01 | 8.41E+01 | -0.23 |
| CAP_Lower_plate.4 | 7.55E+01 | 7.55E+01 | 0.02 | CP_Top_Left_Outlet_He.6 | 2.41E+01 | 2.40E+01 | 0.06 |
| CAP_Lower_plate.5 | 6.11E+03 | 6.11E+03 | 0.00 | CP_Top_Left_Outlet_He.7 | 2.63E+00 | 2.61E+00 | 0.50 |
| CAP_Lower_plate.6 | 1.22E+02 | 1.21E+02 | 0.18 | CP_Top_Left_Outlet_He.8 | 2.24E+01 | 2.24E+01 | -0.10 |
| CAP_Lower_plate.7 | 2.29E+01 | 2.29E+01 | 0.01 | CP_Top_Left_Outlet_He.9 | 2.38E+00 | 2.38E+00 | -0.21 |
| CAP_Lower_plate.8 | 9.14E+01 | 9.12E+01 | 0.18 | Enclosure | 1.47E+07 | 1.47E+07 | 0.00 |
| CAP_Lower_plate.9 | 1.58E+02 | 1.58E+02 | 0.08 | FW.1 | 4.94E+02 | 4.94E+02 | 0.05 |
| CAP_Upper_plate.1 | 6.32E+03 | 6.32E+03 | 0.01 | FW.2 | 2.62E+02 | 2.61E+02 | 0.13 |
| CAP_Upper_plate.10 | 6.19E+00 | 6.20E+00 | -0.09 | FW.3 | 2.62E+02 | 2.61E+02 | 0.03 |
| CAP_Upper_plate.11 | 7.02E-01 | 7.09E-01 | -1.01 | FW.4 | 1.11E+02 | 1.11E+02 | 0.07 |
| CAP_Upper_plate.12 | 3.00E+00 | 3.02E+00 | -0.59 | FW.5 | 1.11E+02 | 1.11E+02 | 0.11 |
| CAP_Upper_plate.13 | 7.38E-01 | 7.36E-01 | 0.35 | Gap | 2.59E+04 | 2.59E+04 | -0.01 |
| CAP_Upper_plate.14 | 6.19E+00 | 6.20E+00 | -0.04 | BP_He | 9.22E+03 | 9.22E+03 | 0.03 |
| CAP_Upper_plate.2 | 5.93E+01 | 5.94E+01 | -0.23 | BSS_He.1 | 1.56E+00 | 1.55E+00 | 0.75 |
| CAP_Upper_plate.3 | 9.35E+01 | 9.35E+01 | 0.08 | BSS_He.10 | 1.20E+02 | 1.20E+02 | 0.02 |
| CAP_Upper_plate.4 | 1.25E+02 | 1.25E+02 | -0.01 | BSS_He.2 | 1.56E+00 | 1.57E+00 | -0.36 |
| CAP_Upper_plate.5 | 4.64E+01 | 4.65E+01 | -0.21 | BSS_He.3 | 1.56E+00 | 1.56E+00 | -0.08 |
| CAP_Upper_plate.6 | 7.49E+01 | 7.49E+01 | 0.04 | BSS_He.4 | 1.56E+00 | 1.57E+00 | -0.17 |
| CAP_Upper_plate.7 | 9.41E+01 | 9.43E+01 | -0.20 | BSS_He.5 | 1.56E+00 | 1.55E+00 | 0.99 |
| CAP_Upper_plate.8 | 4.99E+03 | 4.99E+03 | 0.03 | BSS_He.6 | 1.20E+02 | 1.20E+02 | -0.01 |
| CAP_Upper_plate.9 | 3.00E+00 | 3.01E+00 | -0.17 | BSS_He.7 | 1.20E+02 | 1.20E+02 | -0.02 |
| CP_Bottom_Left_Inlet_He.1 | 1.99E+02 | 1.99E+02 | 0.01 | BSS_He.8 | 1.20E+02 | 1.20E+02 | -0.14 |
| CP_Bottom_Left_Inlet_He.10 | 7.03E+00 | 7.04E+00 | -0.13 | BSS_He.9 | 1.20E+02 | 1.20E+02 | 0.01 |
| CP_Bottom_Left_Inlet_He.11 | 2.47E+01 | 2.47E+01 | -0.12 | Manifolds_He.1 | 1.03E+02 | 1.03E+02 | 0.02 |

| | | | | | | | |
|---------------------------------|----------|----------|-------|----------------|----------|----------|-------|
| CP_Bottom_Lef t_Inlet_He.12 | 6.44E+00 | 6.43E+00 | 0.12 | Manifolds_He.2 | 1.51E+04 | 1.51E+04 | 0.02 |
| CP_Bottom_Lef t_Inlet_He.13 | 2.91E+01 | 2.92E+01 | -0.04 | Manifolds_He.3 | 3.09E+02 | 3.09E+02 | 0.02 |
| CP_Bottom_Lef t_Inlet_He.14 | 3.23E+01 | 3.23E+01 | -0.01 | Manifolds_He.4 | 3.09E+02 | 3.09E+02 | -0.05 |
| CP_Bottom_Lef t_Inlet_He.15 | 3.24E+01 | 3.25E+01 | -0.28 | Manifolds_He.5 | 1.03E+02 | 1.03E+02 | 0.03 |
| CP_Bottom_Lef t_Inlet_He.16 | 3.25E+01 | 3.26E+01 | -0.07 | Manifolds_He.6 | 1.51E+04 | 1.51E+04 | 0.02 |
| CP_Bottom_Lef t_Inlet_He.17 | 3.27E+01 | 3.27E+01 | -0.09 | Manifolds_He.7 | 2.69E+04 | 2.69E+04 | -0.03 |
| CP_Bottom_Lef t_Inlet_He.18 | 3.29E+01 | 3.29E+01 | -0.03 | Manifolds_He.8 | 2.69E+04 | 2.69E+04 | -0.04 |
| CP_Bottom_Lef t_Inlet_He.19 | 3.31E+01 | 3.31E+01 | -0.23 | CAP_He.1 | 1.14E+02 | 1.14E+02 | -0.02 |
| CP_Bottom_Lef t_Inlet_He.2 | 2.85E+00 | 2.79E+00 | 1.91 | CAP_He.10 | 7.38E+01 | 7.37E+01 | 0.05 |
| CP_Bottom_Lef t_Inlet_He.20 | 3.32E+01 | 3.32E+01 | 0.18 | CAP_He.11 | 1.93E+03 | 1.93E+03 | -0.07 |
| CP_Bottom_Lef t_Inlet_He.21 | 3.34E+01 | 3.33E+01 | 0.11 | CAP_He.12 | 3.96E+01 | 3.97E+01 | -0.21 |
| CP_Bottom_Lef t_Inlet_He.22 | 3.86E+01 | 3.86E+01 | -0.12 | CAP_He.13 | 1.14E+02 | 1.14E+02 | -0.02 |
| CP_Bottom_Lef t_Inlet_He.23 | 1.39E+01 | 1.39E+01 | 0.27 | CAP_He.14 | 1.15E+02 | 1.15E+02 | 0.07 |
| CP_Bottom_Lef t_Inlet_He.24 | 1.63E+01 | 1.63E+01 | 0.01 | CAP_He.15 | 3.93E+01 | 3.92E+01 | 0.20 |
| CP_Bottom_Lef t_Inlet_He.25 | 4.02E+00 | 4.03E+00 | -0.23 | CAP_He.16 | 1.91E+03 | 1.91E+03 | 0.07 |
| CP_Bottom_Lef t_Inlet_He.3 | 7.24E+00 | 7.26E+00 | -0.19 | CAP_He.17 | 1.13E+02 | 1.13E+02 | -0.06 |
| CP_Bottom_Lef t_Inlet_He.4 | 2.82E+01 | 2.82E+01 | 0.17 | CAP_He.18 | 1.14E+02 | 1.14E+02 | -0.10 |
| CP_Bottom_Lef t_Inlet_He.5 | 3.62E+00 | 3.58E+00 | 1.11 | CAP_He.19 | 2.15E+03 | 2.15E+03 | 0.06 |
| CP_Bottom_Lef t_Inlet_He.6 | 2.77E+01 | 2.76E+01 | 0.30 | CAP_He.2 | 2.04E+02 | 2.04E+02 | -0.04 |
| CP_Bottom_Lef t_Inlet_He.7 | 3.20E+00 | 3.20E+00 | 0.02 | CAP_He.20 | 8.91E+02 | 8.91E+02 | 0.00 |
| CP_Bottom_Lef t_Inlet_He.8 | 1.20E+01 | 1.20E+01 | -0.01 | CAP_He.21 | 1.27E+03 | 1.27E+03 | 0.13 |
| CP_Bottom_Lef t_Inlet_He.9 | 2.50E+01 | 2.50E+01 | -0.14 | CAP_He.22 | 1.97E+03 | 1.97E+03 | 0.00 |
| CP_Bottom_Lef t_Outlet_He.1 | 1.77E+00 | 1.76E+00 | 0.31 | CAP_He.23 | 3.60E+01 | 3.61E+01 | -0.15 |
| CP_Bottom_Lef t_Outlet_He.10 | 1.20E+01 | 1.20E+01 | 0.06 | CAP_He.24 | 1.70E+03 | 1.70E+03 | 0.06 |
| CP_Bottom_Lef t_Outlet_He.11 | 3.17E+01 | 3.16E+01 | 0.03 | CAP_He.25 | 3.99E+02 | 3.99E+02 | -0.07 |
| CP_Bottom_Lef t_Outlet_He.12 | 3.22E+01 | 3.23E+01 | -0.14 | CAP_He.26 | 2.11E+03 | 2.11E+03 | -0.03 |
| CP_Bottom_Lef t_Outlet_He.13 | 3.24E+01 | 3.24E+01 | -0.15 | CAP_He.27 | 4.40E+02 | 4.40E+02 | 0.06 |
| CP_Bottom_Lef t_Outlet_He.14 | 3.25E+01 | 3.25E+01 | -0.03 | CAP_He.3 | 1.14E+02 | 1.14E+02 | -0.03 |
| CP_Bottom_Lef t_Outlet_He.15 | 3.26E+01 | 3.27E+01 | -0.26 | CAP_He.4 | 1.71E+03 | 1.71E+03 | 0.01 |
| CP_Bottom_Lef t_Outlet_He.16 | 3.28E+01 | 3.28E+01 | 0.13 | CAP_He.5 | 3.94E+01 | 3.94E+01 | 0.05 |
| CP_Bottom_Lef t_Outlet_He.17 | 3.33E+01 | 3.34E+01 | -0.10 | CAP_He.6 | 3.38E+02 | 3.39E+02 | -0.03 |
| CP_Bottom_Lef t_Outlet_He.18 | 3.31E+01 | 3.31E+01 | 0.09 | CAP_He.7 | 1.18E+02 | 1.18E+02 | 0.07 |
| CP_Bottom_Lef t_Outlet_He.19 | 3.30E+01 | 3.29E+01 | 0.07 | CAP_He.8 | 1.18E+02 | 1.18E+02 | -0.03 |

| | | | | | | | |
|---------------------------------|----------|----------|-------|----------------|-----------------|-----------------|---------------|
| CP_Bottom_Lef t_Outlet_He.2 | 6.66E+02 | 6.65E+02 | 0.11 | CAP_He.9 | 7.38E+01 | 7.38E+01 | -0.01 |
| CP_Bottom_Lef t_Outlet_He.20 | 2.73E+01 | 2.73E+01 | -0.01 | Purge_Gas_He.1 | 3.77E+01 | 3.77E+01 | 0.03 |
| CP_Bottom_Lef t_Outlet_He.21 | 2.88E+01 | 2.87E+01 | 0.27 | Purge_Gas_He.2 | 1.70E+02 | 1.70E+02 | -0.06 |
| CP_Bottom_Lef t_Outlet_He.22 | 1.63E+01 | 1.63E+01 | 0.22 | Purge_Gas_He.3 | 2.65E+02 | 2.66E+02 | -0.15 |
| CP_Bottom_Lef t_Outlet_He.23 | 1.39E+01 | 1.40E+01 | -0.25 | Purge_Gas_He.4 | 3.77E+01 | 3.77E+01 | -0.10 |
| CP_Bottom_Lef t_Outlet_He.24 | 4.02E+00 | 4.05E+00 | -0.73 | Purge_Gas_He.5 | 1.70E+02 | 1.70E+02 | 0.25 |
| CP_Bottom_Lef t_Outlet_He.25 | 3.86E+01 | 3.85E+01 | 0.09 | Purge_Gas_He.6 | 2.65E+02 | 2.65E+02 | 0.05 |
| CP_Bottom_Lef t_Outlet_He.26 | 3.34E+01 | 3.33E+01 | 0.20 | Manifold.1 | 1.07E+03 | 1.07E+03 | 0.07 |
| CP_Bottom_Lef t_Outlet_He.27 | 4.50E+00 | 4.54E+00 | -0.91 | Manifold.2 | 1.07E+03 | 1.07E+03 | -0.05 |
| CP_Bottom_Lef t_Outlet_He.3 | 8.40E+01 | 8.38E+01 | 0.20 | Manifold.3 | 3.05E+03 | 3.05E+03 | -0.01 |
| CP_Bottom_Lef t_Outlet_He.4 | 1.09E+03 | 1.08E+03 | 0.14 | Manifold.4 | 3.05E+03 | 3.05E+03 | -0.08 |
| CP_Bottom_Lef t_Outlet_He.5 | 2.63E+00 | 2.61E+00 | 0.42 | TOTAL | 1.51E+07 | 1.51E+07 | -0.002 |
| CP_Bottom_Lef t_Outlet_He.6 | 1.32E+00 | 1.32E+00 | -0.46 | | | | |

Table A.3. Volume estimation and comparison between the reference CAD model and the neutronic model based on Hybrid Modelling for the WCLL BU with serpentine tubes.

| Cell Name | ANSYS DesignModeler | MCNP | Error [%] |
|----------------|------------------------------|------------------------------|----------------|
| | Volume [cm ³] | Volume [cm ³] | |
| Armour | 4.31E+02 | 4.31E+02 | -0.0053 |
| FW | 8.43E+03 | 8.43E+03 | -0.0068 |
| FW Coolant | 1.44E+03 | 1.44E+03 | -0.0035 |
| Plates N/S | 1.36E+04 | 1.36E+04 | -0.0037 |
| Vert. Plates | 7.87E+03 | 7.87E+03 | 0.0000 |
| BZ Tubes 1-3 | 1.21E+03 | 1.21E+03 | -0.0066 |
| BZ Tubes 4-6 | 1.21E+03 | 1.21E+03 | -0.0066 |
| BZ Coolant 1-2 | 4.26E+02 | 4.26E+02 | -0.0063 |
| BZ Coolant 3-4 | 4.56E+02 | 4.56E+02 | -0.0068 |
| BZ Coolant 5-6 | 4.26E+02 | 4.26E+02 | -0.0063 |
| PbLi 1 | 1.91E+04 | 1.91E+04 | 0.0021 |
| PbLi 2 | 2.24E+04 | 2.24E+04 | -0.0013 |
| PbLi 3 | 2.24E+04 | 2.24E+04 | -0.0013 |
| PbLi 4 | 2.24E+04 | 2.24E+04 | -0.0013 |
| PbLi 5 | 2.24E+04 | 2.24E+04 | -0.0013 |
| PbLi 6 | 1.91E+04 | 1.91E+04 | 0.0021 |
| BSS | 4.29E+04 | 4.29E+04 | 0.0009 |
| BSS Coolant | 5.60E+04 | 5.60E+04 | 0.0004 |
| Total | 2.62070E+05 | 2.62069E+05 | -0.0005 |


Table A.4. Volume estimation and comparison between the reference CAD model and the neutronic model based on Hybrid Modelling for the WCLL BU with radial-toroidal tubes.

| Cell Name | ANSYS DesignModeler | MCNP | Error [%] |
|-----------|------------------------------|------------------------------|--------------|
| | Volume [cm ³] | Volume [cm ³] | |
| 1_acqua_1 | 1.49E+02 | 1.49E+02 | 0.01 |
| 2_acqua_2 | 1.49E+02 | 1.49E+02 | 0.00 |
| 3_acqua_3 | 1.49E+02 | 1.49E+02 | -0.03 |
| 4_acqua_4 | 1.49E+02 | 1.49E+02 | -0.02 |
| 5_acqua_5 | 1.43E+02 | 1.43E+02 | 0.01 |
| 6_acqua_6 | 1.43E+02 | 1.43E+02 | 0.01 |

| | | | |
|----------------|------------------|------------------|--------------|
| 7_acqua_7 | 1.37E+02 | 1.37E+02 | -0.02 |
| 8_acqua_8 | 1.37E+02 | 1.37E+02 | 0.02 |
| 9_acqua_9 | 1.37E+02 | 1.37E+02 | -0.01 |
| 10_acqua_10 | 1.37E+02 | 1.37E+02 | -0.01 |
| 11_acqua_11 | 1.31E+02 | 1.31E+02 | -0.02 |
| 12_acqua_12 | 1.31E+02 | 1.31E+02 | -0.02 |
| 13_acqua_13 | 1.26E+02 | 1.26E+02 | -0.03 |
| 14_acqua_14 | 1.26E+02 | 1.26E+02 | -0.03 |
| 15_acqua_15 | 1.11E+02 | 1.11E+02 | -0.03 |
| 16_acqua_16 | 1.11E+02 | 1.11E+02 | -0.05 |
| 17_acqua_17 | 9.84E+01 | 9.84E+01 | 0.02 |
| 18_acqua_18 | 9.84E+01 | 9.83E+01 | 0.05 |
| 19_acqua_19 | 7.98E+01 | 7.99E+01 | -0.07 |
| 20_acqua_20 | 5.30E+01 | 5.30E+01 | -0.01 |
| 21_acqua_21 | 5.30E+01 | 5.30E+01 | -0.01 |
| 22_tubo_1 | 2.76E+02 | 2.76E+02 | 0.01 |
| 23_tubo_2 | 2.76E+02 | 2.76E+02 | -0.02 |
| 24_tubo_3 | 2.76E+02 | 2.76E+02 | -0.04 |
| 25_tubo_4 | 2.76E+02 | 2.76E+02 | -0.02 |
| 26_tubo_5 | 2.65E+02 | 2.65E+02 | -0.01 |
| 27_tubo_6 | 2.65E+02 | 2.65E+02 | 0.01 |
| 28_tubo_7 | 2.54E+02 | 2.54E+02 | 0.01 |
| 29_tubo_8 | 2.54E+02 | 2.54E+02 | 0.00 |
| 30_tubo_9 | 2.54E+02 | 2.54E+02 | 0.00 |
| 31_tubo_10 | 2.54E+02 | 2.54E+02 | -0.02 |
| 32_tubo_11 | 2.43E+02 | 2.43E+02 | 0.00 |
| 33_tubo_12 | 2.43E+02 | 2.43E+02 | -0.01 |
| 34_tubo_13 | 2.33E+02 | 2.33E+02 | -0.02 |
| 35_tubo_14 | 2.33E+02 | 2.33E+02 | -0.04 |
| 36_tubo_15 | 2.05E+02 | 2.05E+02 | 0.02 |
| 37_tubo_16 | 2.05E+02 | 2.05E+02 | -0.01 |
| 38_tubo_17 | 1.82E+02 | 1.82E+02 | 0.05 |
| 39_tubo_18 | 1.82E+02 | 1.82E+02 | 0.02 |
| 40_tubo_19 | 1.47E+02 | 1.48E+02 | -0.08 |
| 41_tubo_20 | 9.79E+01 | 9.79E+01 | -0.03 |
| 42_tubo_21 | 9.79E+01 | 9.79E+01 | 0.00 |
| SP+BP_A_new_2 | 3.79E+04 | 3.79E+04 | 0.00 |
| SB_CHANNEL_1 | 1.59E+02 | 1.59E+02 | 0.01 |
| SB_CHANNEL_2 | 1.59E+02 | 1.59E+02 | 0.00 |
| SB_CHANNEL_3 | 1.59E+02 | 1.59E+02 | 0.02 |
| SB_CHANNEL_4 | 1.59E+02 | 1.59E+02 | 0.05 |
| SB_CHANNEL_5 | 1.59E+02 | 1.59E+02 | 0.01 |
| SB_CHANNEL_6 | 1.59E+02 | 1.60E+02 | -0.04 |
| SB_CHANNEL_7 | 1.59E+02 | 1.59E+02 | 0.01 |
| SB_CHANNEL_8 | 1.59E+02 | 1.59E+02 | 0.02 |
| SB_CHANNEL_9 | 1.59E+02 | 1.60E+02 | -0.03 |
| SB_CHANNEL_10 | 1.59E+02 | 1.60E+02 | -0.03 |
| SB_CHANNEL_11 | 1.59E+02 | 1.60E+02 | -0.01 |
| SB_EUROFER | 1.03E+04 | 1.03E+04 | 0.00 |
| Pb_Li_inter | 6.61E+03 | 6.61E+03 | 0.00 |
| PbLi_1 - tubes | 1.24E+05 | 1.25E+05 | -0.43 |
| Pb_Li_holes | 2.79E+01 | 2.79E+01 | 0.03 |
| BP_B | 6.16E+03 | 6.16E+03 | 0.02 |
| BP_B.3.1 | 7.24E+01 | 7.24E+01 | 0.01 |
| BP_B.3.2 | 4.19E+01 | 4.18E+01 | 0.15 |
| BP_B.3.3 | 4.19E+01 | 4.19E+01 | 0.04 |
| TOTAL | 1.943E+05 | 1.948E+05 | -0.27 |

9.2 PS and GPS Definition

In this Appendix, the setup for the definition on PS and GPS condition in ANSYS Mechanical [66] is reported.

The implementation of the PS condition is straightforward in ANSYS mechanical by means of Coupling command ( Coupling (Beta)), while procedure to implement the GPS condition is more articulated. Practically, the GPS is implemented allowing the poloidal translation of the plane C in Figure A.1-a and its rotation with respect to the x axis. Indeed, using the “Remote Displacement” command, the nodes lying on the surface in which the GPS has to be applied are identified. It is important to block in the “Remote Displacement” command all the Degree of Freedom (DOF) and to impose a “rigid” behaviour. Thanks to this command, in the input file, a target id (tid) and a contact id (cid) numbers are associated to these surfaces. These tid and cid are, then, used for the APDL command as reported below:

APDL COMMAND

```
1 - *set,tid,5
2 - keyo,tid,4,001010
3 - ddele,69238, rotx
4 - ddele,69238, uy
```

With the first line of the APDL command, the target nodes are identified (in this example the number 5 has been assigned to the nodes lying on the surfaces that are indicated with C in Figure A.1-a). The second line of the command enables the KEY-OPTION 4 that allows to activate, using number 1, or to deactivate, using number 0, the constraints of the 6 DOF. The six digits represent ROTZ, ROTY, ROTX, UZ, UY, UX, respectively [66]. With the third and fourth lines, the rotation with respect to the x axis and the translation along the y axis is allowed.

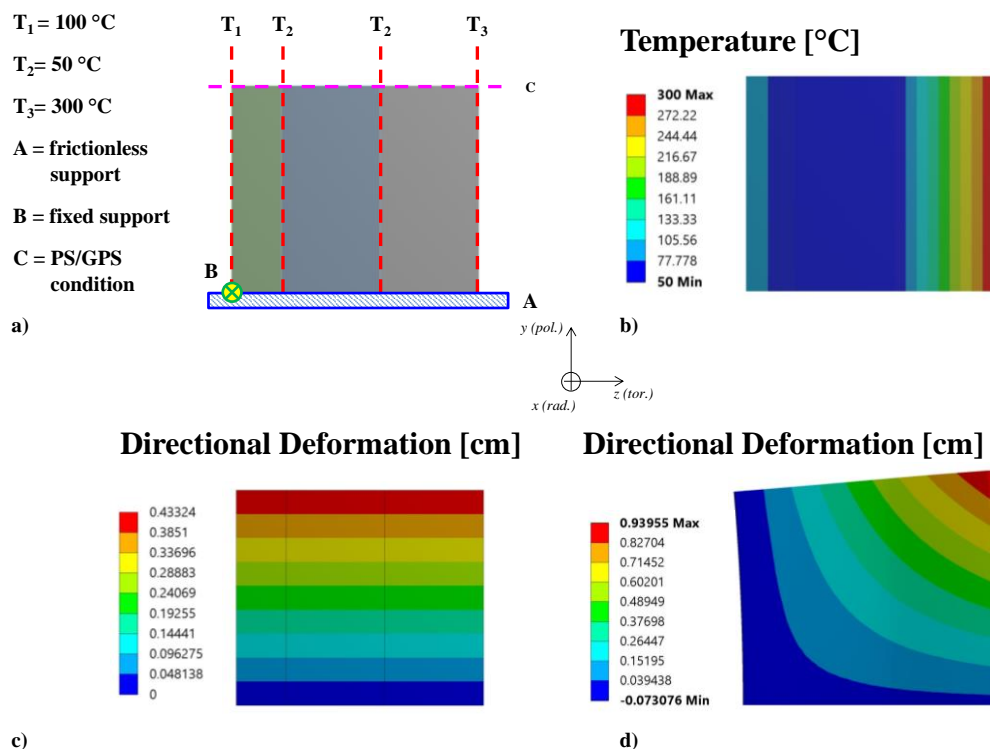


Figure A.1. Investigation and implementation of PS and GPS conditions. Top-left (a): boundary conditions applied to the simplified model. Top-right (b): temperature field. Bottom-Left (c): directional deformation in Y direction using PS condition on the surface C. Bottom-Right (d): directional deformation in Y direction using GPS condition on the surface C.

9.3 MAIA Neutron and Photon Transport Analysis Consistency Verification

In this Appendix, the parametric studies on HCPB slice neutronic boundary conditions are reported.

In Table A.5, the case studies for the HCPB slice and module are reported. In particular, eight analyses have been performed both for the slice and module sub-models: 4 neutron ($_N_$) and 4 photon ($_P_$) transport calculations. All the combination of reflecting and white conditions applied to the toroidal and poloidal boundary surfaces have been identified and analyzed. Some detail about the number of processes, histories and calculation time are also reported.

It is possible to note that the photon calculations are always faster than neutronic ones. Indeed, in photon transport analysis, only the photons are transported. Consequently, the number of interactions is lower with respect to the neutronic calculation where, beyond the neutrons, the photons are also transported.

It is interesting to note that the computational time necessary for the slice sub-model is about four times lower than the one requested for the module. This is mainly due to the model dimension that affects considerably the calculation performances.

Table A.5. Case study matrix.

| Case | Model | Reflecting | White | Name | N° processes | N° Histories | Calculation Time |
|------|----------|------------|----------|------------------------------|--------------|--------------|------------------|
| 3A | Slice_N | Refl2 | | 3A_Slice_N_Refl2 | 448 | 5.0E+08 | 01:54:24 |
| 3B | Slice_N | | White2 | 3B_Slice_N_White2 | 448 | 1.0E+09 | 01:22:52 |
| 3C | Slice_N | ReflTor | WhitePol | 3C_Slice_N_ReflTor_WhitePol | 448 | 1.0E+09 | 01:25:57 |
| 3D | Slice_N | ReflPol | WhiteTor | 3D_Slice_N_ReflPol_WhiteTor | 448 | 5.0E+08 | 02:02:20 |
| 4A | Slice_P | Refl2 | | 4A_Slice_P_Refl2 | 448 | 1.0E+09 | 00:10:20 |
| 4B | Slice_P | | White2 | 4B_Slice_P_White2 | 448 | 1.0E+09 | 00:06:44 |
| 4C | Slice_P | ReflTor | WhitePol | 4C_Slice_P_ReflTor_WhitePol | 448 | 1.0E+09 | 00:06:46 |
| 4D | Slice_P | ReflPol | WhiteTor | 4D_Slice_P_ReflPol_WhiteTor | 448 | 1.0E+09 | 00:09:53 |
| 3A | Module_N | Refl2 | | 3A_Module_N_Refl2 | 448 | 8.0E+08 | 09:13:10 |
| 3B | Module_N | | White2 | 3B_Module_N_White2 | 448 | 7.0E+08 | 07:10:46 |
| 3C | Module_N | ReflTor | WhitePol | 3C_Module_N_ReflTor_WhitePol | 448 | 8.0E+08 | 08:59:27 |
| 3D | Module_N | ReflPol | WhiteTor | 3D_Module_N_ReflPol_WhiteTor | 448 | 5.0E+08 | 04:50:08 |
| 4A | Module_P | Refl2 | | 4A_Module_P_Refl2 | 448 | 1.0E+09 | 00:41:28 |
| 4B | Module_P | | White2 | 4B_Module_P_White2 | 448 | 1.0E+09 | 00:39:54 |
| 4C | Module_P | ReflTor | WhitePol | 4C_Module_P_ReflTor_WhitePol | 448 | 1.0E+09 | 00:41:44 |
| 4D | Module_P | ReflPol | WhiteTor | 4D_Module_P_ReflPol_WhiteTor | 448 | 1.0E+09 | 00:42:58 |

In Table A.6, Table A.7, Table A.8 and Table A.9, the release power Q_{dep} and the contributes Q_{np} and $Q_{p,albedo}$ are reported for the case studies. The Q_{dep} of the HCPB DEMO reference model equipped with full heterogeneous OB4 module is reported for comparison.

Table A.6. Case 3A-4A power released.

| Case 3A-4A | Slice | | | Module | | | DEMO |
|--------------------|-----------------|-----------------------|------------------|-----------------|-----------------------|------------------|------------------|
| Row Labels | Q_{np} [W] | $Q_{p,albedo}$ [W] | Q_{dep} [W] | Q_{np} [W] | $Q_{p,albedo}$ [W] | Q_{dep} [W] | Q_{dep} [W] |
| Armour | 1.47E+03 | 7.74E+02 | 2.24E+03 | 1.53E+03 | 8.08E+02 | 2.34E+03 | 2.43E+03 |
| Beryllium Bed | 2.17E+04 | 3.97E+02 | 2.21E+04 | 2.10E+04 | 3.82E+02 | 2.14E+04 | 2.03E+04 |
| BSS | 2.27E+03 | 5.03E+01 | 2.32E+03 | 1.89E+03 | 4.07E+01 | 1.93E+03 | 1.80E+03 |
| CP | 6.83E+03 | 5.96E+02 | 7.43E+03 | 6.81E+03 | 5.89E+02 | 7.40E+03 | 7.40E+03 |
| FW | 6.48E+03 | 9.94E+02 | 7.47E+03 | 6.62E+03 | 1.01E+03 | 7.63E+03 | 7.71E+03 |
| He_BSS | 2.92E+00 | 6.45E-03 | 2.93E+00 | 2.44E+00 | 5.30E-03 | 2.45E+00 | 2.20E+00 |
| He_CP | 2.85E+01 | 2.05E-01 | 2.87E+01 | 2.80E+01 | 1.99E-01 | 2.82E+01 | 2.79E+01 |
| He_Dummy_Channels | 1.08E+01 | 7.01E-02 | 1.09E+01 | 1.02E+01 | 6.60E-02 | 1.03E+01 | 1.01E+01 |
| He_FW | 3.31E+01 | 4.38E-01 | 3.36E+01 | 3.40E+01 | 4.45E-01 | 3.45E+01 | 3.41E+01 |
| He_Manifold | 1.52E+01 | 1.59E-02 | 1.52E+01 | 1.24E+01 | 1.21E-02 | 1.24E+01 | 1.06E+01 |
| He_Purge_BSS | 7.33E+00 | 3.58E-02 | 7.37E+00 | 6.43E+00 | 3.25E-02 | 6.46E+00 | 6.03E+00 |
| LiSiO4_Bed | 3.60E+04 | 2.30E+02 | 3.63E+04 | 3.55E+04 | 2.20E+02 | 3.58E+04 | 3.56E+04 |
| Manifold | 2.10E+02 | 2.43E+00 | 2.13E+02 | 1.74E+02 | 1.82E+00 | 1.75E+02 | 1.59E+02 |
| Grand Total | 7.51E+04 | 3.04E+03 | 7.81E+04 | 7.37E+04 | 3.06E+03 | 7.67E+04 | 7.55E+04 |

Table A.7. Case 3B-4B power released.

| Case 3B-4B | Slice | | | Module | | | DEMO |
|--------------------|-----------------|-----------------------|------------------|-----------------|-----------------------|------------------|------------------|
| Row Labels | Q_{np} [W] | $Q_{p,albedo}$ [W] | Q_{dep} [W] | Q_{np} [W] | $Q_{p,albedo}$ [W] | Q_{dep} [W] | Q_{dep} [W] |
| Armour | 1.71E+03 | 7.85E+02 | 2.50E+03 | 1.53E+03 | 7.98E+02 | 2.33E+03 | 2.43E+03 |
| Beryllium Bed | 1.29E+04 | 2.14E+02 | 1.31E+04 | 2.08E+04 | 3.74E+02 | 2.11E+04 | 2.03E+04 |
| BSS | 1.68E+02 | 3.31E+00 | 1.71E+02 | 1.67E+03 | 3.81E+01 | 1.71E+03 | 1.80E+03 |
| CP | 4.40E+03 | 3.33E+02 | 4.73E+03 | 6.69E+03 | 5.75E+02 | 7.26E+03 | 7.40E+03 |
| FW | 7.14E+03 | 9.76E+02 | 8.11E+03 | 6.48E+03 | 9.95E+02 | 7.48E+03 | 7.71E+03 |
| He_BSS | 1.76E-01 | 4.42E-04 | 1.77E-01 | 1.90E+00 | 4.71E-03 | 1.91E+00 | 2.20E+00 |
| He_CP | 1.83E+01 | 1.14E-01 | 1.84E+01 | 2.72E+01 | 1.90E-01 | 2.74E+01 | 2.79E+01 |
| He_Dummy_Channels | 4.67E+00 | 2.53E-02 | 4.70E+00 | 1.01E+01 | 6.44E-02 | 1.01E+01 | 1.01E+01 |
| He_FW | 3.56E+01 | 4.46E-01 | 3.60E+01 | 3.33E+01 | 4.37E-01 | 3.37E+01 | 3.41E+01 |
| He_Manifold | 6.01E-01 | 9.49E-04 | 6.02E-01 | 1.12E+01 | 1.32E-02 | 1.12E+01 | 1.06E+01 |
| He_Purge_BSS | 2.24E+00 | 1.62E-02 | 2.26E+00 | 6.21E+00 | 3.19E-02 | 6.24E+00 | 6.03E+00 |
| LiSiO4_Bed | 2.27E+04 | 1.24E+02 | 2.28E+04 | 3.50E+04 | 2.15E+02 | 3.52E+04 | 3.56E+04 |
| Manifold | 1.41E+01 | 1.31E-01 | 1.42E+01 | 1.57E+02 | 1.86E+00 | 1.59E+02 | 1.59E+02 |
| Grand Total | 4.90E+04 | 2.44E+03 | 5.15E+04 | 7.24E+04 | 3.00E+03 | 7.54E+04 | 7.55E+04 |

Table A.8. Case 3C-4C power released.

| Case 3C-4C | Slice | | | Module | | | DEMO |
|--------------------|-----------------|-----------------------|------------------|-----------------|-----------------------|------------------|------------------|
| Row Labels | Q_{np} [W] | $Q_{p,albedo}$ [W] | Q_{dep} [W] | Q_{np} [W] | $Q_{p,albedo}$ [W] | Q_{dep} [W] | Q_{dep} [W] |
| Armour | 1.71E+03 | 7.88E+02 | 2.50E+03 | 1.53E+03 | 8.08E+02 | 2.34E+03 | 2.43E+03 |
| Beryllium Bed | 1.30E+04 | 2.16E+02 | 1.32E+04 | 2.10E+04 | 3.82E+02 | 2.14E+04 | 2.03E+04 |
| BSS | 1.88E+02 | 3.53E+00 | 1.92E+02 | 1.89E+03 | 4.09E+01 | 1.93E+03 | 1.80E+03 |
| CP | 4.43E+03 | 3.35E+02 | 4.77E+03 | 6.81E+03 | 5.89E+02 | 7.40E+03 | 7.40E+03 |
| FW | 7.19E+03 | 9.81E+02 | 8.17E+03 | 6.62E+03 | 1.01E+03 | 7.63E+03 | 7.71E+03 |
| He_BSS | 2.28E-01 | 5.07E-04 | 2.29E-01 | 2.45E+00 | 5.32E-03 | 2.46E+00 | 2.20E+00 |
| He_CP | 1.86E+01 | 1.16E-01 | 1.87E+01 | 2.80E+01 | 1.99E-01 | 2.82E+01 | 2.79E+01 |
| He_Dummy_Channels | 4.71E+00 | 2.55E-02 | 4.74E+00 | 1.02E+01 | 6.60E-02 | 1.03E+01 | 1.01E+01 |
| He_FW | 3.58E+01 | 4.48E-01 | 3.63E+01 | 3.40E+01 | 4.45E-01 | 3.45E+01 | 3.41E+01 |
| He_Manifold | 6.81E-01 | 1.00E-03 | 6.82E-01 | 1.27E+01 | 1.43E-02 | 1.27E+01 | 1.06E+01 |
| He_Purge_BSS | 2.26E+00 | 1.62E-02 | 2.27E+00 | 6.44E+00 | 3.25E-02 | 6.48E+00 | 6.03E+00 |
| LiSiO4_Bed | 2.28E+04 | 1.25E+02 | 2.30E+04 | 3.55E+04 | 2.20E+02 | 3.58E+04 | 3.56E+04 |
| Manifold | 1.58E+01 | 1.39E-01 | 1.59E+01 | 1.76E+02 | 2.00E+00 | 1.78E+02 | 1.59E+02 |
| Grand Total | 1.71E+03 | 7.88E+02 | 2.50E+03 | 1.53E+03 | 8.08E+02 | 2.34E+03 | 7.55E+04 |

Table A.9. Case 3D-4D power released.

| Case 3D-4D | Slice | | | Module | | | DEMO |
|--------------------|-----------------|-----------------------|------------------|-----------------|-----------------------|------------------|------------------|
| Row Labels | Q_{np} [W] | $Q_{p,albedo}$ [W] | Q_{dep} [W] | Q_{np} [W] | $Q_{p,albedo}$ [W] | Q_{dep} [W] | Q_{dep} [W] |
| Armour | 1.50E+03 | 7.96E+02 | 2.29E+03 | 1.53E+03 | 7.98E+02 | 2.33E+03 | 2.43E+03 |
| Beryllium Bed | 2.12E+04 | 3.76E+02 | 2.16E+04 | 2.08E+04 | 3.74E+02 | 2.11E+04 | 2.03E+04 |
| BSS | 1.93E+03 | 4.33E+01 | 1.98E+03 | 1.67E+03 | 3.79E+01 | 1.71E+03 | 1.80E+03 |
| CP | 6.67E+03 | 5.65E+02 | 7.23E+03 | 6.69E+03 | 5.75E+02 | 7.26E+03 | 7.40E+03 |
| FW | 6.43E+03 | 9.73E+02 | 7.40E+03 | 6.48E+03 | 9.95E+02 | 7.48E+03 | 7.71E+03 |
| He_BSS | 2.19E+00 | 5.26E-03 | 2.20E+00 | 1.90E+00 | 4.69E-03 | 1.90E+00 | 2.20E+00 |
| He_CP | 2.73E+01 | 1.90E-01 | 2.75E+01 | 2.72E+01 | 1.90E-01 | 2.74E+01 | 2.79E+01 |
| He_Dummy_Channels | 1.04E+01 | 6.57E-02 | 1.05E+01 | 1.01E+01 | 6.44E-02 | 1.01E+01 | 1.01E+01 |
| He_FW | 3.29E+01 | 4.31E-01 | 3.33E+01 | 3.33E+01 | 4.37E-01 | 3.37E+01 | 3.41E+01 |
| He_Manifold | 1.28E+01 | 1.37E-02 | 1.28E+01 | 1.09E+01 | 1.15E-02 | 1.09E+01 | 1.06E+01 |
| He_Purge_BSS | 6.86E+00 | 3.34E-02 | 6.89E+00 | 6.19E+00 | 3.19E-02 | 6.22E+00 | 6.03E+00 |
| LiSiO4_Bed | 3.49E+04 | 2.18E+02 | 3.51E+04 | 3.50E+04 | 2.15E+02 | 3.52E+04 | 3.56E+04 |
| Manifold | 1.81E+02 | 2.09E+00 | 1.83E+02 | 1.55E+02 | 1.73E+00 | 1.57E+02 | 1.59E+02 |
| Grand Total | 7.29E+04 | 2.97E+03 | 7.59E+04 | 7.24E+04 | 3.00E+03 | 7.54E+04 | 7.55E+04 |

In Table A.10, Table A.11 and Table A.12, the power depositions calculated at different level of full heterogeneous OB4 implemented in HCPB DEMO reference model are reported.

Table A.10. Power deposition in slices adjacent to the top cap.

| Region | Q_{dep} [W] | | | |
|--------------------|-----------------|--------------------------|--------------------------|--------------------------|
| | DEMO Top | DEMO 2 nd Top | DEMO 3 rd Top | DEMO 4 th Top |
| Armour | 2.41E+03 | 2.41E+03 | 2.41E+03 | 2.41E+03 |
| Beryllium Bed | 1.89E+04 | 1.89E+04 | 1.91E+04 | 1.91E+04 |
| BSS | 1.89E+03 | 1.85E+03 | 1.82E+03 | 1.81E+03 |
| CP | 7.24E+03 | 7.18E+03 | 7.16E+03 | 7.15E+03 |
| FW | 7.53E+03 | 7.52E+03 | 7.57E+03 | 7.56E+03 |
| He_BSS | 1.98E+00 | 2.00E+00 | 2.02E+00 | 2.04E+00 |
| He_CP | 2.61E+01 | 2.62E+01 | 2.63E+01 | 2.64E+01 |
| He_Dummy_Channels | 9.08E+00 | 9.17E+00 | 9.23E+00 | 9.33E+00 |
| He_FW | 3.29E+01 | 3.29E+01 | 3.29E+01 | 3.30E+01 |
| He_Manifold | 9.71E+00 | 9.75E+00 | 9.79E+00 | 9.85E+00 |
| He_Purge_BSS | 5.44E+00 | 5.45E+00 | 5.50E+00 | 5.54E+00 |
| LiSiO4_Bed | 4.14E+04 | 3.70E+04 | 3.65E+04 | 3.54E+04 |
| Manifold | 1.62E+02 | 1.62E+02 | 1.61E+02 | 1.61E+02 |
| Grand Total | 7.96E+04 | 7.52E+04 | 7.47E+04 | 7.37E+04 |

Table A.11. Power deposition in slices in the middle area of OB4 module.

| Region | Q_{dep} [W] | | |
|--------------------|-----------------|-----------------|--------------------|
| | DEMO Top Middle | DEMO Middle | DEMO Bottom Middle |
| Armour | 2.44E+03 | 2.43E+03 | 2.45E+03 |
| Beryllium Bed | 2.03E+04 | 2.03E+04 | 2.03E+04 |
| BSS | 1.80E+03 | 1.80E+03 | 1.80E+03 |
| CP | 7.40E+03 | 7.40E+03 | 7.41E+03 |
| FW | 7.72E+03 | 7.71E+03 | 7.72E+03 |
| He_BSS | 2.20E+00 | 2.20E+00 | 2.20E+00 |
| He_CP | 2.79E+01 | 2.79E+01 | 2.80E+01 |
| He_Dummy_Channels | 1.01E+01 | 1.01E+01 | 1.01E+01 |
| He_FW | 3.42E+01 | 3.41E+01 | 3.42E+01 |
| He_Manifold | 1.06E+01 | 1.06E+01 | 1.06E+01 |
| He_Purge_BSS | 6.03E+00 | 6.03E+00 | 6.05E+00 |
| LiSiO4_Bed | 3.56E+04 | 3.56E+04 | 3.56E+04 |
| Manifold | 1.59E+02 | 1.59E+02 | 1.59E+02 |
| Grand Total | 7.55E+04 | 7.55E+04 | 7.56E+04 |

Table A.12. Power deposition in slices adjacent to the bottom cap.

| Region | Q_{dep} [W] | | | |
|-------------------------|-----------------------------|-----------------------------|-----------------------------|-----------------|
| | DEMO 4 th Bottom | DEMO 3 rd Bottom | DEMO 2 nd Bottom | DEMO Bottom |
| Armour | 2.43E+03 | 2.44E+03 | 2.46E+03 | 2.47E+03 |
| Beryllium Bed | 1.96E+04 | 1.95E+04 | 1.94E+04 | 1.93E+04 |
| BSS | 1.78E+03 | 1.79E+03 | 1.80E+03 | 1.84E+03 |
| CP | 7.30E+03 | 7.31E+03 | 7.33E+03 | 7.38E+03 |
| FW | 7.65E+03 | 7.75E+03 | 7.79E+03 | 7.81E+03 |
| He_BSS | 1.97E+00 | 1.94E+00 | 1.91E+00 | 1.88E+00 |
| He_CP | 2.69E+01 | 2.68E+01 | 2.66E+01 | 2.64E+01 |
| He_Dummy_Channels | 9.56E+00 | 9.44E+00 | 9.37E+00 | 9.23E+00 |
| He_FW | 3.34E+01 | 3.34E+01 | 3.35E+01 | 3.35E+01 |
| He_Manifold | 9.62E+00 | 9.54E+00 | 9.46E+00 | 9.38E+00 |
| He_Purge_BSS | 5.61E+00 | 5.56E+00 | 5.50E+00 | 5.47E+00 |
| LiSiO ₄ _Bed | 3.58E+04 | 3.67E+04 | 3.73E+04 | 4.15E+04 |
| Manifold | 1.57E+02 | 1.58E+02 | 1.59E+02 | 1.58E+02 |
| Grand Total | 7.48E+04 | 7.58E+04 | 7.63E+04 | 8.06E+04 |

9.4 MAIA Thermal-hydraulic Symmetry Condition Consistency Verification

In this Appendix, the case studies identified for the consistency check of thermal hydraulic symmetry conditions are reported. In Table A.13 and Table A.14, the combinations of power density and mass flow rates for the three neighbouring HCPB slice are reported.

Table A.13. Power density and mass flow rates for the cases from 0 to 3.

| CASE 0 | Regions | CENTRAL | UP | DOWN | Note | |
|------------------------------|---------------|-----------|-----------|-----------|---|---|
| q''' [W cm ⁻³] | Armour | 22.361284 | 22.361284 | 22.361284 | Same power density and mass flow rates | |
| | Beryllium Bed | 1.492482 | 1.492482 | 1.492482 | | |
| | BSS | 0.222563 | 0.222563 | 0.222563 | | |
| | CP | 2.739606 | 2.739606 | 2.739606 | | |
| | FW | 5.905332 | 5.905332 | 5.905332 | | |
| | LiSiO4_Bed | 6.441772 | 6.441772 | 6.441772 | | |
| G [kg s ⁻¹] | He_Coolant_1 | 0.046072 | 0.046072 | 0.046072 | | |
| | He_Coolant_2 | 0.046072 | 0.046072 | 0.046072 | | |
| CASE 1 | Regions | CENTRAL | UP | DOWN | | Note |
| q''' [W cm ⁻³] | Armour | 22.361284 | 22.442035 | 22.459254 | | Power density calculated on equatorial SLICE with: CASE 1, mass flow rate from power balance CASE 2, mass flow rate min in UP and max in DOWN CASE 3, mass flow rate max in UP and min in DOWN |
| | Beryllium Bed | 1.492482 | 1.493466 | 1.495721 | | |
| | BSS | 0.222563 | 0.223070 | 0.223188 | | |
| | CP | 2.739606 | 2.741598 | 2.743442 | | |
| | FW | 5.905332 | 5.909846 | 5.915464 | | |
| | LiSiO4_Bed | 6.441772 | 6.436210 | 6.441918 | | |
| G [kg s ⁻¹] | He_Coolant_1 | 0.046072 | 0.046067 | 0.046020 | | |
| | He_Coolant_2 | 0.046072 | 0.046067 | 0.046020 | | |
| CASE 2 | Regions | CENTRAL | UP | DOWN | Note | |
| q''' [W cm ⁻³] | Armour | 22.361284 | 22.442035 | 22.459254 | Power density calculated on equatorial SLICE with: CASE 1, mass flow rate from power balance CASE 2, mass flow rate min in UP and max in DOWN CASE 3, mass flow rate max in UP and min in DOWN | |
| | Beryllium Bed | 1.492482 | 1.493466 | 1.495721 | | |
| | BSS | 0.222563 | 0.223070 | 0.223188 | | |
| | CP | 2.739606 | 2.741598 | 2.743442 | | |
| | FW | 5.905332 | 5.909846 | 5.915464 | | |
| | LiSiO4_Bed | 6.441772 | 6.436210 | 6.441918 | | |
| G [kg s ⁻¹] | He_Coolant_1 | 0.046072 | 0.045476 | 0.046327 | | |
| | He_Coolant_2 | 0.046072 | 0.045476 | 0.046327 | | |
| CASE 3 | Regions | CENTRAL | UP | DOWN | | Note |
| q''' [W cm ⁻³] | Armour | 22.361284 | 22.442035 | 22.459254 | | Power density calculated on equatorial SLICE with: CASE 1, mass flow rate from power balance CASE 2, mass flow rate min in UP and max in DOWN CASE 3, mass flow rate max in UP and min in DOWN |
| | Beryllium Bed | 1.492482 | 1.493466 | 1.495721 | | |
| | BSS | 0.222563 | 0.223070 | 0.223188 | | |
| | CP | 2.739606 | 2.741598 | 2.743442 | | |
| | FW | 5.905332 | 5.909846 | 5.915464 | | |
| | LiSiO4_Bed | 6.441772 | 6.436210 | 6.441918 | | |
| G [kg s ⁻¹] | He_Coolant_1 | 0.046072 | 0.046327 | 0.045476 | | |
| | He_Coolant_2 | 0.046072 | 0.046327 | 0.045476 | | |
| | He_Coolant_2 | 0.046072 | 0.046327 | 0.045476 | | |

Table A.14. Power density and mass flow rates for the cases from 4 to 7.

| CASE 4 | Regions | CENTRAL | UP | DOWN | Note | |
|----------------------------|----------------|----------------|-----------|-------------|--|--|
| q''' [W cm ⁻³] | Armour | 22.36128 | 22.36108 | 22.35779 | Power density calculated near the cap with: CASE 4, mass flow rate from power balance CASE 5, mass flow rate min in UP and max in DOWN CASE 6, mass flow rate max in UP and min in DOWN | |
| | Beryllium Bed | 1.49248 | 1.49083 | 1.50587 | | |
| | BSS | 0.22256 | 0.22745 | 0.21954 | | |
| | CP | 2.73961 | 2.76097 | 2.73267 | | |
| | FW | 5.90533 | 5.91289 | 5.94284 | | |
| | LiSiO4_Bed | 6.44177 | 7.20478 | 6.33827 | | |
| G [kg s ⁻¹] | He_Coolant_1 | 0.046072 | 0.043330 | 0.046020 | | |
| | He_Coolant_2 | 0.046072 | 0.043330 | 0.046020 | | |
| CASE 5 | Regions | CENTRAL | UP | DOWN | | |
| q''' [W cm ⁻³] | Armour | 22.36128 | 22.36108 | 22.35779 | | |
| | Beryllium Bed | 1.49248 | 1.49083 | 1.50587 | | |
| | BSS | 0.22256 | 0.22745 | 0.21954 | | |
| | CP | 2.73961 | 2.76097 | 2.73267 | | |
| | FW | 5.90533 | 5.91289 | 5.94284 | | |
| | LiSiO4_Bed | 6.44177 | 7.20478 | 6.33827 | | |
| G [kg s ⁻¹] | He_Coolant_1 | 0.046072 | 0.045476 | 0.046327 | | |
| | He_Coolant_2 | 0.046072 | 0.045476 | 0.046327 | | |
| CASE 6 | Regions | CENTRAL | UP | DOWN | | |
| q''' [W cm ⁻³] | Armour | 22.361284 | 22.361077 | 22.357788 | | |
| | Beryllium Bed | 1.492482 | 1.490828 | 1.505867 | | |
| | BSS | 0.222563 | 0.227447 | 0.219542 | | |
| | CP | 2.739606 | 2.760968 | 2.732668 | | |
| | FW | 5.905332 | 5.912886 | 5.942843 | | |
| | LiSiO4_Bed | 6.441772 | 7.204782 | 6.338269 | | |
| G [kg s ⁻¹] | He_Coolant_1 | 0.046072 | 0.046327 | 0.045476 | | |
| | He_Coolant_2 | 0.046072 | 0.046327 | 0.045476 | | |

9.5 MAIA Thermal-hydraulic Symmetry Condition Sensitivity Analysis

In this Appendix, the probabilistic distribution of the heat fluxes calculated at the boundaries of the central slice due to the statistical variation of the power densities and mass flow rates in the neighboring slices is reported. From Figure A.2 to Figure A.9, the calculated statistical variation of the heat flux in each interface region is shown.

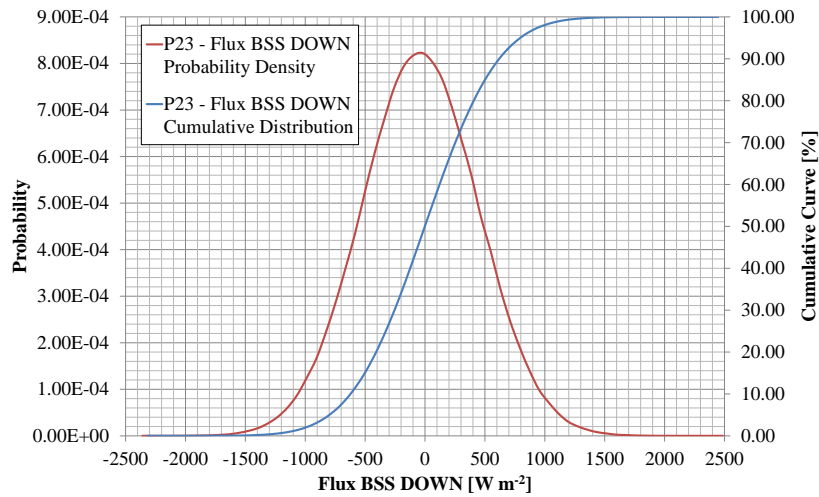


Figure A.2. Statistical distribution of heat flux at the BSS DOWN boundary.

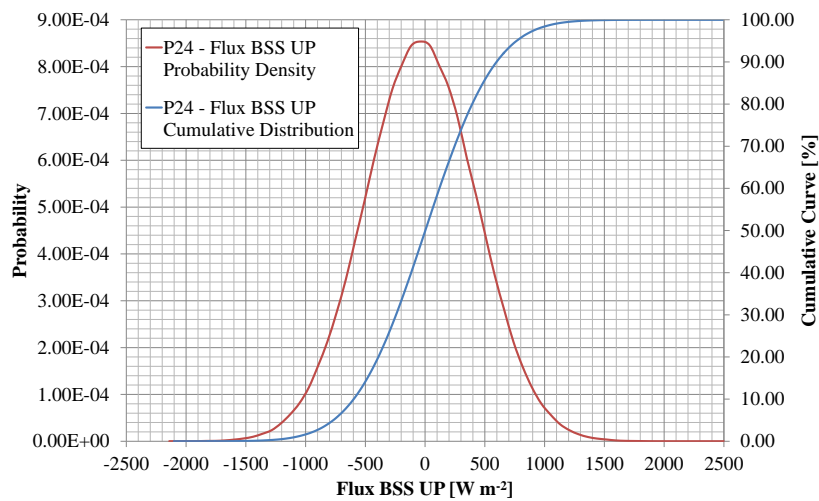


Figure A.3. Statistical distribution of heat flux at the BSS UP boundary.

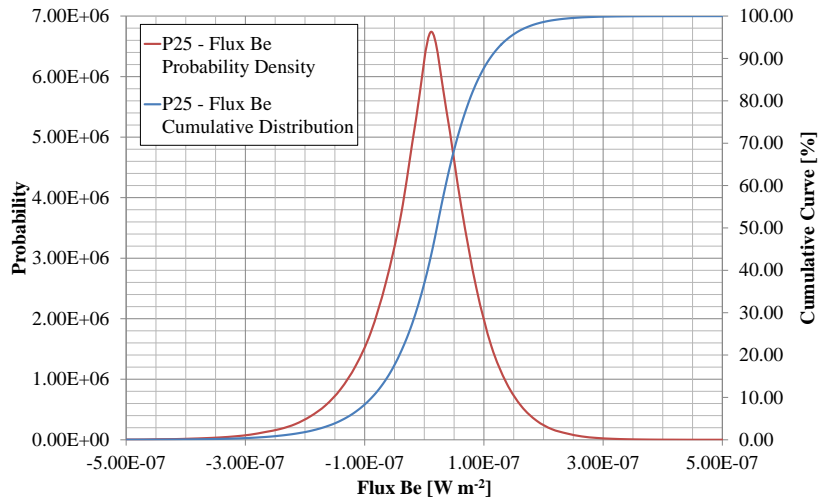


Figure A.4. Statistical distribution of heat flux at the Be bed boundary.

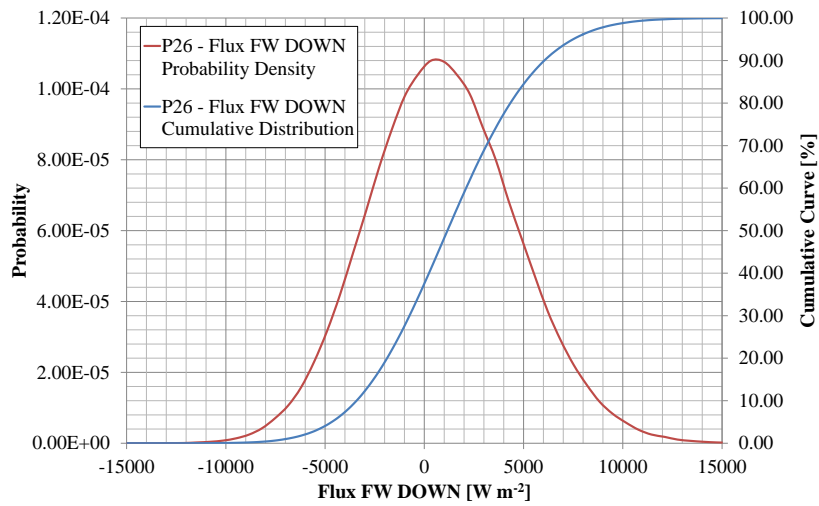


Figure A.5. Statistical distribution of heat flux at the FW DOWN boundary.

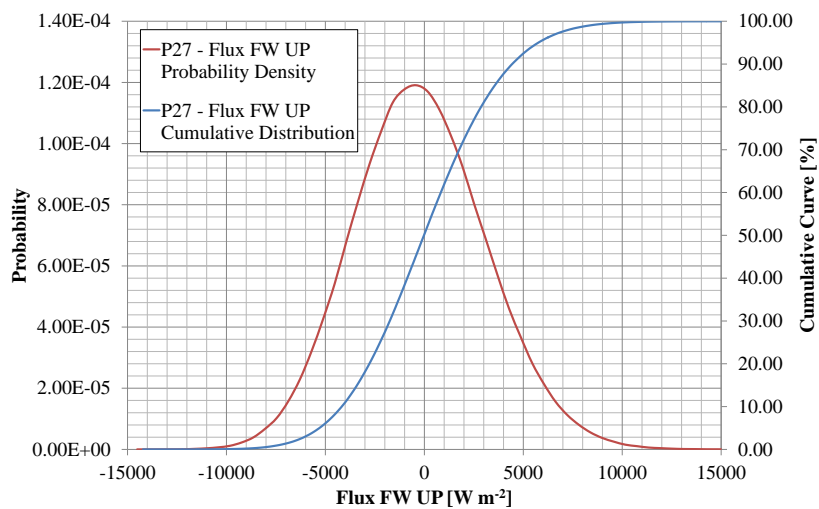


Figure A.6. Statistical distribution of heat flux at the FW UP boundary.

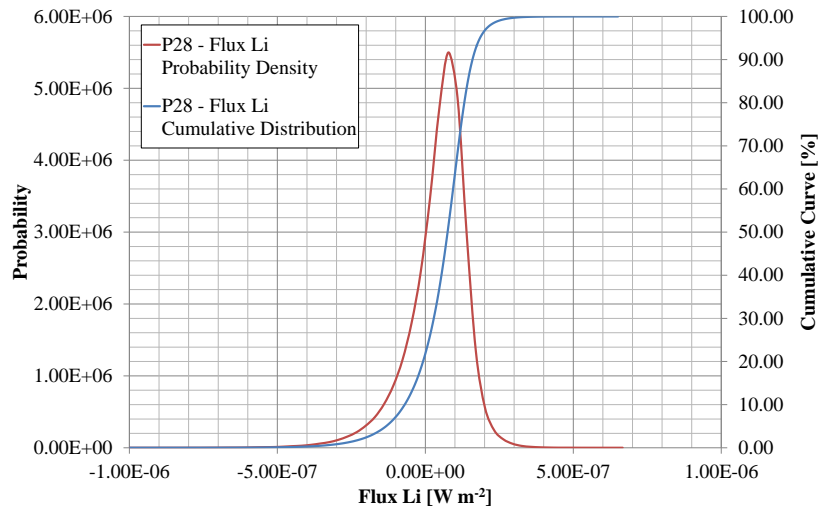


Figure A.7. Statistical distribution of heat flux at the Li_4SiO_4 boundary.

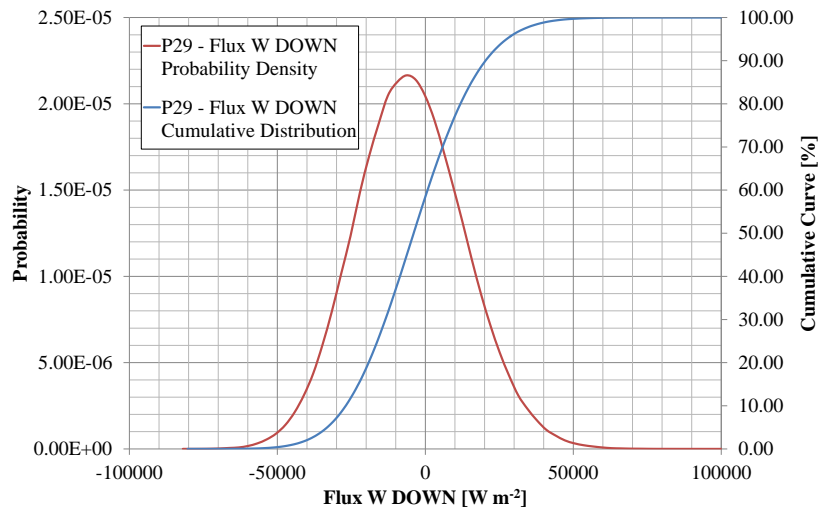


Figure A.8. Statistical distribution of heat flux at the W DOWN boundary.

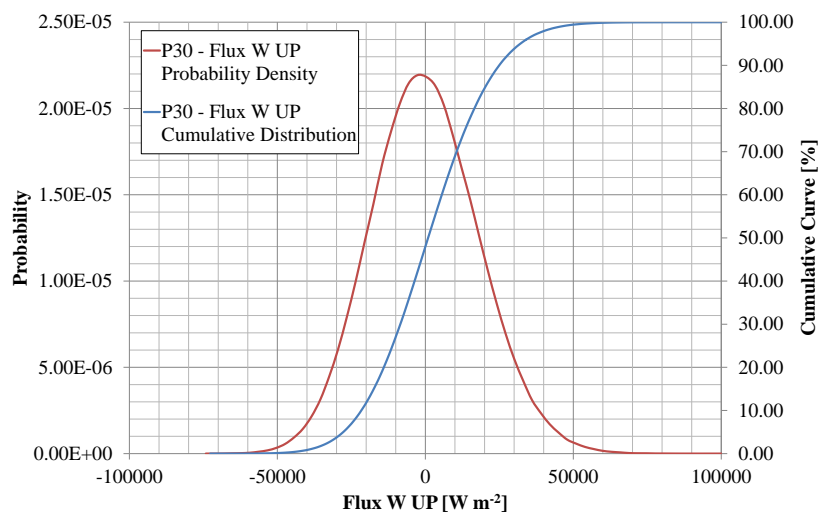


Figure A.9. Statistical distribution of heat flux at the W UP boundary.

9.6 MAIA Thermo-mechanic Conditions Consistency Verification

In this Appendix, the results on primary and secondary stresses calculated for the consistency check of thermo-mechanical boundary conditions are reported.

From Figure A.10 to Figure A.12, the secondary stress tensor components for the reference HCPB module are shown. On the right, the contour map of the error for each stress tensor component between the reference model and the HCPB slice model, on which the boundary conditions are applied, is displayed. A radial profile of temperature has been used for these calculations.

From Table A.15 to Table A.19, the stress linearization and the equivalent secondary stresses for five paths identified are reported. A comparison between the membrane and bending stress for each component and for the equivalent stress is also shown.

From Figure A.13 to Figure A.15, the primary stress tensor components for the reference HCPB module are shown. On the right, the contour map of the error for each stress tensor component between the reference model and the HCPB slice model, on which the boundary conditions are applied, is displayed. An over pressurization scenario has been used for these calculations.

From Table A.20 to Table A.24, the stress linearization and the equivalent primary stresses for five paths identified are reported. A comparison between the membrane and bending stress for each component and for the equivalent stress is also shown.

From Table A.25 to Table A.29, considering the temperature variations identified during the thermal-hydraulic consistency check, the sensitivity of secondary stresses with respect to the temperature fluctuations has been investigated. The stress linearization and the equivalent primary stresses for five paths identified are reported. A comparison between the membrane and bending stress for each component and for the equivalent stress is also shown.

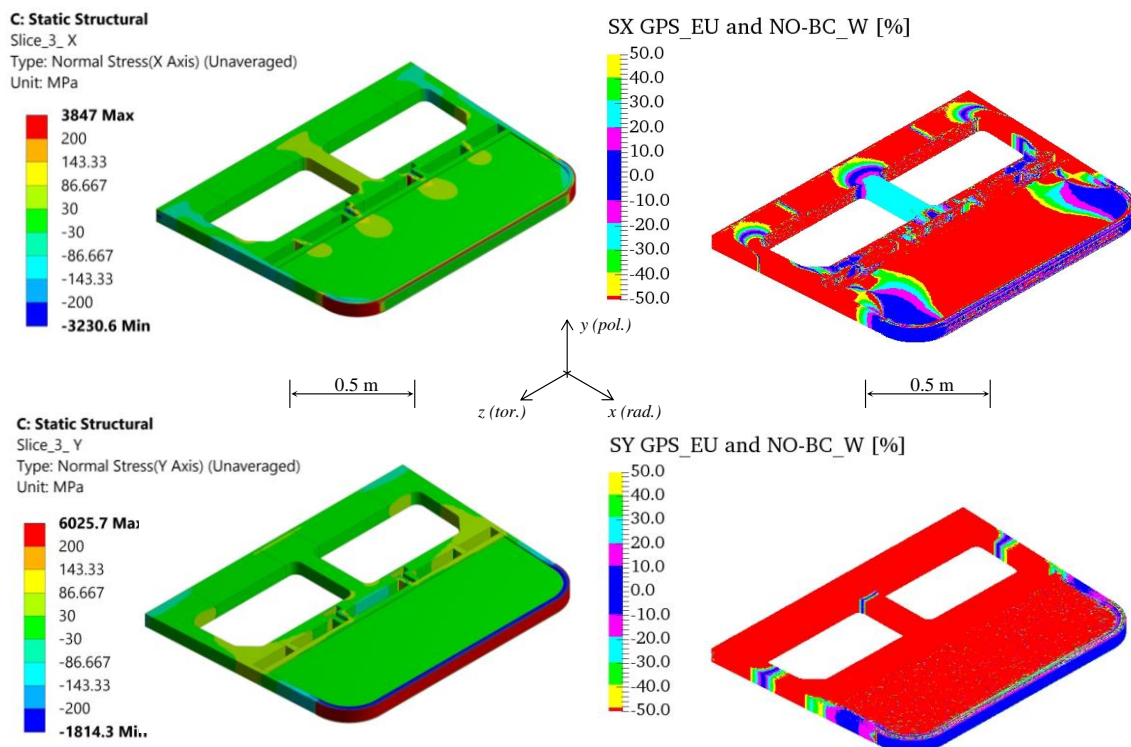


Figure A.10. S_x and S_y secondary stress tensor components of HCPB module model and error contour map of the HCPB slice. In the pictures on the right, the red colour represents the values out of scale.

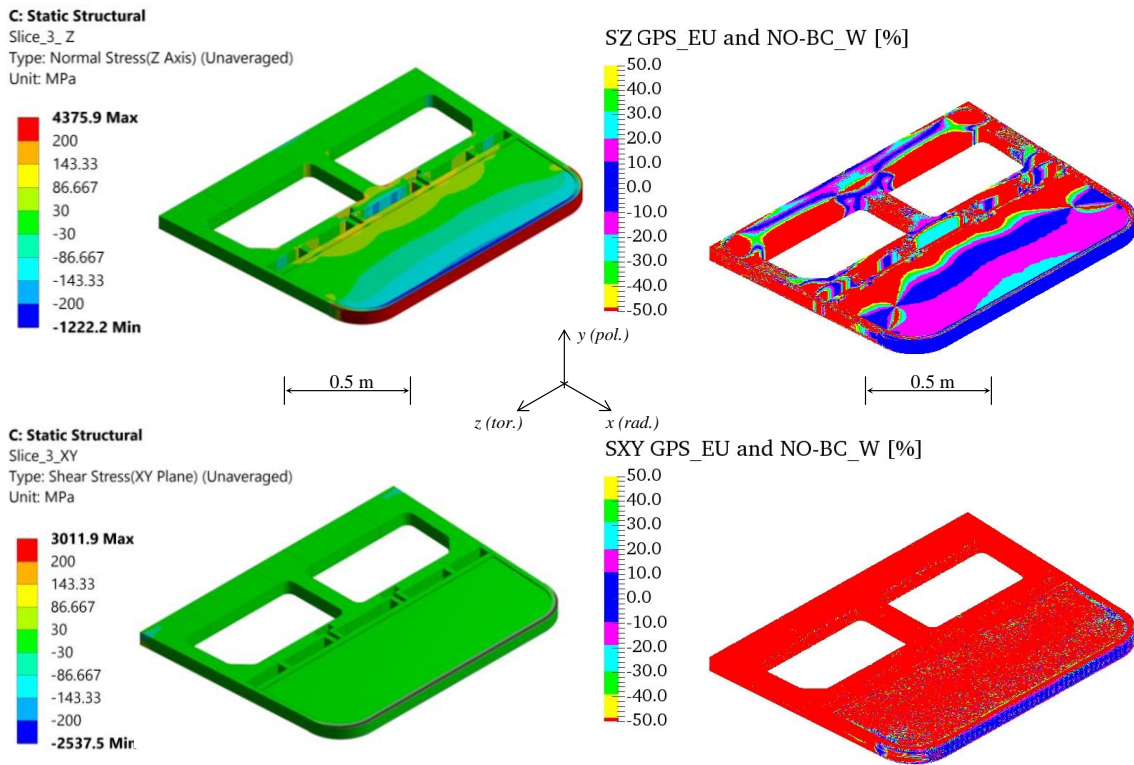


Figure A.11. S_z and S_{xy} secondary stress tensor components of HCPB module model and error contour map of the HCPB slice. In the pictures on the right, the red colour represents the values out of scale.

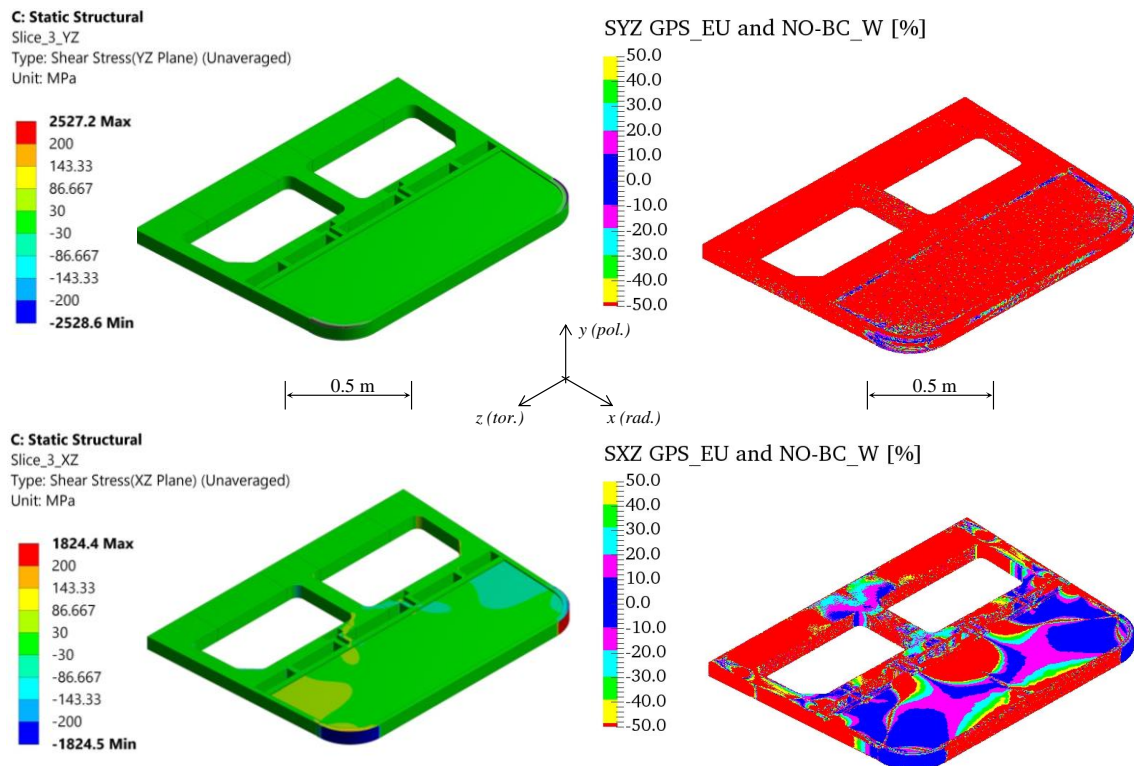


Figure A.12. S_{yz} and S_{xz} secondary stress tensor components of HCPB module model and error contour map of the HCPB slice. In the pictures on the right, the red colour represents the values out of scale.

Table A.15. Membrane and bending secondary stress tensor component for the reference HCPB module and slice models on Path1.

| Path1 | Module_Slice | | Slice_GPS_EU | | Membrane Error | Bending Error |
|----------------------------------|------------------|------------------|------------------|------------------|----------------|---------------|
| | Membrane [MPa] | Bending [MPa] | Membrane [MPa] | Bending [MPa] | | |
| Sx | -2.480E+00 | 7.552E-01 | -2.194E+00 | 6.615E-01 | 11.56% | 12.40% |
| Sy | -3.101E+02 | 5.676E+01 | -4.402E+02 | 5.821E+01 | -41.94% | -2.54% |
| Sz | -2.628E+02 | 2.499E+01 | -2.683E+02 | 2.468E+01 | -2.08% | 1.24% |
| Sxy | 4.243E-02 | -5.191E-02 | 2.123E-02 | -5.450E-02 | 49.98% | -4.99% |
| Syz | -2.453E-03 | -1.626E-03 | -2.646E-03 | -2.328E-03 | -7.87% | -43.14% |
| Sxz | 2.927E-03 | -8.274E-04 | 4.417E-04 | 1.272E-03 | 84.91% | 253.70% |
| Equiv. Stress (Von Mises) | 2.869E+02 | 4.865E+01 | 3.822E+02 | 5.006E+01 | -33.21% | -2.90% |

Table A.16. Membrane and bending secondary stress tensor component for the reference HCPB module and slice models on Path2.

| Path2 | Module_Slice | | Slice_GPS_EU | | Membrane Error | Bending Error |
|----------------------------------|------------------|------------------|------------------|------------------|----------------|---------------|
| | Membrane [MPa] | Bending [MPa] | Membrane [MPa] | Bending [MPa] | | |
| Sx | -1.096E+01 | 9.471E+00 | -1.078E+01 | 9.340E+00 | 1.66% | 1.38% |
| Sy | -3.609E+02 | 5.950E+01 | -4.305E+02 | 5.943E+01 | -19.30% | 0.11% |
| Sz | -2.219E+02 | 1.209E+01 | -2.293E+02 | 1.069E+01 | -3.34% | 11.63% |
| Sxy | 5.029E-02 | -5.448E-02 | 3.635E-02 | -6.111E-02 | 27.72% | -12.17% |
| Syz | 2.487E-02 | -9.094E-04 | -7.661E-02 | -1.821E-02 | 408.09% | -1902.24% |
| Sxz | -4.582E-01 | 4.243E+00 | 5.044E-01 | 4.053E+00 | 210.09% | 4.48% |
| Equiv. Stress (Von Mises) | 3.052E+02 | 4.932E+01 | 3.636E+02 | 4.993E+01 | -19.15% | -1.24% |

Table A.17. Membrane and bending secondary stress tensor component for the reference HCPB module and slice models on Path3.

| Path3 | Module_Slice | | Slice_GPS_EU | | Membrane Error | Bending Error |
|----------------------------------|------------------|------------------|------------------|------------------|----------------|----------------|
| | Membrane [MPa] | Bending [MPa] | Membrane [MPa] | Bending [MPa] | | |
| Sx | -5.900E-03 | -2.629E-03 | 1.081E-01 | 1.509E-02 | 1932.28% | 673.96% |
| Sy | 1.590E+01 | -1.150E+01 | 1.334E+02 | -1.375E+01 | -738.63% | -19.56% |
| Sz | 8.501E+01 | -5.110E+00 | 8.196E+01 | -1.550E+00 | 3.58% | 69.67% |
| Sxy | -2.916E-02 | 2.168E-03 | -2.032E-02 | 1.821E-03 | 30.32% | 15.99% |
| Syz | 8.660E-04 | -3.435E-04 | 9.977E-05 | -2.641E-04 | 88.48% | 23.11% |
| Sxz | 9.778E-05 | -1.226E-04 | -7.905E-05 | 8.658E-05 | 180.85% | 170.62% |
| Equiv. Stress (Von Mises) | 7.828E+01 | 9.976E+00 | 1.164E+02 | 1.305E+01 | -48.69% | -30.82% |

Table A.18. Membrane and bending secondary stress tensor component for the reference HCPB module and slice models on Path4.

| Path4 | Module_Slice | | Slice_GPS_EU | | Membrane Error | Bending Error |
|----------------------------------|------------------|------------------|------------------|------------------|----------------|---------------|
| | Membrane [MPa] | Bending [MPa] | Membrane [MPa] | Bending [MPa] | | |
| Sx | -1.955E+01 | -5.263E+00 | -5.777E+01 | -4.958E+00 | -195.49% | 5.79% |
| Sy | -7.396E+01 | -1.346E+00 | -6.155E+01 | -9.579E-01 | 16.78% | 28.84% |
| Sz | -2.483E-01 | -6.303E-03 | -3.604E-01 | -6.275E-03 | -45.19% | 0.44% |
| Sxy | -1.200E-01 | 1.023E-03 | -9.928E-03 | 3.021E-03 | 91.73% | -195.34% |
| Syz | 1.531E-02 | 1.517E-03 | 4.817E-03 | 1.142E-03 | 68.53% | 24.72% |
| Sxz | 2.201E+00 | 2.314E-01 | 4.433E+00 | 2.095E-01 | -101.40% | 9.45% |
| Equiv. Stress (Von Mises) | 6.631E+01 | 4.748E+00 | 5.988E+01 | 4.566E+00 | 9.69% | 3.84% |

Table A.19. Membrane and bending secondary stress tensor component for the reference HCPB module and slice models on Path5.

| Path5 | Module_Slice | | Slice_GPS_EU | | Membrane Error | Bending Error |
|----------------------------------|------------------|------------------|------------------|------------------|-----------------|----------------|
| | Membrane [MPa] | Bending [MPa] | Membrane [MPa] | Bending [MPa] | | |
| Sx | -1.066E-02 | 1.802E-04 | -6.135E-03 | 1.337E-04 | 42.43% | 25.80% |
| Sy | 1.839E+01 | 8.918E+00 | 9.934E+01 | 1.484E+01 | -440.06% | -66.40% |
| Sz | 1.141E+01 | 1.524E+01 | 4.569E+00 | 1.971E+01 | 59.96% | -29.29% |
| Sxy | -1.338E-04 | 5.177E-05 | 6.746E-05 | -1.299E-04 | 150.40% | 350.95% |
| Syz | -2.706E-02 | 4.200E-04 | -1.821E-05 | 1.351E-04 | 99.93% | 67.83% |
| Sxz | 1.764E+00 | 2.515E-02 | 8.015E-01 | 1.454E-02 | 54.56% | 42.20% |
| Equiv. Stress (Von Mises) | 1.638E+01 | 1.326E+01 | 9.715E+01 | 1.778E+01 | -493.08% | -34.05% |

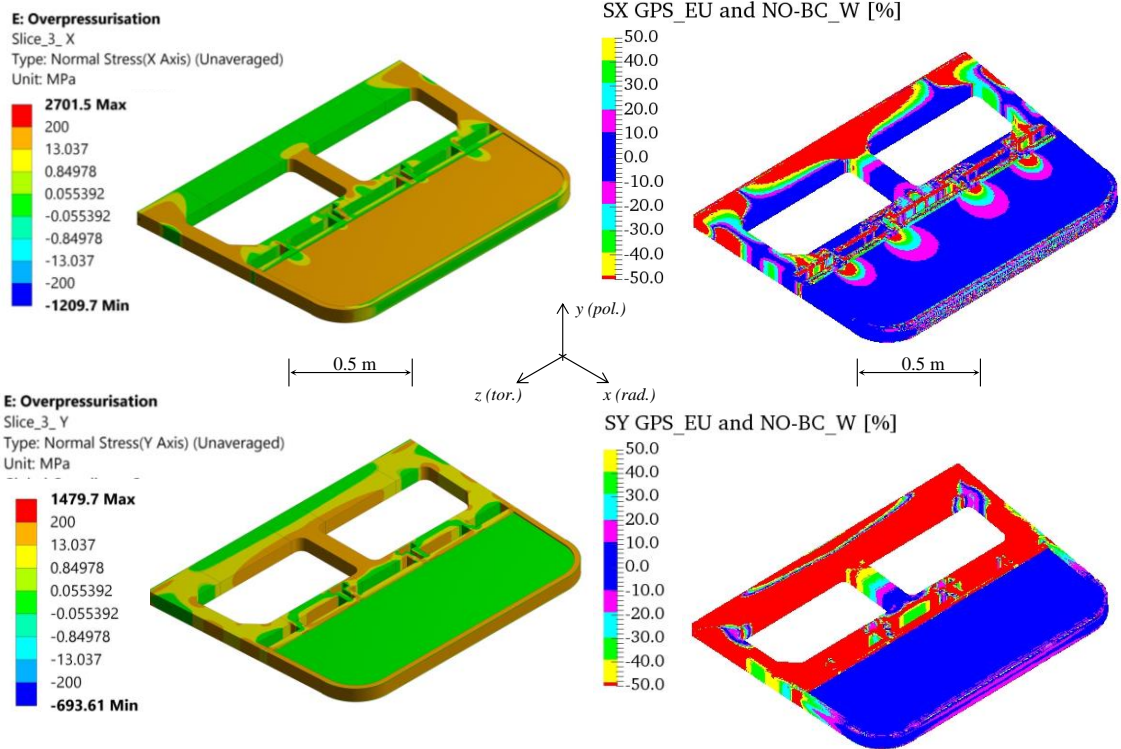


Figure A.13. S_x and S_y primary stress tensor components of HCPB module model and error contour map of the HCPB slice. In the pictures on the right, the red colour represents the values out of scale.

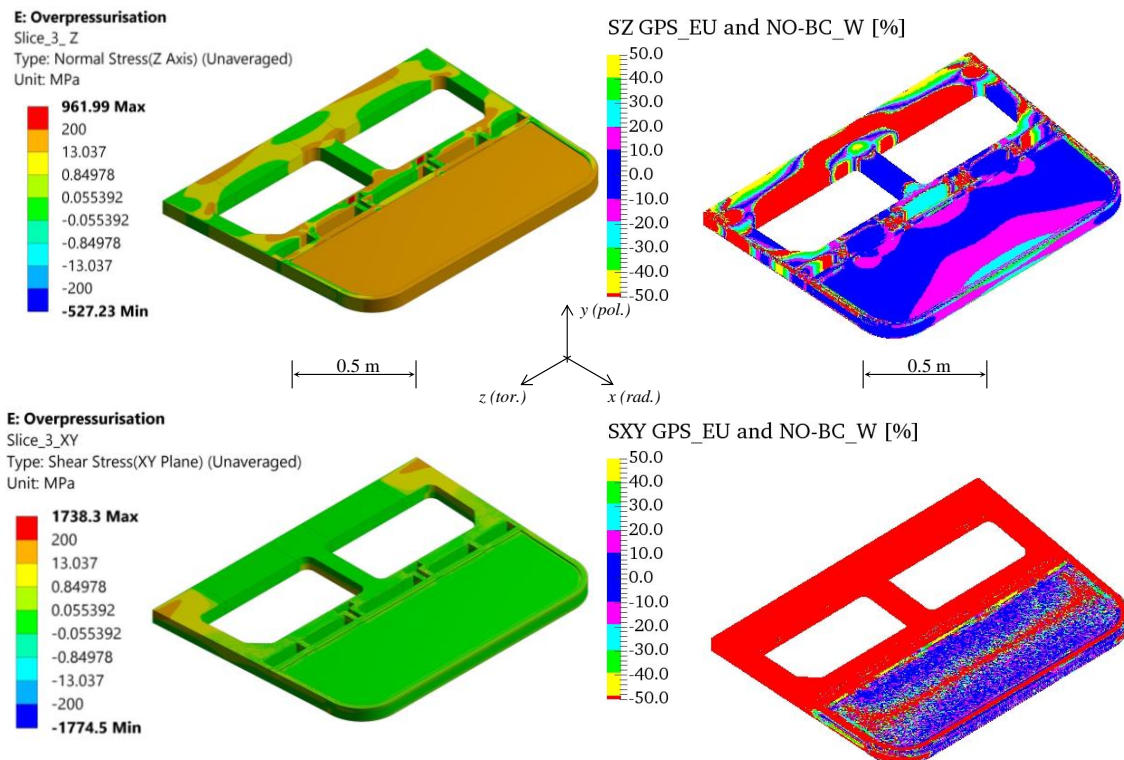


Figure A.14. S_z and S_{xy} primary stress tensor components of HCPB module model and error contour map of the HCPB slice. In the pictures on the right, the red colour represents the values out of scale.

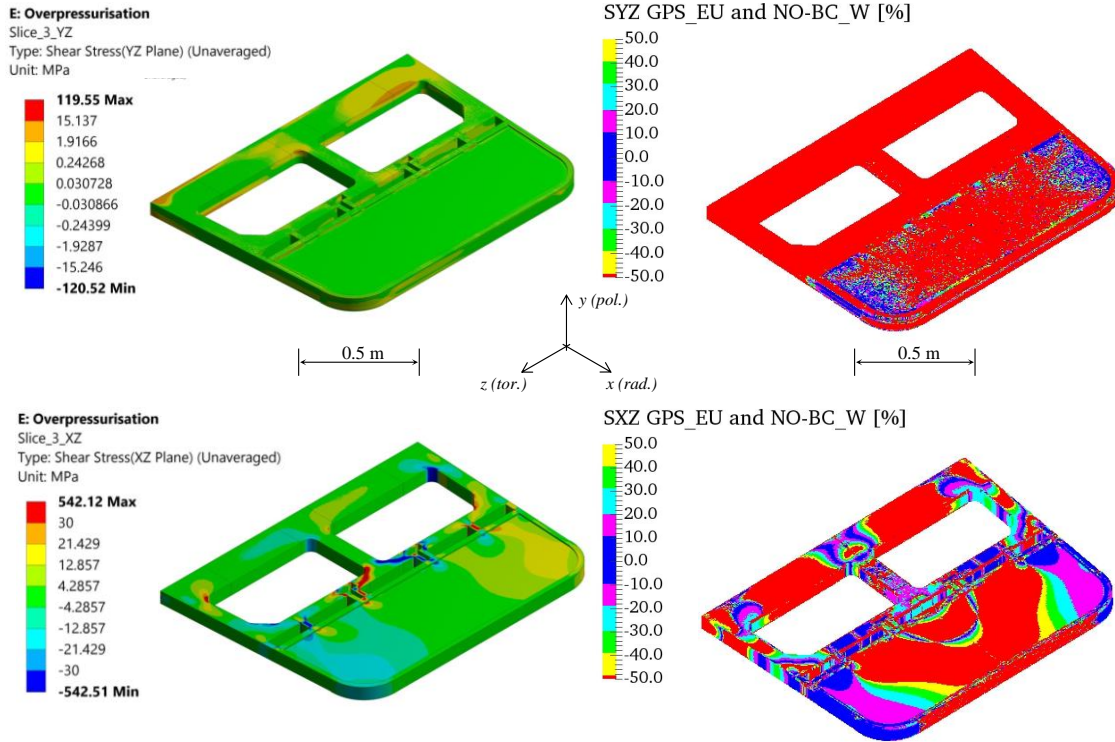


Figure A.15. S_{yz} and S_{xz} primary stress tensor components of HCPB module model and error contour map of the HCPB slice. In the pictures on the right, the red colour represents the values out of scale.

Table A.20. Membrane and bending primary stress tensor component for the reference HCPB module and slice models on Path1.

| Path1 | Module_Slice3 | | Slice3_GPS_EU | | Membrane Error | Bending Error |
|----------------------------------|------------------|------------------|------------------|------------------|----------------|---------------|
| | Membrane [MPa] | Bending [MPa] | Membrane [MPa] | Bending [MPa] | | |
| Sx | -4.726E+00 | -4.430E+00 | -4.716E+00 | -4.433E+00 | 0.20% | -0.07% |
| Sy | 5.081E+01 | -5.716E+00 | 4.527E+01 | -5.825E+00 | 10.91% | -1.91% |
| Sz | 4.019E+01 | -3.791E+00 | 4.803E+01 | -4.438E+00 | -19.52% | -17.05% |
| Sxy | 9.814E-03 | -1.309E-03 | 1.144E-03 | 9.597E-04 | 88.35% | 173.33% |
| Syz | 5.999E-04 | 3.884E-04 | 4.322E-04 | 5.376E-05 | 27.95% | 86.16% |
| Sxz | -3.028E-04 | 1.207E-05 | -2.609E-04 | 7.774E-05 | 13.83% | -544.19% |
| Equiv. Stress (Von Mises) | 5.106E+01 | 1.698E+00 | 5.142E+01 | 1.390E+00 | -0.71% | 18.14% |

Table A.21. Membrane and bending primary stress tensor component for the reference HCPB module and slice models on Path2.

| Path2 | Module_Slice3 | | Slice3_GPS_EU | | Membrane Error | Bending Error |
|----------------------------------|------------------|------------------|------------------|------------------|----------------|---------------|
| | Membrane [MPa] | Bending [MPa] | Membrane [MPa] | Bending [MPa] | | |
| Sx | -4.450E+00 | -4.147E+00 | -4.427E+00 | -4.129E+00 | 0.53% | 0.42% |
| Sy | 4.431E+01 | -2.968E+00 | 4.028E+01 | -2.875E+00 | 9.09% | 3.13% |
| Sz | 3.011E+01 | 6.725E-01 | 3.245E+01 | 1.015E+00 | -7.76% | -50.97% |
| Sxy | 3.157E-03 | 1.114E-04 | 5.270E-04 | 5.357E-04 | 83.31% | -380.77% |
| Syz | 8.701E-02 | 1.285E-03 | -2.228E-03 | -6.782E-05 | 102.56% | 105.28% |
| Sxz | -2.795E+00 | 4.949E-01 | -2.998E+00 | 5.315E-01 | -7.27% | -7.40% |
| Equiv. Stress (Von Mises) | 4.371E+01 | 4.435E+00 | 4.168E+01 | 4.736E+00 | 4.64% | -6.80% |

Table A.22. Membrane and bending primary stress tensor component for the reference HCPB module and slice models on Path3.

| Path3 | Module_Slice3 | | Slice3_GPS_EU | | Membrane Error | Bending Error |
|----------------------------------|------------------|------------------|------------------|------------------|----------------|---------------|
| | Membrane [MPa] | Bending [MPa] | Membrane [MPa] | Bending [MPa] | | |
| Sx | -4.182E+00 | -4.820E+00 | -4.174E+00 | -4.819E+00 | 0.19% | 0.02% |
| Sy | 8.287E+00 | -5.603E+00 | 1.824E+01 | -6.052E+00 | -120.07% | -8.00% |
| Sz | 8.668E+00 | -3.436E+00 | 1.077E+01 | -4.308E+00 | -24.25% | -25.38% |
| Sxy | -8.753E-03 | -2.001E-03 | -8.258E-04 | -2.548E-03 | 90.57% | -27.35% |
| Syz | 1.440E-04 | 1.399E-04 | 1.844E-04 | 4.602E-04 | -28.08% | -228.99% |
| Sxz | -1.102E-04 | 5.727E-05 | -9.830E-05 | 7.502E-05 | 10.80% | -31.01% |
| Equiv. Stress (Von Mises) | 1.266E+01 | 1.901E+00 | 1.977E+01 | 1.553E+00 | -56.09% | 18.32% |

Table A.23. Membrane and bending primary stress tensor component for the reference HCPB module and slice models on Path4.

| Path4 | Module_Slice3 | | Slice3_GPS_EU | | Membrane Error | Bending Error |
|----------------------------------|------------------|------------------|------------------|------------------|----------------|---------------|
| | Membrane [MPa] | Bending [MPa] | Membrane [MPa] | Bending [MPa] | | |
| Sx | 5.002E+01 | 8.612E+00 | 5.078E+01 | 8.677E+00 | -1.53% | -0.76% |
| Sy | 2.971E+01 | 1.031E+01 | 3.559E+01 | 1.031E+01 | -19.79% | -0.02% |
| Sz | -3.987E+00 | 4.773E+00 | -3.976E+00 | 4.773E+00 | 0.28% | 0.00% |
| Sxy | -9.981E-02 | -5.313E-04 | -3.604E-04 | 2.106E-03 | 99.64% | 496.31% |
| Syz | 9.912E-03 | -2.339E-03 | -4.884E-04 | -2.562E-03 | 104.93% | -9.54% |
| Sxz | -3.482E+00 | -2.112E-01 | -3.564E+00 | -2.126E-01 | -2.34% | -0.66% |
| Equiv. Stress (Von Mises) | 4.763E+01 | 4.925E+00 | 4.935E+01 | 4.941E+00 | -3.62% | -0.33% |

Table A.24. Membrane and bending primary stress tensor component for the reference HCPB module and slice models on Path5.

| Path5 | Module_Slice3 | | Slice3_GPS_EU | | Membrane Error | Bending Error |
|----------------------------------|------------------|------------------|------------------|------------------|----------------|---------------|
| | Membrane [MPa] | Bending [MPa] | Membrane [MPa] | Bending [MPa] | | |
| Sx | -4.009E+00 | 4.718E+00 | -4.011E+00 | 4.718E+00 | -0.03% | 0.00% |
| Sy | -5.499E-01 | 2.004E+01 | 1.176E+01 | 1.980E+01 | 2238.75% | 1.19% |
| Sz | 5.534E+00 | 6.029E+01 | 6.716E+00 | 5.981E+01 | -21.36% | 0.80% |
| Sxy | -1.847E-05 | 1.766E-08 | 7.516E-05 | -2.947E-05 | 506.92% | 167021.55% |
| Syz | -2.673E-02 | 1.296E-03 | 2.371E-05 | -7.165E-05 | 100.09% | 105.53% |
| Sxz | -5.149E-01 | 6.382E-02 | -6.892E-01 | 6.824E-02 | -33.86% | -6.92% |
| Equiv. Stress (Von Mises) | 8.416E+00 | 4.971E+01 | 1.400E+01 | 4.931E+01 | -66.38% | 0.81% |

Table A.25. Sensitivity analysis of membrane and bending stress tensor component for the reference HCPB module and slice models on Path1.

| Path1 | Case0_Single Slice | | Case0_3Slice | | Case4 | | Case5 | | Case0 Membr. Error | Case0 Bend. Error | Case4 Membr. Error | Case4 Bend. Error | Case5 Membr. Error | Case5 Bend. Error |
|----------------------------------|--------------------|-----------------|-----------------|-----------------|-----------------|-----------------|-----------------|-----------------|--------------------|-------------------|--------------------|-------------------|--------------------|-------------------|
| | Membr. [MPa] | Bend. [MPa] | Membr. [MPa] | Bend. [MPa] | Membr. [MPa] | Bend. [MPa] | Membr. [MPa] | Bend. [MPa] | | | | | | |
| Sx | 1.87E+00 | -6.53E+00 | 1.67E+00 | -6.29E+00 | 1.29E+00 | -6.12E+00 | 1.51E+00 | -6.26E+00 | 10.86% | 3.69% | 31.16% | 6.18% | 19.22% | 4.16% |
| Sy | 4.35E+01 | 1.65E+02 | 4.85E+01 | 1.59E+02 | 4.84E+01 | 1.60E+02 | 4.92E+01 | 1.60E+02 | -11.38% | 3.53% | -11.17% | 3.04% | -12.88% | 3.10% |
| Sz | 8.19E+01 | 1.46E+02 | 9.03E+01 | 1.36E+02 | 9.35E+01 | 1.36E+02 | 9.10E+01 | 1.36E+02 | -10.19% | 7.34% | -14.12% | 7.14% | -11.11% | 7.29% |
| Sxy | -8.73E-01 | 5.42E-01 | -8.93E-01 | 5.91E-01 | -9.30E-01 | 1.56E-01 | -9.07E-01 | 4.76E-01 | -2.29% | -9.04% | -6.54% | 71.25% | -3.90% | 12.14% |
| Syz | 2.09E-01 | 1.99E-01 | 2.24E-01 | 1.66E-01 | 2.26E-01 | 1.73E-01 | 2.27E-01 | 1.67E-01 | -7.20% | 16.80% | -8.25% | 13.36% | -8.66% | 16.30% |
| Sxz | 1.41E-01 | 3.94E-02 | 1.43E-01 | 1.20E-02 | 1.45E-01 | 1.03E-02 | 1.45E-01 | 8.85E-03 | -1.60% | 69.56% | -3.14% | 73.91% | -3.09% | 77.57% |
| Equiv. Stress (Von Mises) | 6.94E+01 | 1.63E+02 | 7.68E+01 | 1.55E+02 | 7.99E+01 | 1.56E+02 | 7.76E+01 | 1.56E+02 | -10.71% | 4.89% | -15.15% | 4.62% | -11.86% | 4.62% |

Table A.26. Sensitivity analysis of membrane and bending stress tensor component for the reference HCPB module and slice models on Path2.

| Path2 | Case0_Single Slice | | Case0_3Slice | | Case4 | | Case5 | | Case0 Membr. Error | Case0 Bend. Error | Case4 Membr. Error | Case4 Bend. Error | Case5 Membr. Error | Case5 Bend. Error |
|----------------------------------|--------------------|-----------------|-----------------|-----------------|-----------------|-----------------|-----------------|-----------------|--------------------|-------------------|--------------------|-------------------|--------------------|-------------------|
| | Membr. [MPa] | Bend. [MPa] | Membr. [MPa] | Bend. [MPa] | Membr. [MPa] | Bend. [MPa] | Membr. [MPa] | Bend. [MPa] | | | | | | |
| Sx | -9.52E+00 | 6.21E-01 | -9.94E+00 | 1.10E+00 | -1.04E+01 | 1.28E+00 | -1.01E+01 | 1.14E+00 | -4.41% | -77.58% | -8.71% | -105.60% | -6.10% | -83.20% |
| Sy | 3.17E+01 | 1.58E+02 | 3.66E+01 | 1.53E+02 | 3.61E+01 | 1.53E+02 | 3.71E+01 | 1.53E+02 | -15.37% | 3.41% | -13.90% | 3.04% | -17.05% | 3.01% |
| Sz | -3.89E+01 | 1.46E+02 | -3.50E+01 | 1.37E+02 | -3.45E+01 | 1.38E+02 | -3.50E+01 | 1.37E+02 | 10.04% | 6.28% | 11.24% | 5.79% | 10.00% | 6.14% |
| Sxy | -3.52E+00 | 5.02E+00 | -3.56E+00 | 5.63E+00 | -3.62E+00 | 5.31E+00 | -3.58E+00 | 5.54E+00 | -1.15% | -12.05% | -2.67% | -5.77% | -1.55% | -10.35% |
| Syz | -5.26E+00 | -9.26E+00 | -5.39E+00 | -9.37E+00 | -5.46E+00 | -9.52E+00 | -5.40E+00 | -9.40E+00 | -2.40% | -1.18% | -3.70% | -2.85% | -2.68% | -1.53% |
| Sxz | -3.66E+01 | 1.58E+01 | -3.74E+01 | 1.62E+01 | -3.79E+01 | 1.65E+01 | -3.75E+01 | 1.63E+01 | -2.02% | -2.73% | -3.55% | -4.40% | -2.41% | -3.16% |
| Equiv. Stress (Von Mises) | 8.90E+01 | 1.55E+02 | 9.10E+01 | 1.48E+02 | 9.12E+01 | 1.49E+02 | 9.15E+01 | 1.49E+02 | -2.20% | 4.54% | -2.44% | 4.20% | -2.83% | 4.27% |

Table A.27. Sensitivity analysis of membrane and bending stress tensor component for the reference HCPB module and slice models on Path3.

| Path3 | Case0_Single Slice | | Case0_3Slice | | Case4 | | Case5 | | Case0 Membr. Error | Case0 Bend. Error | Case4 Membr. Error | Case4 Bend. Error | Case5 Membr. Error | Case5 Bend. Error |
|----------------------------------|--------------------|-----------------|-----------------|-----------------|-----------------|-----------------|-----------------|-----------------|--------------------|-------------------|--------------------|-------------------|--------------------|-------------------|
| | Membr. [MPa] | Bend. [MPa] | Membr. [MPa] | Bend. [MPa] | Membr. [MPa] | Bend. [MPa] | Membr. [MPa] | Bend. [MPa] | | | | | | |
| Sx | 1.58E+01 | 8.45E-01 | 1.61E+01 | 8.67E-01 | 1.66E+01 | 8.92E-01 | 1.63E+01 | 8.81E-01 | -1.93% | -2.64% | -5.00% | -5.64% | -3.22% | -4.30% |
| Sy | -3.45E+02 | 7.78E+01 | -3.51E+02 | 7.89E+01 | -3.62E+02 | 8.09E+01 | -3.56E+02 | 7.99E+01 | -1.83% | -1.40% | -4.87% | -3.97% | -3.22% | -2.66% |
| Sz | -4.53E+02 | 2.46E+01 | -4.62E+02 | 2.48E+01 | -4.76E+02 | 2.56E+01 | -4.70E+02 | 2.53E+01 | -1.80% | -0.98% | -5.04% | -4.32% | -3.56% | -2.74% |
| Sxy | 3.83E+00 | -1.60E-01 | 3.88E+00 | -1.21E-01 | 4.00E+00 | 3.23E-01 | 3.95E+00 | 2.48E-01 | -1.24% | 24.51% | -4.36% | 301.88% | -2.97% | 255.07% |
| Syz | 2.84E+00 | -1.37E+00 | 2.98E+00 | -1.36E+00 | 3.06E+00 | -1.40E+00 | 3.02E+00 | -1.38E+00 | -4.88% | 0.58% | -7.81% | -2.68% | -6.32% | -0.96% |
| Sxz | -3.14E-01 | 4.47E-01 | -3.32E-01 | 4.52E-01 | -3.43E-01 | 4.62E-01 | -3.37E-01 | 4.55E-01 | -5.66% | -1.02% | -9.08% | -3.35% | -7.46% | -1.68% |
| Equiv. Stress (Von Mises) | 4.26E+02 | 6.83E+01 | 4.33E+02 | 6.93E+01 | 4.47E+02 | 7.10E+01 | 4.40E+02 | 7.01E+01 | -1.81% | -1.42% | -5.00% | -3.93% | -3.47% | -2.64% |

Table A.28. Sensitivity analysis of membrane and bending stress tensor component for the reference HCPB module and slice models on Path4.

| Path4 | Case0_Single Slice | | Case0_3Slice | | Case4 | | Case5 | | Case0 Membr. Error | Case0 Bend. Error | Case4 Membr. Error | Case4 Bend. Error | Case5 Membr. Error | Case5 Bend. Error |
|----------------------------------|--------------------|-----------------|-----------------|-----------------|-----------------|-----------------|-----------------|-----------------|--------------------|-------------------|--------------------|-------------------|--------------------|-------------------|
| | Membr. [MPa] | Bend. [MPa] | Membr. [MPa] | Bend. [MPa] | Membr. [MPa] | Bend. [MPa] | Membr. [MPa] | Bend. [MPa] | | | | | | |
| Sx | 3.07E+02 | 1.43E+01 | 3.13E+02 | 1.22E+01 | 3.19E+02 | 1.26E+01 | 3.15E+02 | 1.20E+01 | -1.84% | 14.72% | -3.64% | 11.43% | -2.39% | 15.99% |
| Sy | 1.37E+02 | -1.31E+02 | 1.40E+02 | -1.35E+02 | 1.41E+02 | -1.36E+02 | 1.41E+02 | -1.36E+02 | -2.04% | -2.97% | -2.81% | -3.68% | -2.74% | -3.75% |
| Sz | 1.03E+01 | 2.62E+01 | 1.02E+01 | 2.65E+01 | 1.03E+01 | 2.66E+01 | 1.02E+01 | 2.66E+01 | 0.10% | -1.08% | -0.07% | -1.62% | 0.14% | -1.52% |
| Sxy | -2.87E+00 | 3.15E+00 | -2.99E+00 | 3.28E+00 | -3.09E+00 | 3.41E+00 | -3.04E+00 | 3.34E+00 | -4.14% | -3.92% | -7.66% | -8.18% | -5.77% | -5.90% |
| Syz | 1.85E+00 | -9.61E+00 | 1.93E+00 | -1.04E+01 | 1.93E+00 | -1.04E+01 | 1.93E+00 | -1.04E+01 | -4.33% | -8.53% | -4.80% | -8.39% | -4.76% | -8.56% |
| Sxz | -2.10E+01 | -1.29E+00 | -2.14E+01 | -1.19E+00 | -2.19E+01 | -1.26E+00 | -2.16E+01 | -1.20E+00 | -2.21% | 7.82% | -4.37% | 2.09% | -2.97% | 7.12% |
| Equiv. Stress (Von Mises) | 2.61E+02 | 1.52E+02 | 2.66E+02 | 1.56E+02 | 2.71E+02 | 1.57E+02 | 2.67E+02 | 1.57E+02 | -1.90% | -2.14% | -3.81% | -2.93% | -2.47% | -2.80% |

Table A.29. Sensitivity analysis of membrane and bending stress tensor component for the reference HCPB module and slice models on Path5.

| Path5 | Case0_Single Slice | | Case0_3Slice | | Case4 | | Case5 | | Case0 Membr. Error | Case0 Bend. Error | Case4 Membr. Error | Case4 Bend. Error | Case5 Membr. Error | Case5 Bend. Error |
|----------------------------------|--------------------|-----------------|-----------------|-----------------|-----------------|-----------------|-----------------|-----------------|--------------------|-------------------|--------------------|-------------------|--------------------|-------------------|
| | Membr. [MPa] | Bend. [MPa] | Membr. [MPa] | Bend. [MPa] | Membr. [MPa] | Bend. [MPa] | Membr. [MPa] | Bend. [MPa] | | | | | | |
| Sx | -4.11E+00 | 4.81E+00 | -4.10E+00 | 4.81E+00 | -4.12E+00 | 4.81E+00 | -4.12E+00 | 4.81E+00 | 0.15% | 0.10% | -0.36% | 0.11% | -0.33% | 0.12% |
| Sy | 3.06E+02 | -5.17E+01 | 3.08E+02 | -5.26E+01 | 3.10E+02 | -5.42E+01 | 3.09E+02 | -5.34E+01 | -0.44% | -1.78% | -1.26% | -4.81% | -0.91% | -3.23% |
| Sz | 1.35E+02 | -7.48E+01 | 1.36E+02 | -7.72E+01 | 1.39E+02 | -8.09E+01 | 1.37E+02 | -7.89E+01 | -1.22% | -3.14% | -3.18% | -8.06% | -2.01% | -5.41% |
| Sxy | 1.28E-03 | -3.00E-03 | 1.86E-03 | -1.44E-02 | 2.10E-03 | 2.27E-02 | 2.02E-03 | 2.20E-02 | -44.95% | -379.93% | -64.05% | 855.09% | -57.55% | 834.07% |
| Syz | 2.87E-04 | -4.17E-04 | -2.87E-03 | -1.24E-02 | -3.00E-03 | -1.24E-02 | -3.02E-03 | -1.23E-02 | 1101.6% | -2881% | 1145% | -2883% | 1151% | -2860% |
| Sxz | 1.81E+01 | 2.19E-01 | 1.84E+01 | 2.36E-01 | 1.88E+01 | 2.39E-01 | 1.86E+01 | 2.37E-01 | -1.82% | -7.90% | -4.09% | -9.19% | -2.68% | -8.28% |
| Equiv. Stress (Von Mises) | 2.71E+02 | 7.10E+01 | 2.72E+02 | 7.29E+01 | 2.74E+02 | 7.59E+01 | 2.74E+02 | 7.43E+01 | -0.43% | -2.70% | -1.23% | -7.00% | -0.90% | -4.69% |

9.7 MAIA Procedure HCPB Test Case

In this Appendix, the results on primary and secondary linearized stresses calculated on the HCPB test case are reported.

From Table A.30 to Table A.34, the linearized primary and secondary stresses as well as the Von Mises equivalent stress for each path are displayed.

Table A.30. Membrane and bending primary stress tensor component for the HCPB slice model on Path1.

| Path1 | Primary Stress | | Secondary Stress | |
|----------------------------------|------------------|------------------|------------------|------------------|
| | Membrane [MPa] | Bending [MPa] | Membrane [MPa] | Bending [MPa] |
| Sx | 1.194E+01 | -7.134E+00 | -2.287E-01 | 2.014E+01 |
| Sy | -3.329E+00 | -8.140E-01 | -8.099E+01 | 3.629E+01 |
| Sz | 2.242E+01 | -3.120E+00 | 5.142E+01 | 1.164E+02 |
| Sxy | -5.770E-02 | 1.940E-01 | 1.727E+00 | 1.966E+01 |
| Syz | -2.621E-02 | -6.146E-03 | 1.100E-01 | 6.128E-02 |
| Sxz | 8.900E-04 | 1.352E-01 | 2.933E-01 | -1.243E-02 |
| Equiv. Stress (Von Mises) | 2.243E+01 | 5.555E+00 | 1.156E+02 | 9.560E+01 |

Table A.31. Membrane and bending primary stress tensor component for the HCPB slice model on Path2.

| Path2 | Primary Stress | | Secondary Stress | |
|----------------------------------|------------------|------------------|------------------|------------------|
| | Membrane [MPa] | Bending [MPa] | Membrane [MPa] | Bending [MPa] |
| Sx | 1.154E+01 | -7.136E+00 | -1.243E+01 | 2.505E+01 |
| Sy | -4.906E+00 | -1.975E+00 | -8.083E+01 | 2.333E+00 |
| Sz | 1.238E+01 | -2.312E+00 | -3.005E+01 | 7.460E+01 |
| Sxy | -2.870E-02 | -2.320E-01 | -2.539E+00 | 2.024E+01 |
| Syz | -2.806E-01 | -3.760E-01 | -4.421E+00 | -1.049E+01 |
| Sxz | -1.791E+00 | 7.060E-01 | -3.962E+01 | 1.779E+01 |
| Equiv. Stress (Von Mises) | 1.717E+01 | 5.205E+00 | 9.258E+01 | 8.127E+01 |

Table A.32. Membrane and bending primary stress tensor component for the HCPB slice model on Path3.

| Path3 | Primary Stress | | Secondary Stress | |
|----------------------------------|------------------|------------------|------------------|------------------|
| | Membrane [MPa] | Bending [MPa] | Membrane [MPa] | Bending [MPa] |
| Sx | 1.073E-01 | 1.169E-02 | 8.550E+00 | 4.328E-01 |
| Sy | -2.720E+00 | 3.350E-01 | -1.903E+02 | 4.621E+01 |
| Sz | -3.150E+00 | -1.187E+00 | -2.150E+02 | 2.895E+01 |
| Sxy | 3.450E-02 | 1.052E-02 | 2.309E+00 | 7.927E-01 |
| Syz | 2.370E-02 | -2.872E-02 | 1.129E+00 | -8.734E-01 |
| Sxz | -1.669E-02 | -3.559E-02 | -1.487E-01 | 2.442E-01 |
| Equiv. Stress (Von Mises) | 3.066E+00 | 1.391E+00 | 2.123E+02 | 4.009E+01 |

Table A.33. Membrane and bending primary stress tensor component for the HCPB slice model on Path4.

| Path4 | Primary Stress | | Secondary Stress | |
|----------------------------------|------------------|------------------|------------------|------------------|
| | Membrane [MPa] | Bending [MPa] | Membrane [MPa] | Bending [MPa] |
| Sx | 3.353E+01 | 1.557E+00 | 1.898E+02 | 1.281E+01 |
| Sy | -7.000E-01 | -1.886E+00 | 4.928E+01 | -4.010E+01 |
| Sz | 1.147E+01 | 7.340E+00 | -8.977E-02 | 7.379E+00 |
| Sxy | -8.608E-01 | 1.383E+00 | 4.096E-01 | -1.217E+00 |
| Syz | 1.126E-01 | 3.490E-02 | 8.032E-01 | -5.977E+00 |
| Sxz | -2.898E+00 | -5.427E-01 | -7.703E+00 | 1.209E+00 |
| Equiv. Stress (Von Mises) | 3.051E+01 | 8.475E+00 | 1.712E+02 | 5.155E+01 |

Table A.34. Membrane and bending primary stress tensor component for the HCPB slice model on Path5.

| Path5 | Primary Stress | | Secondary Stress | |
|----------------------------------|------------------|------------------|------------------|------------------|
| | Membrane [MPa] | Bending [MPa] | Membrane [MPa] | Bending [MPa] |
| Sx | -4.000E+00 | 4.779E+00 | -5.483E-02 | 5.073E-03 |
| Sy | -4.735E+00 | 2.398E+01 | 7.020E+01 | -6.787E+01 |
| Sz | 1.908E+00 | 7.669E+01 | 5.455E+01 | -1.088E+02 |
| Sxy | 2.322E-03 | -8.647E-03 | 1.760E-03 | -1.829E-03 |
| Syz | -1.139E-03 | 6.430E-03 | -2.444E-03 | 9.187E-03 |
| Sxz | 2.610E-02 | 1.745E-02 | 5.571E+00 | 5.927E-02 |
| Equiv. Stress (Von Mises) | 6.308E+00 | 6.449E+01 | 6.461E+01 | 9.516E+01 |

9.8 Validation of the Enhanced MAIA procedure for Water Activation Analysis

In this Appendix, the validation of MAIA procedure for the water activation analysis is reported.

In order to validate the MAIA procedure for the study of water activation, a simplified model of a water pipe has been created as reported in Figure A.16. The water pipe has dimensions in terms of diameter similar to the WCLL tubes and channels (Figure A.16 - b). An UM of the water domain has been created. Some details on the mesh are reported in Figure A.16 - c and in Table A.35. A neutronic input has been created using the Hybrid representation simulating the water by means of the UM. A neutron transport calculation has been performed using a mono-energetic planar neutron source with neutrons at 14.1 MeV as shown in Figure A.16 - d.

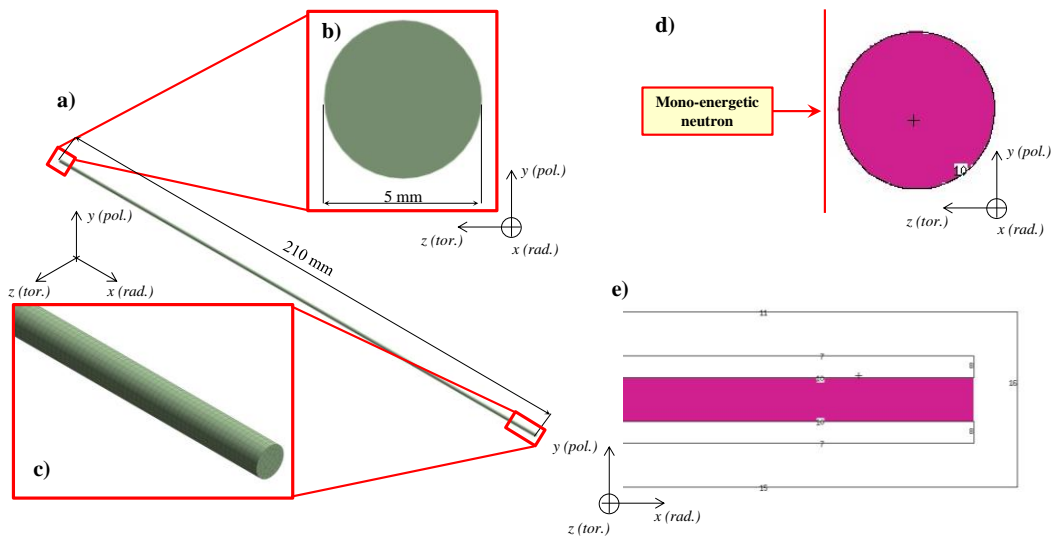


Figure A.16. Simplified model for validation of enhanced MAIA procedure. Left (a) and (b): geometric model. Left (c): detail of the UM. Right (d) and (e): neutronic model realised using the Hybrid representation.

Table A.35. Basic characteristics of UM used for the neutronic model.

| Element type | Number of nodes | Number of elements |
|----------------------|-----------------|--------------------|
| Quadratic Hexahedron | 40461 | 8400 |

From the neutronic calculation, the 3D profile of ^{16}N production rate, calculated using the EMBEE card, has been assessed following the procedure described in paragraph 6.3. The 3D distribution is shown in Figure A.17. The overall nitrogen production rate, calculated by means of F4 card modified with card FM, is equal to $1.53362\text{E}+00$ [$\text{m}^{-3} \text{s}^{-1}$]. In order to validate the coupling, the computational results obtained by means of MAIA procedure have been compared with an analytical solution for the transport of a passive scalar on one dimension. Under the assumptions of steady state condition and uniform nitrogen production rate along x , the analytical problem is described by the following system of equations:

$$\begin{cases} u_x \frac{\partial n_{^{16}\text{N}}(x)}{\partial x} = R^{^{16}\text{N}} - \lambda n_{^{16}\text{N}}(x) \\ n_{^{16}\text{N}}(0) = n_0 \end{cases} \quad (\text{A.1})$$

where for x equal to 0, at the inlet of the pipe, the n_0 is equal to $n(x_{\text{outlet}})e^{-\lambda \tilde{t}}$. \tilde{t} is the transit time of water outside the BB in the PHTS cooling circuit and for this calculation was assumed to be equal to 35.77 s (this value is derived taking into account a rough estimation in terms of distances and velocities in the PHTS

[115, 116]). Solving the system (A.1), the following equation is obtained:

$$n_{16N}(x) = n_0 e^{-\frac{\lambda}{u_r} x} + \frac{R^{16N}}{\lambda} \left(1 - e^{-\frac{\lambda}{u_r} x} \right) \quad (\text{A.2})$$

that is used to compare the computational results in terms of concentration calculated by means of ANSYS CFX as shown in Figure A.18 and in Table A.36 and Table A.37.

As it is possible to observe, the theoretical and computational estimation are in good agreement with a maximum variation of 1.42% that occurs in the first centimeters where the flow is not completely developed (see Figure A.17 - b) and, then, the mixing phenomena slightly modify the results without compromising the correct assessment of nitrogen concentration. For these reasons, the coupling procedure and the set of equations and boundary conditions used in MAIA procedure can be applied for studying the water activation in the WCLL BU.

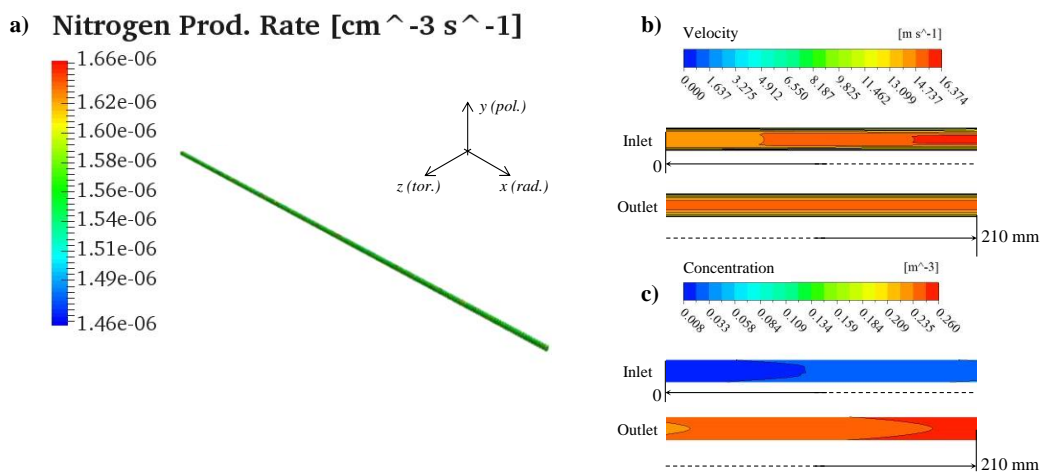


Figure A.17. Neutronic and fluid-dynamic results using MAIA procedure. Left (a): ^{16}N production rate. Right (b): velocity profile at the inlet and outlet of water pipe. Right (c): concentration profile of ^{16}N at the inlet and outlet of water pipe.

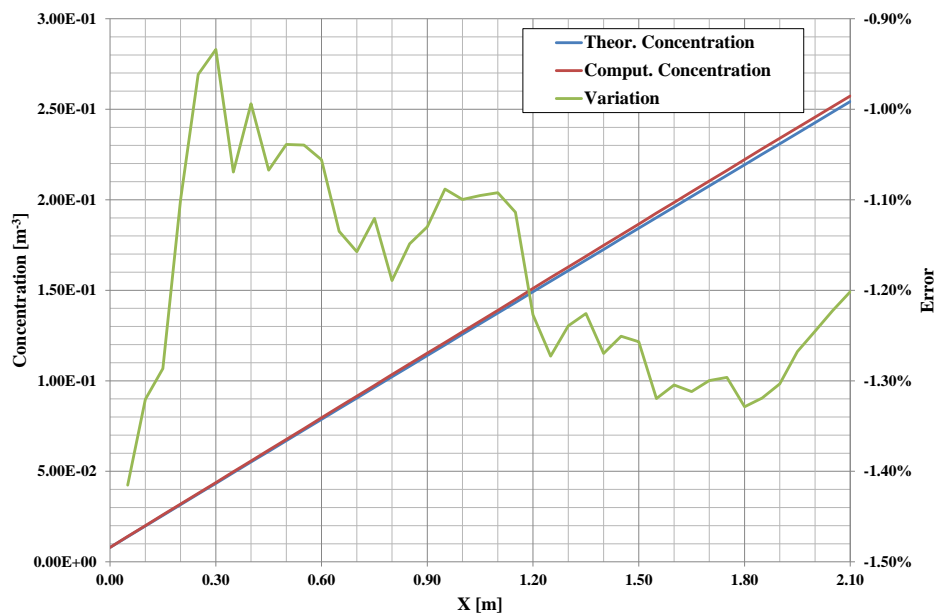


Figure A.18. Comparison between the theoretical calculation of nitrogen concentration by means of eq. (A.2) (blue curve) and the computational assessments at different axial positions (red curve). On the right vertical axes, the deviation between the two trends is reported.

Table A.36. Parameters adopted for the theoretical resolution.

| | | |
|---|-----------|-----------------------------------|
| Nitrogen production rate (F4 modified with FM) | 1.534E+00 | [m ³ s ⁻¹] |
| λ | 9.722E-02 | [s ⁻¹] |
| Velocity | 1.297E+01 | [m s s ⁻¹] |
| Length | 2.100E+00 | [m] |
| BB residence time | 1.619E-01 | [s] |
| PHTS residence time | 35.77 | [s] |

Table A.37. Comparison between theoretical and computational concentration assessment.

| Lenght [m] | Theoretical Concentration [m⁻³] | Computational Concentration [m⁻³] | Variation |
|-------------------|---|---|------------------|
| 0.00 | 7.945E-03 | 7.945E-03 | - |
| 0.05 | 1.385E-02 | 1.405E-02 | -1.42% |
| 0.10 | 1.976E-02 | 2.002E-02 | -1.32% |
| 0.15 | 2.567E-02 | 2.600E-02 | -1.29% |
| 0.20 | 3.157E-02 | 3.192E-02 | -1.10% |
| 0.25 | 3.747E-02 | 3.783E-02 | -0.96% |
| 0.30 | 4.337E-02 | 4.377E-02 | -0.93% |
| 0.35 | 4.926E-02 | 4.979E-02 | -1.07% |
| 0.40 | 5.516E-02 | 5.571E-02 | -0.99% |
| 0.45 | 6.105E-02 | 6.170E-02 | -1.07% |
| 0.50 | 6.694E-02 | 6.764E-02 | -1.04% |
| 0.55 | 7.283E-02 | 7.358E-02 | -1.04% |
| 0.60 | 7.871E-02 | 7.954E-02 | -1.06% |
| 0.65 | 8.460E-02 | 8.556E-02 | -1.13% |
| 0.70 | 9.048E-02 | 9.152E-02 | -1.16% |
| 0.75 | 9.635E-02 | 9.743E-02 | -1.12% |
| 0.80 | 1.022E-01 | 1.034E-01 | -1.19% |
| 0.85 | 1.081E-01 | 1.093E-01 | -1.15% |
| 0.90 | 1.140E-01 | 1.153E-01 | -1.13% |
| 0.95 | 1.198E-01 | 1.212E-01 | -1.09% |
| 1.00 | 1.257E-01 | 1.271E-01 | -1.10% |
| 1.05 | 1.316E-01 | 1.330E-01 | -1.10% |
| 1.10 | 1.374E-01 | 1.389E-01 | -1.09% |
| 1.15 | 1.433E-01 | 1.449E-01 | -1.11% |
| 1.20 | 1.492E-01 | 1.510E-01 | -1.23% |
| 1.25 | 1.550E-01 | 1.570E-01 | -1.27% |
| 1.30 | 1.609E-01 | 1.629E-01 | -1.24% |
| 1.35 | 1.667E-01 | 1.688E-01 | -1.23% |
| 1.40 | 1.726E-01 | 1.748E-01 | -1.27% |
| 1.45 | 1.784E-01 | 1.807E-01 | -1.25% |
| 1.50 | 1.843E-01 | 1.866E-01 | -1.26% |
| 1.55 | 1.901E-01 | 1.926E-01 | -1.32% |
| 1.60 | 1.960E-01 | 1.985E-01 | -1.30% |
| 1.65 | 2.018E-01 | 2.044E-01 | -1.31% |
| 1.70 | 2.076E-01 | 2.103E-01 | -1.30% |
| 1.75 | 2.135E-01 | 2.162E-01 | -1.30% |
| 1.80 | 2.193E-01 | 2.222E-01 | -1.33% |
| 1.85 | 2.251E-01 | 2.281E-01 | -1.32% |
| 1.90 | 2.310E-01 | 2.340E-01 | -1.30% |
| 1.95 | 2.368E-01 | 2.398E-01 | -1.27% |
| 2.00 | 2.426E-01 | 2.456E-01 | -1.25% |
| 2.05 | 2.484E-01 | 2.515E-01 | -1.22% |
| 2.10 | 2.542E-01 | 2.573E-01 | -1.20% |

9.9 Conventional and EMBEE Tallies Comparison for Nitrogen Production Rate

In this Appendix, the comparison between the ENBEE and conventional MCNP tally is reported.

In Table A.38 and Table A.39, the comparison between the conventional F4 card results modified by means of FM card and the integral of the elements results over the pseudo cells volumes is reported.

Table A.38. Comparison between the conventional and ENBEE cards for the ^{16}N production rate calculation.

| ^{16}N Concentration Production Rate [$\text{cm}^{-3} \text{s}^{-1}$] | | | |
|--|------------------|------------------|---------------|
| Cell_UM | Tally F4 with FM | EMBEE CARD | ϵ |
| 4001 | 1.579E+10 | 1.579E+10 | 0.00% |
| 4002 | 1.738E+10 | 1.737E+10 | 0.07% |
| 4003 | 1.741E+10 | 1.743E+10 | -0.09% |
| 4004 | 1.586E+10 | 1.584E+10 | 0.11% |
| 4005 | 1.015E+10 | 1.014E+10 | 0.14% |
| 4006 | 1.021E+10 | 1.018E+10 | 0.21% |
| 4007 | 6.558E+09 | 6.555E+09 | 0.04% |
| 4008 | 6.947E+09 | 6.936E+09 | 0.15% |
| 4009 | 6.958E+09 | 6.953E+09 | 0.08% |
| 4010 | 6.588E+09 | 6.565E+09 | 0.34% |
| 4011 | 4.239E+09 | 4.231E+09 | 0.19% |
| 4012 | 4.252E+09 | 4.244E+09 | 0.20% |
| 4013 | 2.775E+09 | 2.779E+09 | -0.12% |
| 4014 | 2.783E+09 | 2.781E+09 | 0.09% |
| 4015 | 1.140E+09 | 1.137E+09 | 0.32% |
| 4016 | 1.146E+09 | 1.141E+09 | 0.49% |
| 4017 | 3.486E+08 | 3.489E+08 | -0.09% |
| 4018 | 3.505E+08 | 3.503E+08 | 0.06% |
| 4019 | 5.459E+07 | 5.458E+07 | 0.02% |
| 4020 | 3.794E+06 | 3.807E+06 | -0.37% |
| 4021 | 3.946E+06 | 3.955E+06 | -0.22% |
| 5001 | 2.953E+10 | 2.999E+10 | -1.56% |
| 5002 | 3.105E+10 | 3.192E+10 | -2.82% |
| 5003 | 3.042E+10 | 3.128E+10 | -2.84% |
| 5004 | 3.003E+10 | 3.037E+10 | -1.14% |
| 5005 | 2.985E+10 | 3.055E+10 | -2.36% |
| 5006 | 2.978E+10 | 3.006E+10 | -0.94% |
| 5007 | 2.986E+10 | 3.055E+10 | -2.32% |
| 5008 | 3.004E+10 | 3.031E+10 | -0.89% |
| 5009 | 3.043E+10 | 3.088E+10 | -1.49% |
| 5010 | 3.102E+10 | 3.136E+10 | -1.09% |
| 5011 | 2.952E+10 | 2.994E+10 | -1.43% |
| TOTAL | 4.625E+11 | 4.681E+11 | -1.21% |

Table A.39. Comparison between the conventional and ENBEE cards for the ^{17}N production rate calculation.

| ^{17}N Concentration Production Rate [$\text{cm}^{-3} \text{s}^{-1}$] | | | |
|--|------------------|------------------|---------------|
| Cell_UM | Tally F4 with FM | EMBEE CARD | ϵ |
| 4001 | 1.615E+06 | 1.615E+06 | 0.01% |
| 4002 | 1.780E+06 | 1.779E+06 | 0.07% |
| 4003 | 1.783E+06 | 1.785E+06 | -0.09% |
| 4004 | 1.622E+06 | 1.620E+06 | 0.11% |
| 4005 | 1.035E+06 | 1.034E+06 | 0.15% |
| 4006 | 1.040E+06 | 1.038E+06 | 0.22% |
| 4007 | 6.666E+05 | 6.663E+05 | 0.04% |
| 4008 | 7.062E+05 | 7.051E+05 | 0.16% |
| 4009 | 7.076E+05 | 7.070E+05 | 0.08% |
| 4010 | 6.694E+05 | 6.671E+05 | 0.35% |
| 4011 | 4.295E+05 | 4.287E+05 | 0.19% |
| 4012 | 4.310E+05 | 4.301E+05 | 0.20% |
| 4013 | 2.805E+05 | 2.808E+05 | -0.12% |
| 4014 | 2.814E+05 | 2.812E+05 | 0.09% |
| 4015 | 1.147E+05 | 1.143E+05 | 0.33% |
| 4016 | 1.154E+05 | 1.148E+05 | 0.50% |
| 4017 | 3.489E+04 | 3.491E+04 | -0.07% |
| 4018 | 3.515E+04 | 3.513E+04 | 0.07% |
| 4019 | 5.422E+03 | 5.418E+03 | 0.08% |
| 4020 | 3.777E+02 | 3.789E+02 | -0.31% |
| 4021 | 3.886E+02 | 3.887E+02 | -0.04% |
| 5001 | 3.041E+06 | 3.088E+06 | -1.56% |
| 5002 | 3.198E+06 | 3.288E+06 | -2.82% |
| 5003 | 3.133E+06 | 3.221E+06 | -2.84% |
| 5004 | 3.092E+06 | 3.127E+06 | -1.14% |
| 5005 | 3.073E+06 | 3.146E+06 | -2.35% |
| 5006 | 3.067E+06 | 3.096E+06 | -0.94% |
| 5007 | 3.075E+06 | 3.146E+06 | -2.32% |
| 5008 | 3.094E+06 | 3.122E+06 | -0.89% |
| 5009 | 3.134E+06 | 3.181E+06 | -1.49% |
| 5010 | 3.196E+06 | 3.231E+06 | -1.09% |
| 5011 | 3.039E+06 | 3.082E+06 | -1.43% |
| TOTAL | 4.750E+07 | 4.807E+07 | -1.21% |

Acknowledgements

I am really beholden to Prof. Dr.- Ing. Robert Stieglitz and Prof. Dr.- Ing. Pietro Alessandro Di Maio for giving me the opportunity to carry out an international joint supervision PhD work at the Institute of Neutron Physics and Reactor Technology and at the University of Palermo within the framework of scientific cooperation between Italian and German teams.

To all, I would like to express my most sincere gratitude for their precious guidance, their valuable reviewing work and for their advice that put me on the right path for the accomplishment of this challenging PhD project.

My sincere thanks also go to Dr. Lorenzo Boccaccini who provided me with the opportunity to join his team and who gave me access to the research project and data.

I am truly thankful to Dr. Pierluigi Chiovaro and Dr. Ivan Alessio Maione for their continuous and valuable support of my PhD project and related research, for their patience and motivation. Without their precious support, it would not be possible to conduct this research.

I would like to thank the rest of my colleagues: Dr. Gaetano Bongiovi, Mr. Salvatore D'Amico and Dr. Fabrizio Franza for their encouragement and their insightful comments.

I am very grateful to Dr. Francisco Hernandez, Dr. Alessandro Del Nevo and Dr. Fabio Cismondi for their availability, for their prompt assistance in the acquisition of the information related to their design activities and for their hard questions, which stimulated me to widen my research from various perspectives.

Special thanks go to my friends and my family for their unlimited and outstanding support during my whole life, for the opportunities that they provided me and for showing me the importance of education as well as of the human relationships.

Last but surely not least, I would like to give my most sincere and best thanks to my lovely wife Mrs. Cristina Onorato for her patience during the most critical periods of this PhD work, for her continuous encouragement, for her unconditional trust for the accomplishment of this challenging project and for her not obvious love which is the basis of my strength. Without her, this PhD project, as well as many other achievements in my professional and private life, would not be possible.

This work has been carried out within the framework of the EUROfusion Consortium and has received funding from the Euratom research and training programme 2014-2018 and 2019-2020 under grant agreement No 633053. The views and opinions expressed herein do not necessarily reflect those of the European Commission.